

Measuring and Modeling the
Interplay between Planetary
Orbits, Interiors, Surfaces, and
Atmospheres

Thesis by
Peter Benjamin Buhler

In Partial Fulfillment of the Requirements for the
Degree of
Doctor of Philosophy

The logo for the California Institute of Technology (Caltech), featuring the word "Caltech" in a bold, orange, sans-serif font.

CALIFORNIA INSTITUTE OF TECHNOLOGY
Pasadena, California

2018
(Defended May 17, 2018)

© 2018

Peter Benjamin Buhler
ORCID: 0000-0002-5247-7148

*It is the glory of God to conceal a matter;
to search out a matter is the glory of kings.*

Proverbs 25:2

You will know the truth, and the truth will set you free

John 8:32

ACKNOWLEDGEMENTS

First and foremost, I thank my lovely wife Vivian for all her love and support throughout this five-year adventure. I could not have done it without you.

Mom, Dad, and Suzz, thank you for starting me off on the right path, and your continuous love and care throughout all of life's twists and turns. Mami, Babi, and Ian, it is hard to believe we met less than six years ago. You have made graduate school much more enjoyable. Kathryn and Jacob, you always know how to help me unwind from school.

Tris, John, and Kevin, though you did not reach the finish line with me, you taught me to be creative, upright, and confident. That has been integral to my success in graduate school and my happiness in life. Thank you.

To my best friends, Jon and Nate (& family!), looking forward to winter break with you always got me through.

Andy, I could not have asked for a better advisor. Period.

Bethany, Heather, Konstantin, and Dave, thank you for your wisdom, guidance, explanations, and support. They made grad school the most amazing experience of my life.

Jean-Philippe and Victor, thank you for your thoughtful insight and guidance throughout the thesis process.

Henry and Peter, thank you taking me under your wing. I learned how to do grad school from you.

Chris, Dana, Pushkar, Ian, Mike, Lulu, Elizabeth, Nancy, I couldn't imagine grad school without your friendship.

Jim, Caleb, Jay, Laura, and the Seafloor gang. I enjoyed my time so much with you that I became a planetary scientist. Thank you!

To my friends from the Caltech Christian Fellowship: Luke, Stephen, Jonathan, Robb, Andy, Peter, Sam, Tom, Tim, Grace, Daniel, Edward, Abraham, Jay & Mary, Cathy, Mary-Beth, Yuka, Lisa, Jessica, Madeleine, Eliza, Abraham, Andrew, and Wouter. The good times we shared and your prayers and encouragement got me through Caltech (both times). I wouldn't have gotten here without you.

Wang Laoshi and Ming Laoshi, your classes made grad school so much better.

Melissa, thank you for your camaraderie and encouragement in our Xiphosuran adventure.

To the Watson Fellowship, you were exactly what I needed to recharge after my undergraduate years.

ABSTRACT

Typically, we only have access to observations that directly probe the instantaneous state of a planet. However, these instantaneous properties are often set by the long-term interplay between several aspects of the planet. I thus use quantitative models of the interactions between the orbital, interior, surface, and atmospheric evolution in the case of three planetary bodies (Mars, Pluto, and the extrasolar planet HAT-P-13b) to gain insight into the underlying physical processes that govern the evolution of planets.

In chapter 2, the interplay between the interior structure and orbital evolution of the gas giant exoplanet HAT-P-13b allows measurements of its orbit to reveal its interior structure. I use telescopic observations of HAT-P-13b to measure its orbit and thus determine its core mass.

In chapter 3, cell-shaped landforms on Sputnik Planitia, the surface of a vast deposit of nitrogen ice covering 5% of Pluto's surface, are the surface expression of convection within the nitrogen ice that is driven by heat flow from Pluto's interior. The cells have sublimation pits on them, with smaller pits near their centers and larger pits near their edges. Using a simple model, I calculate the sublimation rate of these pits, which allows the determination of a size-age relationship. I then use the spatial size distribution of pits on cells to calculate their convection rate, which constrains the plutonian heat flow and thus the interior properties of Pluto.

In chapter 4, the interplay of condensation and sublimation between the surface and atmosphere of Mars create a baffling array of uniquely martian morphologies carved into the martian residual south polar CO₂ cap (RSPC). Using a multi-year baseline of high-resolution observations to track the evolution of these morphologies, I build a self-consistent conceptual

framework capable of explaining the basic mechanisms that give rise to the diversity of landforms that make up the RSPC.

In chapter 5, the secular evolution of Mars' orbit drives the evolution of the equilibrium relationship between the martian atmospheric pressure and the large CO₂ ice deposit on the martian south polar cap. I construct the first self-consistent conceptual framework capable of predicting the existence and form of the martian residual south polar cap and the buried CO₂ deposit. I then use this framework to compute the secular pressure history of Mars.

Together, the results of these investigations provide new perspective into the fundamental processes driving the formation and evolution of planetary bodies.

PUBLISHED CONTENT AND CONTRIBUTIONS

Buhler, P.B., Knutson, H.A., Batygin, K., Fulton, B.J., Fortney, J.J., Burrows, A., Wong, I. (2016). Dynamical Constraints on the Core Mass of Hot Jupiter HAT-P-13b. In: *The Astrophysical Journal* 821, 26-37. doi:10.3847/0004-637X/821/1/26. Reproduced by permission of the AAS.

P.B.B. participated in the conception of the project, performed the data analysis and statistical analysis, and wrote the manuscript.

Buhler, P.B & Ingersoll, A.P. (2018). Sublimation pit distribution indicates convection cell surface velocities of ~ 10 cm per year in Sputnik Planitia, Pluto. In: *Icarus* 300, 327-340. doi: 10.1016/j.icarus.2017.09.018 © 2018. This manuscript version is made available under the CC-BY-NC-ND 4.0 license <http://creativecommons.org/licenses/by-nc-nd/4.0/>

P.B.B. conceived the project, collected the pit distribution data and performed the data analysis and statistical analysis, and wrote the manuscript.

Buhler, P.B., Ingersoll, A.P., Ehlmann, B.L., Fassett, C.I., Head, J.W. (2017). How the Martian Residual South Polar Cap Develops Quasi-Circular and Heart-Shaped Pits, Troughs, and Moats. In: *Icarus* 286, 69-93. doi:10.1016/j.icarus.2017.01.012. © 2017. This manuscript version is made available under the CC-BY-NC-ND 4.0 license <http://creativecommons.org/licenses/by-nc-nd/4.0/>

P.B.B. conceived the project, collected the image data, performed the data analysis, and wrote the manuscript.

TABLE OF CONTENTS

Acknowledgements.....	iv
Abstract	vi
Published Content and Contributions.....	viii
Table of Contents.....	ix
List of Illustrations	xii
List of Tables.....	xv
Chapter I: Introduction	1
1.1 Hot Love.....	1
1.2 An Overturning Heart.....	3
1.3 A New Heart	4
1.4 A Match Made on Mars	7
Chapter II: Dynamical Constraints on the Core Mass of Hot Jupiter	
HAT-P-13b	14
2.1 Abstract.....	14
2.2 Introduction.....	15
2.3 Methods.....	17
2.3.1 Observations and Photometric Time Series Extraction.....	17
2.3.2 Instrumental Noise Model and Optimal Aperture Selection ..	18
2.3.3 Eclipse Statistical Errors	24
2.3.4 Eccentricity Determination.....	25
2.3.5 Interior Modeling	25
2.3.6 Secular Perturbation Theory.....	28
2.3.7 Core Mass Determination.....	31
2.3.8 Atmospheric Measurements	31
2.4 Results.....	32
2.4.1 Secondary Eclipse Measurements.....	32
2.4.2 Eccentricity and Core Mass.....	34
2.4.3 Atmospheric Properties	35
2.5 Discussion	36
2.5.1 Effects of Coplanarity and Apsidal Alignment.....	36
2.5.2 Interior Structure	39
2.5.3 Dayside Atmosphere.....	42
2.5.4 Comparison to Other Systems.....	43
2.5.5 Future Measurements	45
2.6 Conclusions.....	47
2.7 Acknowledgments.....	48
Chapter III: Sublimation Pit Distribution Indicates Convection Cell Surface Velocities of ~ 10 cm per Year in Sputnik Planitia, Pluto	58

3.1 Abstract.....	58
3.2 Introduction.....	59
3.3 Methods.....	62
3.3.1 Pit Distribution Determination	62
3.3.2 Analytic Sublimation Model	67
3.4 Results.....	70
3.4.1 Pit Distribution and Convection Rates	70
3.5 Discussion	73
3.5.1 Cell Surface Rheology.....	73
3.5.2 Pit Distribution Linearity and Nonzero Intercept.....	78
3.5.3 Mergers between Pits.....	83
3.5.4 Cell Surface Ages	84
3.5.5 Evidence for Convection Instability	85
3.5.6 Speculation about Sparse Pitting Near Cell Edges	88
3.5.7 Comparison to Other Explanations for the Observed Pit Distribution.....	89
3.6 Conclusions.....	90
3.7 Acknowledgments.....	91
Chapter IV: How the martian Residual South Polar Cap Develops Quasi-Circular and Heart-Shaped Pits, Troughs, and Moats	96
4.1 Abstract.....	96
4.2 Introduction.....	97
4.3 Methods.....	100
4.4 Observations.....	102
4.4.1 Dark Fans on Mesa Sides	102
4.4.2 Fracturing of Mesa Upper Surfaces.....	108
4.4.3 Collapse and Deterioration of Upper Mesa Surfaces	114
4.4.4 Inception of Quasi-Circular Pits	120
4.4.5 Gentle Ramps and Steep Scarps Combine to Form Heart-Shaped Pits, Linear Troughs, and Moats	121
4.5 Discussion	127
4.5.1 Mesa Dust Content Generates Dark Fans	127
4.5.2 Interior Sublimation Drives Fracturing and Slab Settling	129
4.5.3 Interior Sublimation Rates Based on Halos around Fractures.....	132
4.5.4 Seasonal CO ₂ Ice Incorporated into the RSPC.....	135
4.5.5 Scarp Steepness and the Deposition-Sublimation Cycle as Landform Drivers	138
4.6 Conclusions.....	140
4.7 Acknowledgments.....	141
Chapter V: Mars' Secular Amazonian Pressure Cycle, as Buffered by its South Polar CO ₂ Deposit.....	148

5.1 Introduction.....	148
5.2 Numerical Methods.....	149
5.3 The Secular Amazonian Pressure Curve	152
5.3.1 Conceptual Framework and Approach	152
5.3.2 The Equilibrium Pressure as a Function of Orbital Elements.....	155
5.3.3 The Pressure History from -21 Ma to +11 Ma	157
5.3.4 The Age of the South Polar CO ₂ Deposit	160
5.3.5 Pressure Characterization over 3 Ga.....	162
5.4 Discussion	166
5.4.1 Self-Stabilization of the RSPC-Buried CO ₂ System	166
5.4.2 Second Order Characteristics of the RSPC.....	170
5.4.3 Future Modeling and Assumptions	171
5.5 Conclusions.....	173
5.6 Appendix. The Effect of an H ₂ O Ice Cap on Buried CO ₂ Ice	174
Chapter VI: Concluding Thoughts.....	184
6.1 Introduction.....	184
6.2 Gas Giant Interior Properties.....	184
6.3 Climates and Surfaces of Bodies with Atmospheres Controlled by Vapor Pressure Equilibrium	188

LIST OF ILLUSTRATIONS

<i>Number</i>	<i>Page</i>
1.1 Mars seasonal pressure curve.....	6
2.1 Pixel level decorrelation performance	22
2.2 Spitzer measurements.....	33
2.3 Probability distribution of the true core mass of HAT-P-13b	34
2.4 Hat-P-13b atmospheric models	36
2.5 Relationship between e_b and k_{2b} for the HAT-P-13 system	40
3.1 Sputnik Planitia	60
3.2 Cells I-IV.....	61
3.3 Mapped pits on all cells.....	64
3.4 Pit radii as a function of distance from the spreading center	65
3.5 Geometrically accurate depiction of pits.....	67
3.6 The probability density function of the pit growth rate	69
3.7 The probability density function of the surface velocity for each cell	71
3.8 Schematic surface velocity profile	80
3.9 The number of pits N per each kilometer bin in cell II.....	81
3.10 Fits to the upper and lower halves of the left side of cell III.....	86
3.11 Fits to the upper and lower halves of the right side of cell I	87
4.1 Visual terminology definitions	99
4.2 Context images for other figures	101
4.3 Examples of fans from all five study locations	103
4.4 Unit B7. a. No dark fan. b. 38 sols later. Dark fan is apparent.....	104
4.5 Dark fan at the base of a CO ₂ mesa.....	104
4.6 5 martian year time series at different L_S	105
4.7 Seasonal timing of different features by unit.....	106

4.8	Unit B7. a. More fans are apparent in MY 29 earlier in summer.	107
4.9	Crack formation	108
4.10	Fractures and tilted slabs	109
4.11	Time series of fracture evolution.....	110
4.12	Fractures with halos	111
4.13	Fractures with halos on thin but not thick mesas	112
4.14	Crack and ridge inversion	114
4.15	Mesa with low, rough perimeter	115
4.16	Polygonal depressions	116
4.17	Vermicular texture.....	118
4.18	Time series of two nascent pits	119
4.19	Evolution from a crack to a pit.....	120
4.20	The smallest pit observed to erode via calving blocks.....	121
4.21	Crescentic pit formation on the edge of mesas	122
4.22	Time series of crescents	123
4.23	Crescents grow into heart shapes or troughs	124
4.24	Crescents, linear troughs, sinuous ridges, and moats.....	125
4.25	Accumulation of CO ₂ ice.....	126
4.26	Interpretation of the development of fractures	130
4.27	Light scattering geometries in the RSPC.....	137
5.1	Schematic of the 1-d thermal model	150
5.2	1-d thermal model outputs.....	154
5.3	The equilibrium pressure solution as a function of e and ϖ	156
5.4	Orbital solutions from Laskar et al. (2004)	158
5.5	The equilibrium pressure solution from -21 Ma to +11 Ma	159
5.6	Fraction of ϖ for which P_{eq} exceeds a given pressure for given $e-\varepsilon$	163
5.7	The probability distribution of P_{eq} values over 3 Ga	166

5.8	Kilometer-scale depressions in the H ₂ O layer	168
5.9	The effect of insolation-dependent albedo.....	172
5.A1	Incoming solar power and outgoing emitted power	175
5.A2	Energy balance of CO ₂ ice under a layer of H ₂ O ice	176
5.A3	The effect of varying latitude, pressure, and obliquity	178
6.1	Eccentricity-Love number relationship for hot Jupiters of interest ..	187

LIST OF TABLES

<i>Number</i>	<i>Page</i>
2.1 HAT-P-13 System Properties	30
3.1 General Cell and Pit Properties	69
3.2 Pit Distribution.....	72
3.3 Pit Distribution Accounting for Resolution	85
5.1 Timing of Pressure Maxima.....	160

Chapter 1

INTRODUCTION

The complex and often non-linear interaction between the orbital, interior, surface, and atmospheric properties of planets gives rise to a huge variety of phenomena that far exceed our experience on Earth or even the solar system. However, due to constraints of the massive time and distance scales inherent to planetary science, we often only have access to limited measurements that directly relate to only one of these properties. We must therefore rely on physical intuition, physical models, and imagination to decipher these restricted observations and elucidate the properties we cannot directly see. These hidden properties offer profound insight into how planets and planetary systems operate and ultimately inform us of our own origins, evolution, and future prospects in the solar system and beyond. I now introduce the stories of *Hot Love*, *An Overturning Heart*, *A New Heart*, and *A Match Made on Mars*, which will shed light on the secret lives of planets.

1.1 Hot Love

HAT-P-13b is a hot Jupiter orbiting a star called HAT-P-13 about 214 parsecs (or 698 light-years) away (Bakos et al., 2009). Hot Jupiters are Jupiter-sized planets that orbit close to their host star; our own solar system has nothing like them. HAT-P-13b has a mass of 0.899 times the mass of Jupiter (M_J , Knutson et al., 2014) and orbits its host star at a distance of 0.0462 AU (Southworth et al., 2012; 1 AU = 1.5×10^{11} m, the average earth-sun distance), which is about ten times closer

than Mercury is to our Sun. And it is not alone. The system also hosts HAT-P-13c, a massive ($14.2 M_J$), eccentric ($e = 0.66$) companion orbiting at a distance of 1.186 au (Winn et al. 2010).

The special dynamical interaction between HAT-P-13, HAT-P-13b, and HAT-P-13c provides leverage to probe the internal structure of HAT-P-13b, as follows. The proximity of HAT-P-13b to its host star means that tidal interaction between HAT-P-13b and the star quickly acts to drain its orbital energy, circularizing its orbit (Mardling, 2007; Ragozzine and Wolf, 2009). However, the presence of the massive and eccentric HAT-P-13c acts to prevent complete circularization of the orbit of HAT-P-13b. Instead, the system tends toward a nearly elliptic equilibrium point (Batygin et al., 2009). The exact equilibrium point depends on the eccentricity, semi-major axis, and mass of HAT-P-13b and HAT-P-13c, the mass of the star, and the radius and tidal Love number of HAT-P-13c. All the system parameters except the tidal Love number can be measured directly.

Calculating the Love number is desirable because it provides information about the mass distribution inside HAT-P-13, including the presence and mass of a core (Love, 1909). The parameter that adds the most uncertainty in the determination of the Love number is HAT-P-13b's eccentricity, which is small and difficult to measure. In **DYNAMICAL CONSTRAINTS ON THE CORE MASS OF HOT JUPITER HAT-P-13b**, I use a combination of transit and secondary eclipse measurements (detecting a dip in light from the system when HAT-P-13b passes in front of and behind its host star, respectively, e.g. Charbonneau et al., 2005) to sensitively characterize HAT-P-13b's orbit. Departures from a half-orbital-phase timing between transit and secondary eclipse encode precise information about the magnitude of the eccentricity. This, in turn allows for an accurate determination of the core mass of HAT-P-13b. This is important because, aside from Jupiter and Saturn, there are no other gas giant planets for which the core mass can be

determined and the presence and mass of a core provide critical ground truth for planet formation theories (e.g. Mizuno 1980; Bodenheimer & Pollack 1986; Pollack et al. 1996; Boss, 1997).

1.2 An Overturning Heart

The New Horizons mission's 2015 arrival at the Pluto system revealed an unexpectedly geologically active planet covered in bizarre and unfamiliar landforms (Stern et al., 2015). Chief among the surprises was Sputnik Planitia, the heart-shaped surface of a vast basin full of N₂ ice that covers an area of approximately one million square kilometers, which is ~5% the area of Pluto or ~1.8 times the area of France (Moore et al., 2016a). Sputnik Planitia is covered by cell-shaped landforms with areas ranging from a few hundred to a few thousand square kilometers (White et al., 2017). These landforms are likely the surface expression of convection within the N₂ ice, driven by the slow release of primordial and radiogenic heat from the interior of Pluto (McKinnon et al., 2016; Trowbridge et al., 2016), which heats Sputnik Planitia from below like a (not particularly hot) stove.

Understanding the convection behavior, particularly convection rates, in Sputnik Planitia thus provides a constraint on heat flow from the interior of Pluto. This, in turn, provides information about its rock-to-ice ratio, constraining its formation location and subsequent dynamical history under the influence of giant planet migration (e.g. Tsiganis et al., 2005).

Providing ground truth of convection rates is thus important for interpreting modeled convection behavior. However, obtaining surface ages, a key step in measuring convection rates requires creativity because the traditional method of using impact crater densities to date the

surface (e.g. Hartmann, 1966) is unavailable because there are no impact craters in Sputnik Planitia observable in the New Horizons data (Greenstreet et al., 2015). While this provides an upper bound of 10 million years for the age of Sputnik Planitia, modeling suggests that convection takes place on the order of a few hundred thousand years. Thus, a more sensitive determination of the age is needed to test and discriminate between model predictions.

Fortunately, the N₂ ice in the cellular terrain in Sputnik Planitia is covered with sublimation pits (e.g. Moore, et al. 2016b), which provides an alternative method for age dating. The cells typically have smaller pits toward their centers and larger pits toward their edges, suggesting that the pits are growing during conveyor-belt-like transit across the cells. By modeling the growth rate of the pits (Ingersoll et al., 1992), the age of the pits can be determined based on their size, and the size distribution used to date the surface and calculate convection rates. I perform this analysis in **SUBLIMATION PIT DISTRIBUTION INDICATES CONVECTION CELL SURFACE VELOCITIES OF ~10 CM PER YEAR IN SPUTNIK PLANITIA, PLUTO.**

1.3 A New Heart

Mars provides a simplified laboratory, compared to the Earth, for studying how the climates of terrestrial planets operate. Thus, the insights gained from understanding the martian climate transcend relevance for Mars (such as habitability and human utilization) and illuminate how climates work in general, including our own.

Early Mars was likely characterized by a more clement climate with at least periodically occurring rivers and standing bodies of water and pervasive aqueous alteration (e.g. Carr, 2007). However,

starting about 3.5 billion years ago, the climate began transitioning into its modern, generally arid and dry state (e.g. Ehlmann and Edwards, 2014).

The modern atmosphere of Mars is primarily (96%, Owen et al., 1979) composed of CO₂ and, on annual timescales, the martian climate is dominated by its CO₂ cycle. Each winter the polar regions become cold enough that the ground temperature drops below the frost point of CO₂ and approximately 25% of the atmosphere condenses onto the winter hemisphere as ground ice (e.g., Kelly et al., 2006). This seasonal CO₂ deposit is typically ~1 m thick near the pole and gradually thins to its most poleward extent near 55° of latitude (Piqueux et al., 2015). Then, with the coming of spring, the entirety of the seasonal deposit gradually sublimates again back into the atmosphere. This creates a semiannual pressure oscillation that was first measured by the Viking Landers (Figure 1.1, Hess et al., 1977).

There is, however, one region of the south pole where CO₂ persists throughout the entire year, called the residual south polar cap (RSPC, a.k.a. unit Aa_{4b}; Tanaka et al., 2014). The RSPC is a 1-10 m thick CO₂ ice deposit that has a mass ~1% of the present-day atmosphere (Thomas et al., 2016) and a general structure that is stable intra- and inter-annually. The RSPC consists of plateaus and mesas of CO₂ ice that are dissected by myriad pits and troughs, which typically change annually at meter-scales (e.g. Malin et al., 2001). Most of these morphologies have been extensively documented (Thomas et al., 2016), although a comprehensive understanding of how these landforms develop has remained elusive.

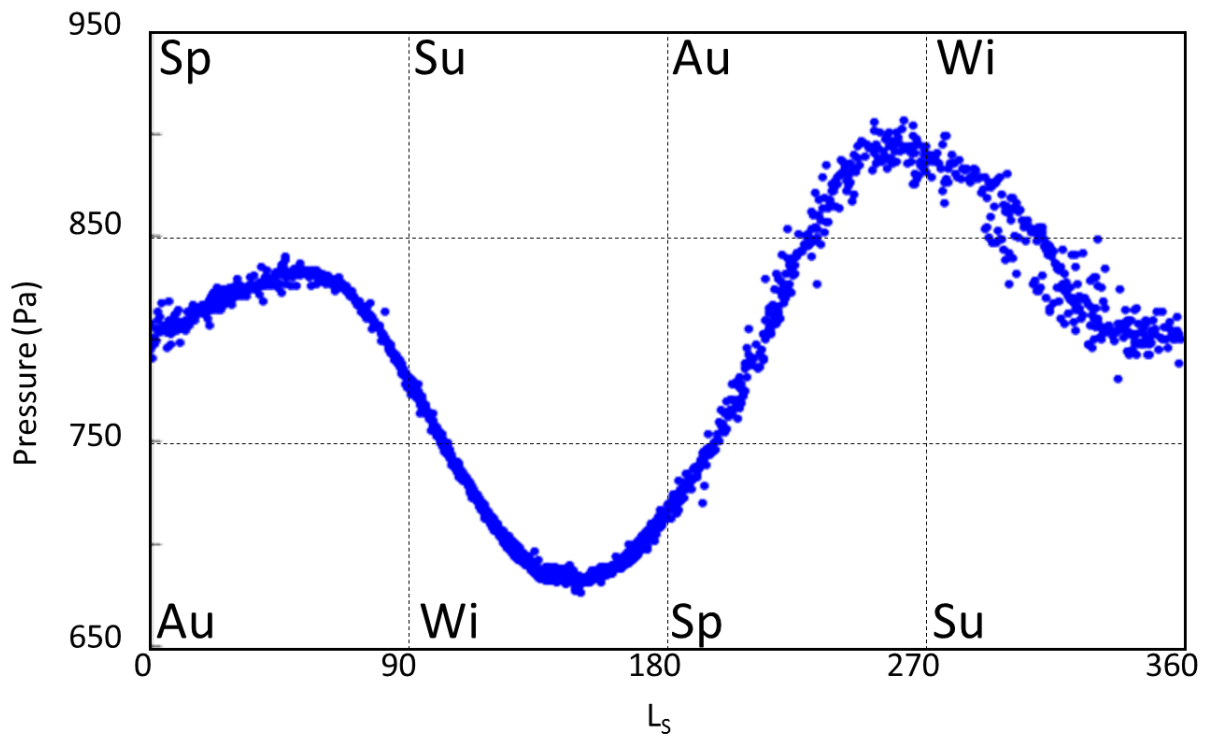


Figure 1.1. The seasonally varying Viking Lander 1 pressure measurements. L_s is solar longitude. Labels (Sp, Su, Au, Wi) on the top indicate the northern season. Labels on the bottom are for the south.

In **HOW THE MARTIAN RESIDUAL SOUTH POLAR CAP DEVELOPS QUASI-CIRCULAR AND HEART-SHAPED PITS, TROUGHS, AND MOATS**, I use use HiRISE (25-50 cm/px) images taken at a cadence of days to months to track meter-scale changes in the RSPC in order to investigate the mechanisms that lead to the development of the distinctive RSPC morphologies. This chapter creates a conceptual framework for understanding how the RSPC evolves and exchanges mass with the atmosphere on longer-than-annual timescales.

1.4 A Match Made on Mars

The existence of the RSPC has long been a mystery because, while Leighton and Murray (1966) proposed that CO₂ deposits at the martian poles could be in exchange equilibrium with the atmosphere, they envisioned that the entire volume of the polar caps were CO₂. Subsequent studies showed that the polar caps are, in fact, mostly H₂O ice (e.g. Ingersoll, 1974; Nye et al., 2000; Byrne and Ingersoll, 2003a; Titus et al., 2003).

Thus, the RSPC is not the equilibrium reservoir of Leighton and Murray (1966) because its small mass (~1% of the martian atmosphere, Thomas et al., 2016) is insufficient to buffer against secular changes in the polar energy budget as Mars' orbit evolves. When the RSPC was first viewed at high resolution, it seemed that we could be viewing the RSPC at a special time, just as the entire RSPC is disappearing, because the extensive distribution of pits (Section 1.3) is eroding the RSPC laterally at rates that, if unbalanced by deposition, would completely destroy the RSPC on the timescale of ~100 years (e.g. Byrne and Ingersoll, 2003b). However, ~100 years is much shorter than the ~50 kyr cycles of varying polar insolation due to variations in Mars' obliquity, eccentricity, and longitude of perihelion with respect to its moving equinox (Laskar et al., 2004; similar to Milankovich cycles on Earth), making the plea to special times even less credulous. Additionally, further study has revealed that the mass balance of the RSPC is likely close to neutral due to thin layers of vertical deposition balancing out the horizontal ablation (Thomas et al., 2016).

The unexpected discovery by Phillips et al. (2011), using radar, that a massive deposit of CO₂, with a mass approximately equivalent to the modern atmosphere, is buried just below the H₂O ice underneath the RSPC, rekindled the possibility of a large reservoir of CO₂ ice in equilibrium with the atmosphere, in the style of Leighton and Murray (1966). However, it appears that the

exchange equilibrium between the atmosphere and the buried deposit takes place on 10^4 yr timescales due to variations in the martian orbit rather than annual timescales, as in Leighton and Murray's original hypothesis (Phillips et al., 2011; Bierson et al., 2016).

There is currently no self-consistent model that explains the first-order features of the buried CO_2 deposit or the existence of the RSPC. In **A MATCH MADE ON MARS: MARS' SECULAR AMAZONIAN PRESSURE CYCLE, AS BUFFERED BY ITS SOUTH POLAR CO_2 DEPOSIT**, I create such a conceptual framework. This framework explains the RSPC presence on top of the buried CO_2 deposit with an intervening H_2O layer as a natural consequence of a large CO_2 deposit (that contains some impurities, such as H_2O ice) in equilibrium with the atmosphere during a part of an orbital cycle when the equilibrium pressure is rising. I then proceed to use this framework to solve for the explicit pressure history of Mars between -21 Ma and +11 Ma and statistically describe the behavior of the martian pressure over the entire Amazonian.

References

Bakos, G. Á., Howard, A. W., Noyes, R. W., Hartman, J., Torres, G., Kovács, G., Fischer, D. A., Latham, D. W., Johnson, J. A., Marcy, G. W., and 9 others, 2009. Hat-p-13b,c: A transiting hot Jupiter with a massive outer companion on an eccentric orbit. *The Astrophysical Journal*, 707, pp. 446-456.

Batygin, K., Bodenheimer, P., and Laughlin, G., 2009. Determination of the Interior Structure of Transiting Planets in Multiple-Planet Systems. *The Astrophysical Journal*, 704, pp. L49-L53.

- Bierson, C. J., Phillips, R. J., Smith, I. B., Wood, S. E., Putzig, N. E., Nunes, D., & Byrne, S. (2016). Stratigraphy and evolution of the buried CO₂ deposit in the Martian south polar cap. *Geophysical Research Letters*, 43(May), 1–8
- Bodenheimer, P. & Pollack, J., 1986. Calculations of the accretion and evolution of giant planets: The effects of solid cores. *Icarus*, 67, pp. 391-408.
- Boss, A.P., 1997. Giant Planet Formation by Gravitational Instability. *Science*, 276, pp. 1836-1839.
- Byrne, S., & Ingersoll, A. P. (2003a). A sublimation model for martian south polar ice features. *Science (New York, N.Y.)*, 299(5609), 1051-1053
- Byrne, S. & Ingersoll, A.P. (2003b). Martian climatic events on timescales of centuries: Evidence from feature morphology in the residual south polar ice cap. *Geophysical Research Letters*, 30(13), 2–5.
- Piqueux et al., 2015
- Carr, Michael H. *The surface of Mars*. Vol. 6. Cambridge University Press, 2007.
- Charbonneau, D., Allen, L.E., Megeath, S.T., Torres, G., Alonso, R., Brown, T.M., Gilliland, R.L., Latham, D.W., Mandushev, G., O'Donovan, F.T., and Sozzetti, A., 2005. Detection of Thermal Emission from an Extrasolar Planet. *The Astrophysical Journal*, 626(1), 523
- Ehlmann, B.L & Edwards, C.S., 2014. Mineralogy of the Martian Surface. *Annual Review of Earth and Planetary Sciences* 42, 291-315
- Greenstreet, S., Gladman, B. & Mckinnon, W.B., 2015. Impact and cratering rates onto Pluto. *Icarus*, 258, pp.267–288.

- Hess, S.L., Henry, R.M., Tillman, J.E., 1979. The seasonal variation of atmospheric pressure on Mars as affected by the south polar cap. *J. Geophys. Res.* 84, 2923–2927.
- Hartmann, W.K., 1966. Early Lunar Cratering. *Icarus* 5, 406-418.
- Ingersoll, A. P. (1974). Mars - The case against permanent CO₂ frost caps. *Journal of Geophysical Research*, 79(24), 3403–3410.
- Ingersoll, A.P., Svitek, T. & Murray, B.C., 1992. Stability of polar frosts in spherical bowl-shaped craters on the Moon, Mercury, and Mars. *Icarus*, 100(1), pp.40–47.
- James, P.B., Briggs, G., Barnes, J., Spruck, A., 1979. Seasonal recession of Mars' south polar cap as seen by Viking. *J. Geophys. Res.* 84, 2889–2922.
- Kelly, N.J, Boynton, W.V., Kerry, K., Hamara, D., Janes, D., Reedy, R.C., Kim, K.J., and Haberle R.M. , 2006. Seasonal polar carbon dioxide frost on Mars: CO₂ mass and columnar thickness distribution. *JGR Planets* 111, E3.
- Knutson, H. A., Fulton, B. J., Montet, B. T., Kao, M., Ngo, H., Howard, A. W., Crepp, J. R., Hinkley, S., Bakos, G. A., Batygin, K., and 3 others, 2014. Friends of Hot Jupiters I: A Radial Velocity Search for Massive, Long-Period Companions to Close-In Gas Giant Planets. *The Astrophysical Journal*, 785, pp. 125-149.
- Laskar, J., Correia, A.C.M., Gastineau, M., Joutel, F., Levrard, B., Robutel, P., 2004. Long term evolution and chaotic diffusion of the insolation quantities of Mars. *Icarus* 170, 343-364.
- Leighton, R. B., & Murray, B. C. (1966). Behavior of carbon dioxide and other volatiles on Mars. *Science* (New York, N.Y.).

- Love, A.E.H., 1909. The Yielding of the Earth to Disturbing Forces. *Proceedings of the Royal Society A: Mathematical, Physical and Engineering Sciences*, 82, pp. 73-88.
- Malin, M. C. (2001). Observational Evidence for an Active Surface Reservoir of Solid Carbon Dioxide on Mars. *Science*, 294(2001), 2146–2148.
- Mardling, R., 2007. Long-term tidal evolution of short-period planets with companions. *Monthly Notices of the Royal Astronomical Society*. 382, pp. pp. 1768-1790.
- McKinnon, W.B., Nimmo, F., Wong, T., Schenk, P.M., White, O.L., Roberts, J.H., Moore, J.M., Spencer, J.R., Howard, A.D., Umurhan, O.M. & 6 others, 2016. Convection in a volatile nitrogen-ice-rich layer drives Pluto's geological vigour. *Nature*, 534(7605), pp.82–85.
- Mizuno, H., 1980. Formation of the Giant Planets. *Progress of Theoretical Physics*, 64, pp. 544-557.
- Moore, J.M., McKinnon, W.B., Spencer, J.R., Howard, A.D., Schenk, P.M., Beyer, R.A., Nimmo, F., Singer, K., Umurhan, O.M., White, O.L., and 32 others, 2016a. The geology of Pluto and Charon through the eyes of New Horizons. *Nature*, 351(6279).
- Moore, J.M., Howard, A.D., Umurhan, O.M., White, O.L., Schenk, P.M., Beyer, R.A., McKinnon, W.B., Spencer, J.R., Grundy, W.M., Lauer, T.R. & 7 others, 2016b. Sublimation as a landform-shaping process on Pluto. *Icarus*, 287, pp. 320-333.
- Nye, J.F., Durham, W.B., Schenk, P.M., Moore, J.M., 1999. The stability of a south polar cap on Mars carbon dioxide.

- Owen, T., Biemann, K., Rushneck, D. R., Biller, J. E., Howarth, D. W., & Lafleur, a. L. (1977). The Composition of the Atmosphere at the Surface of Mars. *Journal of Geophysical Research*, 82(28), 4635–4639.
- Phillips, R. J., Davis, B. J., Tanaka, K. L., Byrne, S., Mellon, M. T., Putzig, N. E., ... Seu, R. (2011). Massive CO₂ ice deposits sequestered in the south polar layered deposits of Mars. *Science* (New York, N.Y.), 332(6031), 838–841
- Pollack, J. B., Hubickyj, O., Bodenheimer, P., Lissauer, J. J., Podolak, M., and Greenzweig, Y., 1996. Formation of the giant planets by concurrent accretion of solids and gas. *Icarus*, 124, pp. 62-85.
- Ragozzine, D. & Wolf, A., 2008. Probing the interiors of very hot Jupiters using transit light curves. *The Astrophysical Journal*, 698, pp. 1778-1794.
- Southworth, John, Bruni, I., Mancini, L., and Gregorio, J., 2012. Refined physical properties of the HAT-P-13 planetary system. *Monthly Notices of the Royal Astronomical Society*, 420, pp. 2580-2587.
- Stern, S A., Bagenal, F., Ennico, K., Gladstone, G.R., Grundy, W. M., McKinnon, W.B., Moore, J.M., Olkin, C.B., Spencer, J.R. & 142 others, 2015. The Pluto system: Initial results from its exploration by New Horizons. *Science*, 350(6258).
- Tanaka, K. L., Skinner, J. a., Dohm, J. M., Irwin, R. P., Kolb, E. J., Fortezzo, C. M., ... Hare, T. M. (2014). Geologic Map of Mars. U.S. Geological Survey Geologic Investigations, 3292.
- Thomas, P. C., Calvin, W., Cantor, B., Haberle, R., James, P. B., & Lee, S. W. (2016). Mass balance of Mars' residual south polar cap from CTX images and other data. *Icarus*, 268, 118–130.

Titus, T. N., Kieffer, H.H., and Christensen, P.R. (2003). Exposed water ice discovered near the south pole of Mars, 1048(2003).

Trowbridge, A.J., Melosh, H.J., Steckloff, J.K. & Freed, A.M., 2016. Vigorous convection as the explanation for Pluto's polygonal terrain. *Nature*, 534(7605), pp.79–81.

Tsiganis, K., Gomes, R., Morbidelli, A., & Levison, H. F. 2005. Origin of the orbital architecture of the giant planets of the Solar System. *Nature* 435, 459

White, O.L., Moore, J.M., McKinnon, W.B., Spencer, J.R., Howard, A.D., Schenk, P.M., Beyer, R.A., Nimmo, F., Singer, K.N., Umurhan, O.M. & 15 others, 2017. Geological mapping of sputnik planitia on pluto. *Icarus*, 287, pp. 261-286.

Chapter 2

DYNAMICAL CONSTRAINTS ON THE CORE MASS OF HOT JUPITER HAT-P-13b

Buhler, P.B., Knutson, H.A., Batygin, K., Fulton, B.J., Fortney, J.J., Burrows, A., Wong, I. (2016). Dynamical Constraints on the Core Mass of Hot Jupiter HAT-P-13b, *The Astrophysical Journal* 821, pp. 26-37.

doi:10.3847/0004-637X/821/1/26

2.1 Abstract.

HAT-P-13b is a Jupiter-mass transiting exoplanet that has settled onto a stable, short-period, and mildly eccentric orbit as a consequence of the action of tidal dissipation and perturbations from a second, highly eccentric, outer companion. Owing to the special orbital configuration of the HAT-P-13 system, the magnitude of HAT-P-13b's eccentricity e_b is in part dictated by its Love number k_{2b} , which is in turn a proxy for the degree of central mass concentration in its interior. Thus, the measurement of e_b constrains k_{2b} and allows us to place otherwise elusive constraints on the mass of HAT-P-13b's core $M_{core,b}$. In this study we derive new constraints on the value of e_b by observing two secondary eclipses of HAT-P-13b with the Infrared Array Camera on board the Spitzer Space Telescope. We fit the measured secondary eclipse times simultaneously with radial velocity measurements and find that $e_b = 0.00700 \pm 0.00100$. We then use octupole-order secular perturbation theory to find the corresponding $k_{2b} = 0.31^{+0.08}_{-0.05}$. Applying structural evolution models, we then find, with 68% confidence, that $M_{core,b}$ is less than 25 Earth masses (M_{\oplus}). The most likely value is $M_{core,b} = 11 M_{\oplus}$, which is similar to the core mass theoretically required for runaway gas accretion. This is the tightest constraint to date on the core mass of a hot Jupiter. Additionally, we find that the measured secondary eclipse depths, which are in the 3.6 and 4.5 μm bands, best match atmospheric model predictions with a dayside temperature inversion and relatively efficient day–night circulation.

2.2 Introduction

The interiors of gas giant planets provide ground truth for planet formation theories and the properties of materials under high pressure and temperature. Accordingly, many studies aimed at deriving the interior states of giant planets in our solar system have been undertaken in the past half century (e.g., Safronov 1969; Mizuno 1980; Stevenson 1982; Bodenheimer & Pollack 1986; Pollack et al. 1996; Ikoma et al. 2000; Hubickyj et al. 2005; Rafikov 2006; Fortney & Nettelmann 2010; Nettelmann et al. 2012; Helled & Guillot 2013). The study of giant planets in our solar system has been recently augmented by the growing body of mass and radius measurements for transiting extrasolar planets. These measurements have enabled the first studies of the heavy-element components of gas giants orbiting other stars, as has been done for the super-Neptune HATS-7b (Bakos et al. 2015) and the hot Saturn HD 149026b (Sato et al. 2005), and in the statistical characterization of heavy-element enrichment in extrasolar gas giant planets (e.g., Burrows et al. 2007; Miller & Fortney 2011). Nonetheless, characterizing the interior structure of exoplanets—in particular, determining the presence of a heavy-element core—remains challenging, since mass and radius measurements alone cannot in general uniquely constrain the interior density profile or the chemical makeup of a planet. In particular, determining whether heavy elements are concentrated in the core or distributed uniformly within the envelope is especially difficult for Jupiter-sized planets since the large, predominantly light-element envelope masks the signal of the radial distribution of heavy elements.

However, the orbital configuration in a subset of multiplanet systems is such that the dynamical evolution of the system depends on the Love number k_2 of its innermost planet

(Batygin et al. 2009). The Love number k_2 quantifies the elastic deformation response of a planet to external forces and thus encodes information about its interior structure, including clues about its core mass (Love 1909, 1911). Utilizing the secular theory of Mardling (2007), Batygin et al. (2009) showed that, in a system of two planets orbiting a central body, k_2 of the inner planet can be determined if (i) the mass of the inner planet is much smaller than the mass of the central body, (ii) the semimajor axis of the inner planet is much less than the semimajor axis of the outer planet, (iii) the eccentricity of the inner planet is much less than the eccentricity of the outer planet, (iv) the planet is transiting, and (v) the planet is sufficiently close to its host star, such that the tidal precession is significant compared to the precession induced by relativistic effects. The HAT-P-13 system is the first and only currently known system to fulfill these criteria.

The HAT-P-13 system consists of three bodies in orbit around a central star with a mass of $M_A = 1.3 M_\oplus$ and radius $R_A = 1.8 R_\oplus$ (Southworth et al. 2012). HAT-P-13b is a low-eccentricity transiting planet with mass $M_b = 0.9 M_J$, radius $R_b = 1.5 R_J$, and an orbital period of 2.9 days (Southworth et al. 2012). HAT-P-13c is a radial velocity companion with a minimum mass $M_c = 14.2 M_J$, an orbital period of 446 days, and an eccentricity of 0.66 (Winn et al. 2010). This system also exhibits a long-term radial velocity trend indicative of a third companion located between 12 and 37 au with a minimum mass of 15–200 M_J (Winn et al. 2010; Knutson et al. 2014). However, Becker & Batygin (2013) demonstrated that the existence of this third companion does not disrupt the secular dynamics that allows the eccentricity of HAT-P-13b e_b to be related to its Love number k_{2b} .

Using existing constraints on the orbital eccentricity of HAT-P-13b from radial velocity measurements, Batygin et al. (2009) were able to place an upper bound on the core mass ($M_{\text{core},b}$) of 120 M_\oplus (41% M_b). In this study we present new observational measurements of

secondary eclipses of HAT-P-13b (i.e., when HAT-P-13b passes behind its host star) obtained using *Spitzer Space Telescope* (SST), which we use to place stronger constraints on the eccentricity of HAT-P-13b. We combine these new secondary eclipse times with the most recent transit and radial velocity measurements of the system (Winn et al. 2010; Southworth et al. 2012; Knutson et al. 2014) in order to derive an improved constraint on k_{2b} and $M_{core,b}$.

The paper is structured as follows. First, we describe our data acquisition, postprocessing, and analysis (Section 2.3). We then present the results of the secondary eclipse measurements and corresponding determination of the eccentricity, k_2 , core mass, and atmospheric properties of HAT-P-13b (Section 2.4). Finally, we discuss the implications of our findings in Section 2.5.

2.3 Methods

2.3.1. Observations and Photometric Time Series Extraction

Two observations of HAT-P-13 were taken using the InfraRed Array Camera (IRAC) onboard SST (Fazio et al. 2004), one using the 3.6 μm band on UT 2010 May 09 and the other using the 4.5 μm band on UT 2010 June 08, 11 orbits later (PI J. Harrington, Program ID 60003). Each data set comprises 68,608 subarray images taken with 0.4 s integration times over 8.7 hr of observation.

We extract the UTC-based Barycentric Julian Date (BJDUTC), subtract the sky background, and remove transient hot pixels from each of the images as described in Knutson et al. (2012) and Kammer et al. (2015). To calculate the flux from the HAT-P-13 system in each image, we first estimate the position of the star on the array using the flux-weighted centroid method (Knutson et al. 2012; Kammer et al. 2015) with radii ranging between 2.0 and 5.0 pixels in 0.5-pixel increments. We then calculate the corresponding stellar flux using a circular aperture with either

a fixed or time-varying radius. We consider fixed radii ranging between 2.0 and 5.0 pixels in 0.5-pixel increments and calculate the time-varying aperture using the square root of the noise pixel parameter as described in Lewis et al. (2013). This parameter is proportional to the full-width half-max (FWHM) of the star's point-spread function and is calculated for each image using a circular aperture with radii ranging between 2.0 and 5.0 pixels in 0.5-pixel increments. We then either multiply the square root of the noise pixel parameter by a constant scaling value of [0.6, 0.7, 0.8, 0.85, 0.9, 0.95, 1.00, 1.05, 1.10, 1.15, or 1.20] or add a constant offset of [-0.9, -0.8, -0.7, -0.6, -0.5, -0.4, -0.3, -0.2, -0.1, 0.0, 0.1, 0.2, 0.3, 0.4, or 0.5] pixels in order to determine the aperture radius for each image.

2.3.2. Instrumental Noise Model and Optimal Aperture Selection

We next create a time series for each photometric aperture where we trim the first 90 minutes (11,904 images) of each time series in order to remove the well-known ramp that occurs at the start of each new telescope pointing (e.g., Deming et al. 2006; Knutson et al. 2012; Lewis et al. 2013; Kammer et al. 2015). We replace non-numerical (NaN) flux values with the median flux value of each time series and replace values that deviate by more than three standard deviations from the local mean, determined from the nearest 100 points, with the local mean. We compare this approach to one in which we instead trim outliers from our light curves and find that our best-fit eclipse depths and times change by less than 0.2σ in both channels; 0.2% of the measurements were outliers or NaN in each channel. We then normalize each time series to one by dividing by the median value.

The photometric time series in both channels is dominated by an instrumental effect related to IRAC's well-known intrapixel sensitivity variations, combined with the pointing

oscillation of the SST. We correct for this effect using pixel-level decorrelation (PLD), as described by Deming et al. (2015). This method models the variation in flux intensity in each image due to this instrumental effect by tracking the change in intensity over time within a small box of pixels centered on the flux-weighted centroid. We use a total of 9 pixels arranged in a 3×3 box centered on the position of the stellar centroid. We remove images from the time series where one of these 9 pixels deviates from its mean flux by more than 3σ (0.3% of the data at $3.6 \mu\text{m}$ and 0.1% of the data at $4.5 \mu\text{m}$). Most of these deviations correlate with large pointing excursions in the photometric time series. We identify two pointing excursions in the $3.6 \mu\text{m}$ data, one of 0.7 pixels for 10 s and one of 0.5 pixels for 20 s, and one of 0.9 pixels for 10 s in the $4.5 \mu\text{m}$ data.

We divide the flux in each individual pixel by the summed flux across all 9 pixels, weighting each pixel by its contribution to the flux and thereby isolating the instrument noise from astrophysical signals (see Deming et al. 2015), and we repeat this operation for each image in our photometric time series. We also incorporate a constant and a linear term in time to model baseline instrument noise. Unlike Deming et al. (2015), we do not include a quadratic term because we found that the linear fit has an equivalent root mean square (RMS) residual to the quadratic fit, and so adding the quadratic parameter is not justified. In addition, the quadratic term was correlated with the eclipse depth in our model fits.

We fit a combined instrumental noise and eclipse (Mandel & Agol 2002) model to the light curve for each combination of photometric apertures listed in Section 2.3.1 using the “leastsq” routine in SciPy v0.14.0 with Python 2.7.6 and examine the residuals from the best-fit solution in order to determine the optimal aperture set for each bandpass. As discussed in Deming et al. (2015) and Kammer et al. (2015), we first bin the photometric light curves and time series for individual pixels by a factor of 512 (~ 4 -minute intervals) before fitting the model and then

apply the resulting best-fit model coefficients to the unbinned light curve. This allows us to identify solutions that minimize noise on longer timescales, which are most important for determining the best-fit eclipse parameters, in exchange for a moderately higher scatter in the unbinned residuals. We allow the center-of-eclipse time, eclipse depth, pixel weights, constant, and linear terms to vary as free parameters in our fits.

We excluded from consideration any apertures with an unbinned RMS more than 1.1 times that of the aperture with the lowest RMS in each band, focusing instead on the subset of apertures with low scatter. We then compared the relative amounts of time-correlated or “red” noise in the remaining apertures by calculating the standard deviation of the residuals as a function of bin size. For light curves with minimal red noise, we would expect the standard deviation of the residuals to vary by the $\sqrt{M/(n \times (M - 1))}$ Gaussian scaling relation (Winn et al. 2008), where n is the number of points in each bin and M is the number of bins. We evaluate the actual amount of red noise in the time series for each aperture by calculating the least-squares difference between the observed and theoretical noise scaling (Figure 2.1) and select the aperture that minimizes this quantity in each bandpass.

We next find the optimal bin size to use to fit the light curve in each channel via the same least-squares approach with which we find the optimal aperture. After determining the optimal bin size in each bandpass, we repeat our aperture optimization at the new bin size. We iterate on searching for the optimal aperture and bin size until we converge on the optimal pairing of aperture and bin size for each bandpass.

After optimizing our choice of bin size and aperture, we found that the 4.5 μm light curve displayed a residual ramp-like signal despite our decision to trim the first 90 minutes of data. We therefore experimented with fits where we trimmed up to 3 hr of data from the start of the light curve (i.e., up to the beginning of the eclipse). We found that the best-fit eclipse times were correlated with the amount of data trimmed from the start of the light curve over the full range of trim durations considered, indicating that the ramp extended to the start of the eclipse. We then considered an alternative approach in which we returned to our original 90-minute trim duration and deliberately used larger than optimal bin sizes in our fits, effectively forcing the models to identify solutions with less structure on long timescales. We found that fits with bin sizes larger than 100 points (40 s) effectively removed the ramp from the light curve, avoiding the need to increase the trim interval to values larger than 90 minutes. These fits resulted in best-fit secondary eclipse times approximately 2 minutes (0.6σ) earlier than our original fits with a smaller bin size. We tested for a residual ramp by repeating the large bin size fits with trim intervals ranging from 30 minutes up to 3 hr and found no evidence for a correlation between the trim interval and the best-fit eclipse time. We then repeated our optimization for bin size considering bin sizes between 128 and 2048 points in powers of two. We found that our best-fit eclipse depths and times varied by less than 0.4σ across this range and were in good agreement with the best-fit values for the 3 hr trim interval using the smaller bin size. We also considered fits using a smaller bin size where we included an exponential function of time to account for the observed ramp, but we found that this exponential function was a poor match for the shape of the observed ramp. We speculate that a sum of several exponentials might provide a better fit (e.g., Agol et al. 2010), but we felt that the added free parameters were not justified given the success of using larger bin

sizes. We also find that enforcing larger bin sizes in the 4.5 μm channel leads to better agreement of the secondary eclipse timing between the two channels.

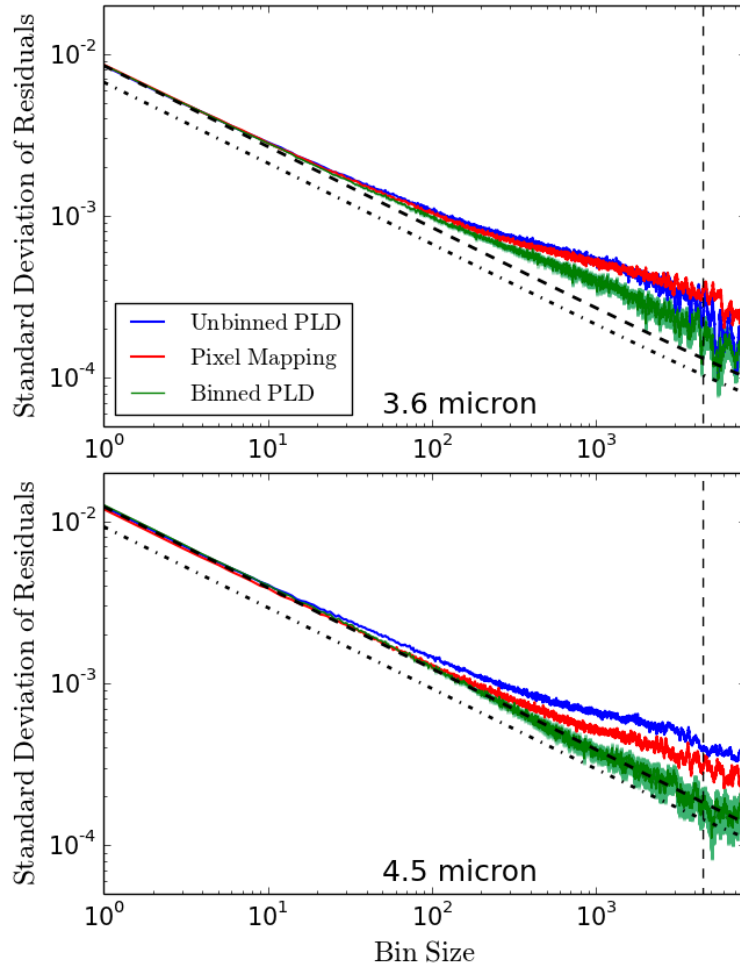


Figure 2.1 Standard deviation of the residuals is normalized to match the standard deviation of the unbinned residuals for the PLD performed on data that was optimally binned before fitting (green), PLD that was not binned before fitting (blue), and the Wong et al. (2014) pixel mapping fit (red) and plotted for each bandpass as a function of bin size. The vertical dashed line indicates the timescale of the eclipse ingress and egress. The expected $\sqrt{M/(n \times (M - 1))}$ Gaussian scaling relation (Winn et al. 2008) of the standard deviation of the residuals as a function of the number of points per bin is also plotted (black dot-dashed line is normalized to the Poisson noise, and black dashed line is normalized to the standard deviation of the unbinned residuals for the PLD performed on data that was optimally binned before fitting; M is the number of bins, n is the bin size). The 1σ uncertainties in the RMS ($\text{RMS}/\sqrt{2M}$) of the binned PLD model are plotted in light green.

We also tried decorrelating instrumental noise in our data using pixel mapping (e.g., Ballard et al. 2010; Lewis et al. 2013; Wong et al. 2014). This nonparametric technique constructs an empirical map of the pixel response across the chip by comparing the measured flux from each image to those of other images with similar stellar positions. We model the pixel sensitivity at each point in our time series using a Gaussian spatial weighting function over the 50 nearest neighbors in stellar centroid x and y position and noise pixel parameter space. The inclusion of the noise pixel parameter in the weighting ensures that the pixel map incorporates systematics unrelated to changes in the star's position that affect the shape of the stellar point-spread function. The number of neighbors was chosen to be large enough to adequately map the pixel response across the range of star positions in each eclipse data set while maintaining a reasonably low computational overhead (Lewis et al. 2013).

Deming et al. (2015) found that PLD is generally more effective in removing time-correlated (i.e., red) noise than other decorrelation methods as long as the range of star positions across the data set remains below ~ 0.2 pixels. The range of star centroid positions in our eclipse data sets lies below this threshold, and therefore we expect PLD to perform optimally. We also directly compare the performance of PLD for cases where we fit to either the unbinned or optimally binned photometry, as well as to the fit acquired from photometry using the Wong et al. (2014) pixel mapping technique described in the previous paragraph. We find that the optimally binned PLD has lower levels of correlated noise than the other methods (Figure 2.1). In addition, binned PLD gives center-of-eclipse phases in the two bandpasses that are most consistent with each other (at the 1.3σ level); the unbinned PLD and pixel mapping techniques produced center-of-eclipse phases consistent at the 2.6σ and 5.0σ levels, respectively. We therefore select the PLD technique applied to the binned data set for our final analysis.

For the fits described in the rest of this paper we use the following optimal aperture set and bin size. For the 3.6 μm channel we select a bin size of 21 points (~ 8 s), a 3.0-pixel radius aperture to find the centroid, and a 2.0-pixel aperture to find the noise pixel parameter, and we add 0.3 pixels to the square root of the noise pixel parameter to obtain the aperture within which we sum the flux. For the 4.5 μm channel we select a bin size of 128 points (~ 50 s), a 4.5-pixel radius aperture to find the centroid, and a 4.0-pixel aperture to find the noise pixel parameter, and we add 0.3 pixels to the square root of the noise pixel parameter to obtain the aperture within which we sum the flux.

2.3.3. Eclipse Statistical Errors

We determine the uncertainties on our model parameters using the Markov Chain Monte Carlo (MCMC) code *emcee* v2.1.0 (Foreman-Mackey et al. 2013) on Python 2.7.6. We allow the center-of-eclipse time, eclipse depth, pixel weights, constant, and linear terms to vary as free parameters in our fits. We set the uncertainties on individual points in each light curve equal to the standard deviation of the residuals after subtracting the best-fit solution in each bandpass. We run the MCMC with 250 walkers for 20,000 steps; the first 5000 steps from each walker were “burn-in” steps and removed from the chain.

For the observations in the 4.5 μm band we found that the 1σ uncertainties on the RMS overlap with the errors theoretically expected in the absence of correlated noise on the timescale of the eclipse ingress and egress (30 minutes; Figure 2.1) and therefore report the uncertainties in measurements from the 4.5 μm band directly from the MCMC analysis. However, for the

observations in the 3.6 μm band, the calculated RMS consistently deviates above the expected improvement with increased binning for timescales longer than 1 minute. We therefore choose a conservative approach and multiply the uncertainties in the center-of-eclipse time derived from the MCMC in the 3.6 μm band by a factor of 1.3, the factor by which the RMS lies above the theoretical improvement at the 30-minute timescale (Pont et al. 2006; Winn et al. 2007). Since the timescale of the eclipse is approximately half of the length of the data set, we are unable to accurately estimate the red noise on that timescale and so adopt the same factor of 1.3 scaling for the eclipse depth uncertainty in this band.

2.3.4. Eccentricity Determination

We next calculate an updated value for the eccentricity of HAT-P-13b using the approach described in Fulton et al. (2013). We fit the available radial velocity observations for this planet from Knutson et al. (2014) simultaneously with the best-fit transit ephemeris from Southworth et al. (2012) and measured secondary eclipse times from this study. We first allow the apsides of each planet (ω_b and ω_c) to vary independently and then repeat the fits imposing a prior that the posterior distribution of ω_b matches the posterior distribution of ω_c that was calculated from the fit in which ω_b and ω_c were allowed to vary independently. We use the latter version of the fits in our final analysis and discuss the rationale for this assumption in Sections 2.3.6 and 2.5.1.

2.3.5. Interior Modeling

We use the MESA code (Paxton et al. 2010), a one-dimensional thermal evolution model, for interior modeling. In the pressure–temperature space relevant to HAT-P-13b, MESA uses the SCvH tables (Saumon et al. 1995) for the equation of state. We adopt a solar composition envelope and evolve an array of interior models of HAT-P-13b with varying core masses and energy dissipation rates. Specifically, we consider core masses of $0.1\text{--}80 M_{\oplus}$ and dissipation rates equal to 0.05%, 0.10%, or 0.50% of the insolation. The thermal dissipation range we adopt here encapsulates both (i) the energy deposition typically quoted for hot Jupiters residing on circular orbits (e.g., ohmic dissipation, kinetic deposition) and (ii) an additional component of energy arising as a result of the sustained tidal dissipation (e.g., Bodenheimer et al. 2003; Batygin et al. 2009). We calculate the insolation (I) using an equilibrium temperature of 1725 K (Southworth et al. 2012).

We assume that the total mass of HAT-P-13b is the best-fit value reported by Winn et al. (2010), $0.906 M_J$, and acknowledge that a more recent value ($0.899 M_J$; Knutson et al. 2014) is available but that the mass–radius relationship for giant planets is famously independent of mass and so our choice of the Winn et al. (2010) mass makes a negligible difference in our analysis. We also note that the errors on the mass are negligible compared to the uncertainties inherent in the equation of state (see Fortney & Nettelmann 2010). We assume a Bond albedo of zero and a core density of 10 g cm^{-3} ; varying the core density by 2 g cm^{-3} has a negligible effect on the radial density profile obtained by MESA. We let the MESA models evolve for 3.0 Gyr, based on the best-fit age of 3.5 Gyr reported by Southworth et al. (2012). However, the radial density structure reaches a quasi-steady solution after ~ 1 Gyr, so the results are insensitive to the assumed system age.

For each pairing of core mass and dissipation rate we calculate k_{2b} based on the density profile, using the equations of Sterne (1939)¹:

$$(2.1) \quad k_{2b} = \frac{3 - \eta_2(R)}{2 + \eta_2(R)}$$

R is the radius of the planet, and $\eta_2(R)$ is a dimensionless quantity that is obtained by integrating the ordinary differential equation radially in $\eta_2(r)$ outward from $\eta_2(0) = 0$:

$$(2.2) \quad r \frac{d\eta_2(r)}{dr} + \eta_2(r)^2 - \eta_2(r) - 6 + \frac{6\rho(r)}{\rho_m(r)} (\eta_2(r) + 1) = 0$$

In the above expression, ρ is the density obtained from the density distribution $\rho(r)$ output from MESA, and $\rho_m(r)$ is the mean density interior to r . Note that if the core density is constant, then $\eta_2(r_{core}) = 0$, where r_{core} is the core radius (i.e., k_2 is 3/2 for a body of constant density; e.g., Ragozzine & Wolf 2009).

We use a linear spline to interpolate the coarse grid of k_{2b} and R_b values, corresponding to various core mass and dissipation input pairings evolved in MESA, along both the core mass axis and the dissipation axis, and extend the grid from 0.1–80 M_\oplus to 0–80 M_\oplus with a linear extrapolation. Once we determine the model values of k_{2b} and R_b for each pair of core mass and dissipation, we evaluate the probability of each core mass and dissipation pairing, given the probability distributions of the measured values of k_{2b} and R_b for the HATP-13 system. While the probability distribution for R_b is measured from observation, the probability distribution of k_{2b} must be calculated. We describe this calculation below.

¹ Note that the definition of $k_{2,1}$ in Sterne (1939) is the apsidal motion constant, i.e., $k_{2b}/2$ in the notation used here.

2.3.6. Secular Perturbation Theory

The octupole-order secular theory of Mardling (2007), augmented with a description of a tidally facilitated apsidal advance (Ragozzine & Wolf 2009), can be used to describe the non-Keplerian components of motion in the HAT-P-13 system and provides a method by which the relationship between e_b and k_{2b} can be obtained (Batygin et al. 2009). In the HAT-P-13 system, tidal dissipation quickly drains energy and acts to circularize the orbit of HAT-P-13b. However, the presence of the distant and highly eccentric HAT-P-13c acts to prevent complete circularization of the orbit of HAT-P-13b. Instead, the system tends toward a nearly elliptic equilibrium point, which acts as an attractor in phase space. As long as the orbits of HAT-P-13b and HAT-P-13c are coplanar, this minimization is achieved through aligning the apsides. Apsidal alignment is typically reached within roughly three circularization timescales (Mardling 2007). However, once orbital equilibrium is achieved, both orbits decay slowly and the orbital configuration remains quasi-stable for the rest of the lifetime of the system. In order to maintain alignment of the apsides, the apsidal precession of both HAT-P-13b and HAT-P-13c must be equal, that is,

$$(2.3) \quad \dot{\omega}_{c_{sec}} = \dot{\omega}_{b_{sec}} + \dot{\omega}_{b_{tid}} + \dot{\omega}_{b_{GR}} + \dot{\omega}_{b_{rot}}$$

The secular apsidal precession of HAT-P-13c $\dot{\omega}_{c_{sec}}$ dominates all other contributions to the total apsidal precession of HAT-P-13c. The terms that dominate the apsidal precession of HAT-P-13b are the secular precession $\dot{\omega}_{b_{sec}}$, the tidal precession $\dot{\omega}_{b_{tid}}$, and general relativistic precession $\dot{\omega}_{b_{GR}}$. The minor effects due to rotational precession $\dot{\omega}_{b_{rot}}$ are also included, but we neglect the negligible contribution to the apsidal precession from the stellar rotational bulge (e.g.,

Batygin et al. 2009). The equations of apsidal precession are comprehensively discussed in Ragozzine & Wolf (2009) and given here for convenience:

$$(2.4) \quad \dot{\omega}_{c_{sec}} = \frac{3}{4} n_c \left(\frac{M_b}{M_*} \right) \left(\frac{a_b}{a_c} \right)^2 \frac{1}{(1-e_c^2)^2} \times \left[1 - \frac{5}{4} \left(\frac{a_b}{a_c} \right) \left(\frac{e_b}{e_c} \right) \frac{1+4e_c^2}{1-e_c^2} \cos(\varpi_b - \varpi_c) \right]$$

$$(2.5) \quad \dot{\omega}_{b_{sec}} = \frac{3}{4} n_b \left(\frac{M_c}{M_*} \right) \left(\frac{a_b}{a_c} \right)^3 \frac{1}{(1-e_c^2)^{3/2}} \times \left[1 - \frac{5}{4} \left(\frac{a_b}{a_c} \right) \left(\frac{e_c}{e_b} \right) \frac{\cos(\varpi_b - \varpi_c)}{1-e_c^2} \right]$$

$$(2.6) \quad \dot{\omega}_{b_{tid}} = \frac{15}{2} k_{2b} n_b \left(\frac{R_b}{a_b} \right)^5 \left(\frac{M_*}{M_b} \right) (1-e_b^2)^{-5} \times \left(1 + \frac{3}{2} e_b^2 + \frac{1}{8} e_b^4 \right)$$

$$(2.7) \quad \dot{\omega}_{b_{GR}} = \frac{3n_b^3}{1-e_b^2} \left(\frac{a_b}{c} \right)^2$$

$$(2.8) \quad \dot{\omega}_{b_{rot}} = \frac{k_{2b}}{2} \left(\frac{R_b}{a_b} \right)^5 \frac{n_b^3 a_b^3}{G m_b (1-e_b^2)^2}$$

In the preceding equations, G is the Newtonian gravitational constant and c is the speed of light. The subscripts “ b ,” “ c ,” and “ $*$ ” denote properties of HAT-P-13b, HAT-P-13c, and the star, respectively. a is the semimajor axis, e is the eccentricity, n is the mean motion, R is the radius, and M is the mass. Under the assumption that the apsides are aligned, the $\varpi_b - \varpi_c$ terms in Equations (2.4) and (2.5) are zero. Since all of the system properties that appear in the equations of apsidal precession have been measured, with the exception of k_{2b} , Equation (2.3) can be rearranged to solve for the Love number of HAT-P-13b purely in terms of known quantities. Note that it is not necessary to measure the apsidal precession rate of either HAT-P-13b or HAT-P-13c; it is sufficient to know only that they are equal.

Table 2.1 HAT-P-13 System Properties

e_b	0.00700 ± 0.00100
e_c	$0.6554^{+0.0021}_{-0.0020}$
$M_b (M_J)^a$	$0.899^{+0.030}_{-0.029}$
$M_c \sin(i_c) (M_J)^a$	$14.61^{+0.46}_{-0.48}$
$M_* (M_\odot)^b$	1.320 ± 0.062
$R_b (R_J)^b$	1.487 ± 0.041
$R_* (R_\odot)^b$	1.756 ± 0.046
$T_b (day)^b$	2.9162383 ± 0.0000022
$T_c (day)^a$	445.82 ± 0.11
$a_b (au)^b$	0.04383 ± 0.00068
$\gamma (m s^{-1})$	$-11.76^{+0.93}_{-0.9}$
$\dot{\gamma} (m s^{-1} day^{-1})$	0.0545 ± 0.0012
jitter ($m s^{-1}$)	$4.7^{+0.48}_{-0.43}$
3.6 μm eclipse depth	$0.0662 \pm 0.0113\%$
3.6 μm eclipse time (BJD_{UTC})	$2,455,326.70818 \pm 0.00406$
3.6 μm eclipse offset (<i>minutes</i>)	-24.2 ± 5.8
3.6 μm eclipse phase	0.49424 ± 0.00139
4.5 μm eclipse depth	$0.1426 \pm 0.0130\%$
4.5 μm eclipse time (BJD_{UTC})	$2,455,355.87672 \pm 0.00226$
4.5 μm eclipse offset (<i>minutes</i>)	-15.5 ± 3.3
4.5 μm eclipse phase	0.49633 ± 0.00079

Notes.

^aKnutson et al. (2014), ^bSouthworth et al. (2012)

2.3.7. Core Mass Determination

We construct the posterior probability distribution for k_{2b} from MCMC chains comprising 10^7 normally distributed values for each of the measured HAT-P-13 system properties (Table 2.1)

using Equations (2.3)–(2.8). We then multiply the probability distributions for k_{2b} and R_b obtained from MESA and map that distribution into a two-dimensional probability distribution of core mass and heat dissipation. Finally, we obtain the one-dimensional probability distribution of the core mass of HAT-P-13b by marginalizing the two-dimensional distribution over dissipation, assuming a uniform prior on dissipation between 0.05% and 0.5% I .

2.3.8. Atmospheric Measurements

We determine the dayside temperature of HAT-P-13b from the measured secondary eclipse depths in each bandpass. To do so, we first calculate the stellar flux by integrating a PHOENIX stellar flux model (Husser et al. 2013) for each bandpass weighted by the subarray average spectral response curve.² We utilize a PHOENIX model with an effective temperature of $T_{eff} = 5700$ K, a surface gravity of $\log g = 4.0$, and a modestly enhanced metallicity of $[Fe/H] = 0.5$. For comparison, HAT-P-13 has a measured $T_{eff} = 5720 \pm 69$ K, $[Fe/H] = 0.46 \pm 0.07$ (Torres et al. 2012), and $\log g = 4.070 \pm 0.020$ (Southworth et al. 2012). We calculate the flux of the planet as a fraction of the total system flux based on the depth of the secondary eclipse. We then find the temperature that gives a blackbody curve that, when integrated over its respective bandpass, matches the planetary flux. We calculate the errors on the temperature by constructing the posterior distribution for the temperature in each wavelength using MCMC chains of length $2.5 \times$

² Curve obtained from “Spectral Response” at <http://irsa.ipac.caltech.edu/data/SPITZER/docs/irac/calibrationfiles>.

10^4 , based on the measured eclipse depths and R_b/R_* . The effective dayside temperature was calculated by taking the error-weighted mean of the best-fit temperatures in each bandpass.

2.4 Results

2.4.1. Secondary Eclipse Measurements

We find that the HAT-P-13b secondary eclipses are centered at $2,455,326.70818 \pm 0.00406$ and $2,455,355.87672 \pm 0.00226$ BJD_{UTC} in the 3.6 and 4.5 μm bands, respectively. These times are 24.2 ± 5.8 minutes and 15.5 ± 3.3 minutes earlier (orbital phase 0.49424 ± 0.00139 and 0.49633 ± 0.00079), respectively, than the predicted time based on a circular orbit (Figure 2.2), where we have accounted for the 41 s light-travel time delay (Loeb 2005) and the uncertainty in the Southworth et al. (2012) ephemeris (9.7 and 11 s for the 3.6 and 4.5 μm observations, respectively). The eclipse depths for the 3.6 and 4.5 μm channel are $0.0662\% \pm 0.0113\%$ and $0.1426\% \pm 0.0130\%$, respectively (Figure 2.2). These secondary eclipse times are consistent at the 1.3σ level. We therefore take the error-weighted mean and find that the observed center of secondary eclipse time occurs 17.6 ± 2.9 minutes earlier (orbital phase 0.49582 ± 0.00069) than the predicted value for a circular orbit.

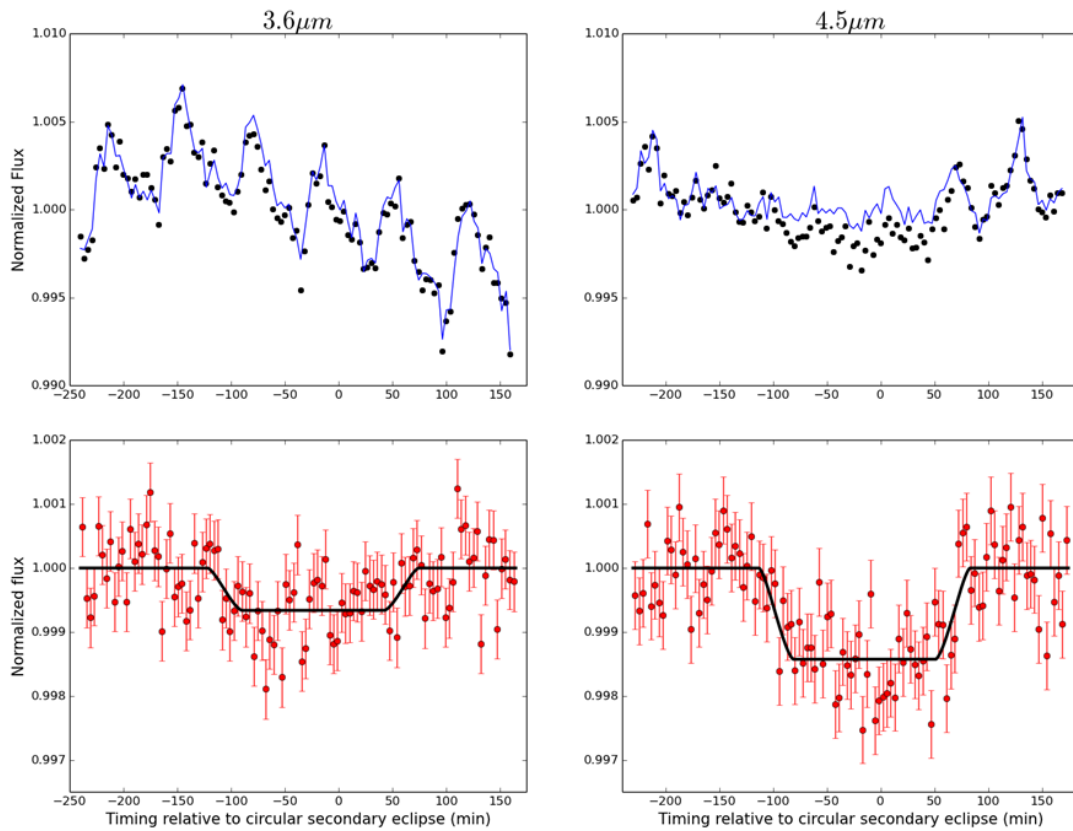


Figure 2.2 Top row: normalized raw flux (black points) compared to the best-fit instrumental noise model (blue line). Bottom row: best-fit eclipse model (black line) and flux measurements after dividing out the instrumental noise model (red points). All data and models are plotted with a bin size of 512 measurements (~ 3.5 minutes) for visual clarity.

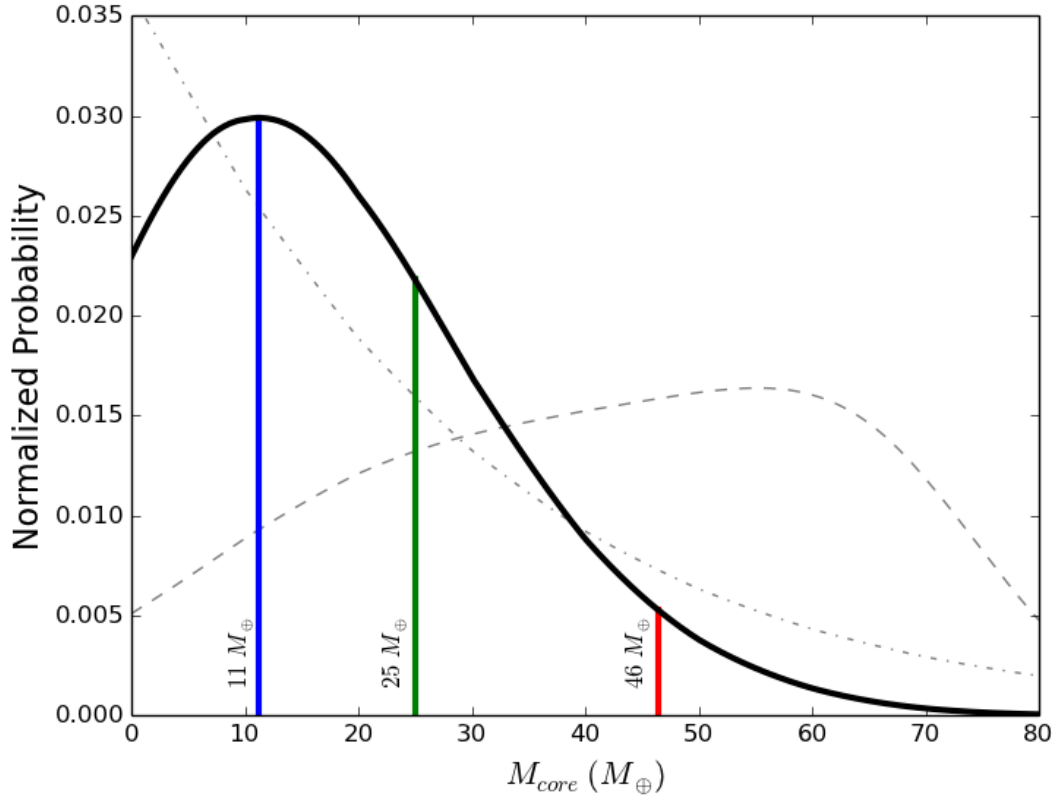


Figure 2.3. Probability distribution of the true core mass of HAT-P-13b (black), along with the most probable core mass ($11 M_{\oplus}$, blue line), 68% confidence interval ($0\text{--}25 M_{\oplus}$, green line), and 95% confidence interval ($0\text{--}46 M_{\oplus}$, red line). The probability distribution of the core mass is the product of the constraints on the core mass probability given by the measurement uncertainty in the Love number (k_{2b} , dot-dashed line) and the radius (R_b , dashed line).

2.4.2. Eccentricity and Core Mass

Assuming apsidal alignment, the eccentricities of the orbits for the two innermost planets in this system are $e_b = 0.00700 \pm 0.00100$ and $e_c = 0.6554^{+0.0021}_{-0.0020}$. We use these eccentricities to calculate a Love number for the innermost planet $k_{2b} = 0.31^{+0.11}_{-0.05}$, where values of $k_{2b} > 0.30$ are inconsistent with the MESA interior models (i.e., would require a negative core mass). When we combine this constraint on k_{2b} with the measured planet radius R_b , we find that the core mass of HAT-P-13b is less than $25 M_{\oplus}$ (less than $9\% M_b$; 68% confidence interval), with a most likely core

mass of $11 M_{\oplus}$ ($4\% M_b$; Figure 2.3). The constraint from k_{2b} strongly favors smaller core masses, while the constraint from R_b modestly favors larger core masses, up to $\sim 60 M_{\oplus}$ (Figure 2.3).

2.4.3. Atmospheric Properties

We find best-fit brightness temperatures of 1680 ± 119 K at $3.6 \mu\text{m}$ and 2265 ± 150 K at $4.5 \mu\text{m}$ and compare our measured eclipse depths in each bandpass with atmosphere models from Burrows et al. (2008) and Fortney et al. (2008) (Figure 2.4). Both models assume a solar composition, plane parallel atmosphere with molecular abundances set to the local thermal equilibrium values. The Fortney et al. (2008) models assume even heat distribution across the day side and vary the amount of energy incident at the top of the dayside atmosphere in order to approximate the effects of redistribution to the night side. In these models the zero redistribution case is labeled as “ 2π ” and the full redistribution case is labeled as “ 4π .” We also consider versions of the model with and without an equilibrium abundance of TiO; when present, this molecule absorbs at high altitudes and produces a temperature inversion in the dayside atmosphere. The Burrows et al. (2008) models account for the presence or absence of a dayside temperature inversion by introducing a gray absorber at low pressures where the opacity κ can be adjusted as a free parameter. Atmospheric circulation is included as a heat sink between 0.01 and 0.1 bars, where the parameter P_n defines the fractional amount of energy redistributed to the night side and ranges from 0% to 50% (from no redistribution to the night side to complete redistribution across both hemispheres). The Fortney et al. (2008) model satisfactorily reproduces the observed eclipse depths in both bandpasses when including a dayside temperature inversion due to absorption from TiO and relatively efficient circulation between the day and night sides. Although

none of the Burrows et al. (2008) models are able to match the observed 3.6 μm eclipse depth within the 3σ uncertainty, we obtain the closest match with models that include an absorber ($\kappa = 0.1$) and relatively efficient circulation ($P_n = 40\%$).

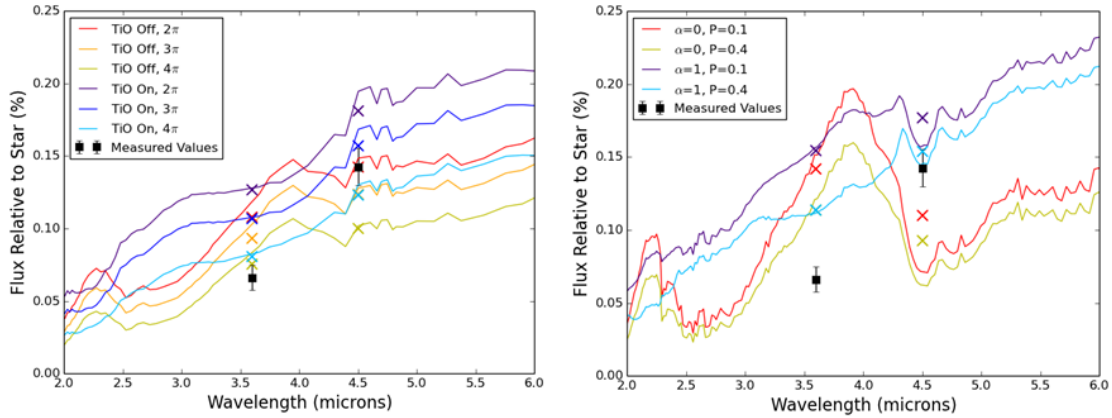


Figure 2.4. Left: six dayside atmosphere models for HAT-P-13b based on Fortney et al. (2008); right: four models based on Burrows et al. (2008). The measured secondary eclipse depths at 3.6 and 4.5 μm are overplotted as black filled squares, and the band-integrated model predictions are shown as colored crosses for comparison. Fortney et al. (2008) model an atmospheric absorber with TiO and either no circulation (2π), partial circulation (3π), or full circulation (4π). Burrows et al. (2008) model opacity with a gray source (α , units of $\text{cm}^2 \text{g}^{-1}$) and the fraction of energy redistributed to the night side (P_n ; 10% is minimal redistribution, 40% is near-maximal redistribution).

2.5. Discussion

2.5.1. Effects of Coplanarity and Apsidal Alignment

Correlations between the apsidal orientation ω and eccentricity e introduce errors on the determination of eccentricity e_b of HAT-P-13b. Since e_b is relatively small, we obtain a correspondingly poor constraint on ω_b of 231^{+17}_{-42} degrees in fits where we allow ω_b to vary independently of ω_c . However, since e_c is large, we are able to measure ω_c with an uncertainty of less than a degree ($\omega_c = 175.28^{+0.21}_{-0.22}$ degrees). The measured apsidal angles for planets b and c

are thus consistent with apsidal alignment, although the relatively large uncertainties on ω_b preclude a definitive determination.

When we allow ω_b to vary freely in our fits, we find that $e_b = 0.0108^{+0.0069}_{-0.0035}$. This eccentricity is nonzero at the 3.1σ level, providing independent confirmation that the orbit of HAT-P-13b has not yet been circularized and therefore that the secular orbital coupling mechanism discussed by Mardling (2007) and Batygin et al. (2009) is applicable to this system. Note that the uncertainty in e_b is more than five times greater than in the case when we assume apsidal alignment.

If the planets are coplanar, their apsides will align in much less than the age of the HAT-P-13 system (Mardling 2007; Batygin et al. 2009). Mardling (2010) showed that an initial mutual inclination between the orbits of HAT-P-13b and HAT-P-13c would evolve to a limit cycle in e_b and apsidal orientation, rather than to a fixed e_b and apsidal alignment. That study explored the effects of the inclination angle between the orbits of HAT-P-13b and HAT-P-13c (Δi_{b-c}) on e_b and found that if the orbits are nearly coplanar ($\Delta i_{b-c} \leq 10^\circ$), then the limit cycle in e_b will have a width of less than 3% e_b and the width of the limit cycle of the angle between the apsides is $\leq 4^\circ$ (calculated from Equations (15), (16), and (17) of Mardling 2010). Thus, the e_b measured at a particular epoch of the HAT-P-13 system is insensitive to this limit cycle if Δi_{b-c} is low.

We propose that Δi_{b-c} is indeed likely to be small, based on both observational constraints and theoretical arguments. First, the exploration by Mardling (2010) found that a configuration of either (i) prograde, near-coplanar orbits or (ii) $130^\circ \leq \Delta i_{b-c} \leq 135^\circ$ is strongly favored. Second, Winn et al. (2010) measured the Rossiter–McLaughlin effect (McLaughlin 1924; Rossiter 1924) during a transit of HAT-P-13b and found that the spin axis of the star and the angular momentum

vector of HAT-P-13b's orbit are well aligned on the sky ($\lambda = 1.9^\circ \pm 8.6^\circ$). This is significant because HAT-P-13b orbits far enough from the star that the orbital precession rate is dominated by torque from HAT-P-13c rather than the J_2 quadrupole moment of the star (Mardling 2010; Winn et al. 2010). If Δi_{b-c} were large, as in case (ii) of Mardling (2010), nodal precession of HAT-P-13b's orbit around HAT-P-13c's orbital axis would ensue, manifesting as cyclic variations in the angle between stellar equator and the orbital plane of HAT-P-13b ($\psi_{*,b}$). Therefore, it is unlikely that a small value for $\psi_{*,b}$ would be measured at a randomly selected epoch unless Δi_{b-c} is small (Winn et al. 2010). However, the initial orbital configuration of the system is unknown and the skyprojected angle λ , rather than the true $\psi_{*,b}$, is measured, so it is not possible to definitively determine Δi_{b-c} from the Rossiter–McLaughlin measurement alone. We therefore argue that Δi_{b-c} must be small, without attempting to place a definitive upper limit on Δi_{b-c} .

A direct measurement of Δi_{b-c} may be forthcoming by studying transit timing variations (TTVs) in the orbit of HAT-P-13b, since mutual inclination can induce a detectable TTV signature (Nesvorný 2009). Southworth et al. (2012) found that there is no compelling evidence for large TTVs in the orbit of HAT-P-13b, although TTVs of less than 100 s are possible (Fulton et al. 2011). Payne & Ford (2011) explored theoretical TTVs for HAT-P-13b and found that HAT-P-13c should induce TTVs on the order of tens of seconds and that a precise determination of TTVs would make it possible to discriminate between the two allowed scenarios (Δi_{b-c} near 0° or 130° – 135°) found by Mardling (2010).

Astrometry of HAT-P-13 could also be used to probe Δi_{b-c} . We calculate an expected astrometric signal from HAT-P-13b of either (i) $61 \mu\text{as}$, if the orbit of HAT-P-13c is effectively edge-on as seen from Earth, or (ii) $86 \mu\text{as}$, if it is inclined at 135° as seen from Earth. Astrometry from

the Gaia mission should be accurate to $\sim 10 \mu\text{as}$ (Lindegren 2009) and thus will be sensitive enough to discriminate between these two scenarios. Although a direct measurement of the apsidal precession of the system (i.e. $\dot{\omega}_c$) would allow a direct check of the secular perturbation theory that allows us to calculate k_{2b} , we calculate that the precession rate for this planet is on the order of $10^{-4} \text{ deg yr}^{-1}$ and is therefore beyond the reach of current radial velocity observations. However, the presence of a third companion (Winn et al. 2010; Knutson et al. 2014) in the system may complicate the determination of Δi_{b-c} using any of these methods.

2.5.2. Interior Structure

The initial characterization of $M_{core,b}$ by Batygin et al. (2009) was limited by the relatively large uncertainty in the published eccentricity for the innermost planet. Based on radial velocity data alone, they concluded that $M_{core,b}$ must be less than $120 M_{\oplus}$ at the 1σ level and argued that core masses greater than $40 M_{\oplus}$ were disfavored based on the required effective tidal dissipation Q_b .³ More recently, Kramm et al. (2012) used updated measurements of the HAT-P-13 system from Winn et al. (2010) to find an allowed range of k_{2b} based on the 1σ error on e_b by using the polynomial relating e_b and k_{2b} given in Batygin et al. (2009). They then used that k_{2b} range to place constraints on the interior structure of HAT-P-13b using the values of M_b and R_b from Bakos et al. (2009) and complex interior models. Their analysis indicated that $M_{core,b}$ is less than $27 M_{\oplus}$. However, caution must be exercised when using the polynomial equation of Batygin et al. (2009), since the shape of the curve strongly depends on all of the measured system parameters (Figure

³ However, their model did not account for other sources of heating, such as ohmic dissipation.

2.5). In addition, the polynomial does not include uncertainties in the e_b - k_{2b} relationship due to observational measurement uncertainties.

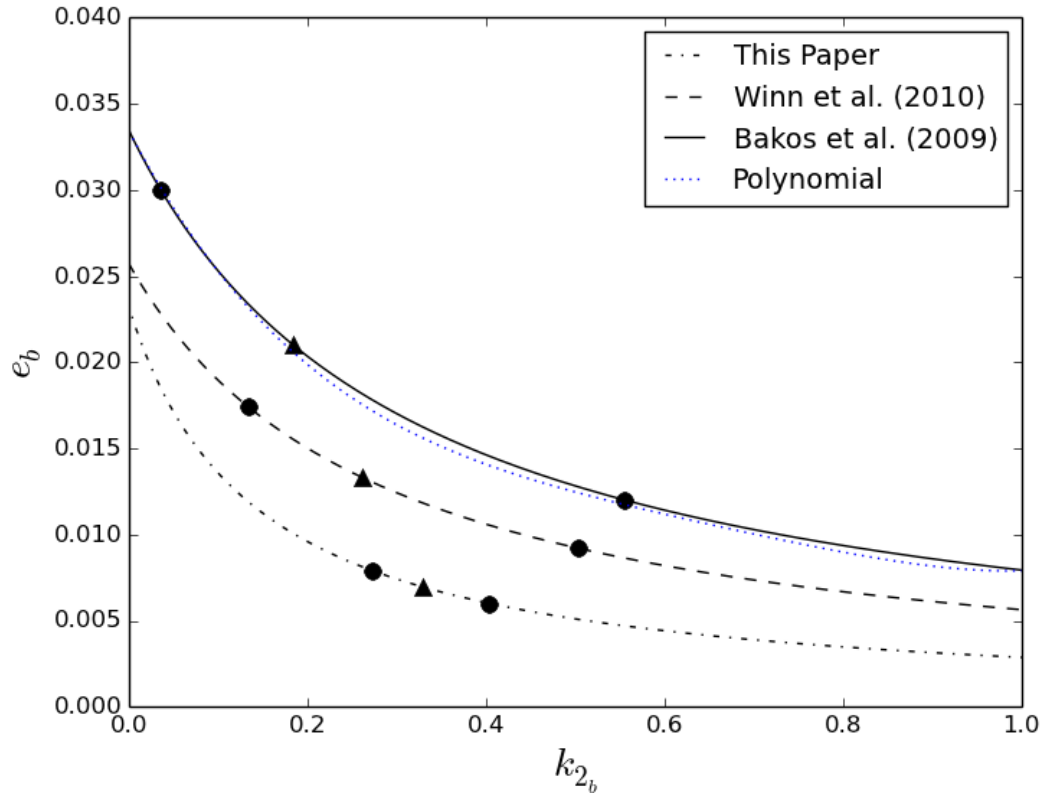


Figure 2.5. Relationship between e_b and k_{2b} for the HAT-P-13 system parameters measured by different studies, including the fourth-order polynomial approximation given in Batygin et al. (2009). The best-fit (triangles) and 1σ (circles) uncertainties in e_b reported by each study are plotted on their respective e_b - k_{2b} curves. The curves do not include uncertainties in the e_b - k_{2b} relationship due to measurement errors, unlike our Bayesian model (Figure 2.3), which does take them into account.

Our analysis offers an improved estimate of $M_{core,b}$ (less than $25 M_{\oplus}$ with 68% confidence) by taking into account both the change in the dependence of k_{2b} on e_b due to updated measurements of M_b , M_c , M_* , R_b , T_b , T_c , and e_c and the effect of the uncertainties in those measured values on the e_b - k_{2b} relationship and $M_{core,b}$ determination, which had been neglected

in previous studies. When combined with new radial velocity measurements from Knutson et al. (2014), the secondary eclipse measurements of HAT-P-13 provide strong constraints on e_b and our assumption of apsidal alignment further reduces uncertainty on this parameter. Our method also allows us to explore the full probability distribution for $M_{core,b}$ instead of only placing an upper bound on its value.

There are several caveats worth mentioning in regard to our estimated core mass. We note that k_2 is only the lowest harmonic describing the internal yielding of a body to external forces and is thus an inherently degenerate quantity (as noted for specific models of HAT-P-13b by Kramm et al. 2012). The effects of metallicity on atmospheric opacity may also affect the thermal evolution and thus the radial structure of the planet (as noted for brown dwarfs by Burrows et al. 2011) but are neglected here. We adopt a solar composition envelope for definitiveness and expect that increasing the metallicity will have only a small effect on our predicted core mass based on the extensive exploration of this effect on interior models performed by Kramm et al. (2012). We also note that an inhomogeneous heavy-element distribution may lead to an overestimation of $M_{core,b}$ (Leconte & Chabrier 2012). Thus, our estimate is specific to a model with a refractory element core and a solar composition envelope. Imperfect knowledge of the equations of state of materials at high pressure and temperature also introduces additional uncertainties (e.g., Fortney & Nettelmann 2010) that are not accounted for in this study.

In addition, strong constraints on the internal heat dissipation are not available, although we can determine how the uncertainty in the internal dissipation impacts our conclusions for $M_{core,b}$ by recalculating the $M_{core,b}$ probability distribution assuming either extremely high or

extremely low dissipation rates. We find that the main effect of the dissipation rate is to shift the peak of the probability distribution for $M_{core,b}$ lower for higher values of dissipation, while maintaining a comparable distribution shape. When we specify dissipation as 0.05% I , the probability distribution peaks at $M_{core,b} = 22 M_{\oplus}$. For a dissipation of 0.50% I , the probability distribution peaks at $M_{core,b} = 3 M_{\oplus}$. We therefore conclude that uncertainties in the internal heat dissipation introduce modest, but not overwhelming, uncertainties in the estimate of $M_{core,b}$ (i.e., lack of knowledge of the heat dissipation yields uncertainties that are within the 1σ errors from the observational uncertainties).

2.5.3. Dayside Atmosphere

Schwartz & Cowan (2015) compare the irradiation temperatures ($T_0 = T_*\sqrt{R_*/a_b}$) of a large sample of hot Jupiters to their measured dayside brightness temperatures (T_d) from secondary eclipse observations and find that hotter planets appear to have relatively inefficient day–night circulation. For HAT-P-13b, $T_0 = 2469$ K, yielding a predicted $T_d \approx 2090$ K (from Figure 2 of Schwartz & Cowan 2015), which is 2σ above the effective dayside temperature we measure (1906 ± 93 K). The T_d/T_0 that we obtain for HAT-P-13b (0.7720 ± 0.0377) indicates relatively efficient redistribution of energy to the night side for the case of zero Bond albedo (see Figure 7 of Cowan & Agol 2011), in good agreement with our findings in Section 2.4.3. The T_0/T_d of HAT-P-13b also fits the trend of decreasing T_0/T_d with lower planetary mass found by Kammer et al. (2015) (their Figure 13). The circulation model of Perez-Becker & Showman (2013), which depends on the equilibrium temperature of the planet, also predicts moderately efficient energy

redistribution such that the nightside flux from HAT-P-13b should be 0.55–0.75 that of its dayside flux, depending on the drag timescale.

2.5.4. Comparison to Other Systems

Our analysis indicates that $M_{core,b}$ is comparable to the core masses of Jupiter ($M_{core,J} < 18 M_{\oplus}$; Fortney & Nettelmann 2010) and Saturn ($M_{core,S} = 5\text{--}20 M_{\oplus}$; Helled & Guillot 2013) in our own solar system. Core accretion models for gas giant planet formation suggest that minimum core masses of approximately $10 M_{\oplus}$ are needed in order to form Jovian planets, although this limit depends on both the composition of the core and the properties of the gas disk near the planet's formation location (e.g. Mizuno 1980; Bodenheimer & Pollack 1986; Pollack et al. 1996; Ikoma et al. 2000; Hubickyj et al. 2005; Rafikov 2006). Although our observation is consistent with core accretion theory (Safronov 1969; Stevenson 1982), our 1σ confidence interval extends down to zero core mass and therefore does not preclude alternative formation models such as disk instability (e.g., Boss 1997), nor does it provide a definitive test of post-formation core erosion (e.g., Stevenson 1982; Guillot et al. 2004).

Work has been undertaken to probe the heavy-element fractions of gas giant planets across a broad range of planets, from the hot super-Neptune HATS-7b (Bakos et al. 2015) and hot Saturn HD 149026b (e.g., Sato et al. 2005; Fortney et al. 2006; Ikoma et al. 2006; Burrows et al. 2007; Southworth 2010) to super-Jupiters (e.g., GJ 436b and HAT-P-2b; Baraffe et al. 2008). The constraints on the heavy-element component of these planets are often accompanied by statements about their inferred core mass, with the caveat that there are degeneracies between

models with heavy-element cores and models with heavy elements distributed throughout the envelope (e.g., Baraffe et al. 2008). Avenues for partially breaking the degeneracies between thermal evolutionary models with heavy elements distributed throughout the planet and models with heavy-element cores are available for extremely metal-rich planets, such as HATS-7b and HD 149026b. However, in general, measurements of mass and radii can only be used to constrain the overall fraction of the planetary mass composed of heavy elements. The inference of a radial distribution of refractory elements and therefore assertions related to the mass of a solid core require additional information (e.g., knowledge of k_2). In this regard HAT-P-13b is unique because it is the only member of the extrasolar planetary census for which this additional information exists. Our constraint on the core mass of HAT-P-13b is consistent with the determination of heavy-element enrichment, with the accompanying inference of the presence of cores in hot Jupiters by Torres et al. (2007) and Burrows et al. (2007). Torres et al. (2007) invoke the presence of heavy-element cores to explain the small radii of the metal-rich $0.60 M_J$ HAT-P-3b and $0.62 M_J$ XO-2b, and Burrows et al. (2007) investigated a sample of 14 hot Jupiters and found that a subset of those planets had smaller radii than allowed by models without either a solid core or metal-rich envelope. We stress, though, that the independent measurement of the degree of central mass concentration, such as done in this paper, is necessary to determine the radial distribution of heavy elements for Jovian-mass planets.

Finally, we also compare the results of our study to empirical scaling relations from Miller & Fortney (2011), which are based on mass and radius measurements from a sample of 15 planets with moderate irradiation levels (incident flux $< 2 \times 10^8 \text{ erg s}^{-1}$) around stars with metallicities ranging from $[Fe/H]_* = -0.030$ to $+0.390$. That study found a positive correlation between the bulk metallicity of a planet and that of its host star and a negative correlation between a planet's

mass and its metallicity. It also provided an empirical relationship relating the heavy-element complement of giant planets (M_Z) to their host star: $\log_{10}(M_Z) = (0.82 \pm 0.08) + (3.40 \pm 0.39) [Fe/H]_*$. Applying this relation to HAT-P-13b, which orbits a relatively metal-rich star ($[Fe/H]_* = 0.46 \pm 0.07$; Torres et al. 2012), we find an estimated heavy-element mass of $242^{+568}_{-160} M_\oplus$, i.e., 84% of the total mass of HAT-P-13b, a much higher percentage than we determine for the core mass of HAT-P-13b and also a higher percentage than is found for most of the planets considered by Miller & Fortney (2011). This may indicate that the empirical relation cannot be extrapolated to planets around stars with metallicities higher than those of the stars they studied, or that there are additional parameters, such as formation location, that can affect the final core masses for these planets.

2.5.5. Future Measurements

Other systems analogous to the HAT-P-13 system, i.e., systems that allow us to measure the k_2 of the inner planet, will be useful for exploring the distribution of core masses over a larger sample of giant planets. In order to exploit the models utilized in this study, we require that such a planet (i) be transiting, (ii) have a circularization timescale less than one third of the age of the system, (iii) have an equilibrium eccentricity large enough to be measured with high precision (Equation (36) of Mardling 2007), and (iv) have a $\dot{\omega}_{tid}$ comparable to or larger than $\dot{\omega}_{DGR}$ (Equation (12) of Batygin & Laughlin 2011). Radial velocity observations of the Kepler 424 (Endl et al. 2014), WASP-41 (Neveu-VanMalle et al. 2015), HAT-P-44, HAT-P-45, and HAT-P-46 (Hartman et al. 2014) systems indicate that they may have architectures that would make them amenable

to this kind of study. We note that many of the hot Jupiters detected by ongoing transit surveys have relatively sparse radial velocity observations, making it difficult to determine whether or not they have a suitable outer companion. Knutson et al. (2014) find that approximately half of all hot Jupiters have massive long-period companions, suggesting that there is a high probability that future radial velocity campaigns will discover additional systems analogous to HAT-P-13b.

Although the current observations of HAT-P-13 provide an improved estimate of the innermost planet's orbital eccentricity, the uncertainty in this parameter is still the single largest contribution to the uncertainty in the Love number. We therefore conclude that this system could benefit from additional secondary eclipse measurements.

One of our model limitations is the lack of constraint on the metallicity of HAT-P-13b's envelope (see Kramm et al. 2012). Therefore, further atmospheric studies are critical to refine our understanding of HAT-P-13b's structure and composition. Atmospheric circulation models for tidally locked planets suggest that high-metallicity atmospheres may have less efficient atmospheric circulation than their lower-metallicity counterparts (Lewis et al. 2010), which does not appear to be the case for HAT-P-13b based on the atmospheric models we perform. Since HAT-P-13 is currently one of the most metal-rich stars known to host a hot Jupiter, it is intriguing that neither HAT-P-13b's core mass nor its atmosphere suggests significant heavy-element enrichment. The HAT-P-13 system will likely provide invaluable leverage when exploring the relationship between host star and planetary metallicity. In addition, full-orbit phase curve observations with Spitzer would also allow us to break degeneracies between the planet's dayside albedo and the efficiency of its atmospheric circulation (e.g., Schwartz & Cowan 2015). The

possibility of independently constraining both the core mass and the atmospheric properties of HAT-P-13b makes this planet an ideal target for future observations.

2.6. Conclusions

In this study we present observations of two secondary eclipses of HAT-P-13b centered at $2,455,326.70818 \pm 0.00406$ and $2,455,355.87672 \pm 0.00226$ BJD_{UTC}. This corresponds to an error-weighted mean eclipse time that is 17.6 ± 2.9 minutes earlier (at orbital phase 0.49582 ± 0.00069) than the predicted time for a circular orbit, indicating that this planet has a nonzero orbital eccentricity. We fit the measured eclipse times simultaneously with the available radial velocity data in order to derive an eccentricity of $e_b = 0.00700 \pm 0.00100$ for this planet, under the assumption that the orbits of HAT-P-13b and HAT-P-13c are coplanar. Using this eccentricity, we calculate a corresponding constraint on the planet's Love number k_2 . We then use this k_2 and the measured radius of HAT-P-13b as constraints on interior structure models, which allow us to directly estimate the mass of the planet's core. Moderate mutual inclinations (up to $\sim 10^\circ$ between the orbits of HAT-P-13b and HAT-P-13c) do not significantly alter the constraint from e_b on the determination of the core mass. We calculate that the core mass of HAT-P-13b is less than $25 M_\oplus$ (9% of the planet's mass; 68% confidence interval), with a most likely core mass of $11 M_\oplus$ (4% of the planet's mass). We also use the secondary eclipse depths to find that the dayside temperature is 1906 ± 93 K. Comparing these depths and the dayside temperature to models, we find that it is likely that HAT-P-13b has a strong atmospheric absorber and efficient dayside energy redistribution. Obtaining the Love number of HAT-P-13b is crucial to determining its core mass because the presence of a modest core in a Jupiter-mass planet is typically masked by its overlying

envelope. The unique opportunity to independently constrain the core mass and atmospheric properties of this hot Jupiter with a modestly sized core makes the HAT-P-13 system an important case study for dynamical constraints on the core masses of gas giant planets.

2.7 Acknowledgments

We thank Henry Ngo and Joseph Harrington for insightful discussions. This work is based on observations made with the Spitzer Space Telescope, which is operated by the Jet Propulsion Laboratory, California Institute of Technology, under contract with NASA. This material is based on work supported by the National Science Foundation Graduate Research Fellowship under grant No. 2014184874. Any opinion, findings, and conclusions or recommendations expressed in this material are those of the authors(s) and do not necessarily reflect the views of the National Science Foundation. This work was based in part on observations obtained at the W.M. Keck Observatory using time granted by the University of Hawaii, the University of California, and the California Institute of Technology. We thank the observers who contributed to the measurements reported here and acknowledge the efforts of the Keck Observatory staff. We extend special thanks to those of Hawaiian ancestry on whose sacred mountain of Mauna Kea we are privileged to be guests.

References

Agol, E., Cowan, N.B, Knutson, H.A., Deming, D., Steffen, J. H., Henry, G. W., and Charbonneau, D., 2010. The climate of HD 189733b from fourteen transits and eclipses measured by Spitzer. The

Astrophysical Journal, 721, pp. 1861-1877.

Bakos, G. Á., Howard, A. W., Noyes, R. W., Hartman, J., Torres, G., Kovács, G, Fischer, D. A., Latham, D. W., Johnson, J. A., Marcy, G. W., and 9 others, 2009. Hat-p-13b,c: A transiting hot Jupiter with a massive outer companion on an eccentric orbit. The Astrophysical Journal, 707, pp. 446-456.

Bakos, G. Á., Penev, K., Bayliss, D., Hartman, J. D., Zhou, G., Brahm, R., Mancini, L., de Val-Borro, M., Bhatti, W., Jordán, A., and 18 others, 2015. HATS-7b: A Hot Super Neptune Transiting a Quiet K Dwarf Star. The Astrophysical Journal, 813, pp. 813-823.

Ballard, S., Charbonneau, D., Deming, D., Knutson, H. A., Christiansen, J. L., Holman, M. J., Fabrycky, D., Seager, S., and A'Hearn, M. F., 2010. A Search for a Sub-Earth-Sized Companion to GJ 436 and a Novel Method to Calibrate Warm Spitzer IRAC Observations. Publications of the Astronomical Society of the Pacific, 122, pp. 1341-1352.

Baraffe, I., Chabrier, G., and Barman, T., 2008. Structure and evolution of super-Earth to super-Jupiter exoplanets-I. Heavy element enrichment in the interior. Astronomy and Astrophysics, 482, pp. 315-332.

Batygin, K., Bodenheimer, P., and Laughlin, G., 2009. Determination of the Interior Structure of Transiting Planets in Multiple-Planet Systems. The Astrophysical Journal, 704, pp. L49-L53.

Batygin, K. & Laughlin, G., 2011. Resolving the $\sin(i)$ Degeneracy in Low-mass Multi-planet System. The Astrophysical Journal, 730, pp. 95-104.

Becker, J. C. & Batygin, K., 2013. Dynamical Measurements of the Interior Structure of Exoplanets. The Astrophysical Journal, 778, pp. 100-111.

Bodenheimer, P., Laughlin, G., and Lin, D. N. C., 2003. On the Radii of Extrasolar Giant Planets. The Astrophysical Journal, 592, pp. 555-563.

- Bodenheimer, P. & Pollack, J., 1986. Calculations of the accretion and evolution of giant planets: The effects of solid cores. *Icarus*, 67, pp. 391-408.
- Boss, A.P., 1997. Giant Planet Formation by Gravitational Instability. *Science*, 276, pp. 1836-1839.
- Burrows, A., Budaj, J., and Hubeny, I., 2008. Theoretical Spectra and Light Curves of Close-in Extrasolar Giant Planets and Comparison with Data. *The Astrophysical Journal*, 678, pp. 1436-1457.
- Burrows, A., Heng, K., Nampaisarn, T., 2011. The Dependence of Brown Dwarf Radii on Metallicity and Cloud: Theory and Comparison with Observations. *The Astrophysical Journal*, 736, pp. 47-61.
- Burrows, A., Hubeny, I., Budaj, J., and Hubbard, W. B., 2007. Possible Solutions to the Radius Anomalies of Transiting Giant Planets. *The Astrophysical Journal*, 661, pp. 502-514.
- Cowan, N. & Agol, E., 2011. The statistics of albedo and heat recirculation on hot exoplanets. *The Astrophysical Journal*, 729, pp. 54-65.
- Deming, D., Harrington, J., Seager, S., and Richardson, L. J., 2006. Strong Infrared Emission from the Extrasolar Planet HD189733b. *The Astrophysical Journal*, 644, pp. 560-564.
- Deming, D., Knutson, H. A., Kammer, J., Fulton, B. J., Ingalls, J., Carey, S., Burrows, A., Fortney, J. J., Todorov, K., Agol, E., and 6 others, 2014. Spitzer Secondary Eclipses of the Dense, Modestly-irradiated, Giant Exoplanet HAT-P-20b Using Pixel-Level Decorrelation. *The Astrophysical Journal*, 805, pp. 132-151.
- Endl, M., Caldwell, D. A., Barclay, T., Huber, D., Isaacson, H., Buchhave, L. A., Brugamyer, E., Robertson, P., Cochran, W. D., MacQueen, P. J., and 6 others, 2014. Kepler-424 b: A "Lonely" Hot Jupiter That Found A Companion. *The Astrophysical Journal*, 795, pp. 151-164.
- Fazio, G. G., Hora, J. L., Allen, L. E., Ashby, M. L. N., Barmby, P., Deutsch, L. K., Huang, J.-S., Kleiner,

- S., Marengo, M., Megeath, S. T., and 55 others, 2004. *The Astrophysical Journal Supplement Series*, 154, pp. 10-17.
- Foreman-Mackey, D., Hogg, D. W., Lang, D., Goodman, J., 2012. *emcee: The MCMC Hammer*. *Publications of the Astronomical Society of the Pacific*, 125, pp. 306-312.
- Fortney, J. J., Lodders, K., Marley, M. S., Freedman, R. S., 2008. A Unified Theory for the Atmospheres of the Hot and Very Hot Jupiters: Two Classes of Irradiated Atmospheres. *The Astrophysical Journal*, 678, pp. 1419-1435.
- Fortney, J. J. & Nettelmann, N., 2010. The interior structure, composition, and evolution of giant planets. *Space Science Reviews*, 152, pp. 423-447.
- Fortney, J. J., Saumon, D., Marley, M. S., Lodders, K., and Freedman, R. S., 2006. Atmosphere, Interior, and Evolution of the Metal-rich Transiting Planet HD 149026b. *The Astrophysical Journal*, 642, pp. 495-504.
- Fulton, B. J., Howard, A. W., Winn, J. N., Albrecht, S., Marcy, G. W., Crepp, J. R., Bakos, G. A., Johnson, J. A., Hartman, J. D., Isaacson, H., and 2 others, 2013. The Stellar Obliquity and the Long-Period Planet in the Hat-P-17 Exoplanetary System. *The Astrophysical Journal*, 772, pp. 80-89.
- Fulton, B. J., Shporer, A., Winn, J. N., Holman, M. J., Pál, A., and Gazak, Z. J., 2011. Long-term transit timing monitoring and refined light curve parameters of HAT-P-13b. *The Astronomical Journal*, 142, pp. 84-92.
- Guillot T., Stevenson D. J., Hubbard W. B. and Saumon D., 2004. Jupiter: The Planet, Satellites and Magnetosphere, ed F. Bagenal, T. E. Dowling and W. B. McKinnon (Vol 1; Cambridge: Cambridge Univ. Press), pp. 35.
- Hartman, J. D., Bakos, G. Á., Torres, G., Kovács, G., Johnson, J. A., Howard, A. W., Marcy, G. W., Latham, D. W., Bieryla, A., Buchhave, L. A., and 19 others, 2013. HAT-P-44b, HAT-P-45b, and

- HAT-P-46b: Three Transiting Hot Jupiters in Possible Multi-Planet Systems. *The Astronomical Journal*, 147, pp. 128-146.
- Helled, R. & Guillot, T., 2013. Interior Models of Saturn: Including the Uncertainties in Shape and Rotation. *The Astrophysical Journal*, 767, pp. 113-120.
- Hubickyj, O., Bodenheimer, P., and Lissauer, J. J., 2005. Accretion of the gaseous envelope of Jupiter around a 5-10 Earth-mass core. *Icarus*, 179, pp. 415-431.
- Husser, T-O., von Berg, S. W., Dreizler, S., Homeier, D., Reiners, A., Barman, T., and Hauschildt, P. H., 2013. A new extensive library of PHOENIX stellar atmospheres and synthetic spectra. *Astronomy & Astrophysics*, 553, pp. A6(1-9).
- Ikoma, M., Guillot, T., Genda, H., Takayuki, T., and Ida, S., 2006. On the Origin of HD149026b. [arXiv:0607212](https://arxiv.org/abs/0607212).
- Ikoma, M., Nakazawa, K., and Emori, H., 2000. Formation of Giant Planets: Dependences on Core Accretion Rate and Grain Opacity. *The Astrophysical Journal*, 537, 1013-1025.
- Kammer, J. A., Knutson, H. A., Line, M. R., Fortney, J. J., Deming, D., Burrows, A., Cowan, N. B., Triaud, A. H. M. J., Agol, E., Desert, J-M., and 8 others, 2015. Spitzer Secondary Eclipse Observations of Five Cool Gas Giant Planets and Empirical Trends in Cool Planet Emission Spectra. *The Astrophysical Journal*, 810, pp. 118-134.
- Knutson, H. A., Fulton, B. J., Montet, B. T., Kao, M., Ngo, H., Howard, A. W., Crepp, J. R., Hinkley, S., Bakos, G. A., Batygin, K., and 3 others, 2014. Friends of Hot Jupiters I: A Radial Velocity Search for Massive, Long-Period Companions to Close-In Gas Giant Planets. *The Astrophysical Journal*, 785, pp. 125-149.
- Knutson, H. A., Lewis, N., Fortney, J. J., Burrows, A., Showman, A. P., Cowan, N. B., Agol, E., Aigrain, S., Charbonneau, D., Deming, D., and 4 others, 2012. 3.6 and 4.5 μm phase curves and evidence

- for non-equilibrium chemistry in the atmosphere of extrasolar planet HD 189733b. *The Astrophysical Journal*, 754, pp. 22-38.
- Kramm, U., Nettelmann, N., Fortney, J. J., Neuhäuser, R., and Redmer, R., 2012. Constraining the interior of extrasolar giant planets with the tidal Love number k_2 using the example of HAT-P-13b. *Astronomy & Astrophysics*, 538, pp. A146(1-8).
- Leconte, J. & Chabrier, G., 2012. A new vision of giant planet interiors: Impact of double diffusive convection. *Astronomy & Astrophysics*, 540, pp. A20(1-13).
- Lewis, N. K., Knutson, H. A., Showman, A. P., Cowan, N. B., Laughlin, G., Burrows, A., Deming, D., Crepp, J. R., Mighell, K. J., Agol, E., and 13 others, 2013. Orbital Phase Variations of the Eccentric Giant Planet HAT-P-2b. *The Astrophysical Journal*, 766, pp. 95-117.
- Lewis, N. K., Showman, A. P., Fortney, J. J., Marley, M. S., Freedman, R. S., and Lodders, K., 2010. Atmospheric circulation of eccentric hot Neptune GJ436b. *The Astrophysical Journal*, 720, pp. 344-356.
- Lindegren L., 2009. Gaia: Astrometric performance and current status of the project, In *IAU Proc. 5, Relativity in Fundamental Astronomy: Dynamics, Reference Frames, and Data Analysis* (Cambridge: Cambridge Univ. Press) pp. 296-305.
- Loeb, A., 2005. A Dynamical Method for Measuring the Masses of Stars with Transiting Planets. *The Astrophysical Journal*, 623, pp. L45-L48.
- Love, A.E.H., 1909. The Yielding of the Earth to Disturbing Forces. *Proceedings of the Royal Society A: Mathematical, Physical and Engineering Sciences*, 82, pp. 73-88.
- Love, A.E.H., 1911. Some Problems of Geodynamics: Being an Essay to which the Adams Prize in the University of Cambridge was Adjudged in 1911. Cambridge University Press Archive.
- Mandel, K. & Agol, E., 2002. Analytic Light Curves for Planetary Transit Searches. *The Astrophysical*

Journal, 580, L171-L175.

Mardling, R., 2007. Long-term tidal evolution of short-period planets with companions. *Monthly*

Notices of the Royal Astronomical Society, 382, pp. 1768-1790.

Mardling, R., 2010. The determination of planetary structure in tidally relaxed inclined systems.

Monthly Notices of the Royal Astronomical Society, 407, pp. 1048-1069.

McLaughlin, D., 1924. Some results of a spectrographic study of the Algol system. *The Astrophysical*

Journal, 60, pp. 22-31.

Miller, N. & Fortney, J.J., 2011. The Heavy Element Masses of Extrasolar Giant Planets, Revealed.

The Astrophysical Journal Letters, 736, pp. L29-L34.

Mizuno, H., 1980. Formation of the Giant Planets. *Progress of Theoretical Physics*, 64, pp. 544-557.

Nesvorný, D., Transit Timing Variations for Eccentric and Inclined Exoplanets. *The Astrophysical*

Journal, 701, pp. 1116-1122.

Nettelmann, N., Becker, A., Holst, B., and Redmer, R., 2012. Jupiter models with improved ab initio

hydrogen equation of state (H-REOS.2). *The Astrophysical Journal*, 750, pp. 52-62.

Neveu-VanMalle, M., Queloz, D., Anderson, D. R., Brown, D. J. A., Collier Cameron, A., Delrez, L.,

Díaz, R. F., Gillon, M., Hellier, C., Jehin, E., and 7 others, 2016. Hot Jupiters with relatives:

discovery of additional planets in orbit around WASP-41 and WASP-47. *Astronomy &*

Astrophysics, 586, pp. A93(1-12).

Paxton, B., Bildsten, L., Dotter, A., Herwig, F., Lesaffre, P., and Timmes, F., 2010. Modules for

Experiments in Stellar Astrophysics (MESA). *The Astrophysical Journal*, 192, pp. 3-38.

Payne, M. & Ford, E., 2011. An analysis of jitter and transit timing variations in the HAT-P-13 system.

The Astrophysical Journal, 729, pp. 98-113.

Perez-Becker, D. & Showman, A., 2013. Atmospheric heat redistribution on hot Jupiters. *The*

Astrophysical Journal, 776, pp. 134-150.

Pollack, J. B., Hubickyj, O., Bodenheimer, P., Lissauer, J. J., Podolak, M., and Greenzweig, Y., 1996.

Formation of the giant planets by concurrent accretion of solids and gas. *Icarus*, 124, pp. 62-85.

Pont, F., Zucker, S., and Queloz, D., 2006. The effect of red noise on planetary transit detection.

Monthly Notices of the Royal Astronomical Society, 373, pp. 231-242.

Rafikov, R., 2006. Atmospheres of Protoplanetary Cores: Critical Mass for Nucleated Instability. *The*

Astrophysical Journal, 648, pp. 666-682.

Ragozzine, D. & Wolf, A., 2008. Probing the interiors of very hot Jupiters using transit light curves.

The Astrophysical Journal, 698, pp. 1778-1794.

Rossiter, R. A., 1924. On the detection of an effect of rotation during eclipse in the velocity of the

brigher component of beta Lyrae, and on the constancy of velocity of this system. *The Astrophysical Journal*, 60, pp. 15-21.

Safronov V. 1969 *Evolution of the Protoplanetary Cloud and Formation of the Earth and Planets*

(Moscow: Nauka) English translation: NASA TTF-677. 1972.

Sato, B., Fischer, D. A., Henry, G. W., Laughlin, G., Butler, R. P., Marcy, G. W., Vogt, S. S.,

Bodenheimer, P., Ida, S., Toyota, E., and 11 others, 2005. The N2K consortium. II. A transiting hot Saturn around HD 149026 with a large dense core. *The Astrophysical Journal*, 663, pp. 465-473.

Saumon, D., Chabrier, G., and van Horn, H. M., 1995. An equation of state for low-mass stars and

giant planets. *Astrophysical Journal Supplement*, 99, pp. 713-741.

Schwartz, J. & Cowan, N., 2015. Balancing the energy budget of short-period giant planets: Evidence

for reflective clouds and optical absorbers. *Monthly Notices of the Royal Astronomical Society*,

449, pp. 4192-4203.

Southworth, J., 2010. Homogeneous studies of transiting extrasolar planets - III. Additional planets and stellar models. *Monthly Notices of the Royal Astronomical Society*, 408, pp. 1689-1713.

Southworth, John, Bruni, I., Mancini, L., and Gregorio, J., 2012. Refined physical properties of the HAT-P-13 planetary system. *Monthly Notices of the Royal Astronomical Society*, 420, pp. 2580-2587.

Sterne, T., 1939. Apical Motion in Binary Stars. *Monthly Notices of the Royal Astronomical Society*, 99, pp. 451-462.

Stevenson, D. J., 1982. Formation of the giant planets. *Planetary and Space Science*, 30, pp. 755-764.

Torres, G., Bakos, G. Á., Kovács, G., Latham, D. W., Fernández, J. M., Noyes, R. W., Esquerdo, G. A., Sozzetti, A., Fischer, D. A., Butler, R. P., and 6 others, 2007. HAT-P-3b: A heavy-element-rich planet transiting a K dwarf star. *The Astrophysical Journal*, 666, pp. L121-L124.

Torres, G., Fischer, D. A., Sozzetti, A., Buchhave, L. A., Winn, J. N., Holman, M. J., and Carter, J. A., 2012. Improved spectroscopic parameters for transiting planet hosts. *The Astrophysical Journal*, 757, pp. 161-175.

Winn, J. N., Holman, M. J., Bakos, G. A., Pal, A., Johnson, J. A., Williams, P. K. G., Shporer, A., Mazeh, T., Fernandez, J., Latham, D. W., and 1 other, 2007. The transit light curve project. VII. The not-so-bloated exoplanet HAT-P-1b. *The Astronomical Journal*, 134, pp. 1707-1712.

Winn, J. N., Holman, M. J., Torres, G., McCullough, P., Johns-Krull, C. M., Latham, D. W., Shporer, A., Mazeh, T., Garcia-Melendo, E., Foote, C. and 2 others, 2008. The transit light curve project. IX. evidence for a smaller radius of the exoplanet XO-3b. *The Astrophysical Journal*, 683, pp. 1076-1084.

Winn, J. N., Johnson, J. A., Howard, A. W., Marcy, G. W., Bakos, G. Á., Hartman, J., Torres, G.,

Albrecht, S., and Narita, N., 2010. The Hat-P-13 exoplanetary system: evidence for spin-orbit alignment and a third companion. *The Astrophysical Journal*, 718, pp. 575-582.

Wong, I., Knutson, H. A., Cowan, N. B., Lewis, N. K., Agol, E., Burrows, A., Deming, D., Fortney, J. J., Fulton, B. J., Langton, J., and 2 others, 2014. Constraints on the atmospheric circulation and variability of the eccentric hot Jupiter XO-3b. *The Astrophysical Journal*, 794, pp. 134-146.

Chapter 3

SUBLIMATION PIT DISTRIBUTION INDICATES CONVECTION CELL SURFACE VELOCITIES OF ~10 CENTIMETERS PER YEAR IN SPUTNIK PLANITIA, PLUTO

Buhler, P.B. and Ingersoll, A.P. (2018). Sublimation pit distribution indicates convection cell surface velocities of ~10 cm per year in Sputnik Planitia, Pluto. *Icarus* 300, pp. 327-340.

doi:10.1016/j.icarus.2017.09.018

3.1. Abstract.

The $\sim 10^6$ km² Sputnik Planitia, Pluto is the upper surface of a vast basin of nitrogen ice. Cellular landforms in Sputnik Planitia with areas in the range of a few $\times 10^2$ - 10^3 km² are likely the surface manifestation of convective overturn in the nitrogen ice. The cells have sublimation pits on them, with smaller pits near their centers and larger pits near their edges. We map pits on seven cells and find that the pit radii increase by between $2.1 \pm 0.4 \times 10^{-3}$ and $5.9 \pm 0.8 \times 10^{-3}$ m per meter away from the cell center, depending on the cell. This is a lower bound on the size increase because of the finite resolution of the data. Accounting for resolution yields upper bounds on the size vs. distance distribution of between $4.2 \pm 0.2 \times 10^{-3}$ and $23.4 \pm 1.5 \times 10^{-3}$ m m⁻¹. We then use an analytic model to calculate that pit radii grow via sublimation at a rate of $3.6_{-0.6}^{+2.1} \times 10^{-4}$ m yr⁻¹, which allows us to convert the pit size vs. distance distribution into a pit age vs. distance distribution. This yields surface velocities between $1.5_{-0.2}^{+1.0}$ and $6.2_{-1.4}^{+3.4}$ cm yr⁻¹ for the slowest cell and surface velocities between $8.1_{-1.0}^{+5.5}$ and $17.9_{-5.1}^{+8.9}$ cm yr⁻¹ for the fastest cell. These convection rates imply that the surface ages at the edge of cells reach $\sim 4.2 - 8.9 \times 10^5$ yr. The rates are comparable to rates of ~ 6 cm yr⁻¹ that were previously obtained from modeling of the convective overturn in Sputnik Planitia [McKinnon, W.B. et al., *Nature*, 534(7605), 82–85].

Finally, we investigate the surface rheology of the convection cells and estimate that the minimum ice viscosity necessary to support the geometry of the observed pits is of order 10^{16} – 10^{17} Pa s, based on the argument that pits would relax away before growing to their observed radii of several hundred meters if the viscosity were lower than this value.

3.2. Introduction

The New Horizons mission revealed that Pluto is a geologically active planet with a dynamic surface (Stern et al., 2015; Moore et al., 2016a). In particular, the crater-free surface of Sputnik Planitia (SP, informal name)—which is thought to be the upper surface of a several-kilometer deep basin filled with nitrogen ice—is evidence that SP is < 10 Myr old (Greenstreet et al. 2015; Stern et al. 2015; Moore et al. 2016a). Cellular patterns in SP (Fig. 3.1, 3.2) have been interpreted as the upper surface of convection cells within the nitrogen ice that replenish the surface on the timescale of ~500,000 years (McKinnon et al., 2016; Trowbridge et al., 2016). Since there are no impact craters in SP, alternative methods are needed to independently date the surface.

Sublimation pits on the upper surface of SP (Moore et al. 2016a; Moore, et al. 2016b; White et al., 2017) provide such an alternative dating method. Cells in SP typically have smaller pits toward their centers and larger pits toward their edges (Fig. 3.1, 3.2; see also McKinnon et al. 2016; White et al. 2017), suggesting that the pits are growing larger by sublimation during transport from the centers to the edges of the convection cells. This motivates us to calculate the rate at which pit radii enlarge in order to use the spatial distribution of pit sizes to determine the

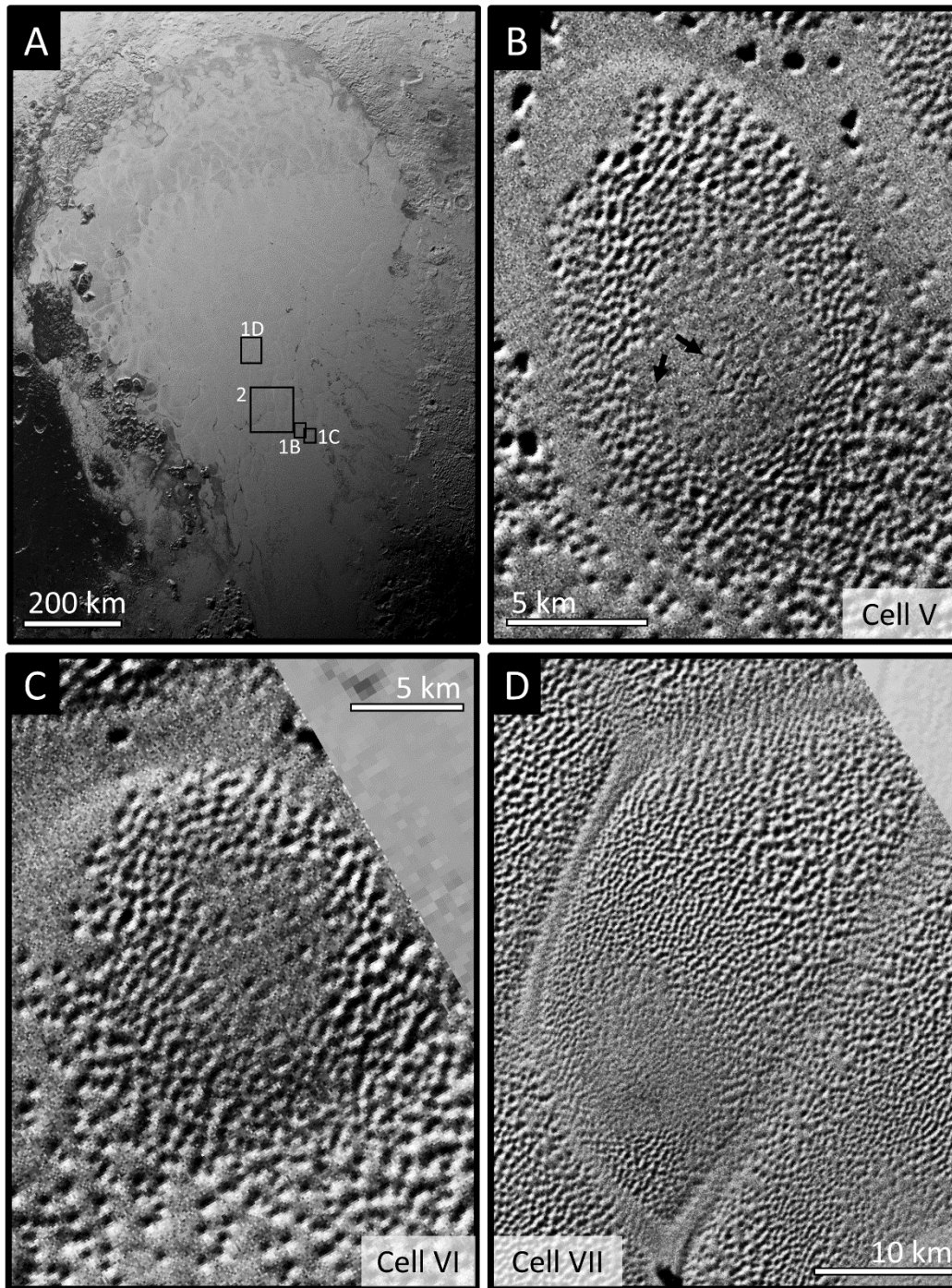


Figure 3.1. **A.** Sputnik Planitia with context for Fig. 3.1B-D, and 2 (black boxes). **B.** Zoom of cell V. Note dense pitting in center, surrounded by region of sparser pitting. Arrows denote edges of sparsely pitted region. Zooms of **C.** cell VI and **D.** cell VII. **A.** Multispectral Visible Imaging Camera (MVIC) image mp2_0299179552. **B-C** LORRI images lor_0299179724 and **D.** lor_0299179715 (**B-D** contrast enhanced).

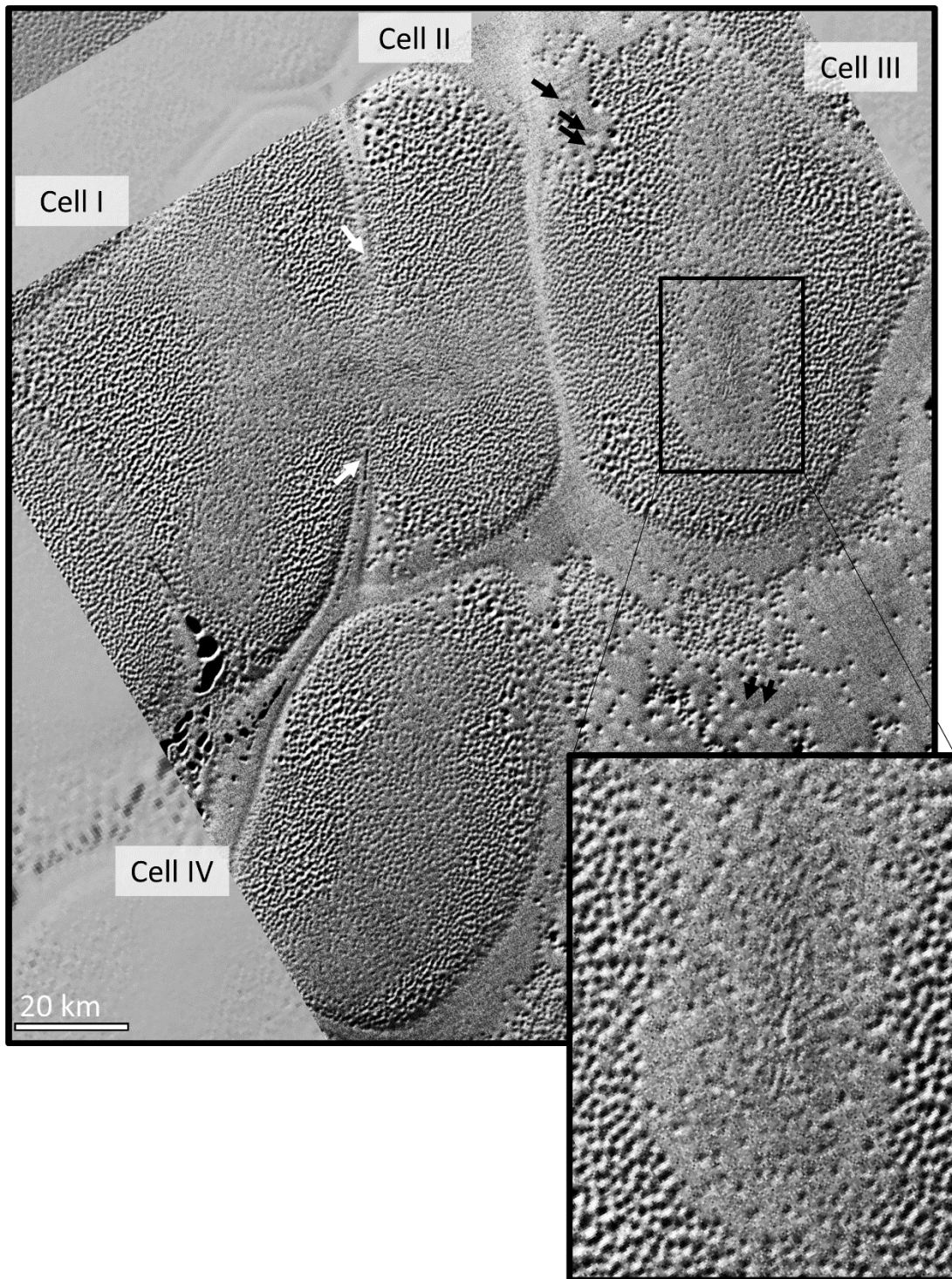


Figure 3.2. Cells I-IV. Note the zoom in on the central texture of cell III. Black arrows indicate shallow pits. White arrows indicate where the boundary between cell I and II is disrupted. LORRI images lor_0299179718 and lor_0299179724 on MVIC background.

surface velocity of the convection cells. We also determine the minimum viscosity required to support the pits. Finally, we discuss our results in the context of other surface measurements and other hypotheses for the spatial distribution of pits on the cells in SP, such as control of the pit distribution due to a thermal gradient across the cells (e.g. White et al., 2017).

3.3. Methods

3.3.1 Pit Distribution Determination

We map pits on seven cells in 80 m/px Long Range Reconnaissance Imager (LORRI; Weaver et al. 2008) imagery using ArcMap 10 (Fig. 3.1, 3.2, 3.3). We select the cells based on complete (or nearly complete) LORRI data coverage. We estimate a 1σ Gaussian error of 1 px (80 m) in the mapped diameter of each pit.

After mapping, we prepare the data for spatial analysis. We divide cells I, II, III, and IV into top, bottom, left, and right quadrants based on their elongated shape and obviously radially asymmetrical pit distributions (Fig. 3.2, 3.3). We fit the quadrants separately. In the left and right quadrants we take distance x to be the perpendicular distance from a line segment that maps the spreading center. In the top and bottom quadrants, we take x to be the distance from the top (or bottom) termination of the line segment mapping the spreading center (Fig. 3.3). For cells V, VI, and VII we take x to be the distance from the estimated central point. We map the central spreading line (or point) based on the approximate bisecting line (or central point) of the contiguous central region of the cell that has low variance at LORRI resolution (e.g. White et al.

2017). These regions correspond to distinctive textures (e.g. Fig. 3.2). We test the sensitivity to our choice of spreading center by shifting the line (or point) by 10% of the maximum width of each cell (several kilometers) and by rotating the lines by 10 degrees. In all but two cases, the fits to pit radius r vs. x are affected by $<20\%$ (also $<2\sigma$). The exceptions are the fit to the left quadrant of cell IV, which varies by up to 40% (2.5σ), and the left quadrant of cell III, which appears to have a complex history and is discussed in more detail in Section 3.5.5.

Top and bottom quadrants typically contain many fewer pits than left and right quadrants and the r vs. x distribution is strongly dependent on the mapped location of the spreading center. Therefore, we choose only to analyze r vs. x in the left and right quadrants of cells I, II, III, and IV.

We fit a linear, analytic least-squares regression to r vs. x for each cell (Fig. 3.4; e.g., Press et al., 1987). We also perform higher-order polynomial fits to the r vs. x distribution. However, the nonlinear coefficients in these fits are indistinguishable from zero and the constant and linear terms do not differ from the linear fit at the 0.5σ level. Calculating the Bayesian Information Criteria (BIC) for each model—which quantifies the trade-off between model goodness of fit (favored) and complexity (disfavored)—the difference in BIC (ΔBIC) between the linear and quadratic models for each cell ranges from 5.9 to 7.2. This strongly indicates that nonlinear models are not justified by the data (e.g., Kass & Raftery, 1995); higher-order polynomials are even more strongly disfavored. In other words, r vs. x is linear within error, even though we do not generally expect constant velocity spreading (see Section 3.5.2).

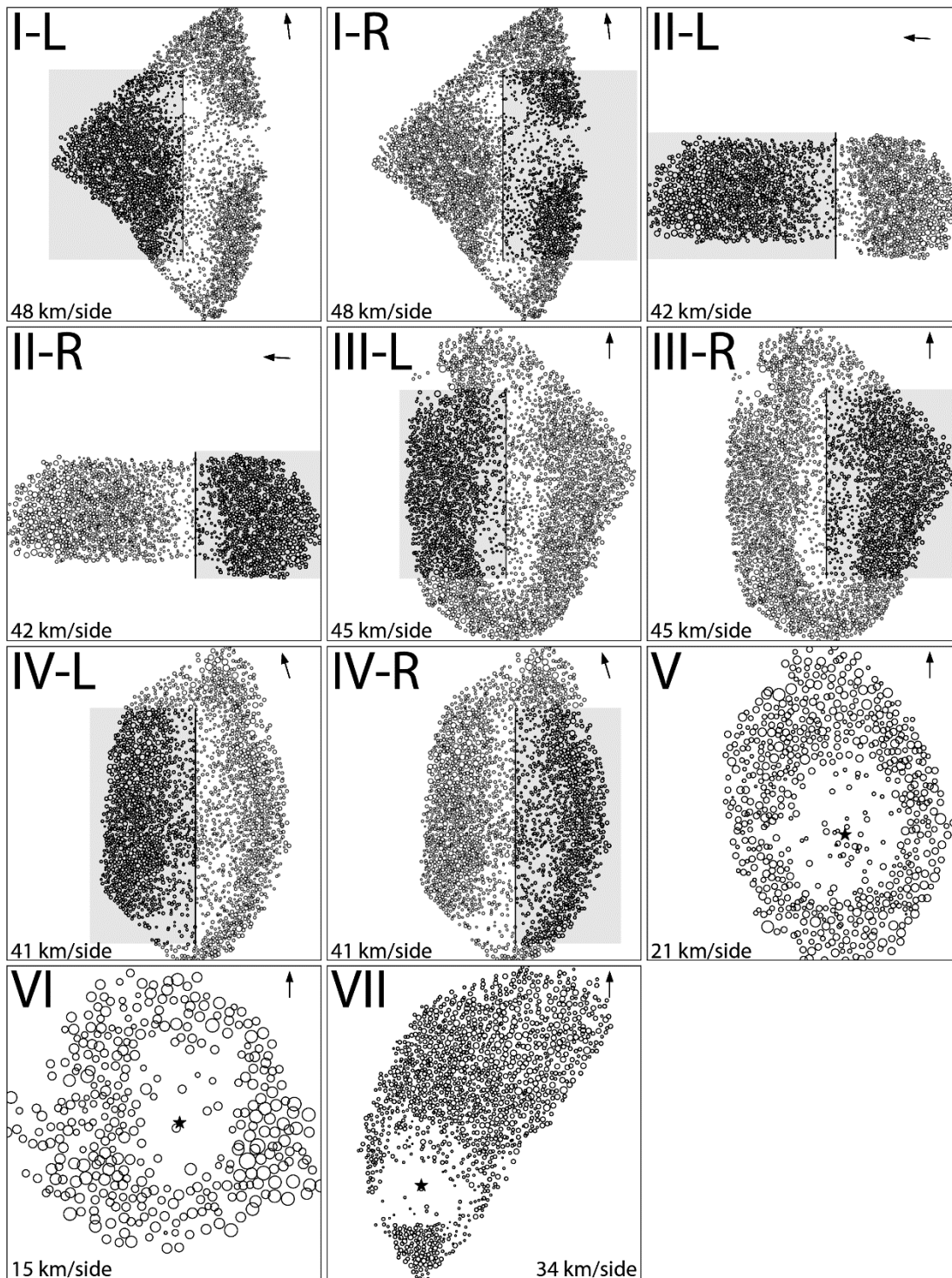


Figure 3.3. Mapped pits on all cells. Circles in the grayed region are the pits used for fits in Fig. 3.4 & 3.7. “L” and “R” designations correspond to “Left” and “Right”. Arrows point north. Vertical lines/stars denote spreading center used for the fits in figures 4 and 7. Note map of cell II is rotated ~ 270 degrees.

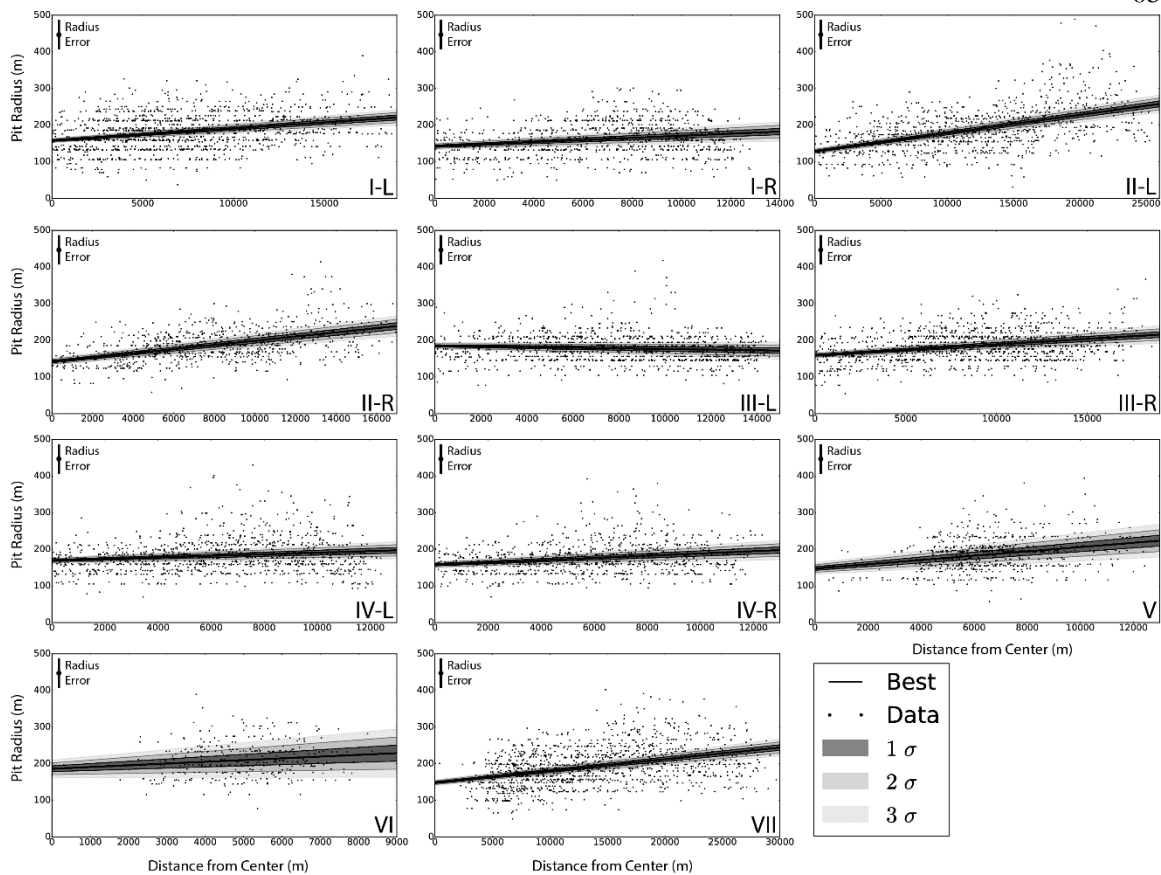


Figure 3.4. Pit radii as a function of distance from the spreading center, with best fit and 1σ , 2σ , and 3σ uncertainty.

3.3.2 Analytic Sublimation Model

We use the r vs. x distribution to determine the age vs. x distribution (i.e., the surface velocity v) by calculating the rate of pit enlargement using a simple analytic model. The model provides a closed-form expression for the total energy absorbed by the walls of a pit under the assumption that the pit is a spherical cap (Ingersoll et al. 1992).

Pit walls receive power from both direct insolation and from scattered sunlight. The extra power absorbed by scattering means that an area subtended by a pit receives more power, as compared to a flat surface, according to (Ingersoll et al., 1992):

$$(3.1) \quad P_{pit} = I_0 \left(\frac{1-A}{1-Af} \right)$$

Here P_{pit} is the power per area absorbed by a flat surface subtended by a pit (including both direct insolation and scattered light), I_0 is the solar insolation (irradiance times the cosine of the incidence angle), and A is the albedo. The factor $f = 1/(1 + D^2/4)$ describes the geometry of the pit (D is the diameter/depth ratio); $f = 1/2$ describes a hemisphere and $f = 0$ describes a flat surface (see Ingersoll et al., 1992; Fig. 3.5). Eq. 3.1 assumes Lambert scattering. Thus, if both A and f are nonzero, then P_{pit} is greater than the power per area absorbed by a flat surface $P_{Flat} = I_0(1 - A)$.

Similarly, the outgoing emitted power per area from a surface subtended by a pit E_{pit} is (Ingersoll et al., 1992):

$$(3.2) \quad E_{pit} = \frac{\varepsilon \sigma_B T_{pit}^4}{1 - (1 - \varepsilon)f}$$

Here ε is the emissivity, σ_B is the Stefan-Boltzmann constant, and T_{pit} is the temperature of the pit walls. Notice that if $T_{pit} = T_{Flat}$ (the temperature of a flat surface) and $\varepsilon = 1$, then E_{pit} is the same as the emitted power per area from a flat surface $E_{Flat} = \varepsilon \sigma_B T_{Flat}^4$. Thus, when both these conditions are fulfilled, the reradiated thermal energy does not enhance sublimation within a pit relative to a flat surface. The N_2 ice in SP is likely in exchange equilibrium with the atmospheric

N_2 , implying the surface is isothermal and thus that $T_{pit} = T_{Flat}$ (e.g. Hansen & Paige 1996; Moore et al. 2016a). Protopapa et al. (2016) report 59 cm grain sizes in SP based on Hapke analysis (with unreported error). This grain size implies that $\varepsilon = 1$, according to the model of Stansberry et al. (1996) for $\beta-N_2$, the stable phase at the surface of SP (e.g., McKinnon et al., 2016). Therefore, we take $E_{pit} = E_{flat}$, which means that the net outgoing reradiated power per area from an area subtended by a pit equals that of a flat surface.

Based on the analysis above, the net difference in power per area between a flat surface and a flat surface subtended by a pit is the scattered power per unit area P_S , which is (Ingersoll, 1992):

$$(3.3) \quad P_S = I_0 A f \left(\frac{1-A}{1-Af} \right)$$

An equivalent statement is $P_S = P_{pit} - P_{Flat}$. We thus take P_S to be the power per unit area available to sublimate the pit walls and cause radial growth of the pits.

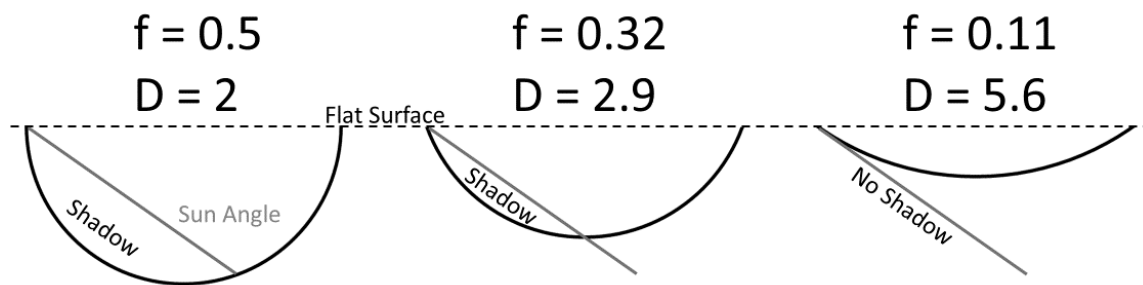


Figure 3.5. Geometrically accurate depiction of pits with diameter/depth ratios D of 2 (hemisphere), 2.9, and 5.6. The corresponding value of f is also given. The sun angle and shadowing indicated is faithful to the illumination in Figs. 1 and 2. Pits with these values of D receive P_S of 1.1, 0.8, and 0.3 mW/m² of scattered power, respectively.

Under the assumption that the pit is a spherical cap, every point on the surface receives the same P_S (Ingersoll et al., 1992). Because P_S is comparable to P_0 and Pluto's high obliquity will cause the angle of the sun on the sky to sample a wide region of parameter space, power will be absorbed approximately evenly over the pit walls. Thus, as N_2 ice is lost to sublimation, we assume the pit remains a spherical cap with constant D , and determine the growth rate due to sublimation evenly distributed over the surface area of the curved walls of the pit $S_{pit} = \pi r^2(1 + 4/D^2)$.

We use A between 0.95 and 0.98, with uniform probability (see Buratti et al., 2017; J. Hofgartner, per. comm.), $I_0 = 0.22 \text{ W m}^{-2}$ (average value over the past 1.3 Myr at 0° latitude (Earle & Binzel, 2015)), N_2 ice density of 1027 kg m^{-3} , and N_2 ice latent heat of $2 \times 10^5 \text{ J kg}^{-1}$. Shadows typically extend 0.5 ± 0.25 of the way across pits, which we take to be a Gaussian distribution accounting for observational uncertainty and actual variation in pit depths. Based on photogrammetry⁴, we estimate that pits have depth/diameter ratios of 0.35 ± 0.09 (with Gaussian errors), yielding $f = 0.32^{+0.11}_{-0.10}$. We also impose a prior that pits are shallower than hemispheres (i.e. $f \leq 1/2$) and that pits are deep enough to have shadows, which is a universal feature of all pits we map (e.g. Fig. 3.1, 3.2) and implies that $f \geq 0.11$ (Fig. 3.5).

The radiative transfer model is potentially sensitive to A because the power per area depends on $1-A$ and A is near 1. However, as long as $A > 0.9$, the growth rate we report remains the same within a factor of ~ 3 . Likewise, as long as $\epsilon > 0.9$, which we expect for grain sizes larger than $\sim 5 \text{ cm}$ (see figure 2 of Stansberry et al., 1996), the growth rate we report remains the same within a factor of ~ 3 . We note that, while the global plutonian atmosphere may periodically

⁴ Illumination geometry calculated based on ephemeris from Pluto Ephemeris Generator 2.6 (http://pds-rings.seti.org/tools/ephem2_plu.html by Mark Showalter)

collapse, a local atmosphere will likely remain over regions covered by large N₂ ice deposits, like Spunik Planitia (Hansen and Paige, 1996). Thus, we expect radiative balance, not vapor diffusion into the atmosphere, will always control sublimation. “Year” refers to terrestrial year throughout this paper.

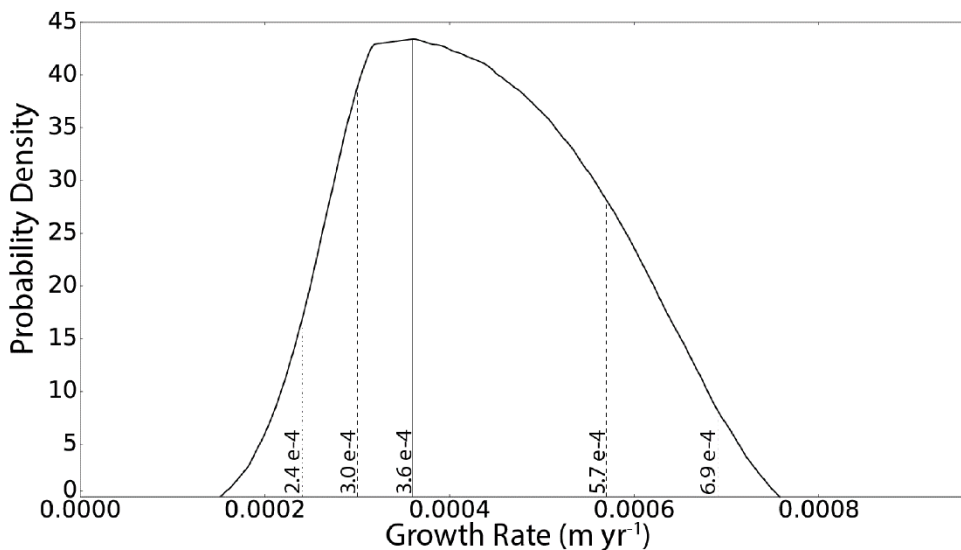


Figure 3.6. The probability density function of the pit growth rate, with most likely rate (solid), 1σ (dash), and 2σ (dash-dot) uncertainties indicated.

Table 3.1. General Cell and Pit Properties

Cell #	# Pits	Cell Area (km ²)	Average Pits/km ²	Total Area (km ²)	Pit Area	Pit Coverage
I	2889	998	2.9	294		29%
II	1848	659	2.8	220		33%
III	2989	1184	2.5	338		29%
IV	2254	826	2.7	247		30%
V	636	275	2.3	74		27%
VI	354	160	2.2	51		32%
VII	1327	678	2.0	165		24%

Table 3.1. Cell designations, the number of pits per cell, the cell area, the average number of pits per area, the total area covered by pits, and the total fraction of the cell covered by pits at LORRI resolution.

3.4. Results

3.4.1 Pit Distribution and Convection Rates

We map 12,297 pits across all seven cells (Fig. 3.1, 3.2, 3.3). Cells range in area from 150-1050 km², with 354-2989 pits per cell and an average of 2.0-2.9 pits per km² (Table 3.1). At LORRI resolution, pits cover between 24%-33% of the surface of the cells (Table 3.1). The slope of the r vs. x distribution of pits ranges from $2.1 \pm 0.4 \times 10^{-3} \text{ m m}^{-1}$ to $5.9 \pm 0.8 \times 10^{-3} \text{ m m}^{-1}$. The intercept of the r vs. x distribution of pits ranges from $128 \pm 3 \text{ m}$ to $186 \pm 8 \text{ m}$. Table 3.2 contains the complete list of best-fit parameters.

The analytic sublimation model yields a growth rate of $3.6_{-0.6}^{+2.1} \times 10^{-4} \text{ m yr}^{-1}$ (Fig. 3.6). This implies that surface velocities range from $6.2_{-1.4}^{+3.8} \text{ cm yr}^{-1}$ to $19.9_{-4.4}^{+11.7} \text{ cm yr}^{-1}$ (Fig. 3.7). This surface velocity is similar to the results of the McKinnon et al. (2016) convection model, which predicts $\sim 6 \text{ cm yr}^{-1}$ convection rates (with a factor of a few uncertainty; W. McKinnon (pers. comm.)), supporting the hypothesis that the cells are the surface expression of convection in the sluggish lid regime. The errors quoted here take into account the uncertainty in A and f , but do not take into account the possible effects of viscous relaxation of pits, resolution limit of the dataset, or mergers between pits. We discuss these in Sections 3.5.1, 3.5.2, and 3.5.3.

The r vs. x distributions for all cells except the left quadrant of cell III have slopes that are nonzero at the 3σ level (Table 3.2). We infer that a complex geologic history, including unstable convective interaction between cells I, II, and III, causes the left quadrant of cell III to be different and discuss this further in Section 3.5.5.

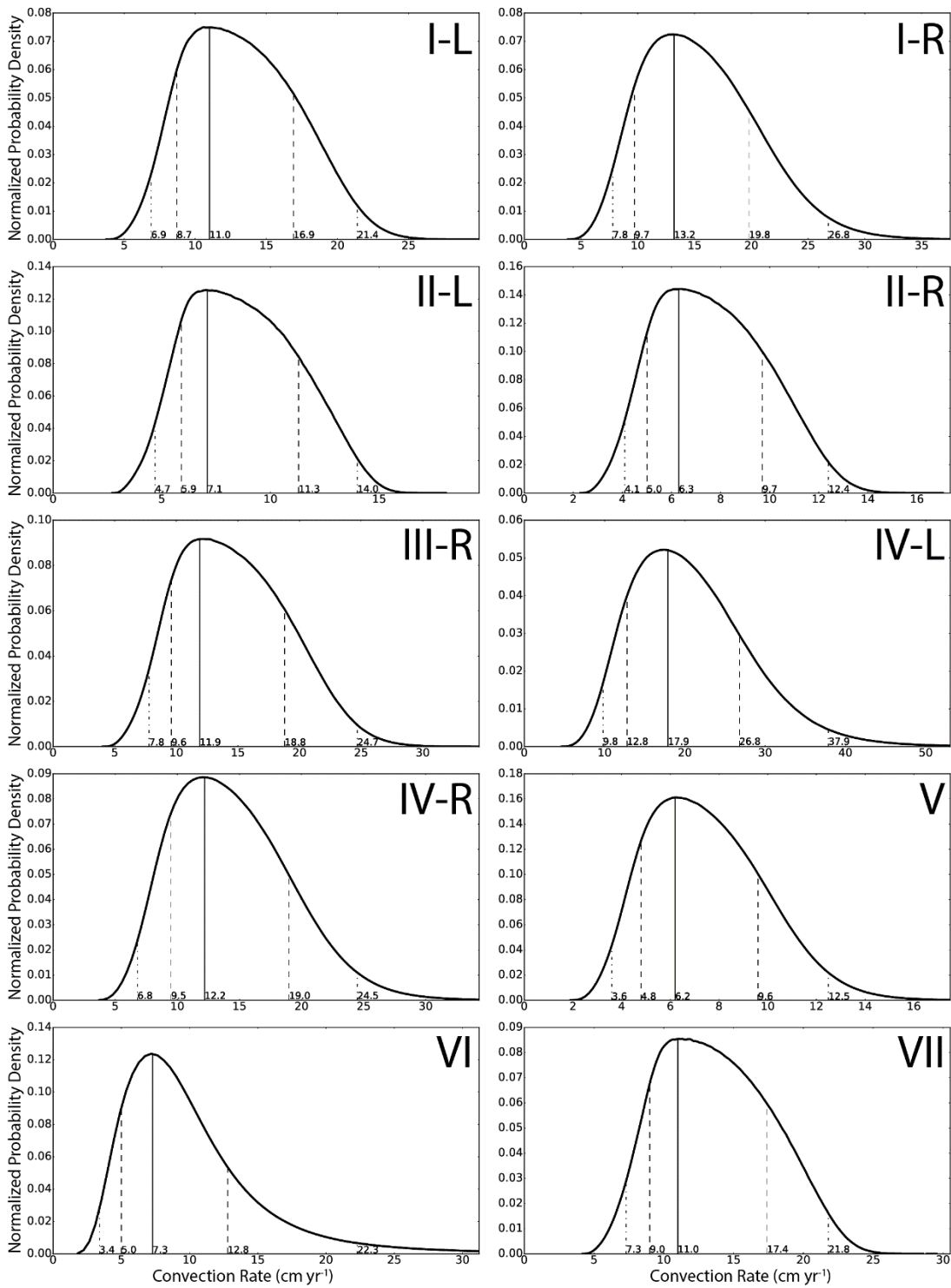


Figure 3.7. The probability density function of the surface velocity for each cell, with most likely rate (solid), 1σ (dash), and 2σ (dash-dot) uncertainties indicated. Cell III-L has not been included here (see Fig. 3.10, Table 3.2).

Table 3.2. Pit Distribution

Map Area	# Pits	Intercept (m)	Slope (m m ⁻¹)	Best-fit Velocity (cm yr ⁻¹)	68% Interval (cm yr ⁻¹)	95% Interval (cm yr ⁻¹)	Convection Length (km)	Convection Time (yr)
I-L	1281	158 ± 2	0.00330 ± 0.00025	11.0	8.7-16.9	6.9-21.4	19	1.73E+05
I-R	927	143 ± 3	0.00285 ± 0.00040	13.2	9.7-19.8	7.8-26.8	13	9.85E+04
II-L	1029	128 ± 3	0.00498 ± 0.00021	7.1	5.9-11.3	4.7-14.0	25	3.52E+05
II-R	819	142 ± 3	0.00570 ± 0.00036	6.3	5.0-9.7	4.1-12.4	17	2.70E+05
III-L	1361	185 ± 3	-0.00087 ± 0.00033	-	-	-	-	-
III-R	1113	159 ± 3	0.00298 ± 0.00028	11.9	9.6-18.8	7.8-24.7	17	1.43E+05
IV-L	1049	170 ± 3	0.00214 ± 0.00039	17.9	12.8-26.8	9.8-37.9	13	7.26E+04
IV-R	897	158 ± 3	0.00307 ± 0.00044	12.2	9.5-19.0	6.8-24.5	13	1.07E+05
V	636	148 ± 5	0.00585 ± 0.00075	6.2	4.8-9.6	3.6-12.5	13	2.10E+05
VI	354	186 ± 8	0.00474 ± 0.00156	7.3	5.0-12.8	3.4-22.3	8	1.10E+05
VII	1327	148 ± 3	0.00319 ± 0.00017	11.0	9.0-17.4	7.3-21.8	29	2.64E+05
I-R (top)	424	129 ± 4	0.00324 ± 0.00043	11.5	9.0-18.0	6.6-22.9		
I-R (bot)	503	145 ± 4	0.00318 ± 0.00048	11.8	9.6-19.2	6.4-23.6		
III-L (top)	638	171 ± 3	0.00188 ± 0.00031	15.9	12.3-24.5	9.3-31.3		
III-L (bot)	723	161 ± 3	0.00235 ± 0.00028	19.9	15.5-31.6	11.1-41.1		

Table 3.2. Map area names corresponding to designations in Figs. 3.1-3.4 and 3.7-3.9, the number of pits per map area, the best-fit intercept and slope with 68% confidence, the best-fit velocity with 68% and 95% confidence intervals, the length from the spreading center to cell edge, and duration of convection. Values are based on raw data, not accounting for resolution. We only report the number of pits, slope, and intercept for III-L because the other values would be unphysical (see Section 3.5.5).

3.5. Discussion

3.5.1 Cell Surface Rheology

The main components of SP are likely N_2 and CH_4 ice (Protopapa et al., 2017). However, the rheology of N_2 and CH_4 ice under conditions relevant to the surface of Pluto is uncertain (see, e.g. Moore et al., 2016b). For CH_4 , Moore et al. (2016b) find a nine order-of-magnitude discrepancy in viscosity between extrapolated laboratory measurements from Yamashita et al. (2010) and theoretical predictions from Eluszkiewicz and Stevenson (1991). Moore et al. (2016) suggest that the use of laboratory-annealed CH_4 ice in the Yamashita et al. (2010) experiments may lead to the divergent results. Similarly, we calculate a nine order-of-magnitude difference in N_2 viscosity between extrapolated laboratory measurements from Yamashita et al. (2010) and theoretical predictions from Eluszkiewicz and Stevenson (1991).

3.5.1a Laboratory and Theoretical Predictions for N_2 Rheology at Plutonian Surface Conditions

Yamashita et al. (2010) perform compression experiments on N_2 ice at 45 K and 56 K and stresses between ~ 0.1 -1 MPa. Pluto's surface temperature is 37 K (Gladstone et al., 2016; Stern et al., 2015) and the stress at the bottom of a pit Σ is $\sim 7 \times 10^{-2}$ MPa (from $\Sigma = \rho gh$; ρ is the density of N_2 ice, g is the plutonian surface gravity (0.617 m s^{-2}), and we set $h = 100$ m for definitiveness). We extrapolate from the stresses in the Yamashita et al. (2010) experiment to those in a pit bottom using the empirical relation for scaling the N_2 viscosity η reported by

Yamashita et al. (2010). To extrapolate the experimental results to the plutonian surface temperature we use (Weertman, 1970):

$$(3.4) \quad \eta_1 = \eta_0 \exp \left[-a \left[\frac{T_m}{T_0} - \frac{T_m}{T_1} \right] \right]$$

Here T_0 is the temperature at which the viscosity is known, T_1 is the temperature at which the viscosity is desired. $T_m = 63.15$ K (Eluzkiewicz & Stevenson, 1991) is the melting temperature of N_2 ice, and a is an empirical constant (estimated here to be ~ 5 by applying Eq. 3.4 to the viscosities measured by Yamashita et al. (2010) at 45 K and 56 K). This yields an expected viscosity of approximately 10^{10} Pa s.

A theoretical derivation of the rheology of N_2 in the diffusion limit (Eluzkiewicz and Stevenson, 1991) indicates that the viscosity may be much higher. Following the suggestion of Eluzkiewicz and Stevenson (1991), we use their Figure 1 to scale derived CH_4 rheologic properties to N_2 rheologic properties. This exercise implies strain rates of $\sim 10^{-15} \text{ s}^{-1}$ for applied stresses at pit bottoms (~ 0.1 MPa) for an N_2 ice shear stress of 20 GPa (Eluzkiewicz and Stevenson, 1991), implying a viscosity of $\sim 10^{19}$ Pa s. We note (i) that the theoretical prediction is based on sparse data, extrapolations over many orders of magnitude, and reliance on the similarity between CH_4 and N_2 and (ii) we have extrapolated beyond the pressure and temperature ranges measured in the Yamashita et al. (2010) experiment. It is clear that rheology of N_2 ice at plutonian surface conditions is not well known.

3.5.1b Estimate of Surface Viscosity Based upon the Presence of Pits

We may estimate the viscosity-dependent relaxation timescale for pits (i.e., the characteristic timescale for pits to flatten due to viscous flow). The relaxation timescale appropriate to pits embedded in a homogeneous viscous layer of thickness d overlying an inviscid, vigorously convecting layer is (Solomon et al., 1982):

$$(3.5) \quad t_r = \frac{2\eta k}{\rho g} \left[\frac{e^{2kd} + e^{-2kd} - 4(kd)^2 - 2}{e^{2kd} - e^{-2kd} + 4kd} \right]$$

Here k is the wavenumber (2π divided by the pit diameter (300 m, for definitiveness)), and t_r is the time for topography to relax by a factor of $1/e$; t_r is insensitive to d when d exceeds the pit depth. Note that we could also choose a prescription in which the viscosity decreases exponentially with depth (e.g. due to increasing temperature with depth). Under this prescription, the long wavelength limit approaches Eq. 3.5 and the short wavelength limit approaches relaxation in a uniform viscosity material, $t_r = 2\eta k / \rho g$ (see equations 8.4.10-8.4.15 of Melosh, 1989); this does not change our conclusions.

Using $\eta = 10^{10}$ Pa s (based upon Yamashita et al. (2010)) yields a t_r of ~ 7 days. Using $\eta = 10^{19}$ Pa s (based upon Eluzkiewicz and Stevenson (1991)) yields a t_r of $\sim 2 \times 10^7$ yr. Based on the $3.6_{-0.6}^{+2.1} \times 10^{-4}$ m yr⁻¹ radial growth rate of pits that we calculate, the observed pits with radii of a few hundred meters should take on the order of 10^5 yr to form. This implies that relaxation timescales should be at least this large; otherwise, the pits would relax away before reaching their observed size. Relaxation timescales of $>10^5$ yr imply a minimum viscosity of at least $\sim 10^{16} - 10^{17}$ Pa s.

We therefore conclude that the observation of pits in SP is consistent with the theoretical prediction of N₂ ice viscosity from Eluzkiewicz and Stevenson (1991), but inconsistent

with the values reported by Yamashita et al. (2010) (also noted by Moore et al., 2016b). There are several potential reasons for the inconsistency. First, the laboratory-annealed N₂ ice may not be representative of the ice in SP (Moore et al., 2016b). Second, the mixture of different ices (N₂, CH₄, and others) present at the surface of SP may have an increased viscosity compared to the single phases (Moore et al., 2016b). Third, power-law flow—as was observed for N₂ ice by Yamashita et al. (2010)—is typically strongly grain-size dependent (e.g. Durham et al., 2010), and scales as the inverse square (“Nabarro-Herring creep”) or inverse cube (“Coble creep”) of the grain size. While Yamashita et al. (2010) do not report grain sizes in their N₂ ice experiments, they report that the ice was polycrystalline and the experimental chamber was 10 x 15 mm, implying that the grain sizes were several mm or smaller. Eluszkiewicz & Stevenson (1991) derive rheologies based on 0.1 mm grain sizes. Grain sizes for the surface of SP are reported to be 59 cm (Protopappa et al., 2017) based on Hapke modeling. While there is uncertainty associated with the Hapke modeling, grains may realistically reach this scale based upon modeling by Zent et al. (1989), which shows that N₂ ice grains on Triton, under conditions similar to Pluto, should sinter to meter-scale grains within ~100 yr. We note, though, that nonvolatile impurities, such as tholins, could arrest grain growth (e.g. Barr and Milkovich, 2008). If the grain sizes reach tens of centimeters or larger, the viscosity reported by Yamashita et al. (2010) could scale up by six to nine orders of magnitude, which would be consistent with the observed pits in SP.

Finally, we note that, while grains can coarsen due to annealing, grain size can also decrease due to dynamic recrystallization under high stress (e.g., Durham et al., 2010), such as might occur in underlying convecting ice. Therefore, the grain sizes and viscosities relevant to pit relaxation need not be the same as those relevant to convection (e.g. Umurhan et al., 2017). Clearly, there is much to learn about the rheologic properties of these ices.

3.5.1c Radial Growth Dominated by Sublimation

We argue that viscous relaxation will not significantly affect the radial growth rate of the pits, as follows. We observe pits (they have not relaxed away), and so expect that the sublimation of the pit floor is at least in equilibrium with relaxation at the bottom of the pit. Long-wavelength relaxation (e.g. uplift of the pit floor) will proceed on much shorter timescales than short-wavelength relaxation (e.g. flow of pit walls) (e.g., Melosh, 1989; Moore et al., 2016b). Therefore, the uplift rate of the pit floor will exceed the flow rate of the walls near the rim, and sublimation rates will dominate viscous flow in setting the radial growth rate. Thus, the dominant topographic influence of viscous relaxation on large (~100 m radius) pits will be to set the depth of the pits, similarly to the way craters on icy satellites relax in depth while preserving their diameters (e.g. Parmentier and Head, 1981). We conclude, then, that viscous relaxation does not strongly affect our measurement of the pit radius distribution, except inasmuch as viscous control of pit depths may influence growth rates of pits through the depth/diameter ratio (Section 3.3.2, Eq. 3.3, Figs. 3.5 & 3.6).

3.5.2 Pit Distribution Linearity and Nonzero Intercept

3.5.2a Expected Surface Velocity Profile and Pit Distribution

An upwelling plume of finite width should have a distally accelerating surface velocity gradient over the plume, with horizontal velocities near stagnation at the center of the plume (Fig. 3.8; McKinnon et al., 2016). If the surface velocity reaches large enough values, such that

lateral transport of pits significantly outpaces the formation of new pits, then, in the accelerating region, pit density should decrease because the flux of pits carried into a region will be lower than the flux out. Thus, in the central region of the cell, we expect a stagnant, densely pitted region surrounded by a less densely pitted, accelerating region.

Distal to the upwelling region, we expect two end-member possibilities. If the cell is axially symmetric, the velocity will asymptotically decrease (due to continuity) at a rate inversely proportional to the distance from the cell center (Fig. 3.8; McKinnon et al., 2016). If the cell is bilaterally symmetric, the velocity will remain near a constant value (also due to continuity) (Fig. 3.8). In both cases, we expect an evenly dense distribution of pitting because the inward and outward flux of surface material is constant across this region.

Therefore, distal to the central upwelling region, we expect the bilaterally symmetric cells (I, II, III, and IV) to have a linear increase in pit size due to a transport at a constant surface velocity. We expect the axially symmetric cells (V, VI) to have a quadratic increase in pit size due to transport at a velocity that is decreasing at a rate inversely proportional to the distance from the cell center. Cell VII is neither radially nor axially symmetric but, due to its elongated nature, we expect the surface velocity profile to more closely resemble the bilaterally symmetric, constant velocity case. We also expect that the scatter in pit sizes, coupled with effects from viewing the cells at finite resolution, will affect our determination of the slope and intercept of all of the pit distributions.

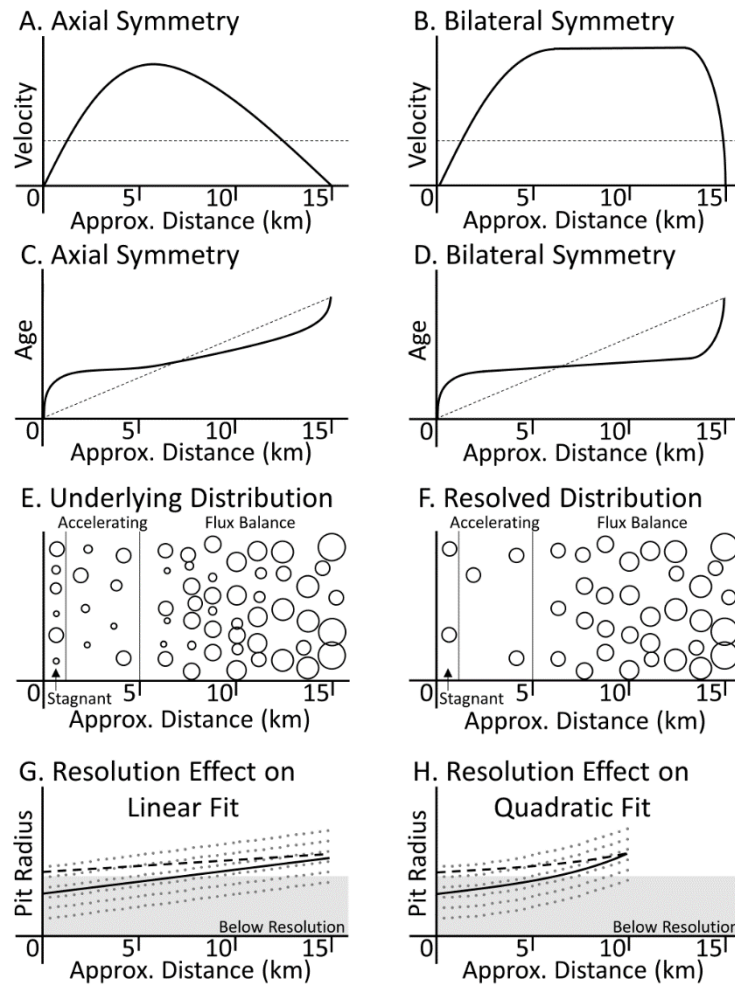


Figure 3.8. **A.** Schematic surface velocity profile (thick black) for an axially symmetric cell adapted from figure 4 of McKinnon et al. (2016). Dashed line of constant velocity added for reference. **B.** Schematic surface velocity profile for a bilaterally symmetric cell. The sharp drop off indicates the termination of the cell. **C.** Schematic age vs. distance plot based on the velocity profile in A. **D.** Schematic age vs. distance plot based on B. Note that the slopes in C and D are inversely proportional to velocity and so the age (i.e. residence time) gradient near the cell center is steep. **E.** Schematic depiction of the underlying pit distribution. Note that the accelerating region has a lower density of pits than both the stagnant region and the region where the flux of pits per unit area is constant. **F.** Schematic depiction of pit distribution when viewed at finite resolution. **G.** Schematic representation of the effect of finite resolution to decrease the inferred slope and increase the inferred intercept (dashed line) compared to that of the true distribution (solid line). The gray dots represent a pit radius distribution with high scatter. Gray box indicates region below resolution. **H.** Same as G, but for a quadratic distribution. Note the curvature in the dashed line is reduced compared to the curvature in the solid line. The fit truncates to indicate that the axially symmetric cells have smaller lateral extent, further complicating the fit.

3.5.2b Qualitative Resolution Effects

Resolution limits will conceal the small-radius population of pits. This means that only the largest pits on the younger, more central surfaces will be visible and these surfaces will appear less densely pitted. We attribute the nonzero intercept to this effect and interpret that the intercept probes the maximum timescale over which pits reside near the stagnant cell center (see Section 3.5.4). The large scatter in pit radii may be partially due to variable duration spent near the stagnant region of the cell, because residence time (and thus growth time) near the cell center will vary strongly as a function of distance from the center of the cell because the surface is accelerating (Fig. 3.8C and 3.8D).

As a parcel of the cell surface moves away from the cell center and ages, the pits in that parcel grow larger and become visible at LORRI resolution. This causes the density of observable pits to increase with distance from the cell center, which is consistent with observation (Fig. 3.3 & 3.9). This effect also artificially decreases the observable pit size distribution on older surfaces relative to younger surfaces, which will decrease the best-fit slope and increase the intercept (Fig. 3.8). The increased observability of the small-radius population with age will also dilute the signal of surface velocity deceleration, if present. We propose that this dilution, compounded with the large measurement errors relative to the absolute pit sizes, means that the second order features (acceleration) in the velocity curve expected in the axially symmetric cells (V and VI) could not be resolved with the current data. Note that cells V and VI are also significantly smaller and have proportionally fewer pits relative to other cells (Table 3.1), further reducing the ability to fit higher order features in their distribution (Fig. 3.8H).

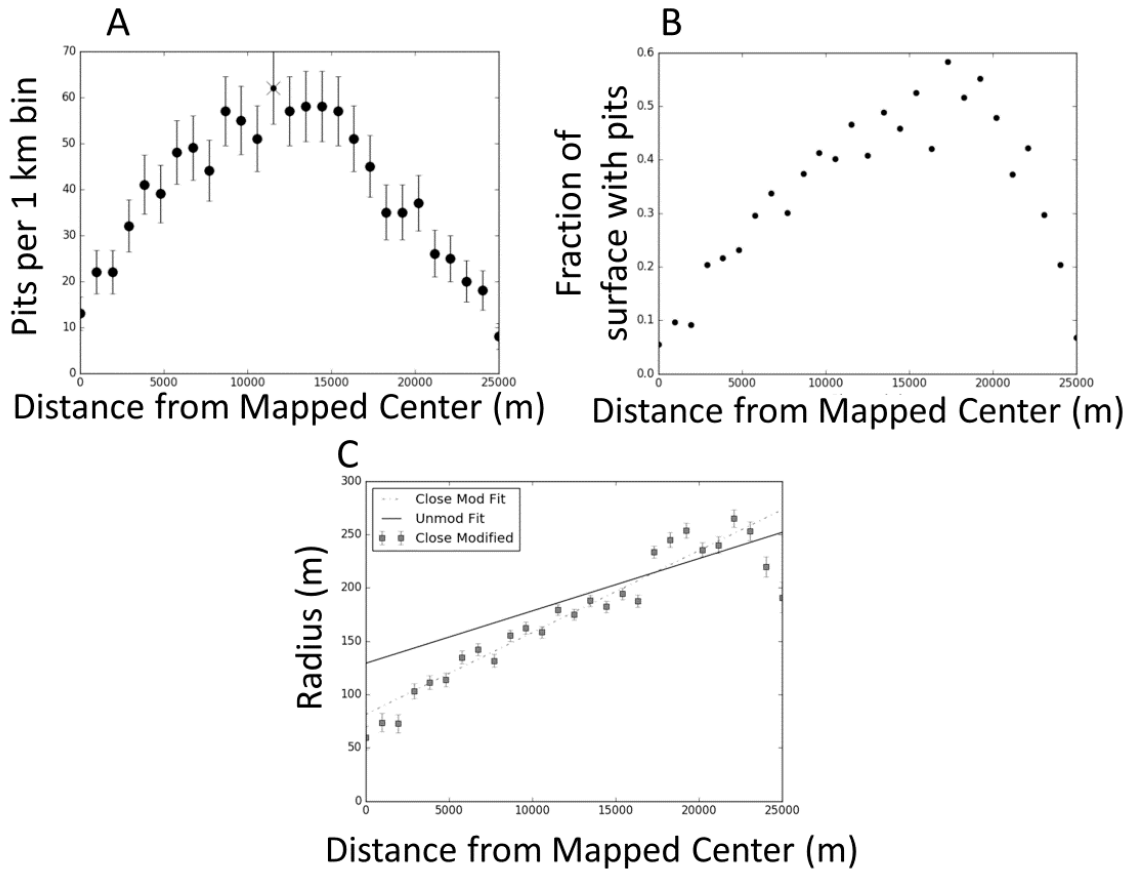


Figure 3.9. **A.** The number of pits N per each kilometer bin in cell II. The “x” indicates the bin with the largest number of pits per bin. Poisson \sqrt{N} error bars are given. **B.** The fractional area covered by pits in 1 km bins. Note the decrease beyond ~ 20 km. **C.** Fit to the binned data (dash-dot) after scaling the radii (squares) of the bins interior to bin with the largest number of pits in order to account for pits hidden by resolution. The scaling is described in Section 3.5.2c. Solid line is the fit to the data before accounting for resolution (cf. Fig. 3.4), for comparison. Poisson \sqrt{N} error bars based on the number of pits in the data before accounting for resolution.

3.5.2c Quantitative Resolution Effects

Pits with radii of 80 m (i.e., distinguishable at the 2σ level, for 1 px errors on pit diameters) should take $2.2_{-0.8}^{+0.5} \times 10^5$ yr to grow at our calculated radial growth rate of $3.6_{-0.6}^{+2.1} \times 10^{-4}$ m yr $^{-1}$. This means that the resolvable pit distribution within ~ 10 km of cell centers should

be dominated by pits forming in the stagnant, central region of the cell because pits forming on distal, more rapidly moving regions (e.g. $>5 \text{ cm yr}^{-1}$; cf. Table 3.2) will travel $\sim 10 \text{ km}$ before growing large enough to be resolved. In other words, we expect that most pits forming in the stagnant region will have grown large enough to be visible at LORRI resolution at $\sim 10 \text{ km}$ distance from the cell center and most pits forming distal to the stagnant center will not yet be visible. Thus, we expect that the *real* pitting density in the stagnant region should be approximately the same as the *observed* pitting density at a distance of $\sim 10 \text{ km}$ from the cell center. We use this expectation to estimate the effect of resolution on the intercept and the slope by assuming that only resolution effects cause decreased pitting density near the center of the cell. Note that this will overestimate the effects of resolution because the region of accelerating surface velocity should have intrinsically fewer pits (Section 3.5.2a).

To perform this estimate, we divide the pits into 1 km-wide bins and find the bin with the highest pitting density, which is typically $\sim 10 \text{ km}$ from the center, in a region where the pitting density plateaus (e.g. Fig. 3.9A). We then inject an artificial population of small pits such that the pitting density is the same as the maximum pitting density in each bin interior to the bin with the maximum pitting density (Fig. 3.9C). We respect the geometry of the cells when calculating the pits per area, i.e. bins in the bilaterally symmetric cells are strips, whereas the bins in the radially symmetric cells are annuli. We assign 40 m radii to the injected pits to simulate the mean value of a population of pits that is equally dispersed between a radius of zero (just formed) and a radius of 80 m (just below resolution at the 2σ level). We summarize the effect of artificially injecting pits below resolution in Table 3.3.

As expected, injecting small-radius pits causes the intercept to decrease and the slope to increase, leading to a decrease in the inferred average velocity by a factor of $\sim 2-4$. Because we

expect pits to be below resolution, we expect the velocities quoted in Table 3.3 to be more accurate than the velocities quoted without taking resolution effects into account (Table 3.2; Fig. 3.8G). However, this injection method overestimates the effect of resolution because the region of accelerating surface velocity should have intrinsically fewer pits (Section 3.5.2a). Thus, our preferred interpretation is that the velocities of cells lie in the range between the best-fit values reported in Tables 3.2 and 3.3. Notably, these fits show that the axially symmetric cells (V and VI) have lower average velocities than the bilaterally symmetric cells (I, II, III, IV) and the distorted cell (VII). We speculate that this may be a signal of the averaged effect of the decreasing velocity gradient with distance from the cell center in radially symmetric cells, even though the velocity gradient itself cannot be resolved.

Finally, we note that the density of pits is low not only near the centers of cells, but also near the edges (Fig. 3. 9; see also Moore et al., 2016b; White et al., 2017). The lower pitting density near the edges cannot be explained by resolution effects; we speculate on the cause of this low density in Section 3.5.6.

3.5.3 Mergers between Pits

We can estimate how mergers between pits affect the fit, under the assumption that pits with radii separated by a distance Δx less than one pixel (80 m) are erroneously mapped as a single pit. The average pit density across most cells is 2-3 pits per km^2 , with the most densely packed locations reaching ~ 4 pits per km^2 . For a small number of pits n we can approximate the probability of two pits overlapping as being independent and thus estimate probability that any particular mapped pit is actually two merged pits as $\sum_{n=1}^{n=4} n\pi(\Delta x)^2 / 1 \text{ km}^2 = 12\%$. Thus, we

expect that merging between large pits (visible at LORRI resolution) will minimally affect our fit. However, we cannot probe the smaller-radius distribution of pits, and mergers between small pits forming on the relatively small stagnant region may act to increase the pit radii there more rapidly than sublimation alone, acting to increase the intercept in the fit to the r vs. x distribution.

Table 3.3. Pit Distribution Accounting for Resolution

Map Area	Intercept (m)	Slope (m m^{-1})	Best-fit Velocity (cm yr^{-1})	68% Interval (cm yr^{-1})	95% Interval (cm yr^{-1})	Convection Time (yr)	Preferred Velocity (cm yr^{-1})
I-L	128 ± 2	0.00608 0.00025	± 5.8	5.2-9.8	3.8-11.3	$3.28\text{E}+05$	5.8-11.0
I-R	76 ± 3	0.00954 0.00039	± 3.7	3.1-5.9	2.5-7.3	$3.51\text{E}+05$	3.7-13.2
II-L	81 ± 3	0.00768 0.00020	± 4.6	3.8-7.3	3.1-9.1	$5.43\text{E}+05$	4.6-7.1
II-R	95 ± 3	0.00998 0.00035	± 3.6	3.0-5.8	2.3-7.0	$4.72\text{E}+05$	3.6-6.3
III-R	105 ± 3	0.00748 0.00027	± 4.8	4.1-7.8	3.2-9.4	$3.54\text{E}+05$	4.8-11.9
IV-L	114 ± 3	0.00834 0.00037	± 4.3	3.8-7.1	2.9-8.6	$3.02\text{E}+05$	4.3-17.9
IV-R	101 ± 3	0.00969 0.00042	± 3.7	3.2-6.1	2.4-7.2	$3.51\text{E}+05$	3.7-12.2
V	83 ± 5	0.01357 0.00072	± 2.6	2.2-4.2	1.8-5.3	$5.00\text{E}+05$	2.6-6.2
VI	72 ± 7	0.02344 0.00146	± 1.5	1.3-2.5	1.0-3.1	$5.33\text{E}+05$	1.5-7.3
VII	129 ± 3	0.00422 0.00017	± 8.1	7.1-13.6	5.7-17.0	$3.58\text{E}+05$	8.1-11.0

Table 3.3. As in Table 3.2, but adjusting for resolution. “Preferred velocity” is the range between the best-fit velocity in Tables 3.2 and 3.3.

3.5.4 Cell Surface Ages

The directly measured pit distribution (Section 3.4.1, Table 3.2) and the distribution after taking into account likely bias from resolution (Section 3.5.2c, Table 3.3) allow us to estimate

surface ages of the cells. The intercepts of the r vs. x fits using the directly measured distribution range from 128-186 m (Table 3.2), implying that pits spend $3.5 - 5.2 \times 10^5$ yr near the stagnant cell centers, based on a radial growth rate of 3.6×10^{-4} m yr⁻¹. The resolution-adjusted fit (Table 3.3) yields intercepts of 71-128 m, implying that pits spend $2.0 - 3.5 \times 10^5$ yr near cell centers. The convection length divided by the convection rate yields the characteristic convection timescales. For the directly measured distribution, this yields timescales of $7.3 \times 10^4 - 3.5 \times 10^5$ yr (Table 3.2). For the resolution-adjusted fit, this yields timescales of $3.0 - 5.3 \times 10^5$ yr (Table 3.3). Therefore, our preferred interpretation is that surfaces near cell edges reach ages of $4.2 - 8.9 \times 10^5$ yr, i.e., the sum of the time spent near stagnation and of the time spent traveling across the cell. These ages refine the age constraints on the surface of SP of < 10 Myr from the lack of observed impact craters (Moore et al., 2016a) and of $\sim 5 \times 10^5$ years from the convection model of McKinnon et al. (2016), and provide error bars on the age estimate.

3.5.5 Evidence for Convection Instability

All r vs. x distributions have nonzero slopes in the direction perpendicular to the mapped spreading center at the 3σ level, except for the left quadrant of cell III (Table 3.2). However, the left quadrant of cell III has a non-zero slope at the 3σ level in the direction *parallel* to the mapped spreading center of cell III, with bilateral symmetry (Fig. 3.10). Only the right quadrant of cell I also has this property (Fig. 3.11). The right quadrant of cell I and the left quadrant of cell III border cell II, which has a convection pattern perpendicular to those of cell I and III (Fig. 3.2-3). Thus, there is a pattern on cell I and cell III with increasing pit radius with distance from the spreading

center of cell II, which we interpret to indicate interaction between the convection underlying these three cells.

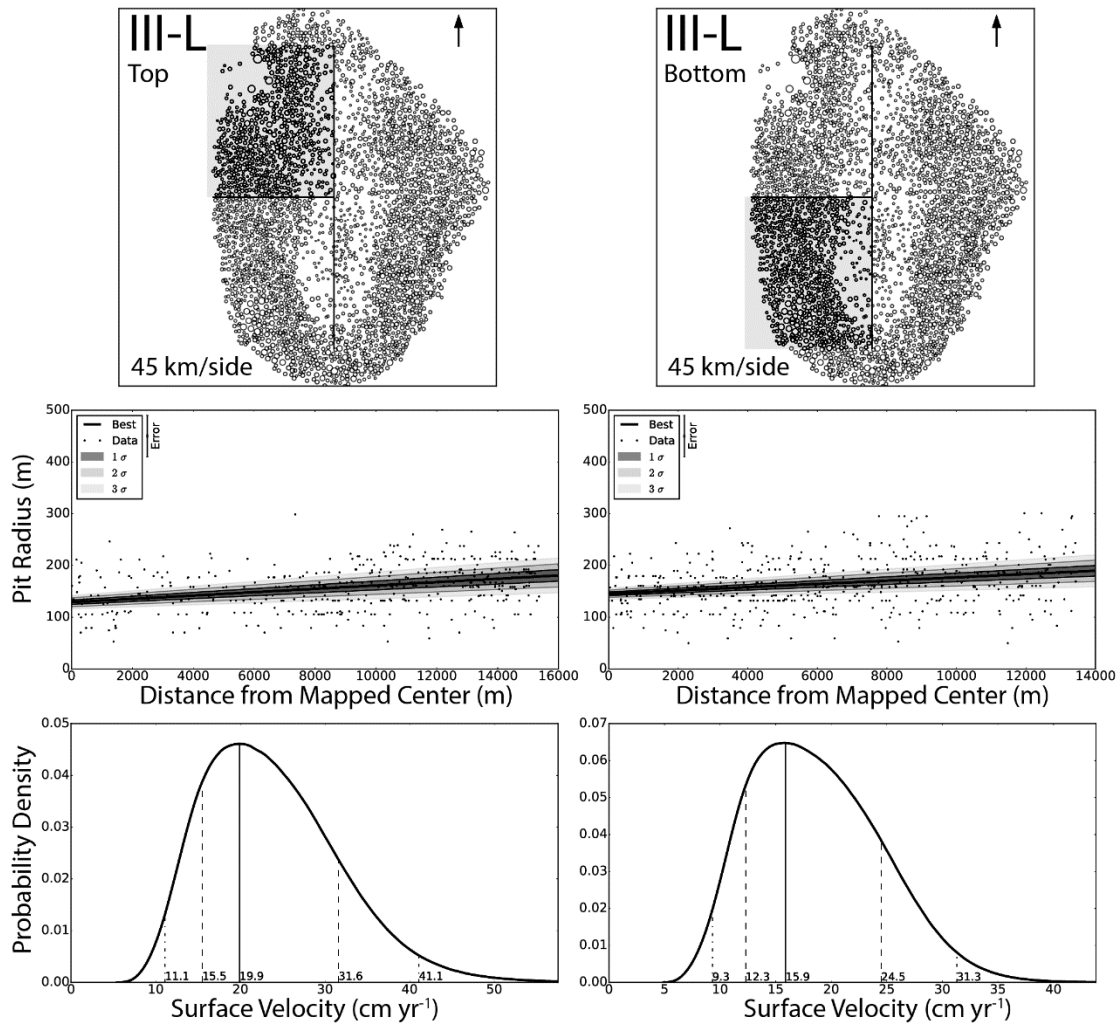


Figure 3.10. Fits to the upper and lower halves of the left side of cell III, in the same style as Figs. 3.3, 3.4, and 3.7.

The bounding trough between cell I and cell II is also disrupted approximately symmetrically about the inferred spreading center of cell II (Fig. 3.2). We interpret this as evidence that convection under cell II has been migrating laterally from east to west and that new upwelling material has covered an older convective boundary between these cells. Between cell II and cell

III, the intact trough (Fig. 3.2) may correspond to the development of a downwelling limb after the convection pattern under cell II migrated west. We also note that the lateral distance from the spreading center to the edge of the cell is greater in the direction away from cell II, for both cell I and cell III (i.e. cell I extends farther west and cell III extends farther east). We interpret this asymmetry to be the result of the convection under cell II interacting with cells I and III and causing transport to be more efficient away from cell II. Finally, we interpret these observations as evidence for instability in the convective overturn on timescales comparable to the age of the cells, as predicted by modeling by Umurhan et al. (2017).

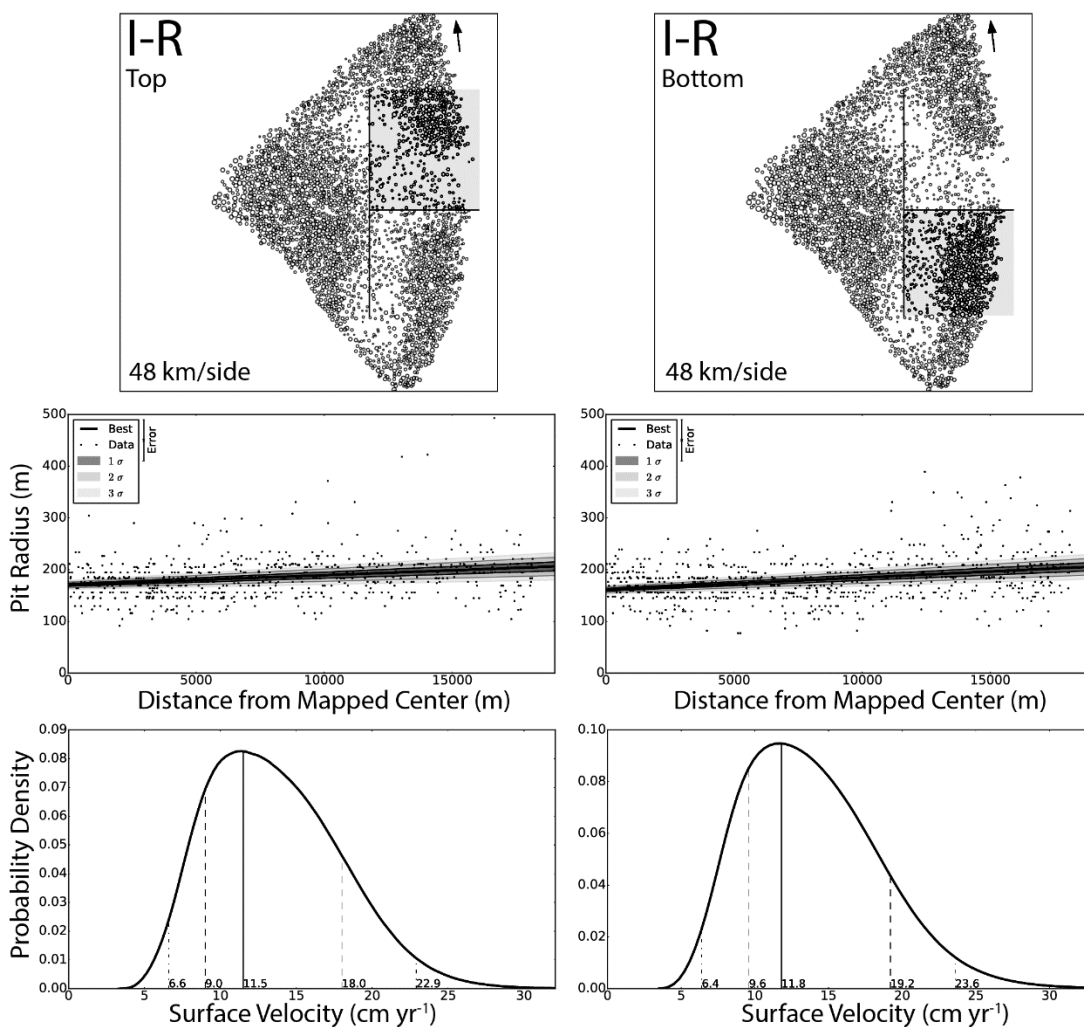


Figure 3.11. Fits to the upper and lower halves of the right side of cell I, in the same style as Figs. 3.3, 3.4, and 3.7.

3.5.6 Speculation about Sparse Pitting Near Cell Edges

Both the number of pits per area and the fraction of surface area covered by pits decreases toward cell edges (Fig. 3.9), and some pits near cell edges appear shallower (Fig. 3.2). Mergers between pits cannot account for this observation, but the decay of formerly deeper and denser pitting can (Moore et al., 2016b). The convection timescales of a few 10^5 yr are a significant

fraction of Pluto's ~ 3 Myr obliquity-driven climate cycle (Dobrovolskis and Harris, 1983; Earle and Binzel, 2015). In particular, modeling by Stern et al. (2017) suggests that the average annual atmospheric pressure has been waning from a much higher value that peaked $\sim 9 \times 10^5$ yr ago. Deposition of N_2 onto the surface as the atmosphere waned would be thicker on older surfaces, such as the periphery of cells. We speculate that there may be a compositional difference between an atmospherically deposited layer of N_2 ice and underlying upwelled N_2 ice, which will be well-mixed with impurities from other ices, like CH_4 (e.g. McKinnon et al., 2016; Protopapa et al., 2017). Because solid CH_4 and N_2 do not appreciably diffuse into each other under plutonian surface conditions, even over the age of the solar system (Eluszkiewicz and Stevenson, 1991), these two layers would remain chemically distinct. We further speculate that such a chemical difference may lead to a rheologic difference, allowing a potentially purer- N_2 atmospheric deposit blanketing the surface to relax faster than the underlying ice, particularly if chemical impurities are important in increasing the viscosity of the ice (Moore et al., 2016b). Clearly, this hypothesis requires substantial testing, but we present it here because there are currently no other published hypotheses for the sparse and occasionally shallow pitting near cell edges (see Moore et al., 2016b).

3.5.7 Comparison to Other Explanations for the Observed Pit Distribution

White et al. (2017) discuss an alternative hypothesis for the apparent smoothness of cell centers. They propose that high subsurface heat flux near cell centers leads to lower ice viscosity and the erasure of pits via relaxation, while lower heat flux near cell edges leads to a higher viscosity that is capable of supporting pit topography. They also suggest that the formation and maintenance of pits on the cells probably occurs on much shorter timescales than the convective

flow of N_2 in the sluggish lid regime. However, we calculate sublimation rates indicating that pits grow to radii of a few hundred meters on timescales comparable to the timescales of convective overturn (Section 3.5.4, McKinnon et al., 2016). We also observe pitting down to the limits of resolution, even in the centers of cells, where the heat flux is highest (e.g. figure 4 of McKinnon et al., 2016). In particular, we often observe a densely pitted central region surrounded by a more sparsely pitted region, further encircled by a densely pitted outer region (e.g. Fig 3.1B, 3.2). We interpret this pattern to be consistent with pits forming on a stagnant region, moving through a region of accelerating surface velocity, and then entering into a region of equilibrium flux of surface material (Section 3.5.2a). We interpret the observation of a densely pitted central region surrounded by a less densely pitted region to be inconsistent with surface smoothness controlled by viscous relaxation alone, in which case the most central region should be the smoothest because the heat flux should be highest through the center. We therefore infer that viscous relaxation is not completely erasing pits on the timescale of convective overturn. Nevertheless, the viscosity of N_2 ice remains poorly constrained, and viscous relaxation may be in equilibrium with sublimation at the bottoms of pits, thereby setting the depth of pits (see Section 3.5.1c).

3.6. Conclusion

We map the distribution of sublimation pits on the surface of seven convection cells in Sputnik Planitia, Pluto. We find that a linear model with a nonzero intercept best fits the size distribution of pits, which we interpret as being consistent with lateral transport of surface

material on a cell with a nearly stagnant center viewed at a finite resolution in which pits are typically only a few pixels wide. We assess and account for the effect of resolution, which causes an overestimation of the intercept and underestimation of the slope of the linear fit. Using the size distribution of pits, we estimate that average convection velocities across the cells are approximately 10 cm yr^{-1} . This implies that the cell edges reach ages of approximately $4.2 - 8.9 \times 10^5 \text{ yr}$. We argue that sublimation is the process that primarily sets the radius of the pits because viscous relaxation acts preferentially on long wavelengths (i.e. determining pit depth) as compared to short wavelength (i.e. pit rims) and the pits have not relaxed away. We also contrast our hypothesis that the pitting pattern on cells indicates cell surface velocities (due to transportation of pits growing by sublimation) against the hypothesis that the pitting pattern results from a thermal gradient inducing a viscosity gradient across the cells. We prefer the hypothesis that surface motion of the cell sets the pitting distribution because (i) the sublimation rates we calculate indicate that the production of $\sim 100 \text{ m}$ -scale pits takes place on the same timescale as convection and (ii) the presence of dense pitting surrounded by a region of sparser pitting at the centers of some cells is inconsistent with viscous relaxation governed by a monotonic temperature gradient. However, we also note that N_2 ice viscosity is poorly known, with theory and experiment diverging by many orders of magnitude when extrapolated to the conditions relevant to pits in Sputnik Planitia. Finally, correlation between the pitting distributions of three adjacent cells (I, II, and III), along with the disruption of the bounding trough between cells I and II, indicates that the underlying convection cells interact and are unstable on timescales comparable to the age of the cells.

3.7 Acknowledgements

We thank Heather Knutson for insightful conversations on statistical analysis and Dave Stevenson for illuminating discussions about ice rheology. We also appreciate helpful discussions with Orkan Umurhan and Bill McKinnon. Input from Francis Nimmo and two anonymous reviewers improved the quality of this paper. We are grateful for funding from NESSF grant #16-PLANET16F-0071.

References

- Barr, A.C. & Milkovich, S.M., 2008. Ice grain size and the rheology of the martian polar deposits. *Icarus*, 194, pp. 513-518.
- Buratti, B.J., Hofgartner, J.D., Hicks, M.D., Weaver, H.A., Stern, S.A., Momary, T., Mosher, J.A., Beyer, R.A., Verbiscer, A.J., Zangari, A.M. & 7 others, 2017. Global Albedos of Pluto and Charon from LORRI New Horizons Observations. *Icarus*, 287, pp.207-217.
- Dobrovolskis, A.R. & Harris, A.W., 1983. The obliquity of Pluto. *Icarus*, 55, pp. 231-235.
- Durham, W.B., Prieto-Ballesteros, O., Goldsby, D.L. & Kargel, J.S., 2010. Rheological and thermal properties of icy materials. *Space Science Reviews*, 153(1–4), pp.273–298.
- Earle, A.M. & Binzel, R.P., 2015. Pluto's insolation history: Latitudinal variations and effects on atmospheric pressure. *Icarus*, 250, pp.405–412.
- Eluszkiewicz, J., 1991. On the microphysical state of the surface of Triton. *Journal of Geophysical Research*, 96(91), pp.217–229.
- Gladstone, G.R., Stern, S.A., Ennico, K., Olkin, C.B., Weaver, H.A., Young, L.A., Summers, M.E., Strobel, D.F., Hinson, D.P., Kammer, J.A. & 24 others, 2016. The atmosphere of Pluto as observed by New Horizons. *Science*, 351(6279), pp. aad8866-1 - aad8866-6

- Greenstreet, S., Gladman, B. & Mckinnon, W.B., 2015. Impact and cratering rates onto Pluto. *Icarus*, 258, pp.267–288.
- Hansen, C.J. & Paige, D.A., 1996. Seasonal Nitrogen Cycles on Pluto. *Icarus*, 120(2), pp.247–265.
- Ingersoll, A.P., Svitek, T. & Murray, B.C., 1992. Stability of polar frosts in spherical bowl-shaped craters on the Moon, Mercury, and Mars. *Icarus*, 100(1), pp.40–47.
- Kass, R.E. & Raftery, A.E., 1995. Bayes Factors. *Journal of the American Statistical Association*, 430, pp. 773-795.
- McKinnon, W.B., Nimmo, F., Wong, T., Schenk, P.M., White, O.L., Roberts, J.H., Moore, J.M., Spencer, J.R., Howard, A.D., Umurhan, O.M. & 6 others, 2016. Convection in a volatile nitrogen-ice-rich layer drives Pluto's geological vigour. *Nature*, 534(7605), pp.82–85.
- Melosh, H.J., 1986. Impact cratering : a geologic process. Research supported by NASA. New York, Oxford University Press (Oxford Monographs on Geology and Geophysics, No. 11), ch. 9.
- Moore, J.M., McKinnon, W.B., Spencer, J.R., Howard, A.D., Schenk, P.M., Beyer, R.A., Nimmo, F., Singer, K., Umurhan, O.M., White, O.L., and 32 others, 2016a. The geology of Pluto and Charon through the eyes of New Horizons. *Nature*, 351(6279).
- Moore, J.M., Howard, A.D., Umurhan, O.M., White, O.L, Schenk, P.M., Beyer, R.A., McKinnon, W.B., Spencer, J.R., Grundy, W.M., Lauer, T.R. & 7 others, 2016b. Sublimation as a landform-shaping process on Pluto. *Icarus*, 287, pp. 320-333.
- Parmentier, E.M. & Head, J.W., 1981. Viscous relaxation of impact craters on icy planetary surfaces: Determination of viscosity variation with depth. *Icarus*, 47, pp. 100-111.
- Protopapa, S., Grundy, W. M., Reuter, D. C., Hamilton, D. P., Ore, C. M., Dalle, Cook, J. C., Cruikshank, D. P., Schmitt, B., Philippe, S. & 13 others, 2017. Pluto's global surface composition through pixel-by-pixel Hapke modeling of New Horizons Ralph/LEISA data. *Icarus*, 287, pp. 218-228.

- Scott, T.A., 1976. Solid and liquid nitrogen. *Physics Reports*, 27(3), pp.89–157.
- Solomon, S.C., Comer, R.P. & Head, J.W., 1982. The Evolution of Impact Basins: Viscous Relaxation of Topographic Relief. *Journal of Geophysical Research*, 87(B5), pp.3975–3992.
- Stansberry, J.A., Pisano, D.J. & Yelie, R. V, 1996. The emissivity of volatile ices on Triton and Pluto. *Planetary and Space Science*, 44(9). pp. 945-955
- Stern, S A., Bagenal, F., Ennico, K., Gladstone, G.R., Grundy, W. M., McKinnon, W.B., Moore, J.M., Olkin, C.B., Spencer, J.R. & 142 others, 2015. The Pluto system: Initial results from its exploration by New Horizons. *Science*, 350(6258).
- Stern, S.A., Binzel, R.P., Earle, A.M., Singer, K.N., Young, L.A., Weaver, H.A., Olkin, C.B., Ennico, K., Moore, J.M., McKinnon, W.B. & 2 others. Past epochs of significantly higher pressure atmospheres on Pluto. *Icarus*, 287, pp. 47-53.
- Trowbridge, A.J., Melosh, H.J., Steckloff, J.K. & Freed, A.M., 2016. Vigorous convection as the explanation for Pluto’s polygonal terrain. *Nature*, 534(7605), pp.79–81.
- Umurhan, O.M., Howard, A.D., Moore, J.M., Earle, A.M., White, O.L., Schenk, P.M., Binzel, R.P., Stern, S.A., Beyer, R.A., Nimmo, F., & 5 others, 2017. Modeling glacial flow on and onto Pluto’s Sputnik Planitia. *Icarus*, 287, 301-319.
- Weaver, H. A., Gibson, W.C., Tapley, M.B., Young, L. A. & Stern, S.A., 2008. Overview of the New Horizons Science Payload. *Space Science Review*, 140, pp.75–91.
- Weertman, J., 1970. The creep strength of the Earth’s mantle. *Reviews of Geophysics*, 8(1), pp.145–168.
- White, O.L., Moore, J.M., McKinnon, W.B., Spencer, J.R., Howard, A.D., Schenk, P.M., Beyer, R.A., Nimmo, F., Singer, K.N., Umurhan, O.M. & 15 others, 2017. Geological mapping of sputnik planitia on pluto. *Icarus*, 287, pp. 261-286.

Yamashita, Y., Kato, M. & Arakawa, M., 2010. Experimental study on the rheological properties of polycrystalline solid nitrogen and methane: Implications for tectonic processes on Triton. *Icarus*, 207(2), pp.972–977.

Zent, A.P., McKay, C.P., Pollack, J.B., Cruikshank, D.P., 1989. Grain Metamorphism in Polar Nitrogen Ice on Triton. *Geophysical Research Letters*, 16(8), pp.965–968.

*Chapter 4***HOW THE MARTIAN RESIDUAL SOUTH POLAR CAP DEVELOPS QUASI-CIRCULAR AND HEART-SHAPED PITS, TROUGHS, AND MOATS**

Buhler, P.B., Ingersoll, A.P., Ehlmann, B.L., Fassett, C.I., and Head, J.W. (2017). How the martian residual south polar cap develops quasi-circular and heart-shaped pits, troughs, and moats. *Icarus* 286, pp. 69-93. doi:10.1016/j.icarus.2017.01.012

4.1. Abstract.

The martian Residual South Polar Cap (RSPC) is a 1-10 m thick deposit of permanent CO₂ ice perched on the much larger H₂O ice cap. The CO₂ ice is dissected into mesas by erosional landforms that can be broadly classified as (i) quasi-circular pits, (ii) heart-shaped pits, (iii) linear troughs, and (iv) moats. We use HiRISE (25-50 cm/px) images taken at a cadence of days to months to track meter-scale changes in the RSPC in order to investigate the mechanisms that lead to the development of these four distinct morphologies.

For the first time, we report the development of dark fans on the sides of the CO₂ mesas and the fracturing and deterioration of the initially smooth upper surface of CO₂ mesas. We interpret these features as indicating the sublimation and subsequent escape of CO₂ from the interiors of mesas, which undermines structural support of mesa tops, causing them to collapse. The collapse of mesa tops, along with uneven deposition of CO₂ ice, creates steep scarps that erode during the summer due to preferential sunlight absorption. During the winter, CO₂ deposition acts to smooth topography, creating gently sloping ramps. We propose that the interplay between the steep scarps and gentle slopes leads to either quasi-circular pits, heart-shaped pits, linear troughs, or moats, depending on local conditions.

4.2. Introduction

Huygens made the first recorded sketch of a bright south polar spot on Mars in 1672 (Sheehan, 1996), and additional notable observations of the martian south pole were made by Maraldi, Herschel, and Schroeter in the eighteenth century, leading Herschel to propose that Mars hosted northern and southern polar ice caps (Herschel, 1784; Sheehan, 1996). These early observers did not know the composition or structure of these caps but did note that they changed seasonally, indicating that they were primarily observing the seasonal polar caps. In the mid-twentieth century, Leighton and Murray (1966) proposed that the caps were a reservoir composed entirely of CO₂ in equilibrium with the atmosphere, but, over the next few decades, others presented evidence and later demonstrated that the residual summertime north polar ice is entirely H₂O, and that the residual summertime south polar ice deposit is predominantly a $\sim 10^6$ yr old (Herkenhoff and Plaut, 2000), $2-3 \times 10^6$ km³ deposit made of H₂O ice (e.g. Ingersoll, 1974; Durham 1999; Smith et al., 1999; Nye et al., 1999; Byrne and Ingersoll, 2003a; Titus et al., 2003). Radar observations of the south polar ice (Phillips et al., 2011) have subsequently revealed that a $\sim 10^4$ km³ CO₂ ice reservoir (i.e. a mass of CO₂ similar to the mass of the current, 96% CO₂ atmosphere (Owen et al., 1977)) with an age of $\sim 10^5$ yr is entombed within the H₂O ice at a depth of <8 m (Bierson et al., 2016), reviving the concept of an equilibrium between the atmosphere and a comparably large, solid CO₂ reservoir, albeit on longer than annual timescales. No permanent CO₂ reservoirs have been observed in the northern hemisphere.

In this paper we present observations and interpretations of annual and seasonal changes in the residual south polar cap (RSPC; a.k.a. unit Aa_{4b} (Tanaka et al., 2007, 2014)). The RSPC is a 1-10 m

thick CO₂ ice deposit that has a mass of ~1% of the present-day atmosphere (Thomas et al., 2016) that overlies the mostly inert H₂O ice and buried CO₂ deposit just described. It is the only known CO₂ deposit in contact with the atmosphere that has a general structure that is stable intra- and inter-annually. Each winter a ~1 m-thick seasonal deposit of CO₂ ice blankets the southern pole, including the RSPC (e.g., Piqueux et al., 2015), but this seasonal deposit sublimates entirely each summer (e.g., Hess et al., 1979; James et al., 1992; Kieffer et al., 1992). The RSPC as a whole appears quasi-stable on decadal timescales.

The RSPC consists of plateaus and mesas of CO₂ ice that are dissected by myriad pits and troughs, which typically change annually at meter-scales (e.g. Malin et al., 2001). Most of these morphologies have been extensively documented (Thomas et al., 2005, 2009, 2013, 2016), although a comprehensive understanding of how these landforms develop has remained elusive. In the published literature, the growth of quasi-circular pits has been shown to occur through the erosion of their steep walls via sublimation and calving (e.g. Byrne and Ingersoll, 2008a), which has been modeled by Byrne et al. (2008, 2015). However, a description of the inception of quasi-circular pits and of the systematic development of the other CO₂-ice dissection morphologies has not been put forth.

Before describing landform development and endeavoring to understand the mechanisms leading to the development of the morphology of the RSPC, we first direct the reader to Fig. 4.1, a visual definition of the terminology used here and in the literature to describe the four main categories of landforms dissecting the RSPC: quasi-circular pits, heart-shaped pits, linear troughs, and moats (see also Thomas et al., 2016). Most of these terms are self-evident, but we specifically note that ‘moat’ describes the lower elevation, non-smooth region surrounding a smooth-topped mesa that is wholly within another smooth-topped mesa.

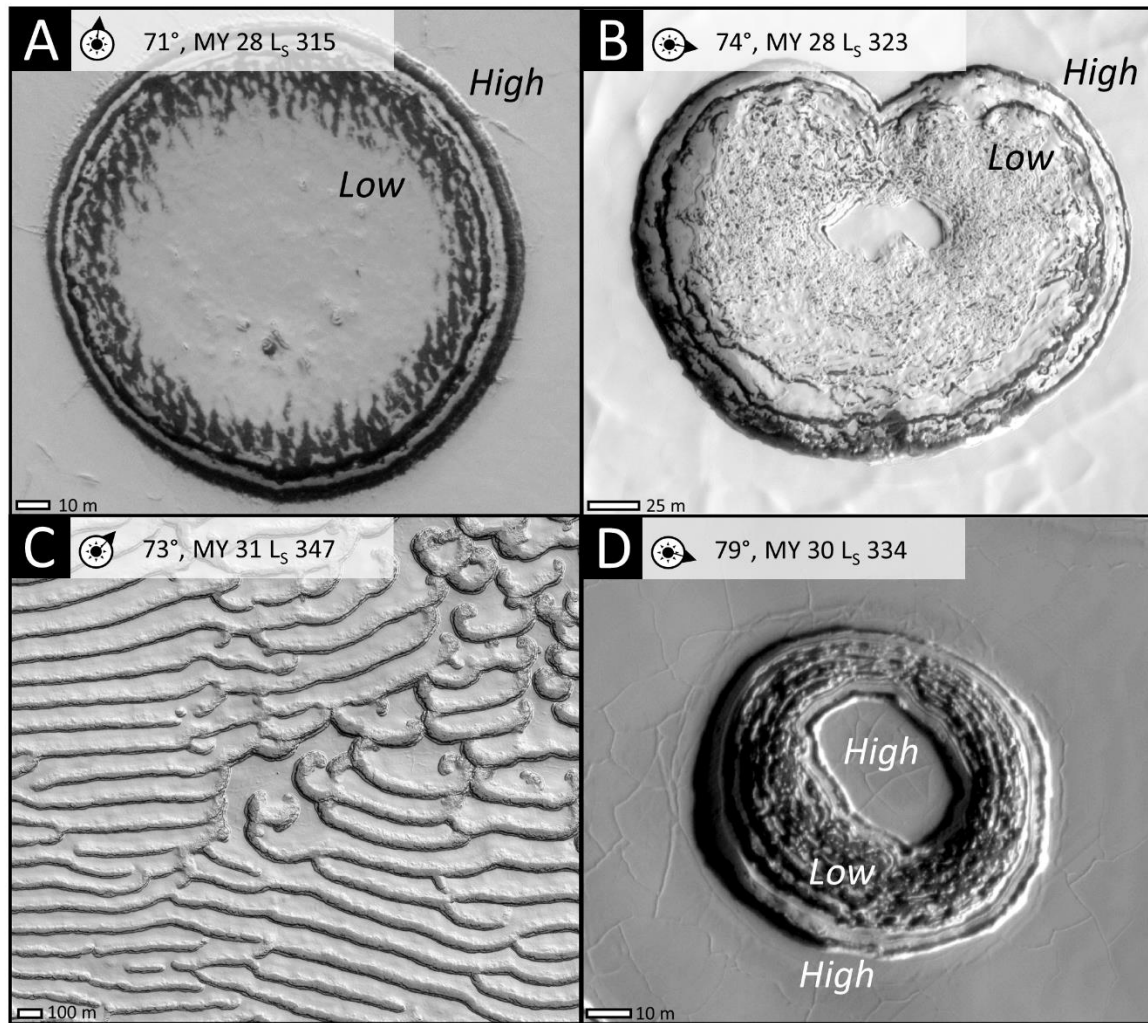


Figure 4.1. **a.** Quasi-circular pit. **b.** Heart-shaped pit (note cusp). **c.** A field of linear troughs. **d.** A smooth-topped mesa surrounded by a low-elevation, rough moat, contained wholly within another smooth-topped mesa. Selected high (H) and low (L) terrains are marked as an aid to the eye. HiRISE images (A) PSP_005349_0930 (B) PSP_005517_0930 (C) PSP_006007_0925 (D) ESP_023410_0930.

Understanding the mechanisms leading to the variety of morphologies in the RSPC is not only intrinsically interesting, but also important to our understanding of the martian climate in general, since current climate models do not predict the existence of the RSPC (e.g. Guo et al., 2009). Understanding the processes governing the development of the RSPC, therefore, likely

provides insight into the past and future of the martian climate and into the processes leading to the development of the much larger buried CO₂ deposit.

Documenting the mechanisms of meter-scale morphologic changes is challenging, since it is difficult to find clear examples of morphologic change that have repeated coverage at high cadence. However, there are now five consecutive martian years of 25-50 cm/px coverage of some locations on the RSPC by the High Resolution Imaging Science Experiment (HiRISE) camera (McEwen et al., 2007), which makes the problem tractable. We therefore use these data to infer the processes leading to the emergence of the multitude of morphologic forms of the RSPC.

4.3. Methods

We use 25-50 cm/px images from the HiRISE camera on board the Mars Reconnaissance Orbiter (McEwen et al., 2007) to document the morphology at five locations on the RSPC at a cadence of, at best, 4 sols between images. The maximum number of HiRISE images obtained from any single study location in any particular Mars Year was 11, while some study areas have no HiRISE coverage during some Mars Years. We made use of a total of 95 HiRISE images. The selected locations cover seven different units of the RSPC, including units representing each of the three broader unit groups A, B, and C (as defined by Thomas et al. (2016)) in order to sample spatially distinct and morphologically diverse regions of the RSPC (Fig. 4.2). We refer to the units using the nomenclature from Thomas et al. (2016), and 'Un' refers specifically to the 'unmapped' portion of the RSPC in the box approximately bounded by ([10 E, -86.6 N], [13 E, -86.5 N], [21 E, -87 N], [23 E, -86.9 N]) (Fig. 4.2b).

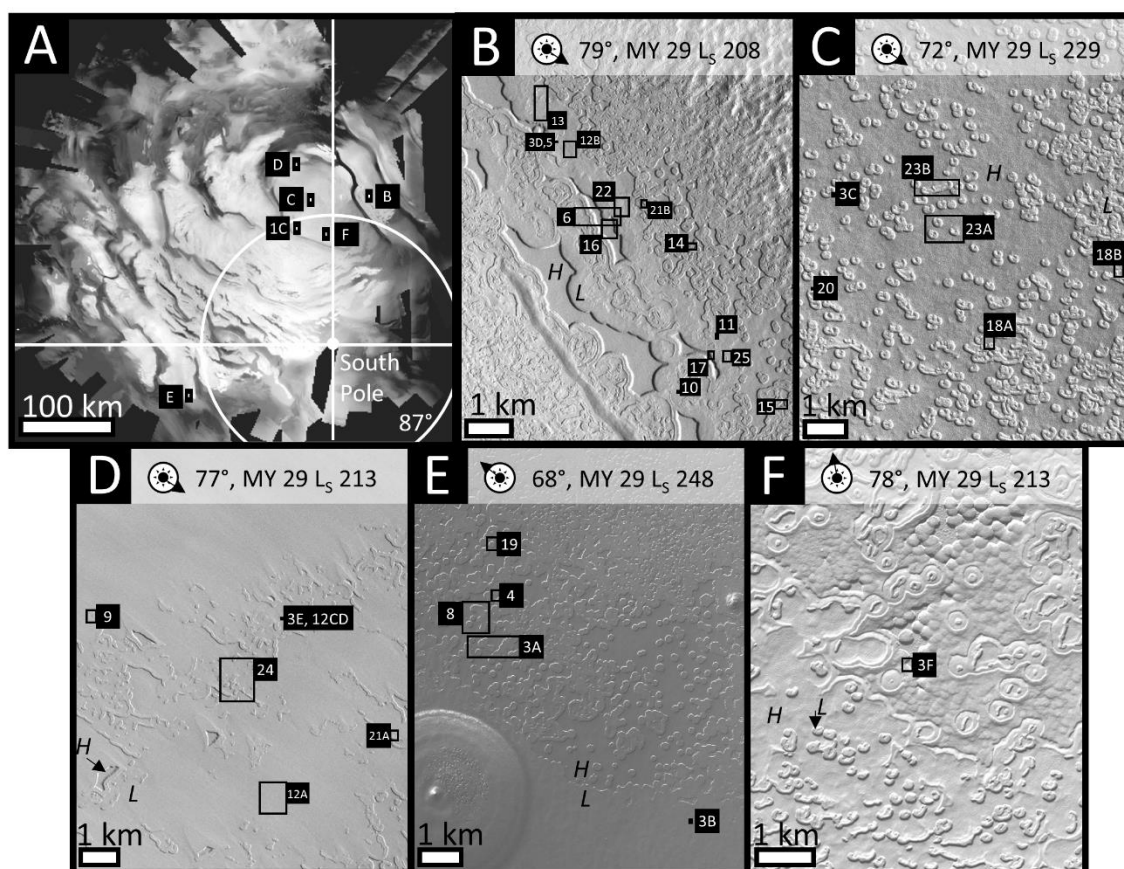


Figure 4.2. Context images for other figures (labelled black boxes). Units that appear in the image are given in the caption (based upon Thomas et al., 2016). **a.** Mosaic of CTX images taken in southern spring MY 29, showing context for panels **b-f** and Fig. 4.1c. White boxes give the true sizes of panels **b-f** relative to panel **a**, black outline provides visual clarity of the locations. **b.** Units A0 and Un. **c.** Unit A1. **d.** Units B2 and B8. **e.** Unit B7. **f.** Unit C1. CTX images (B) B06_011951_0933 (C) B07_012374_0931 (D) B06_012044_0945 (E) B08_012760_0933 (F) CTX B06_012047_0884.

Images were imported with martian polar stereographic projection and co-registered in ArcMap 10 onto a basemap constructed from Mars Reconnaissance Orbiter Context Camera images (Malin et al., 2007). Repeat images were finely co-registered by hand at each location using multiple fiducial points, such as the polygonal pattern on the H₂O ice basement. We estimate that the accuracy between images is within ~1 pixel over features of interest. In all images illumination direction is indicated by a sun symbol, followed by the solar incidence angle

(solar elevation measured from a normal to the surface), Mars Year, and solar longitude (L_s , where L_s is 0° at the vernal equinox, 90° at summer solstice, 180° at autumnal equinox, and 270° at winter solstice). Most HiRISE images shown in figures are contrast enhanced in order to highlight subtle features; the contrast stretch is the same for all images within the same figure. Photogrammetry was used to determine the vertical offset of features on mesa tops by using measurements of the length of shadows cast by the fractures in HiRISE images with low-angle solar illumination.

4.4. Observations

We observe the intra- and inter-annual development of RSPC morphology, describing features and processes not previously documented: (i) dark fans emanating from mesa sides; (ii) fracturing and (iii) collapse of mesa tops; and the initiation and evolution of (iv) quasi-circular and (v) heart-shaped pits, troughs, and moats.

4.4.1 Dark Fans on Mesa Sides

During southern spring, dark fans with typical surface areas of $\sim 1\text{-}10\text{ m}^2$ ubiquitously appear on the sides and bases of the RSPC CO_2 mesas (Fig. 4.3, 4.4). The darkest and narrowest segment of fans is located closest to the mesa side, and fans become gradationally lighter moving away from the mesa side. Occasionally, fans are draped over the sides and onto the upper surface of the mesas (Fig. 4.3b). Over tens of sols, areas with fans become uniformly dark as underlying

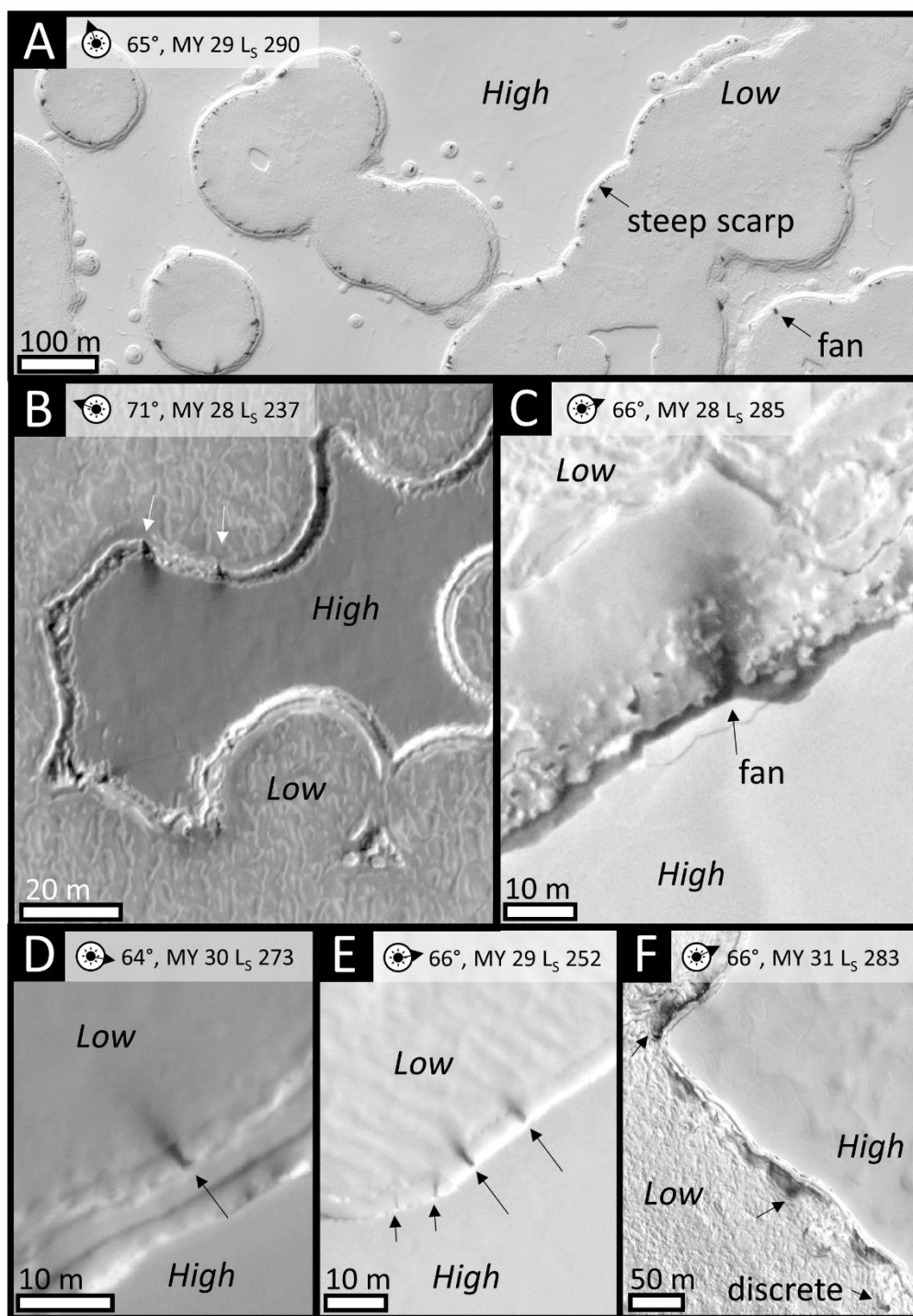


Figure 4.3. Examples of fans from all five study locations. **a.** Unit B7. Dark fans appear exclusively near the edges of CO₂ deposits. **b.** Unit B7. Dark fans on the upper surface of a mesa. **c.** Unit A1. Close-in view of typical fan morphology. **d.** The Un. **e.** Unit B2. **f.** Unit C1. Note both discrete fans and broad dark band. HiRISE images (A) ESP_013617_0930 (B) PSP_003716_0930 (C) PSP_004687_0930 (D) ESP_022210_0930 (E) ESP_012835_0940 (F) ESP_031099_0925.

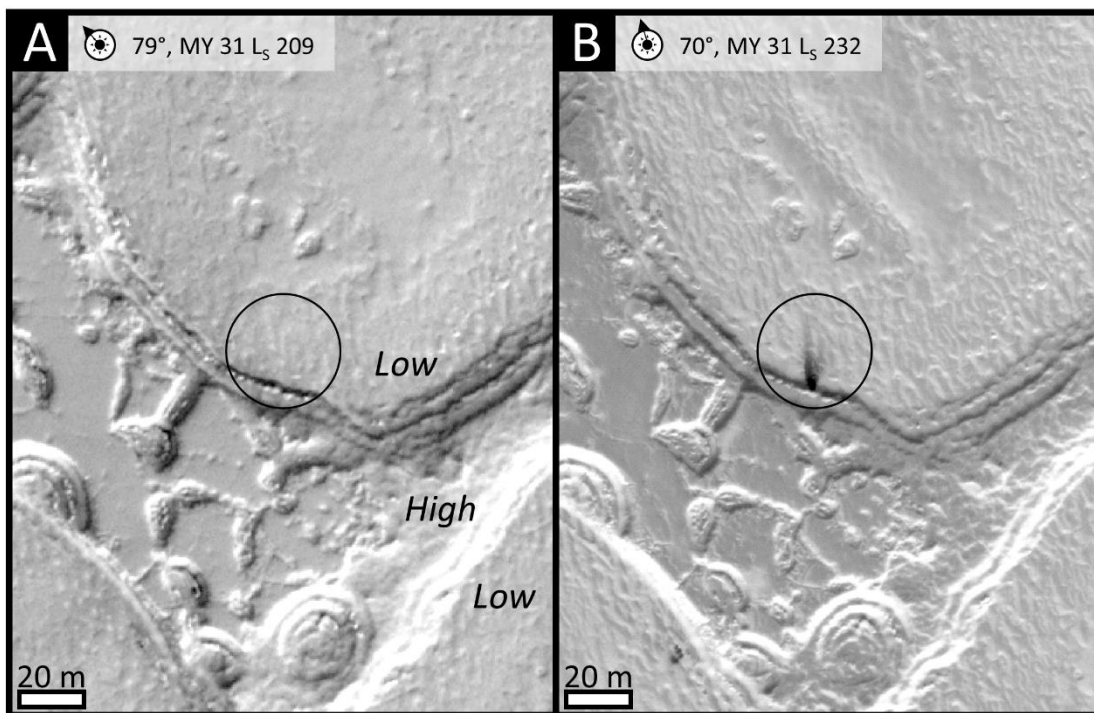


Figure 4.4. Unit B7. **a.** No dark fan. **b.** 38 sols later. Dark fan is apparent. HiRISE images (A) ESP_029586_0930 (B) ESP_030073_0930.

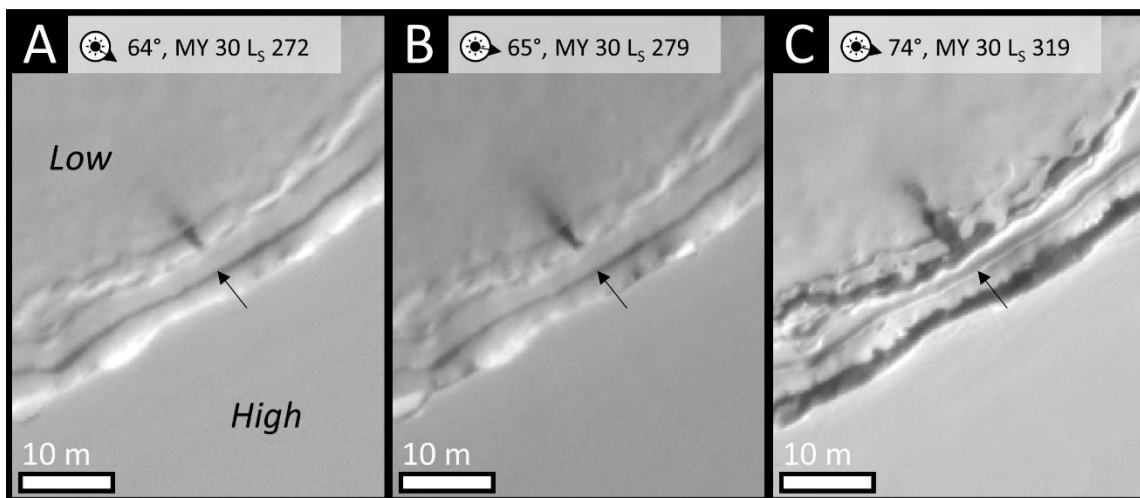


Figure 4.5. The Un. **a.** Dark fan at the base of a CO₂ mesa. **b.** 12 sols later. **c.** 77 sols later. Seasonal frost has begun to sublimate completely, revealing underlying dark material. Note preferential sublimation at the location of the fan. HiRISE images (A) ESP_022064_0930 (B) ESP_022210_0930 (C) ESP_023054_0930.

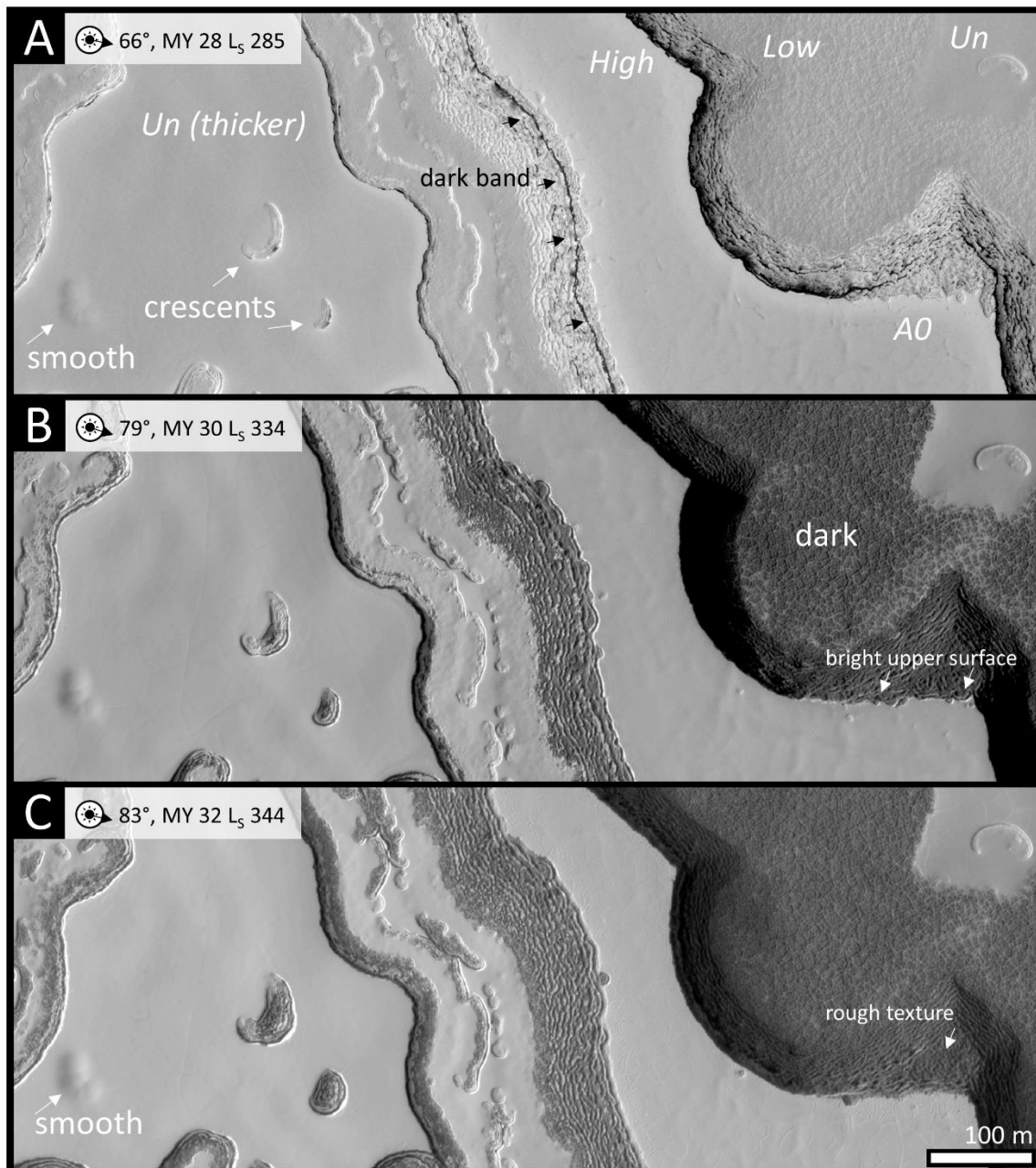


Figure 4.6. Unit A0 and Un (labelled in image). 5 martian year time series at different L_s. **a.** Note dark band, smooth depression, and crescents. **b.** Note dark polygonal basement, dark sides of mesa and L_s. Also note that the thickness of bright upper surface (white arrows) is a few tens of centimeters. The height of the entire mesa is 10 m (based on shadow measurements). **c.** Smooth depression has not evolved. Crescents in thicker region of Un have enlarged more than crescent in thinner Un deposit (upper right). Note dark, rough texture below bright upper surface. HiRISE images (A) PSP_004686_0930, (B) ESP_023410_0930, (C) ESP_041278_0930.

seasonal CO₂ frost preferentially sublimates (Fig. 4.5). By mid-summer it is no longer possible to distinguish fans from underlying terrain, which has darkened (Fig. 4.6b-c).

The timing of dark fan appearance is typically during southern spring, prior to L_s 240, but varies slightly by location and by unit (Fig. 4.7). The earliest fans are apparent in the first images of Unit A0 in Mars Year (MY) 28, at solar longitude (L_s) 184. However, the Un, which appears in the same images, does not have fans until L_s 195 in MY 28. Additionally, although Unit A1 has coverage at L_s 201 in MY 28, the first fans do not appear in images until L_s 221.

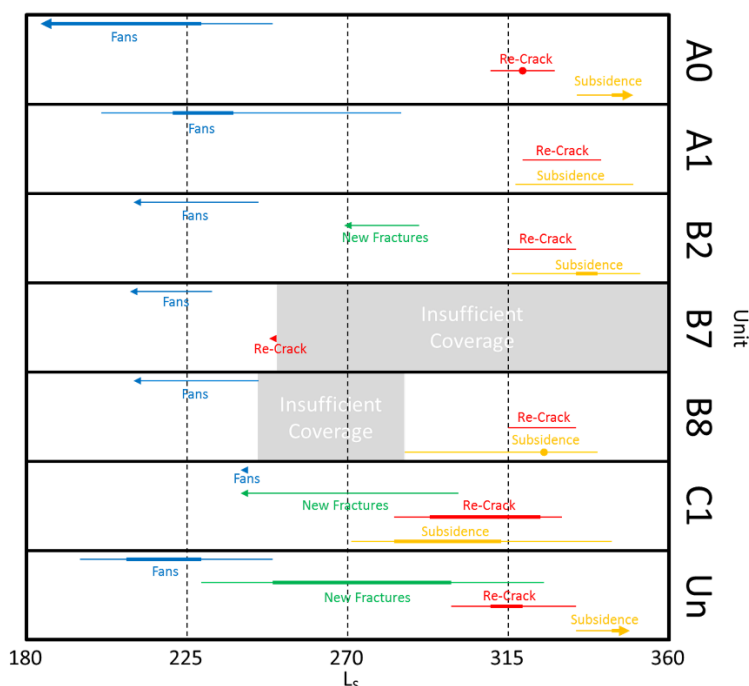


Figure 4.7. Seasonal timing of different features by unit. Thin lines represent the interval between an image with no new features and an image in which new features have appeared (i.e. maximum activity duration). Thick lines represent the interval between two images that each have new features appearing (i.e. minimum activity duration). Arrows indicate that new features are present in the first or the final image of a particular year. “Insufficient Coverage” indicates low temporal cadence of high-quality images. All intervals are constructed between images taken in the same martian year. For features that have sufficient coverage in more than one year to construct intervals, the interval shown in this figure spans the interval from both years (i.e., making the interval longer). Since many locations have sufficient coverage of a particular morphologic phenomenon to construct intervals in only one martian year, it is not yet practical to compare seasonal timing of features between years. Note: no new fractures were observed in Units A0 or A1.

The rate of fan formation varies by location, with the highest spatial density of dark fans found in Unit B7. The lowest density of discrete dark fans is found in Unit C1, although broad, equal elevation, dark bands appear around the edges of mesas within Unit C1 (Fig. 4.3f) and Unit A0 (Fig. 4.6a).

The number of dark fans formed per year martian year varies within our study areas in Units B7, A0, and the Un, with more dark fans appearing in Mars Year (MY) 29 than in MY 28 and 31 (e.g., Fig. 4.8). However, variation in the annual rate of dark fan formation in other units cannot be confidently determined, due to lack of sufficient spatial and temporal coverage.

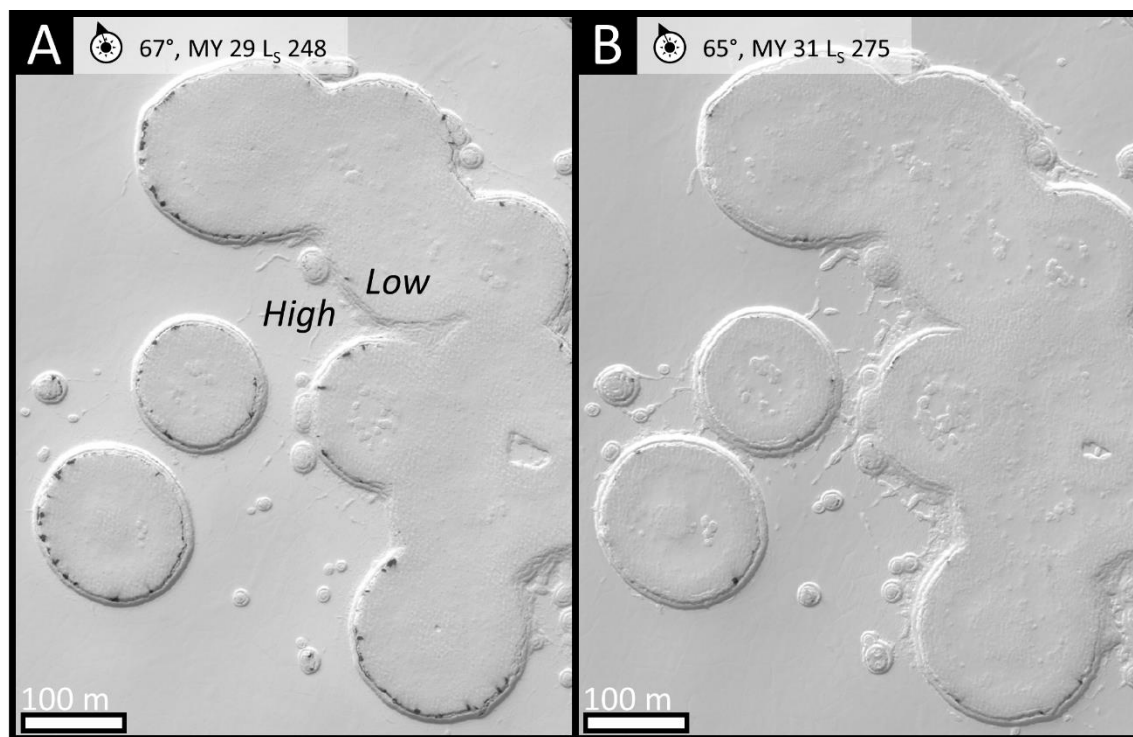


Figure 4.8. Unit B7. **a.** More fans are apparent in MY 29 earlier in summer. **b.** Fewer fans are apparent in MY 31 later in summer. This is the closest timing (seasonality) in images available of this area comparing MY 29 and MY 31. HiRISE images (A) ESP_012760_0930 (B) ESP_030944_0930.

4.4.2 Fracturing of Mesa Upper Surfaces

In our study areas mesas typically have a bright, tens-of-centimeter-thick upper surface layer overlying a darker interior (as measured from HiRISE images, e.g. Fig. 4.6b-c). Thin fractures with a vertical offset of $\sim 10 \pm 3$ cm (determined from photogrammetry) and a lateral extent of ~ 10 -100 m occur on the upper surface of this bright layer in Units B2, C1, and the Un (Fig. 4.9-11). Fractures often appear to be the boundary between two vertically offset slabs (Fig. 4.10, 4.11). Some fractures have a single sense of offset (Fig. 4.9, 4.10), but others have a scissoring offset, i.e., the offset direction changes along the strike of the fracture (Fig. 4.11). The fractures sometimes occur in isolation (Fig. 4.9, 4.11) and sometimes in clusters (Fig. 4.10).

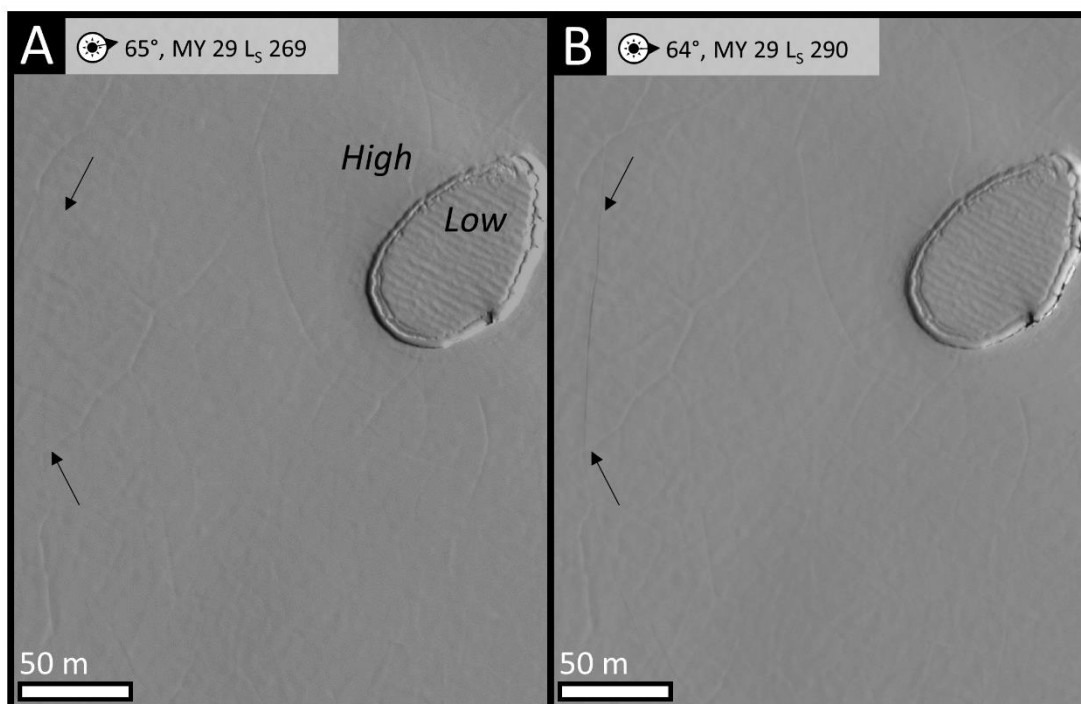


Figure 4.9. Unit B2. Two images taken under nearly identical viewing conditions. **a.** MY 29 L_s 269 with solar incidence angle 65°, phase angle 63°, and emission angle 2.1°. **b.** 34 sols later, MY 29 L_s 289.8, with solar incidence angle 66°, phase angle 66°, and emission angle 0.5°. Crack appears. Note unchanged background pattern of thin ridges throughout scene. HiRISE images (A) ESP_013178_0940 (B) ESP_013613_0940.



Figure 4.10. The Un. **Inset.** The same area of the upper surface of the mesa as shown in the main panel is smooth 32 sols earlier. **Main.** Fractures and tilted slabs have appeared on the upper surface of the CO₂ mesa. Arrows point to the same locations in both the main and inset panels. HiRISE images (Inset) ESP_013731_0930 (Main panel) ESP_013309_0930.

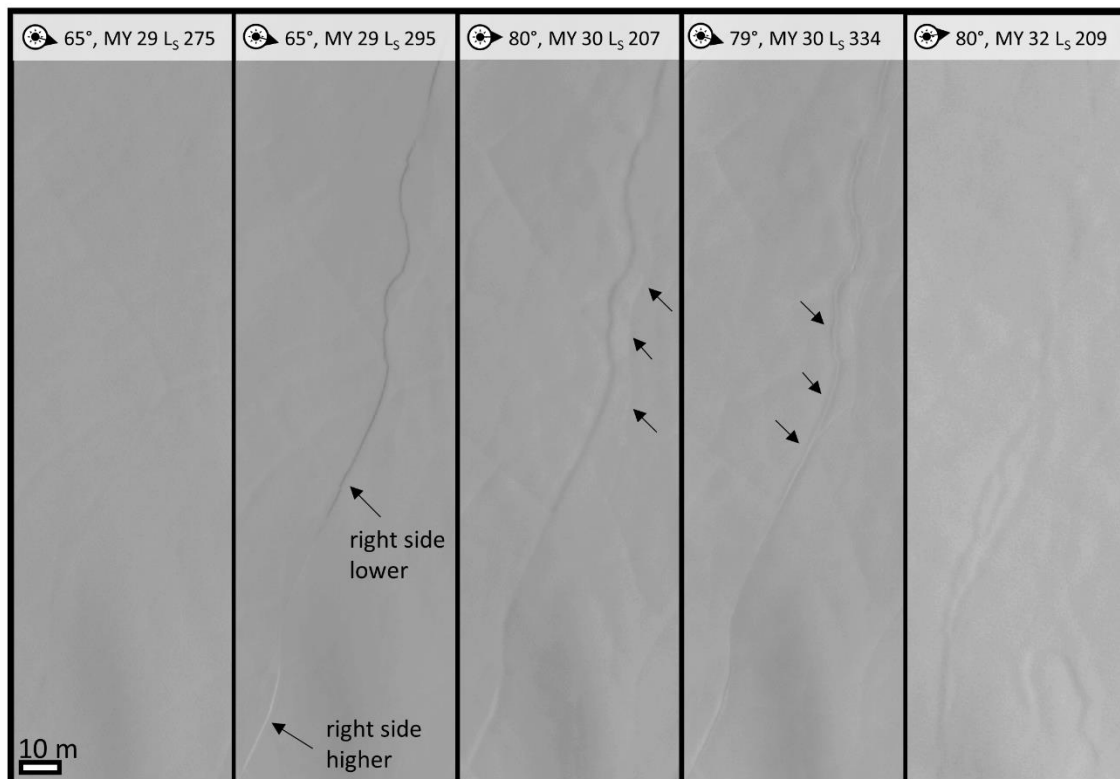


Figure 4.11. The Un. Time series from left to right. **i.** Smooth upper surface of mesa. **ii.** Fracture with a vertical offset appears. **iii.** MY 30 spring. Crack is muted. Note second, approximately parallel, ridge (arrows). **iv.** MY 30 summer. Fracture has a double-ridged morphology (arrows). **v.** MY 32 spring. Ridge is strongly muted. HiRISE images (A) ESP_013309_0930 (B) ESP_013731_0930 (C) ESP_020733_0930 (D) ESP_023410_0930 (E) ESP_038403_0930.

In MY 32, some newly formed fractures viewed after L_s 320 exhibit bright halos with a radius of ~2-4 m on either side of a crack, highlighting the outlines of polygonal slabs, which have areas of 10⁴-10⁵ m² (Fig. 4.12a-b). In MY 28, some new fractures are also bright, but with less pronounced halos than those in in MY 32 (Fig. 4.12c-d; black arrow). However, fractures with halos are restricted to portions of mesas that, based on shadow measurements of bounding scarps, are only between ~0.5 - 2 m thick. New fractures on thicker parts of mesas occur without halos in the same scenes (Fig. 4.13).

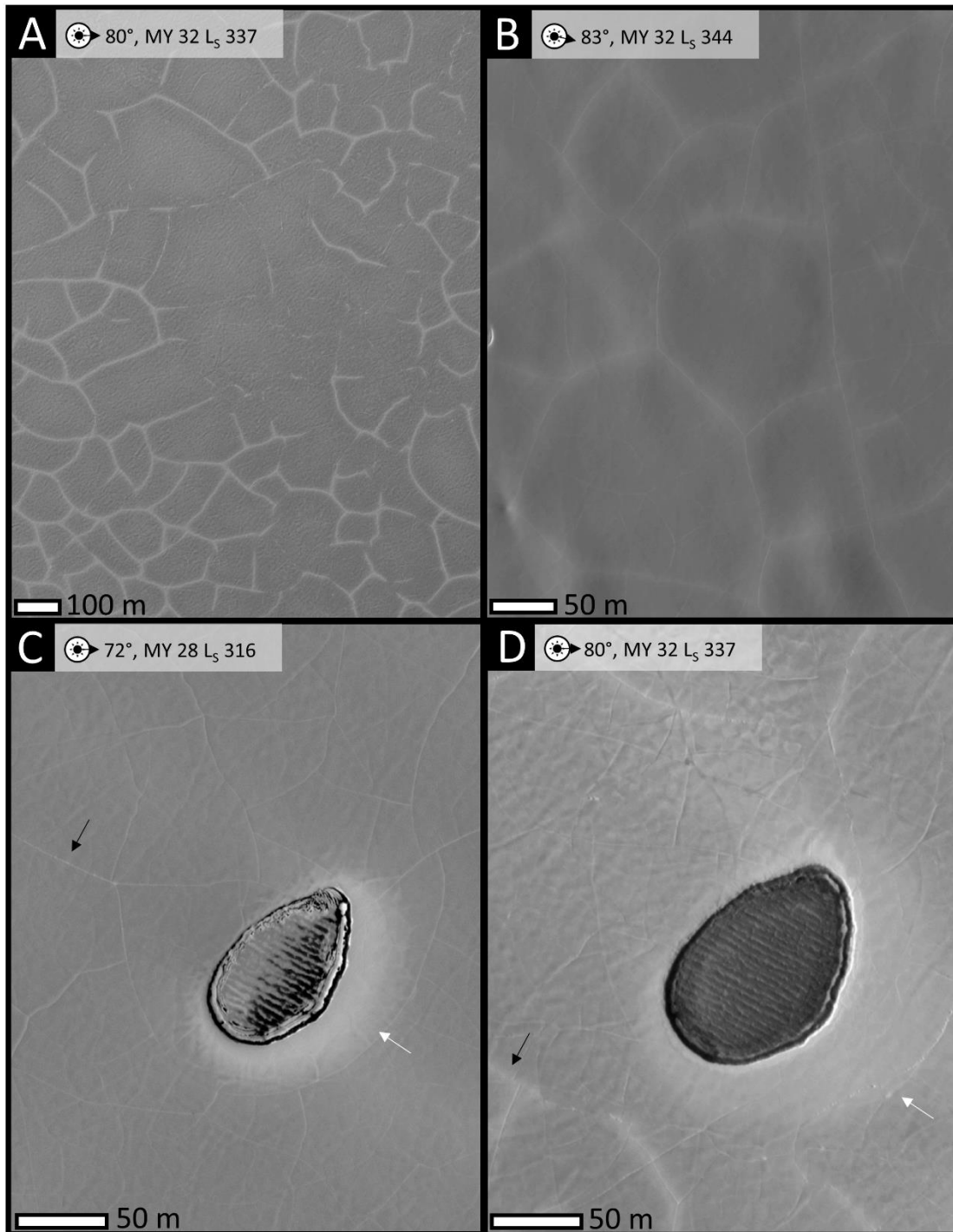


Figure 4.12. **a.** Unit B2. **b.** The Un. In both locations new fractures have bright halos with widths of $\sim 4\text{--}8$ m. Note polygonal pattern of fracturing. **c.** Fractures are subtly bright after MY 28 dust storm (black arrow), and there are halos around steep scarps (white arrow). **d.** Halos around fractures and steep scarps after MY 32 dust cloud. HiRISE images (A) ESP_041107_0940 (B) ESP_041278_0930 (C) PSP_005359_0940 (D) ESP_041107_0940.

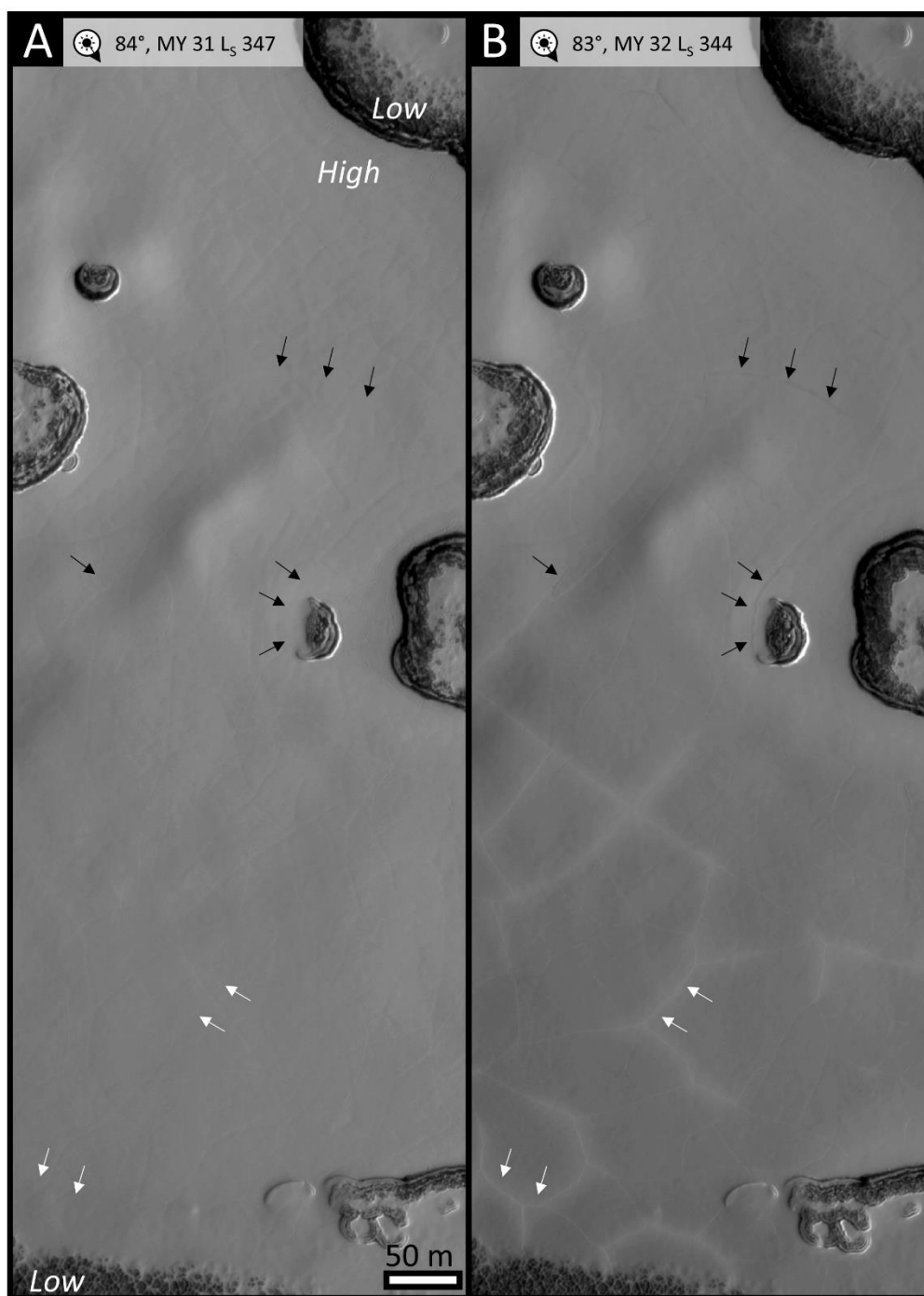


Figure 4.13. **a.** The Un in late summer of MY 31. The CO₂ mesa is thinner toward the bottom of the image, where it smoothly drapes onto the H₂O ice basement, and thicker near the top of the image, where it terminates in a steep scarp. **b.** The same location one year later. New fractures with halos are apparent in the thinner part of the mesa (e.g. the features marked with white arrows), while new fractures without halos are apparent in the thicker part of the mesa (black arrows). HiRISE images (A) ESP_032535_0930, (B) ESP_041278_0930.

The earliest new fractures are observed by L_s 249 and continue to appear until at least L_s 299 (Fig. 4.7). New fractures have not been observed in Units A0 and A1, despite extensive imaging coverage, and there is insufficient coverage to determine whether new fractures form in Units B7 and B8.

Fractures initially have a crisp scarp, which is retained until the end of summer (Fig. 4.9-11). By the following spring, the edge is typically muted, and, in subsequent summers, the fractures can (i) maintain a single-ridged morphology (Fig. 4.11, 3rd panel), (ii) develop a double-ridged morphology (Fig. 4.11, 4th panel), or (iii) become strongly muted and almost invisible (Fig. 4.11, 5th panel). The progression from an initially crisp offset to an increasingly muted offset is typical of the newly forming fractures we observe.

Ridges in regions of the RSPC will sometimes re-crack, forming wider cracks (Fig. 4.14b-c, 4.14f, 4.14i). Re-cracking has been observed as early as L_s 248 and continues until at least L_s 319. Re-cracking preferentially occurs within ~10-40 m of meters of mesa edges bounded by steep scarps (Fig. 4.14i). The upper surface of the mesa within ~10-40 m of the mesa edges also tends to be lower than the central region, when bounded by a steep scarp, and lowering of the edges appears to accompany re-cracking (Fig. 4.15b).

4.4.3 Collapse and Deterioration of Upper Mesa Surfaces

Flat-bottomed polygonal depressions with areas on the order of 10² m², with ~10 ± 3 cm of relief (determined from photogrammetry), and typically 3-6 sides develop on the upper surfaces of mesas in mid- to late summer (Fig. 4.14d, 4.16). The polygonal depression edges tend to be coincident with ridges (Fig. 4.14d, 4.16), and, in areas within ~10-40 m of the mesa edge,

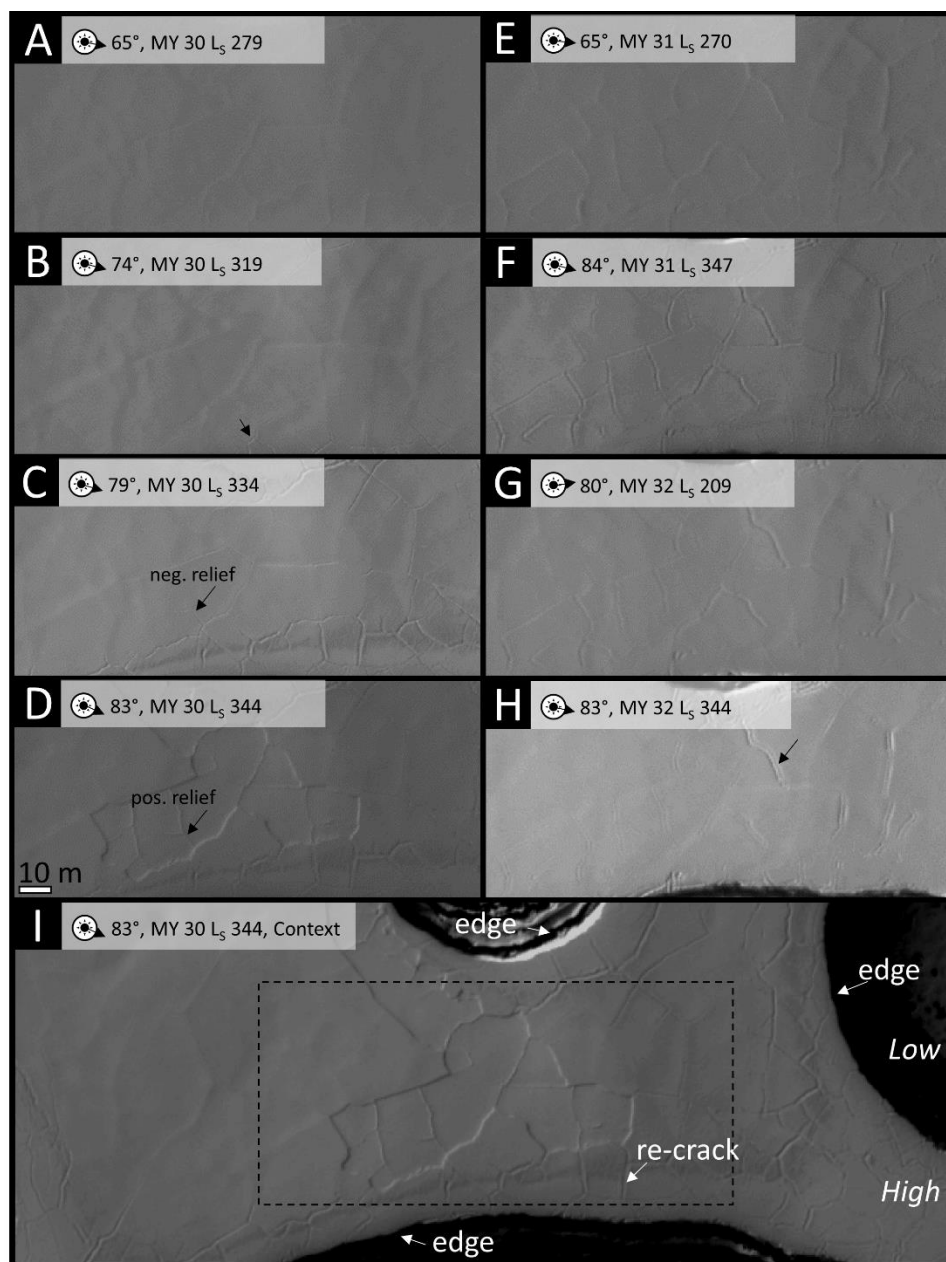


Figure 4.14. **a.** Surface is generally smooth but some thin ridges are visible. **b.** Cracks form on some ridges (e.g. arrow). **c.** Cracking is more pronounced. **d.** A depression with an angular boundary appears. Note coincidence of boundary with ridges in panels A-C. **e.** Next year. Ridges are less crisp than in D, but more pronounced than in A. Note that the illumination geometry is similar to panel A. **f.** Cracks form on ridges. **g.** Next spring. Cracks are still apparent, but muted. **h.** Some cracks have a central ridge, forming a ‘double crack’ (e.g. arrow). **i.** Expanded view of D to give context for other panels. Note proximity to edge of mesa and re-cracking preferentially near mesa edges. HiRISE images (A) ESP_022210_0930 (B) ESP_023054_0930 (C) ESP_023410_0930 (D and I) ESP_023647_0930 (E) ESP_030834_0930 (F) ESP_032535_0930 (G) ESP_038403_0930 (H) ESP_041278_0930.

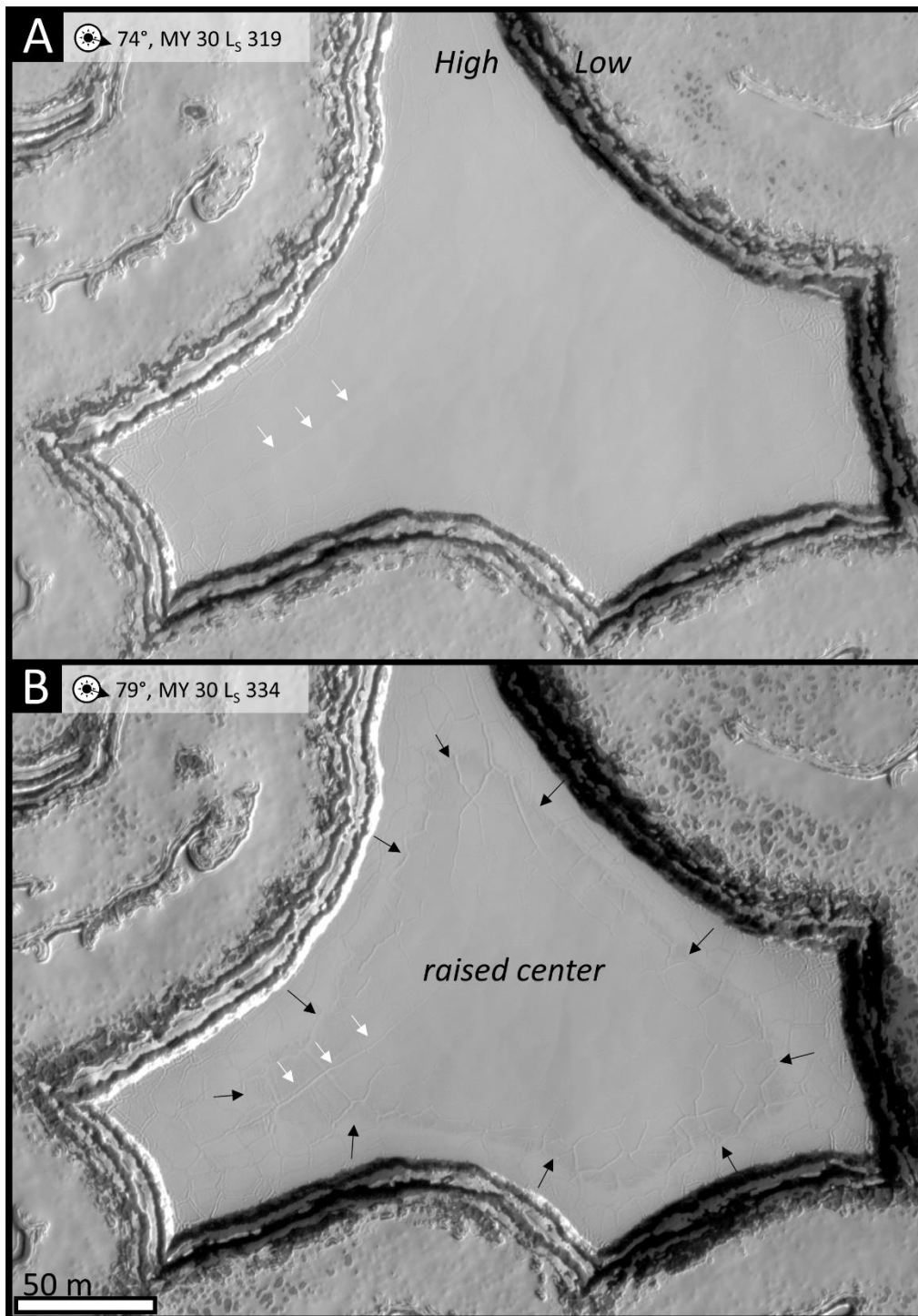


Figure 4.15. The Un. **a.** Smooth upper surface of a mesa. **b.** 28 sols later, the mesa has a smooth, raised, lower albedo center and a lower, rougher perimeter. Black arrows indicate the approximate perimeter of the raised center. Also note re-cracking (white arrows). HiRISE images (A) ESP_023054_0930, (B) ESP_023410_0930.

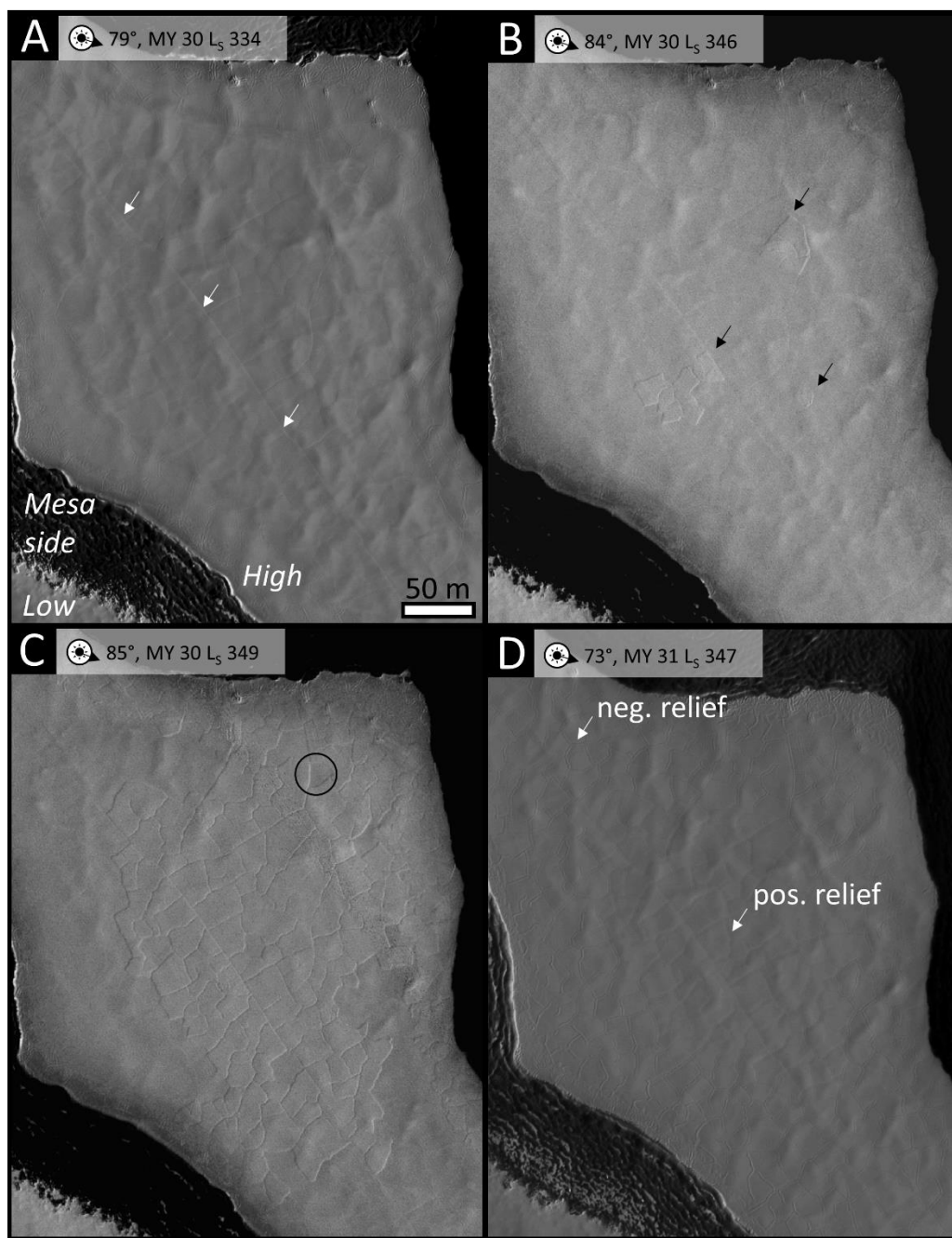


Figure 4.16. Unit A0. Time series spanning 29 sols. **a.** Note long ridge. **b.** Polygonal depressions appear. **c.** 6 sols later. Nearly entire upper surface is covered in polygonal depressions. Note some polygonal shapes are still in positive relief (e.g. circled). **d.** One martian year later. Note positive relief of ridges further than ~40 m from the mesa edge and negative relief of ridges within ~40 m of the edge. HiRISE images (A) ESP_023410_0930, (B) ESP_023700_0930, (C) ESP_023779_0930, (D) ESP_032535_0930.

ridges typically re-crack before polygonal depressions appear (Fig. 4.14b-c). The polygonal depressions form abruptly, in the span of ≤ 4 sols (Fig. 4.16). By late summer, large fields of adjacent polygons form; the largest fields can comprise up to several hundred polygons and have areas of up to 10^5 m^2 (Fig. 4.16). The fields of polygons can cover nearly the entirety of the upper surface of mesas in Unit A0 (Fig. 4.16), but tend to be restricted to the edges of mesas in thinner units (e.g. Fig. 4.14i). Polygonal depressions develop by L_s 283 and continue to form until at least L_s 349 (Fig. 4.7). Polygonal depressions are observed in every unit except B7, though this may be due to a lack of coverage of B7 in late summer.

As an example, we show the development and evolution of polygons in the Un (Fig. 4.14). In the spring following polygon formation the raised ridges between the polygons are muted, but still present in positive relief (Fig. 4.14e). By late the next summer, the boundaries between polygons within ~ 10 -40 m of the sides of the mesa re-crack (Fig. 4.14f) and, two martian years later, have negative relief and have either developed a shallow single trough (Fig. 4.16d) or double-trough morphology (Fig. 4.14g-h). On the other hand, after two martian years, the boundaries between polygons that are more than ~ 40 m from the edges of the mesa still have muted positive relief (e.g., Fig. 4.16d, in unit A0).

Polygonal depressions were observed to form in MY 28 in Units B2 and B8, MY 30 in Units A0, A1, C1, and the Un, and MY 31 in Units B2, B8, and C1. In most cases, there is insufficient late-summer coverage of the same locations in other years to determine whether polygons form again. However, in A0 and in the Un, polygonal depressions do not form twice in the same location during MY 28-31 within the entirety of the area shown in Fig. 4.2b.

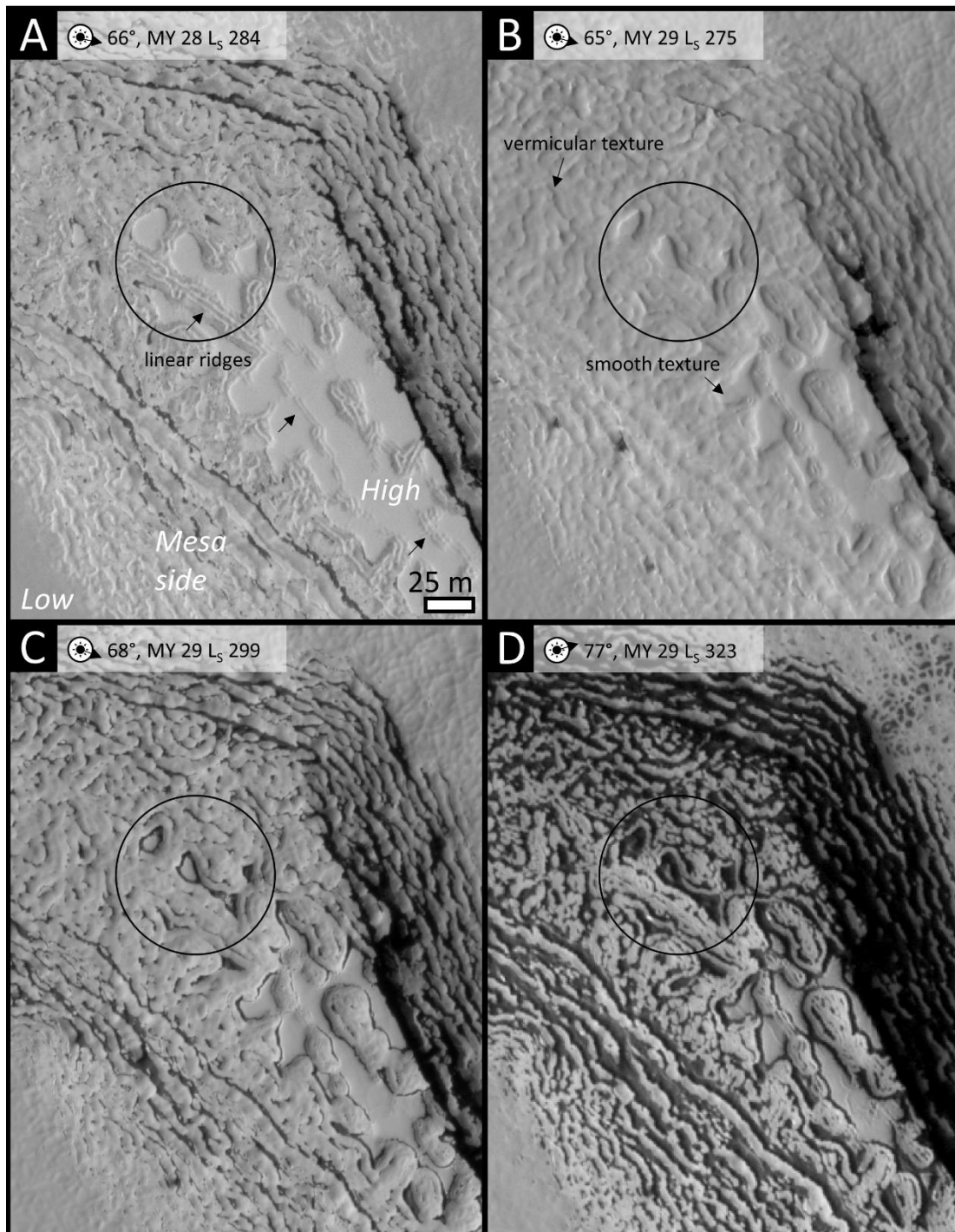


Figure 4.17. Unit A0. **a.** Vermicular texture of mesa interior apparent under smooth, upper surface. Note linear ridges between broader smooth patches. **b.** ~1 martian year later. Smooth patches are smaller. **c.** Note change of albedo as upper surface deteriorates. **d.** Upper surface and sides of mesa are becoming dark. HiRISE images (A) PSP_004686_0930, (B) ESP_013309_0930, (C) ESP_013810_0930, (D) ESP_014339_0930.

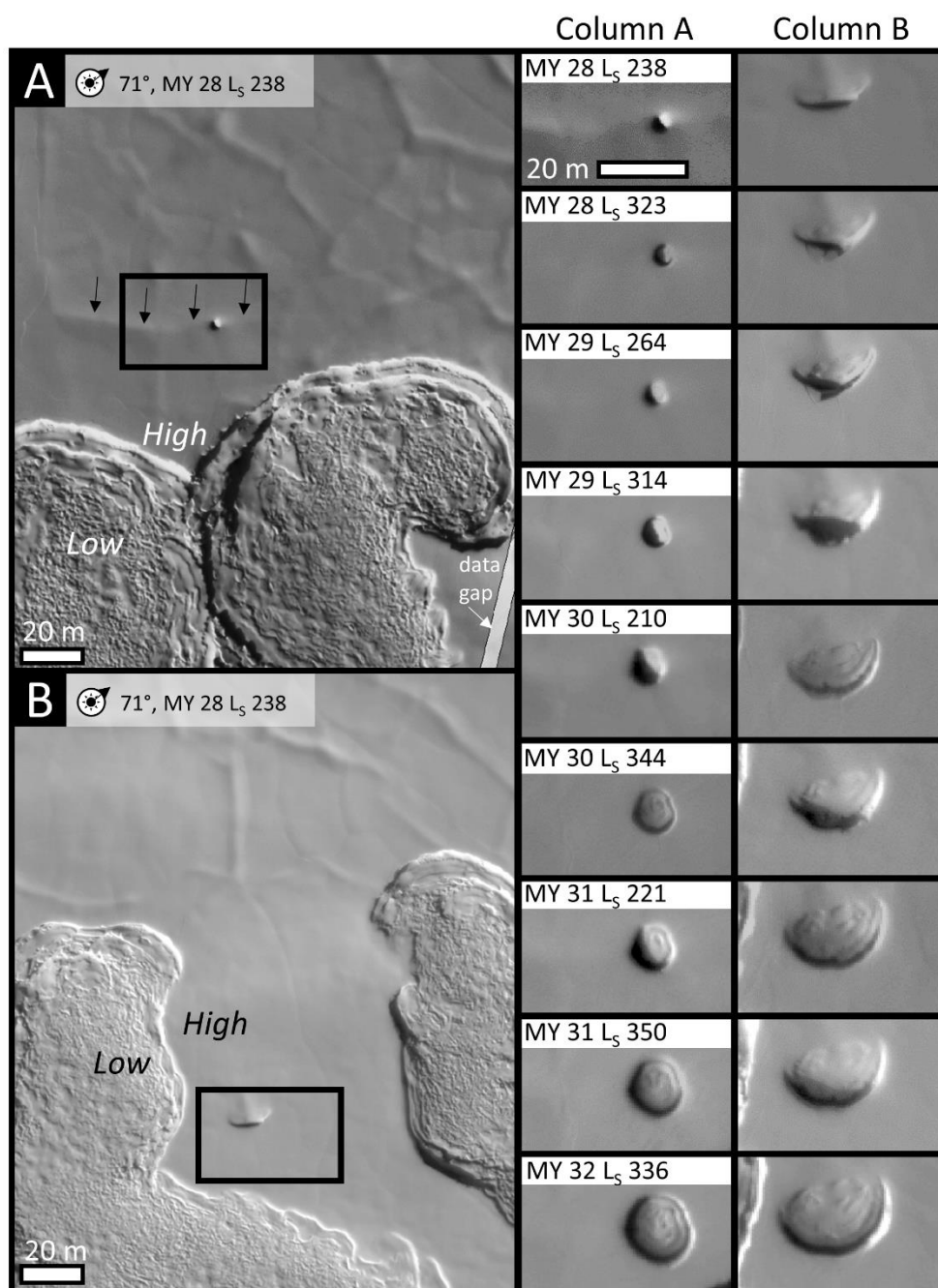


Figure 4.18. Unit A1. **a.** Context for Column A. Note pit forming along crack (arrows). **b.** Context for Column B. Columns A and B are a time series of two nascent pits from mid-spring of MY 28 to late summer of MY 32. The context images are the same as the first image in each time series. Note the pit in Column A has a flat floor, while the pit in Column B has a slanted floor that smoothly connects to the upper surface of the mesa along the upper margin. HiRISE images PSP_003738_0930, PSP_005517_0930, ESP_013086_0930, ESP_014141_0930, ESP_020800_0930, ESP_023661_0930, ESP_029846_0930, ESP_032615_0930, ESP_038483_0930, ESP_041094_0930.

Near the sheer edges of thick mesas, particularly in locations where high mesas become thin in planform, the bright, smooth upper surface sometimes deteriorates, revealing an underlying vermicular texture (Fig. 4.17). As the upper surface deteriorates, thin, bright, linear ridges parallel to the edges of the retreating upper surface are usually evident. The interior of the mesa is immediately dark once the smooth upper surface disappears.

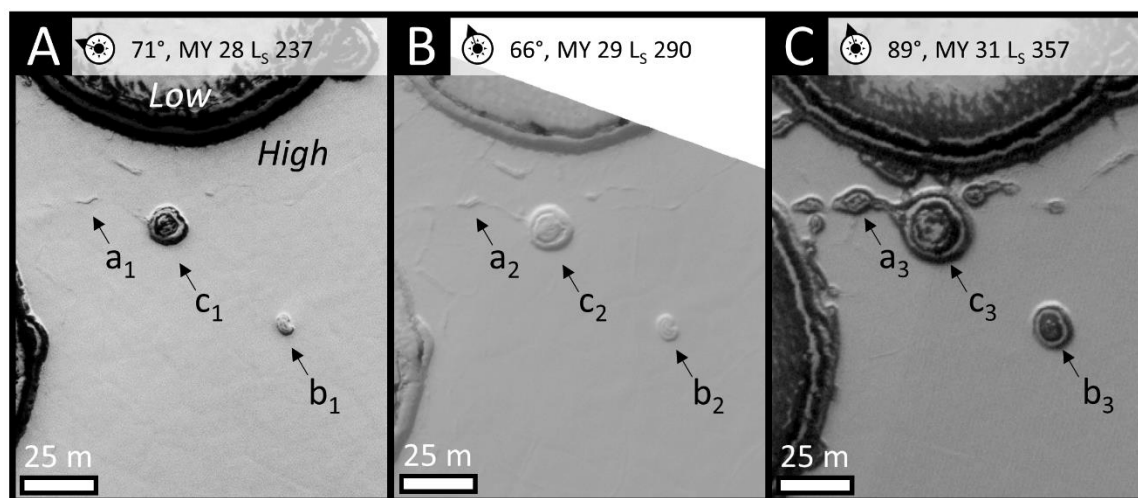


Figure 4.19. Unit B7. **a.** Cracks on the top surface of the CO₂ deposit. **b.** 1 martian year later. **c.** Another 2 martian years later. The evolution of a fracture widening into a quasi-circular pit can be tracked by observing changes from a₁ to c₃ in sequential order: a₁ is a fracture that evolves to a₃; a₃ and b₁ have similar size and morphology; b₁ evolves to b₃; b₃ and c₁ have similar size and morphology; c₁ evolves to c₃, a quasi-circular pit. HiRISE images (A) PSP_003716_0930, (B) ESP_013617_0930, (C) ESP_032790_0930.

4.4.4 Inception of Quasi-Circular Pits

Some fractures have points of collapse ~1-2 m in radius that become the inception locations of quasi-circular pits (Fig. 4.18a), while other fractures widen into a quasi-circular pit (Fig. 4.19, a₁). In both cases, we measure that the steep scarps that encompass the pits erode at a rate of ~2 m/martian year by sublimation over the five martian years of observations. This is

similar to the erosion rates observed for larger pits by Thomas et al. (2005, 2009). The smallest pit we observe that exhibits erosion via calving blocks on its walls has a radius of ~ 10 m (Fig. 4.20).

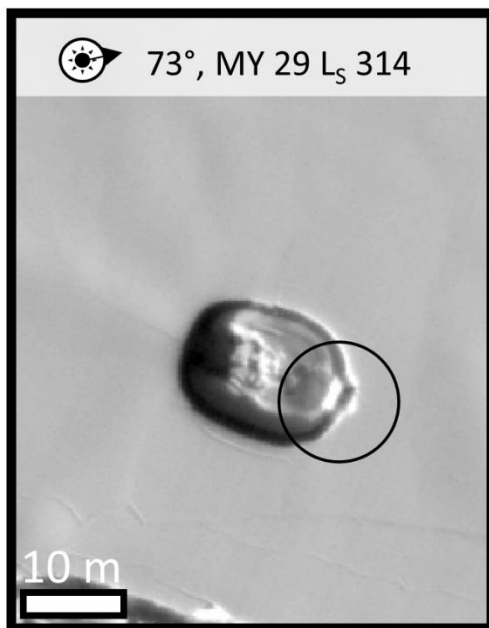
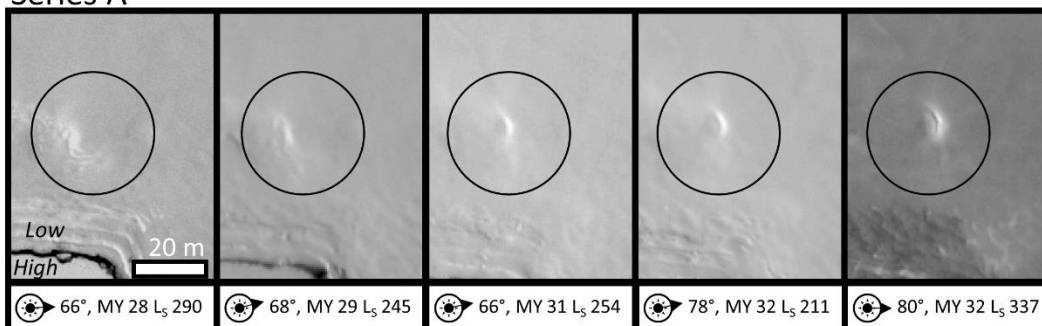


Figure 4.20. Unit A1. The smallest pit observed to erode via calving blocks. Calving block is about 1 x 3 m and is circled. HiRISE image ESP_014141_0930.

4.4.5 Gentle Ramps and Steep Scarps Combine to Form Heart-Shaped Pits, Linear Troughs, and Moats

In some cases, crescentic features develop instead of circular pits. In one typically observed case, a portion of a collapsing area along a fracture remains attached to the upper surface of the mesa, forming a crescentic pit: a pit that has a smooth ramp abutting a steep scarp (Fig. 4.18b). The same crescentic morphology also develops in ~ 5 m-wide alcoves that occur at the termini of gentle slopes of CO₂ ice (Fig. 4.21a). Additionally, surface irregularities on smooth ramps can develop into new, crescentic pits (Fig. 4.22), while small crescents sometimes disappear between summer and the spring of the following year (Fig. 4.21b).

Series A



Series B

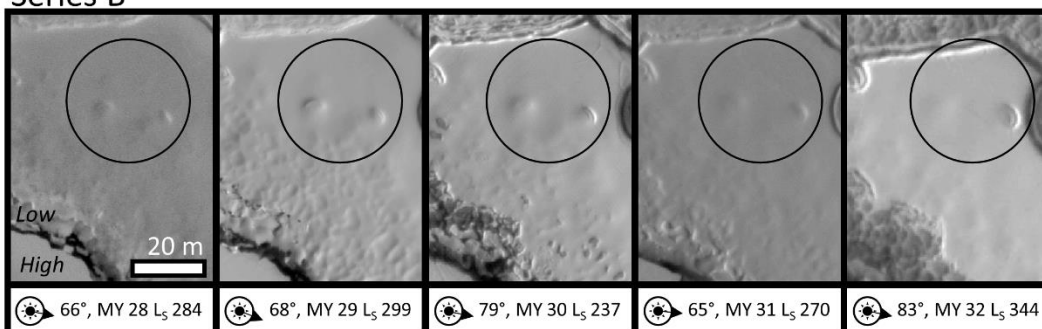


Figure 4.21. Unit B2. 5-martian-year time series. **a.** The edge of a thin CO₂ deposit. Note roughness on the edge of the deposit in the first image. A crescent is clearly recognizable in the final image. **b.** Two crescents are apparent in the first image. Left crescent is muted, but still apparent in third image. Only one crescent is apparent in the final image. Note low illumination angle. HiRISE images (A) PSP_004792_0940, ESP_012690_0940, ESP_030518_0940, ESP_038443_0940, ESP_041107_0940 (B) PSP_004686_0930, ESP_013810_0930, ESP_023410_0930, ESP_030834_0930, ESP_041278_0930.

Crescentic pits evolve along one of two different paths. In one scenario, the steep scarp may erode into the smooth ramp, dissecting it and forming a cusp, leading to a heart-shape. In this case, the portion of the ramp cut off from the upper surface becomes an isolated smooth-topped mesa within the pit, i.e., a moat forms (Fig. 4.23a). When many crescentic pits are in close proximity, the steep scarps of different pits can intersect, forming sinuous ridges, cusps, and moats (Fig. 4.24). In the second scenario, crescents also evolve into linear troughs when the smooth ramp instead expands laterally, encroaching onto the steep scarp (Fig. 4.23b, 4.24). Note that heart-shaped pits and linear troughs are intimately associated (Fig. 4.2c, 4.23b, 4.24).

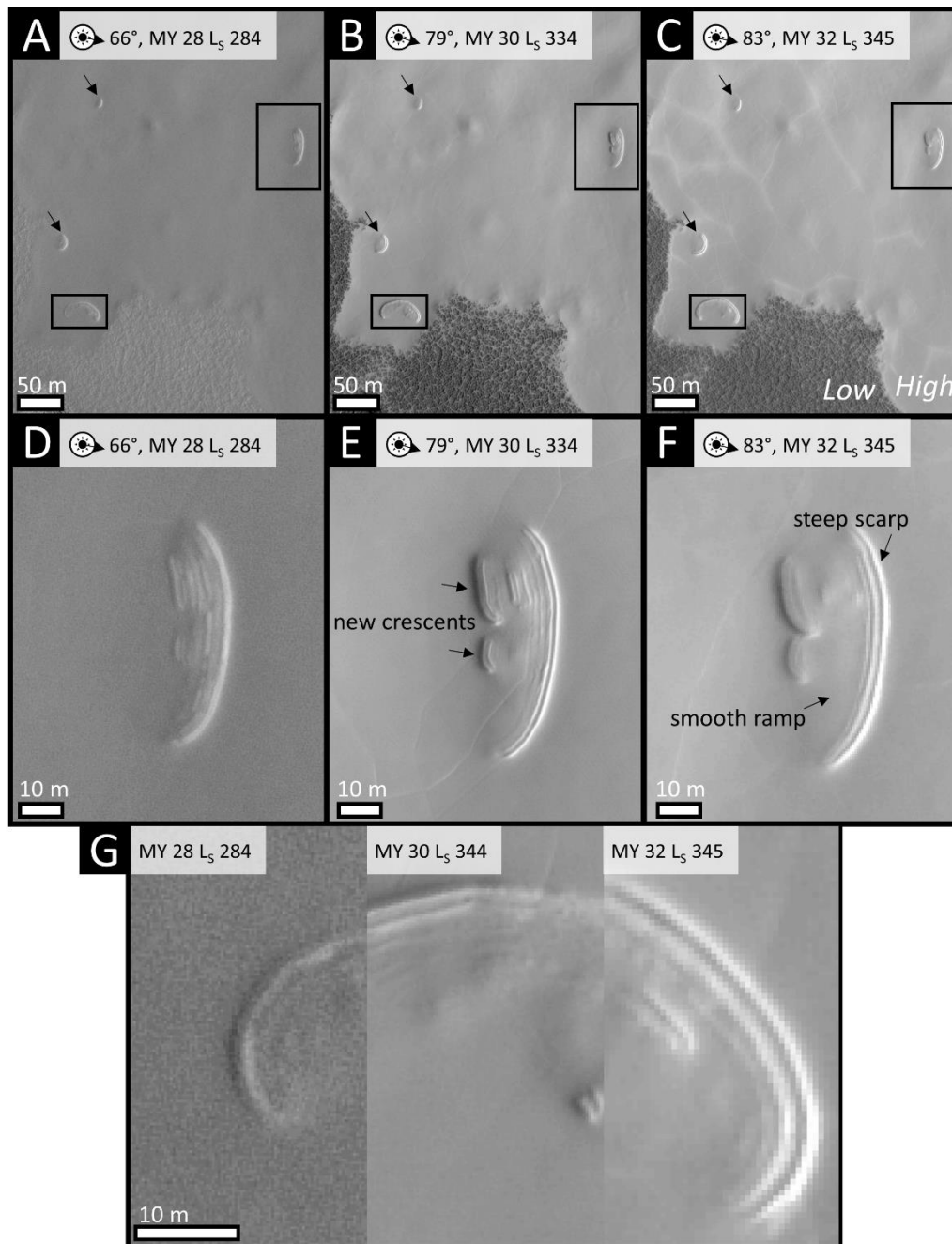


Figure 4.22. The Un. **a-c.** Time series of crescents. Arrows are georeferenced and mark fixed locations between the images. Note positions of small crescents change relative to the arrows. Black boxes indicate the locations of panels **d-g**. Lower panels are insets of upper panels (black box). **d.** Zoom in on crescent. **e.** Note that two new crescents have formed from roughness on the gentle slope. **f.** The new crescents and the original scarp have eroded away from each other. **g.** Georeferenced slices of a crescent in three different years. Note that the smooth ramp still abuts the steep scarp in the rightmost slice, despite the fact that the steep scarp has eroded. HiRISE images PSP_004686_0930, ESP_023410_0930, ESP_041278_0930.

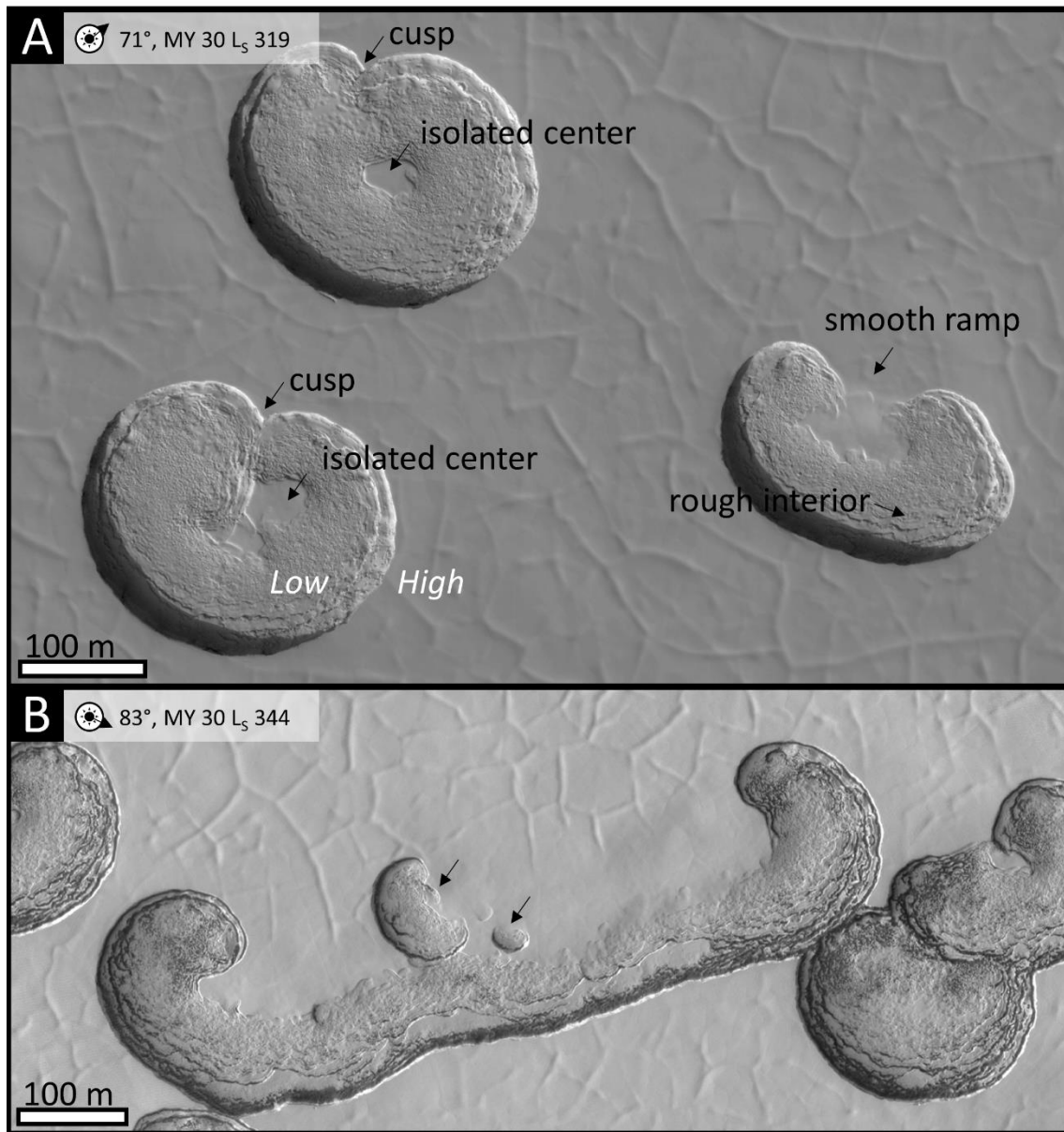


Figure 4.23. a. Heart-shaped pits can exhibit smooth ramps and smooth, isolated centers. Note encroachment of steep scarp on smooth ramp. **b.** Half-circle pits can also form elongated troughs with curled ends in which the length of the ramp is greater than the width of the pit. Note forms intermediate between half-circle pits (Fig. 4.18b) and heart-shaped pits in panel **a** (arrows). HiRISE images (A) PSP_003738_0930, (B) ESP_023661_0930.



Figure 4.24. Unit B2. Crescents, linear troughs, sinuous ridges, and moats. Note cusps where ridges intersect. HiRISE image ESP_032654_0940.

Steep scarps in crescentic pits in our study areas erode at ~ 2 m/martian year, but the smooth ramp often remains abutting the steep scarp for the entire five-martian-year span of our observations (Fig. 4.18b, 4.22d-g), thus indicating that the horizontal extent of the smooth ramp is also increasing. Smooth ramps on the edges of mesas also increase in extent between martian years. Fig. 4.25 shows two smooth ramps initially separated by ~ 10 m merge together over the course of two martian years, yielding a growth rate of ~ 2.5 m/martian year on each scarp edge, although the magnitude of growth appears to vary locally during different Mars years.

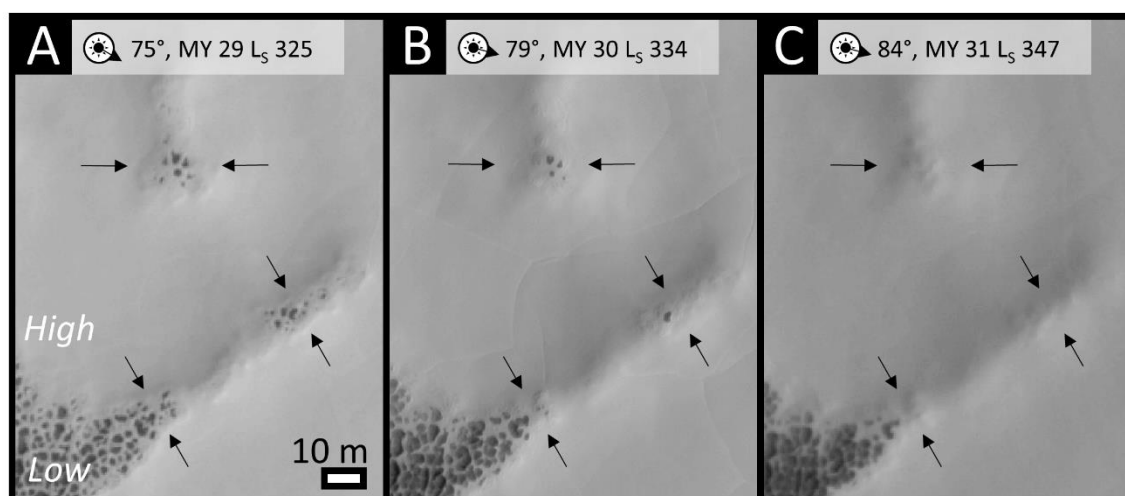


Figure 4.25. a, b, c. The Un. Time series of the smooth edge of a CO₂ mesa over three martian years, with each successive image taken later in the summer. Smooth, bright texture is CO₂ ice. Dark, rough texture is H₂O ice. Note growth of CO₂ ice (arrows). Note roughness in panel B. **d.** Context. Note distance between gentle scarp and nearest steep scarp. HiRISE images (A,D) ESP_014390_0930, (B) ESP_023410_0930, (C) ESP_032535_0930.

4.5. Discussion

4.5.1 Mesa Dust Content Generates Dark Fans

The morphology and seasonality of dark fans associated with the RSPC is similar to that of the dark fans seen in the seasonal CO₂ ice deposits on the araneiform ('spider-like') terrain in the cryptic region of the south polar cap (e.g. Kieffer, 2003, 2007; Kieffer et al., 2006; Piqueux et al., 2003; Hansen et al., 2010). This suggests that the dark fans on the sides of RSPC mesas likewise form from the deposition of (dark) dust lofted by a pressurized gas jet rupturing a sintered layer of CO₂ ice (see, e.g., Kieffer et al., 2006; Kieffer, 2007; Hansen et al., 2010). The fact that some dark fans drape over the top of CO₂ mesas (Fig. 4.3b) also indicates such an explosive deposition process.

In this scenario, the mesa must be sealed by an outer confining layer strong enough to at least temporarily confine the pressurized gas. Deposition and subsequent annealing (Eluszkiewicz, 1993; Kieffer, 2007) of a layer of CO₂ blanketing the RSPC mesas during the winter would readily create such a confining layer, as discussed for seasonal CO₂ ice by Portyankina et al. (2012). The crisp edges of the fractures that appear on the upper surfaces of RSPC mesas (Fig. 4.9-11) indicate that the upper surface of the RSPC mesas undergo brittle failure, which is consistent with impermeable, annealed CO₂ ice. CO₂ deposited onto the sloped, uneven surface of the mesa sides (e.g. Fig. 4.6a) or near the angled intersection between the mesa sides and mesa base (e.g. Fig. 4.3a) would have more imperfections and weaknesses than CO₂ deposited onto the generally smooth mesa tops. This would make it easier for pressurized gas to break through mesa sides and would explain why fans are observed on the sides but not on the tops of mesas.

Dust falling onto the CO₂ ice will migrate downward through the ice (Kieffer, 2003, 2007), creating a layer of nearly pure ice overlying dirtier ice (Portyankina et al., 2010). This is consistent with our observations that the edges of mesas turn dark in summer, with an overlying tens-of-centimeters-thick layer of bright material (Fig. 4.6b-c). The interiors of mesas are also immediately dark once the upper surface deteriorates (Fig. 4.17). Dusty ice will absorb sunlight much more readily than clean ice and thus drive sublimation of CO₂ ice in mesa interiors, leading to pressurized gas, similar to how fans are thought to form in the seasonal CO₂ ice (e.g. Kieffer, 2003, 2007). Fans may appear earlier in the season on the sides of Unit A0 than on the Un because they are taller and will therefore intercept more sunlight in early spring, when the sun is low on the horizon.

The length of the fans emanating from RSPC mesas allows us to estimate the pressure sourcing the vents by comparing to models of the CO₂ gas geysers rupturing the seasonal CO₂ ice. Thomas et al. (2011) use a comprehensive fluid dynamic model to calculate that dust entrained in the geysers in the seasonal ice reaches heights of ~20-80 m with source pressures of ~10³ Pa. This is slightly longer than the typical fan lengths on mesa sides (< ~10 m; Fig. 4.3), suggesting similar or slightly lower pressures within the mesas. Due to differences in geometry and latitudinal differences between our study sites and the locations modeled by Thomas et al. (2011), it is difficult to compare the RSPC fans directly to the Thomas et al. (2011) models, but < ~10³ Pa lies within the yield stresses of H₂O Ice I and Ice II (~10²-10⁴ Pa; the yield stress of CO₂ ice is unknown; Portyankina et al. (2010)). Given the similarity between the fans we observe on the side of mesas and the fans modeled by Thomas et al. (2011), we conclude that pressures of ~<10³ can be contained within the mesas, but fan formation on the sides of mesas could be modeled in more detail.

Fans do not develop in the seasonal CO₂ ice deposit between the RSPC CO₂ mesas, as they do in the seasonal deposits elsewhere on the south pole (Hansen et al., 2010; Portyankina et al., 2012). We speculate that this may be due to a lack of a mobile dust source on the H₂O ice basement—perhaps because it is blown away by wind—and thus no darkening agent. Consequently, even if pressurization and venting occurs between the mesas of the RSPC, this venting would be invisible.

Finally, we observe more fans forming on the sides of RSPC mesas in MY 29 than in MY 28 or 31, which is similar to the variability in dark fan activity in the seasonal ice (Hansen et al., 2011). The variability in fan formation also correlates with the global dust storm in MY 28; however the correlation between enhanced fan activity and dust storms is not unambiguous (Hansen et al., 2011).

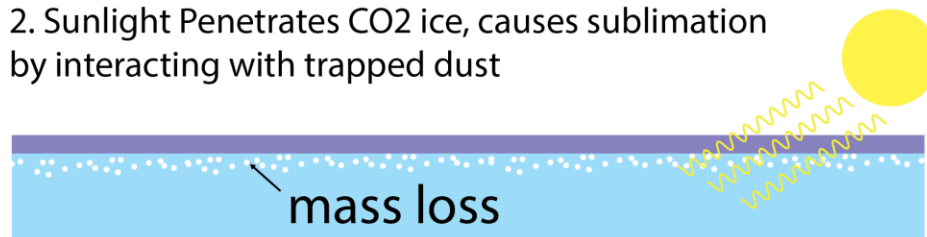
4.5.2 Interior Sublimation Drives Fracturing and Slab Settling

The bright, upper surface layer of mesas undergoes brittle failure, fracturing and breaking into slabs (Fig. 4.9-12). We interpret this failure as resulting from the loss of underlying structural support as the interiors of mesas sublimate and lose mass (Fig. 4.26). As new fractures form across the CO₂ mesas, the upper surface breaks into progressively smaller slabs, until the slabs reach a surface area of $\sim 10^2$ m² (Fig. 4.14d, 4.16), which appears to be the scale on which slabs have enough strength not to break further. The natural result of internal sublimation and mass loss, fracturing, and collapse of mesas is the destruction of coherent layering, even if the CO₂ ice is originally deposited in layers. Others have also noted that it is impossible to find distinct layers within the RSPC deposits (e.g., Thomas et al., 2009).

1. Coherent Upper Layer



2. Sunlight Penetrates CO₂ ice, causes sublimation by interacting with trapped dust



3. Sublimation not uniform, collapse compresses interior ice, slabs settle on uneven surface, fractures are evident



4. Deposition occurs the following winter, smoothing the fracture



4b. Further subsidence occurs, forming double ridge



5. Deposition following year smooths topography



Figure 4.26. Interpretation of the development of fractures. Compare to Fig. 11. Note that development of double ridge is not ubiquitous among fractures.

The vermicular texture exposed in the interiors of mesas immediately after the erosion of the bright, upper surface indicates that sublimation and mass loss in the interiors of mesas is inhomogeneous (see Fig. 4.17 and figure 5d of Thomas et al. (2005)). The vermicular texture may be the result of channels formed by the lateral flow of pressurized gas (cf. Kieffer, 2003, 2007; Kieffer et al., 2006; Villiers et al., 2012). Non-uniform structural support from the uneven, vermicular texture directly underlying the bright, upper surface may be the reason that slabs tilt during collapse.

The vertical offset in the fractures between adjacent slabs is initially crisp, but becomes muted by the time observations are made the following spring (Fig. 4.11). Since fractures only become muted during the winter, the muting is likely due to the deposition of new CO₂ ice (Fig. 4.26). After becoming muted, some fractures become double-ridged and, in one instance, a new subtle ridge simultaneously appears ~10 m away and parallel to the original fracture (Fig. 4.11). We therefore interpret that double ridges occur when slabs undergo additional settling. Fractures also sometimes re-crack (Fig. 4.14c, 4.14f, 4.16d), which we interpret as evidence of additional settling of slabs exploiting preexisting fracture boundaries. Re-cracking occurs preferentially within a few tens of meters of mesa edges that are bounded by ~1-10 m-tall shear scarps (Fig. 4.14i, 4.16d), and some mesas bound by tall, shear scarps have raised centers (Fig. 4.15). These observations indicate that internal sublimation and mass loss is enhanced close to mesa sides, leading to increased subsidence, likely due to sunlight efficiently penetrating horizontally into the mesas because the sun is low on the horizon near the pole.

Fractures with negative relief sometimes become positive relief ridges that later return to negative relief (Fig. 4.14c-f), and some fractures that have re-cracked develop a ridge within the fracture (Fig. 4.14h). We interpret these observations as the infilling of fractures between

slabs with new CO₂ ice, forming a wedge that vertically settles independently of the adjacent slabs. We interpret the bright, ~1-m-wide ridges left behind between slabs as the upper surface deteriorates (Fig. 4.17) as the remnants of these wedges.

Finally, the occurrence of fields of polygonal depressions in at least one location each year indicates that the formation of polygonal depressions is a common process. However, the timing between widespread subsidence events at a particular location appears to be longer than our five-martian-year observational baseline, because we do not observe these subsidence events more than once in any specific location. Nevertheless, the nearly ubiquitous development of polygonal depressions on Unit A0, where there is HiRISE coverage during MY 30, indicates ~1% of local mass loss from the interior, since polygonal depressions settle downwards by ~10 cm and the A0 mesas are ~10 m thick (Thomas et al., 2016). If the entirety of Unit A0 underwent this subsidence, then $\sim 3 \times 10^7$ m³ of CO₂ would be lost (on the order of 0.01% of the mass of the entire RSPC). Continued observations of polygonal slab settling are warranted because, once a settling frequency can be established, the rate of interior sublimation can be calculated. For now, we estimate an upper bound of 2 cm/martian year of internal sublimation loss in Unit A0 (10 cm of settling over 5 martian years).

4.5.3 Interior Sublimation Rates Based on Halos around Fractures

Bright halos that developed around new fractures in MY 32 (Fig. 4.12) may signal gas venting from fractures on the upper surface of the mesas. The bright halos occurred after a large

dust cloud was present over the south polar cap from $\sim L_s$ 310-320 in MY 32⁵, suggesting a connection between the halos and the dust cloud. Becerra et al. (2014) also note bright halos on mesa edges following a dust storm in MY 28 and develop a conceptual model for their formation in which pressure from sublimating gas on the sides of mesas deflects falling dust, such that, while other regions of the RSPC darken from dust deposition, the mesa edges are protected and remain bright. Becerra et al. (2014) also consider two alternatives of halo formation by either (i) inclusion of H₂O ice impurities or (ii) the deposition of fine-grained CO₂ frost, but reject both alternatives based on spectral data. Our data are consistent with Becerra's interpretation of sublimation, and we find that halos occur almost exclusively around new fractures that were not visible in previous years, which likely indicates that most older fractures become sealed, thus stopping gas outflow.

Under the interpretation that the halos are caused by CO₂ outflow deflecting dust, the halos provide an opportunity to estimate the sublimation rates within the mesas. Dust will be deflected when the velocity of the venting gas approximately equals the velocity of the settling dust (v_s). Dust falls in the Stokes regime (Becerra et al., 2014), so v_s can be found with:

$$(4.1) \quad v_s = \frac{1}{18} \frac{(\sigma - \rho)d^2g}{\eta}$$

Here we adopt the same values as Becerra et al. (2014): ρ is the atmospheric density ($\sim 0.02 \text{ kg m}^{-3}$), σ is the density of the dust particle ($\sim 2700 \text{ kg m}^{-3}$), g is martian gravity (3.7 m s^{-2}), and η is the atmospheric viscosity ($\sim 1.3 \times 10^{-5} \text{ Pa s}$). We use a particle diameter of $2 \text{ }\mu\text{m}$ (d , Wolff and Clancy, 2003; Wolff et al., 2009).

The gas velocity (v_g) at a distance r from the fracture depends on mass flux per unit length (\dot{m}) and is given by:

⁵ MRO MARCI weather reports on 03/25/2015 and 04/15/2015 from Malin Space Science Systems.

$$(4.2) \quad v_g = \frac{\dot{m}}{\pi r \rho}$$

We can now calculate the total CO₂ gas flux through the linear fractures for the areas shown in Fig. 4.12a-b. The average lateral extent of the halos in both locations in MY 32 is $r \sim 3$ m, so rearranging Eq. 4.1 & 4.2 and solving for \dot{m} , the flux of CO₂ gas from the vents is 3×10^{-5} kg m⁻¹ s⁻¹. The total length of fractures in Fig. 4.12a (Unit B2) is 1.6×10^4 m, so the total flux through the vents is 0.5 kg s⁻¹. Assuming a local source area for the sublimating gas, i.e., the area of Fig. 4.12a (1.7×10^6 m²), the internal sublimation rate is 3×10^{-7} kg m⁻² s⁻¹. The total length of fractures in Fig. 4.12b (the Un) is 2.2×10^3 m, and the total area is 1.3×10^5 m², yielding a similar internal sublimation rate of 5×10^{-7} kg m⁻² s⁻¹. We note that our estimate of mass flux is lower than the one modeled by Becerra et al. (2014), which makes sense since they modeled the outflow from the sublimation of the surface of the pit walls, where the halos are also observed to be larger.

Assuming a mean density of 1500 kg m⁻³ for CO₂ ice (see Aharonson et al., 2004; Blackburn et al., 2010; Smith and Zuber, 2011, Hayne et al., 2012, 2014; Thomas et al., 2016), and assuming an average thickness of ~ 1 m for the deposits displaying fractures with halos (Sec. 4.4.2), the area of B2 shown in Fig. 4.12a loses 2.0×10^{-10} of its total mass each second and the area of the Un shown in Fig. 4.12b loses 3.6×10^{-10} of its total mass each second. If these rates continue through the entire spring and summer season, then $\sim 0.6\%$ of the mass (a thickness of ~ 0.6 cm) from the B2 area (Fig. 4.12a) and $\sim 1.1\%$ of the mass (a thickness of ~ 1.1 cm) from the Un area (Fig. 4.12b) is lost to internal sublimation. These rates are about half the upper bound placed on sublimation in the thicker mesas based on slab settling.

It is interesting that the thicker mesas do not have halos around new fractures. The phenomenon is likely real, since thicker mesas with new fractures are within the HiRISE image of the Un. This may be due to the fact that thicker mesas are typically surrounded by tall, steep scarps, whereas

the boundaries of the thinner mesas are typically thin, smooth ramps. We hypothesize that gas can therefore more easily escape through the sides of thick mesas, leading to decreased flux through their tops, and thus inhibiting halo formation.

Finally, we extend two caveats. First, the vertical settling speed of dust is $\sim 2 \times 10^{-4} \text{ m s}^{-1}$ (Eq. 4.1), while Smith et al. (2015) model the ambient wind speed at a height of 20 m above the RSPC to be on the order of several meters per second or greater. Even though wind speeds are well-known to decrease quickly approaching the atmosphere-ground interface, ambient wind may still strongly effect the ability of wind from sublimating CO_2 to deflect dust grains. Second, while observations of Unit B2 following the dust storm in MY 28 show that fractures are brighter than the surrounding areas, the lateral extent of the brightening is only $\sim 0.75 \text{ m}$ on either side of the fracture, suggesting that the sublimation rate in the MY 28 observations is only one-fourth that of the observations in MY 32; the halos around the mesa edges are also less extensive in MY 28 than in MY 32 (Fig. 4.14c-d). This may indicate (i) decreased interior sublimation after the larger and longer-lived MY 28 dust storm, perhaps because more sunlight was blocked during summer, (ii) intra- or inter-annual variation in internal sublimation rates, or (iii) a difference in halo degradation due to post-dust storm surface changes, caused by a difference in seasonality (and thus insolation) or amount of dust deposition (and thus albedo).

4.5.4 Seasonal CO_2 Ice Incorporated into the RSPC

The development of smooth ramps, which is necessary for the development of linear troughs and moats, requires vertical accumulation (Sec. 4.4.4 and 4.4.5), and thus indicates the importance of deposition in determining the morphology of the RSPC. Additionally, the striking

change in relative albedo of mesa sides and the H₂O ice basement adjacent to RSPC mesas compared to the tops of mesas over the course of spring and summer (e.g. compare Fig. 4.6a and 6b) clearly indicates the deposition of seasonal CO₂ ice on both mesa sides and the H₂O ice basement. Given the scale and proximity of this deposition to mesa tops, significant amounts of CO₂ are likely also deposited on the upper surface of the mesas.

Thomas et al. (2016) also report growth of smooth mesa edges over three martian years (between MY 28 and 30) in Unit A2 (their figure 4); although, due to limited HiRISE coverage of Unit A2, their observations in MY 30 (L_s 309) are at an earlier time in the summer than their observations in MY 28 (L_s 323). This leaves open the possibility that the increased extent of the gentle scarp could be due to the presence of seasonal CO₂ ice that will sublimate later in the summer. However, the progressive muting of fractures (Fig. 4.11) and progressive growth along mesa edges (Fig. 4.25) observed in our multi-year data indicates that at least some of the seasonal deposition is permanently incorporated into the RSPC on annual timescales, particularly since the extent of the gentle scarps in Fig. 4.25 is greater later into the summer in two successive Mars years. Moreover, we observe widespread fracturing and settling of the upper surface, with an enhanced rate of settling near steep mesa edges, whereas Thomas et al. (2016) made shadow measurements indicating that there has been almost no change in mesa thickness over periods of 3-22 martian years (depending on coverage). Therefore, the rates of subsidence of the upper surface of mesas and net deposition onto the upper surface of mesas seem to be nearly balanced on annual to decadal timescales.

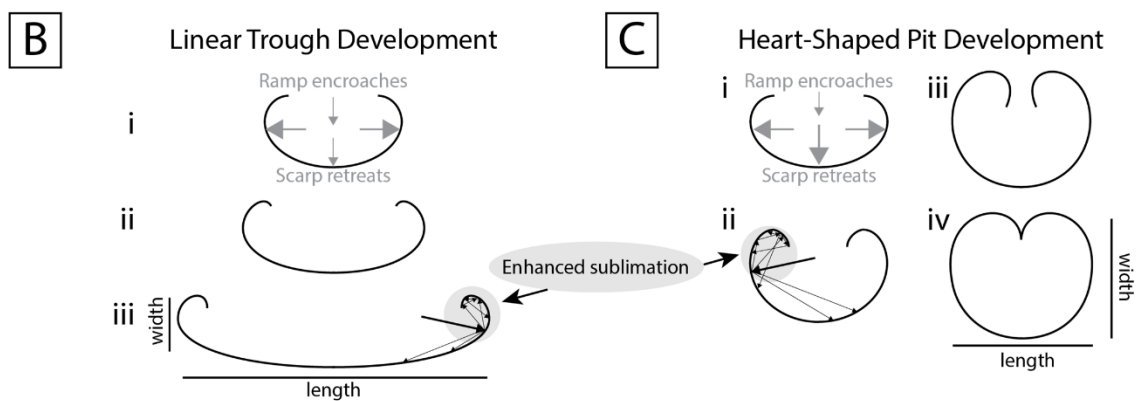
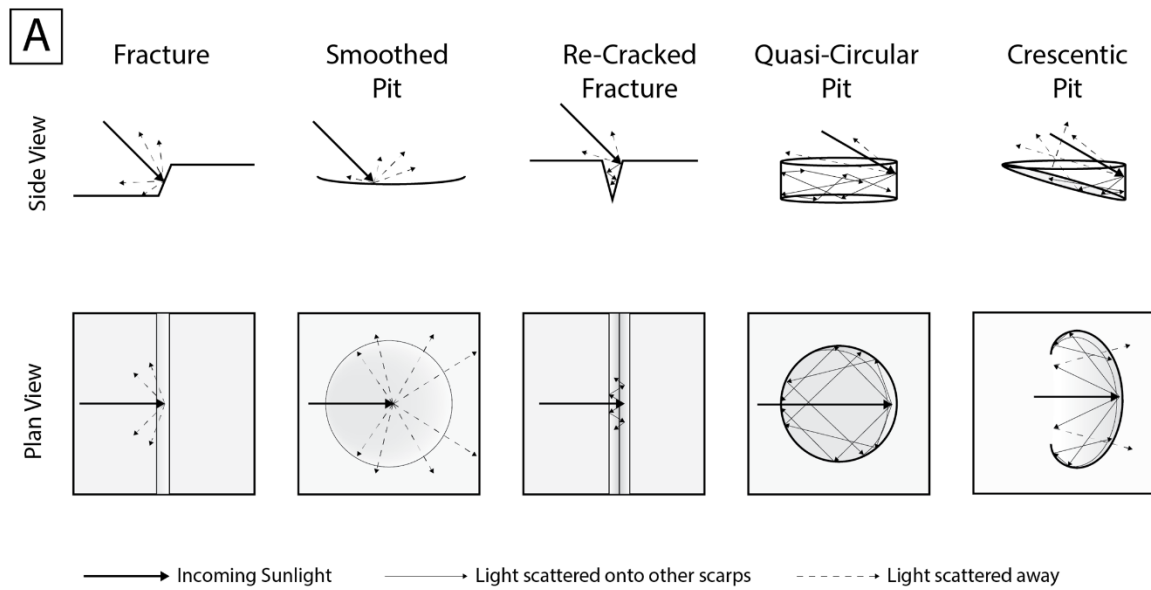


Figure 4.27. a. Light scattering geometries in the RSPC. Light is scattered away from fracture scarps and smoothed pits (e.g. Fig. 4.6). Sunlight is scattered into and absorbed by the steep scarps in meter-wide re-cracked fractures and quasi-circular pits. The low-angle, smooth ramp in crescentic pits reflects light away, but the steep-scarped, curled ends efficiently trap light. **b.** The smooth ramp in crescentic pits lengthens and the scarp retreats lengthwise, while the ramp extends into the pit, approximately maintaining the same distance between the ramp and the opposite scarp from year to year. This creates a linear trough. **c.** The scarp retreat cuts into the smooth ramp, until the scarps meet in a cusp, creating a heart-shaped pit. Retreat of the scarp opposite the ramp also outpaces growth of the ramp into the pit, widening the pit.

4.5.5 Scarp Steepness and the Deposition-Sublimation Cycle as Landform Drivers

Fractures and smooth ridges that have vertical offsets of $< \sim 10$ cm and lengths of tens to hundreds of meters do not, once formed, retreat backward in subsequent years (Fig. 4.11). Additionally, smoothed pit-shaped depressions are stable morphologies in all locations we observe, despite having vertical relief on the order of tens of centimeters (Fig. 4.6, 4.21b). However, rough alcoves that are ~ 5 m long and have ~ 10 s of centimeters of relief develop into crescentic pits (Fig. 4.21a), and steep-walled pits with ~ 2 m radii and ~ 10 cm of relief will enlarge (Fig. 4.18). Thus, ~ 10 cm of steep vertical offset along a curved extent of a few meters is the threshold for a steep scarp that will continue to erode in subsequent years despite winter deposition. The two crescents in Fig. 4.21b illustrate this threshold. Each initially has a vertical scarp with ~ 10 cm offset (based on shadow measurements, with an uncertainty of ~ 3 cm) and a curved extent of a few meters, but the left pit is smoothed over, while the right pit maintains a steep scarp.

Scarp steepness, curvature, and albedo play an important role in the development of pits (Fig. 4.27). Scarps will absorb, reflect, and reemit sunlight. Steeper scarps expose the dustier, darker interior of mesas and therefore absorb more energy than smooth ramps, which are protected by the bright capping layer of cleaner ice (Sec. 4.5.1; Fig. 4.24). In addition, steep scarps reflect and re-emit more energy back into a pit than a shallow ramp (Fig. 4.27a). Curved scarps will also reflect and reemit energy onto neighboring sections of the scarp, whereas a linear scarp will reflect energy away (Fig. 4.27a). Surface roughness in general will focus energy, such as in the development of quasi-circular pits from points of collapse or fracture widening (Fig. 4.27a). We note that the landscape evolution model of Byrne et al. (2008, 2015) predicts that pits will form

once a critically steep slope is developed, which supports this theory. However, the Byrne et al. (2008, 2015) model achieves steep slopes via differential accumulation of CO₂ ice, whereas we prefer a framework in which steep, sublimating slopes form from the fracturing and collapse of the upper surface of mesas, because we only observe pit formation in intimate association with fractures (e.g. Fig. 4.18).

The balance of deposition and erosion at the boundary between the steep scarp and the smooth ramp in half-circle pits (Fig. 4.18b) drives its evolution either toward a linear trough or a heart-shaped pit (Sec. 4.4.5; Fig. 4.27b-c). If deposition along the ramp approximately keeps pace with erosion along the opposing scarp face, the distance between the ramp and the opposing steep scarp face remains approximately constant; however, the increased curvature at the edges of the pits focuses reflected energy (Fig. 4.27biii), causing increased erosion and lengthening the pit, which creates a linear trough (Fig. 4.27b). On the other hand, if scarp erosion definitively outpaces deposition, the pit widens and lengthens approximately symmetrically. The most strongly curved portion of the pit erodes most rapidly (Fig. 4.27cii), cuts into the ramp, and eventually dissects it, forming a cusp and making a heart-shaped pit (Fig. 4.27c).

The spatial variation of morphologies in the RSPC indicates that differences in insolation, deposition rates (e.g. Brown et al., 2014), composition, or winds (e.g. Smith et al., 2015) across the RSPC may lead to greatly different outcomes in morphology. Additional observation and modeling of the RSPC is warranted in order to uncover which of these parameters are most important in developing the final morphology of a particular unit.

4.6. Conclusions

We use high-resolution, high-cadence time series observations of the martian residual south polar cap (RSPC) to understand its morphologic evolution at the meter-scale. We document, for the first time, dark fans on the sides of mesas, and fracturing and collapse of the upper surface of mesas. We interpret that the dark fans result from pressurized gas escape from the sides of mesas carrying entrained dust, and indicate sublimation of CO₂ ice in the interior of RSPC mesas. Our analysis indicates that sublimation within mesas is mediated by mesa thickness as well as by vertically stratified dust content. Under this scenario, the sublimation leads to mass loss and therefore loss of structural support for the brittle upper layer of the mesas, which fractures into collapsing polygonal slabs. Thin (~1 m) mesas have an internal sublimation rate of 6×10^{-6} to 1×10^{-5} kg m⁻² s⁻¹ of CO₂, leading to gas escape through fractures that is sufficient to prevent localized dust deposition, while thick (several meter) mesas appear to have sublimation rates that are 5-10 times lower.

We find that the collapse of mesa tops creates slabs separated by fractures. Small areas of collapse along the fractures and fractures that appear to settle and re-crack evolve into steep-walled, quasi-circular pits. The steep walls act to focus sunlight, enhancing erosion and preventing winter deposition from smoothing them back over. We infer that steep scarps need to have at least ~10 cm of sheer vertical relief, lengths of ~>5 m, and curvature in order for summer erosion of the scarps to outpace smoothing over by wintertime deposition.

Our analysis indicates that localized collapse along pre-existing fractures where a portion of the collapsing material remains attached to the upper surface leads to crescentic pits, which are pits

that have smooth ramps that abut steep scarps. Uneven deposition along the edges of smooth ramps can create steep-scarped alcoves that can also develop into crescentic pits. We interpret that the relative effectiveness of deposition and erosion at the boundary between the smooth ramp and the steep scarp determines whether a crescentic pit develops into a heart-shaped pit or a linear trough.

The processes we infer from our observations are capable of explaining the morphologies present in the RSPC and provide a framework for landscape evolution models that would lead to better insight into the material properties of the RSPC. Ultimately, the processes we describe in this paper shed light on the subtle interplay of deposition and erosion on the RSPC and inform our understanding of the global martian CO₂ cycle.

4.7 Acknowledgments

We gratefully acknowledge funding from NESSF grant #16-PLANET16F-0071 and MFRP grant #NNX14AG54G. We also thank Timothy Titus and an anonymous reviewer for their feedback, which helped to improve this work.

References

- Aharonson, O., Zuber, M.T., Smith, D.E., Neumann, G.A., Feldman, W.C., Prettyman, T.H., 2004. Depth, distribution, and density of CO₂ deposition on Mars. *J. Geophys. Res. E Planets* 109, 1–10. doi:10.1029/2003JE002223
- Becerra, P., Byrne, S., & Brown, A. J. (2014). Transient bright “halos” on the South Polar Residual Cap

of Mars: Implications for mass-balance. *Icarus*, 251, 211–225.

<http://doi.org/10.1016/j.icarus.2014.04.050>

Bierson, C. J., Phillips, R. J., Smith, I. B., Wood, S. E., Putzig, N. E., Nunes, D., & Byrne, S. (2016).

Stratigraphy and evolution of the buried CO₂ deposit in the Martian south polar cap.

Geophysical Research Letters, 43(May), 1–8. <http://doi.org/10.1002/2016GL068457>

Blackburn, D.G., Bryson, K.L., Chevrier, V.F., Roe, L.A., White, K.F., 2010. Sublimation kinetics of CO₂

ice on Mars. *Planet. Space Sci.* 58, 780–791. doi:10.1016/j.pss.2009.12.004

Brown, A.J., Piqueux, S., Titus, T.N., 2014. Interannual observations and quantification of

summertime H₂O ice deposition on the Martian CO₂ ice south polar cap. *Earth Planet. Sci.*

Lett. 406, 102–109. doi:10.1016/j.epsl.2014.08.039

Byrne, S., Hayne, P. O., & Becerra, P. (2015). Evolution and stability of the the residual CO₂ ice cap.

46th Lunar and Planetary Science Conference, #1657

Byrne, S., & Ingersoll, A. P. (2003a). A sublimation model for martian south polar ice features. *Science*

(*New York, N.Y.*), 299(5609), 1051–1053. <http://doi.org/10.1126/science.1080148>

Byrne, S. & Ingersoll, A.P. (2003b). Martian climatic events on timescales of centuries: Evidence from

feature morphology in the residual south polar ice cap. *Geophysical Research Letters*, 30(13),

2–5. <http://doi.org/10.1029/2003GL017597>

Byrne, S., Russell, P. S., Fishbaugh, K. E., Hansen, C. J., Herkenhoff, K. E., McEwen, A. S., & HiRISE

Team. (2008). Explaining the Persistence of the Southern Residual Cap of Mars: HiRISE Data

and Landscape Evolution Models. *39th Lunar and Planetary Science Conference*, 10–11.

Retrieved from <http://adsabs.harvard.edu/abs/2008LPI....39.2252B>

de Villiers, S., Nermoen, A., Jamtveit, B., Mathiesen, J., Meakin, P., & Werner, S. C. (2012). Formation

of Martian araneiforms by gas-driven erosion of granular material. *Geophysical Research*

Letters, 39(13), 1–5. <http://doi.org/10.1029/2012GL052226>

Durham, W.B., Kirby, S.H., Stern, L.A., 1999. Steady-state flow of solid CO₂: Preliminary results.

Geophys. Res. Lett. doi:10.1029/1999GL008373

Eluszkiewicz, J. (1993). On the microphysical state of the martian seasonal caps. *Icarus*, (103), 43–48.

Guo, X., Lawson, G.W., Richardson, M.I., Toigo, A., 2009. Fitting the Viking lander surface pressure cycle with a Mars General Circulation Model. *Journal of Geophysical Research*, 114, E07006, 1-19. doi:10.1029/2008JE003302

Hansen, C. J., Thomas, N., Portyankina, G., McEwen, A. S., Becker, T., Byrne, S., ... Russell, P. S. (2010).

HiRISE observations of gas sublimation-driven activity in Mars' southern polar regions: II. Surficial deposits and their origins. *Icarus*, 205(1), 283–295. <http://doi.org/10.1016/j.icarus.2009.07.021>

Hansen, C. J., McEwen, A., Mellon, M., Portyankina, G., Thomas, N. (2011). Year 3 of HiRISE Observations of Southern Spring on Mars. LPSC 42, Abstract #1651.

Hayne, P.O., Paige, D.A., Heavens, N.G. (2014). The role of snowfall in forming the seasonal ice caps of Mars: Models and constraints from the Mars Climate Sounder. *Icarus* 231, 122–130. doi:10.1016/j.icarus.2013.10.020

Hayne, P.O., Paige, D.A., Schofield, J.T., Kass, D.M., Kleinbhl, A., Heavens, N.G., McCleese, D.J., 2012. Carbon dioxide snow clouds on Mars: South polar winter observations by the Mars Climate Sounder. *J. Geophys. Res. E Planets* 117, 1–23. doi:10.1029/2011JE004040

Herkenhoff, K. E. & Plaut, J. J. (2000). Surfaceages and resurfacing rates of the polar layered deposits on Mars. *Icarus* 144, 243-253. doi:10.1006/icar.1999.6287

Herschel, W. (1784). On the remarkable appearances at the polar regions of the planet Mars, the

inclination of its axis, the position of its poles, and its spheroidal figure; with a few hints relating to its real diameter and atmosphere. In: The scientific papers of Sir William Herschel, Volume 1. John Louis Emil Dreyer, *ed.* Cambridge University Press. p. 131.

Hess, S.L., Henry, R.M., Tillman, J.E., 1979. The seasonal variation of atmospheric pressure on Mars as affected by the south polar cap. *J. Geophys. Res.* 84, 2923–2927. doi:10.1029/JB084iB06p02923

Ingersoll, A. P. (1974). Mars - The case against permanent CO₂ frost caps. *Journal of Geophysical Research*, 79(24), 3403–3410. <http://doi.org/10.1029/JC079i024p03403>

James, P. B., H. H. Kieffer, & D. A. Paige (1992). The seasonal cycle of carbon dioxide on Mars, in Mars, 934–968, Univ. of Ariz. Press, Tucson, Ariz., 1992.

Kieffer, H. H. (2003). Behavior of Solid CO₂ on Mars: A Real Zoo. *Sixth International Conference on Mars*, 0–3. Retrieved from <http://adsabs.harvard.edu/abs/2003mars.conf.3158K>

Kieffer, H. H. (2007). Cold jets in the Martian polar caps. *Journal of Geophysical Research*, 112, E08005, 1–15. doi:10.1029/2006JE002816

Kieffer, H. H., Christensen, P. R., and Titus, T. N. (2006). CO₂ jets formed by sublimation beneath translucent slab ice in Mars' seasonal south polar ice cap. *Nature* 442, 793–796. doi:10.1038/nature04945

Leighton, R. B., & Murray, B. C. (1966). Behavior of carbon dioxide and other volatiles on Mars. *Science (New York, N.Y.)*. <http://doi.org/10.1126/science.153.3732.136>

Malin, M. C. (2001). Observational Evidence for an Active Surface Reservoir of Solid Carbon Dioxide on Mars. *Science*, 294(2001), 2146–2148. <http://doi.org/10.1126/science.1066416>

Malin, M. C., and 13 colleagues, 2007. Context Camera Investigation on board the Mars Reconnaissance Orbiter. *Journal of Geophysical Research*, 112, E05S04.

doi:10.1029/2006JE002808

- McEwen, A.S., Eliason, E.M., Bergstrom, J.W., Bridges, N.T., Hansen, C.J., Delamere, W.A., Grant, J.A., Gulick, V.C., Herkenhoff, K.E., Keszthelyi, L., Kirk, R.L., Mellon, M.T., Squyres, S.W., Thomas, N., Weitz, C.M., 2007. Mars reconnaissance orbiter's high resolution imaging science experiment (HiRISE). *J. Geophys. Res. E Planets* 112, 1–40. doi:10.1029/2005JE002605
- Nye, J.F., Durham, W.B., Schenk, P.M., Moore, J.M., 1999. The stability of a south polar cap on Mars carbon dioxide. doi:10.2172/8347
- Owen, T., Biemann, K., Rushneck, D. R., Biller, J. E., Howarth, D. W., & Lafleur, a. L. (1977). The Composition of the Atmosphere at the Surface of Mars. *Journal of Geophysical Research*, 82(28), 4635–4639. <http://doi.org/10.1029/JS082i028p04635>
- Phillips, R. J., Davis, B. J., Tanaka, K. L., Byrne, S., Mellon, M. T., Putzig, N. E., ... Seu, R. (2011). Massive CO₂ ice deposits sequestered in the south polar layered deposits of Mars. *Science (New York, N.Y.)*, 332(6031), 838–841. <http://doi.org/10.1126/science.1203091>
- Piqueux, S. (2003). Ice Cap and the Formation of Spiders. *Journal of Geophysical Research*, 108(E8), 1–9. <http://doi.org/10.1029/2002JE002007>
- Piqueux, S., Kleinböhl, A., Hayne, P. O., Kass, D. M., Schofield, J. T., McCleese, D. J. (2015). Variability of the martian seasonal CO₂ cap extent over eight Mars Years. *Icarus* 251, 164-180. <http://dx.doi.org/10.1016/j.icarus.2014.10.045>
- Portyankina, G., Markiewicz, W.J., Thomas, N., Hansen, C.J., Milazzo, M. (2010). HiRISE observations of gas sublimation-driven activity in Mars' southern polar regions: III. Models of processes involving translucent ice. *Icarus* 205, 311–320.
- Portyankina, G., Pommerol, A., Aye, K. M., Hansen, C. J., & Thomas, N. (2012). Polygonal cracks in the seasonal semi-translucent CO₂ ice layer in Martian polar areas. *Journal of Geophysical*

Research E: Planets, 117(2), 1–13. <http://doi.org/10.1029/2011JE003917>

Sheehan, W. (1996). *The Planet Mars: A History of Observation and Discovery*. The University of Arizona Press, Tucson. Chapter 3.

Smith, D.E. & Zuber, M.T. (2011). Volumes of the seasonal polar caps of Mars and implications for density. Fourth International Workshop on the Mars Atmosphere: Modelling and Observation (pp. 285-286).

Smith, D. E., Zuber, M. T., & Neumann, G. A. (2001). Seasonal variations of snow depth on Mars. *Science (New York, N.Y.)*, 294(5549), 2141–2146. <http://doi.org/10.1126/science.1066556>

Smith, D. E., Zuber, M. T., Solomon, S. C., Phillips, R. J., Head, J. W., Garvin, J. B., ... Duxbury, T. C. (1999). The global topography of Mars and implications for surface evolution. *Science (New York, N.Y.)*, 284(5419), 1495–1503. <http://doi.org/10.1126/science.284.5419.1495>

Smith, I. B., Spiga, A., & Holt, J. W. (2015). Aeolian processes as drivers of landform evolution at the South Pole of Mars. *Geomorphology*, 240, 54–69. <http://doi.org/10.1016/j.geomorph.2014.08.026>

Tanaka, K., Kolb, E., & Fortezzo, C. (2007). Recent Advances in the Stratigraphy of the Polar Regions of Mars. *LPI Contributions*, 3–6. Retrieved from <http://adsabs.harvard.edu/abs/2007LPICo1353.3276T>

Tanaka, K. L., Skinner, J. a., Dohm, J. M., Irwin, R. P., Kolb, E. J., Fortezzo, C. M., ... Hare, T. M. (2014). Geologic Map of Mars. *U.S. Geological Survey Geologic Investigations*, 3292. <http://doi.org/10.3133/sim3292>

Thomas, N., Portyankina, G., Hansen, C.J., Pommerol, A., 2011. HiRISE observations of gas sublimation-driven activity in Mars' southern polar regions: IV. Fluid dynamics models of CO₂ jets. *Icarus* 212, 66–85. doi:10.1016/j.icarus.2010.12.016

- Thomas, P. C., Calvin, W., Cantor, B., Haberle, R., James, P. B., & Lee, S. W. (2016). Mass balance of Mars' residual south polar cap from CTX images and other data. *Icarus*, *268*, 118–130. <http://doi.org/10.1016/j.icarus.2015.12.038>
- Thomas, P. C., Calvin, W. M., Gierasch, P., Haberle, R., James, P. B., & Sholes, S. (2013). Time scales of erosion and deposition recorded in the residual south polar cap of Mars. *Icarus*, *225*(2), 923–932. <http://doi.org/10.1016/j.icarus.2012.08.038>
- Thomas, P. C., James, P. B., Calvin, W. M., Haberle, R., & Malin, M. C. (2009). Residual south polar cap of Mars: Stratigraphy, history, and implications of recent changes. *Icarus*, *203*(2), 352–375. <http://doi.org/10.1016/j.icarus.2009.05.014>
- Thomas, P. C., Malin, M. C., James, P. B., Cantor, B. A., Williams, R. M. E., & Gierasch, P. (2005). South polar residual cap of Mars: Features, stratigraphy, and changes. *Icarus*, *174*(2 SPEC. ISS.), 535–559. <http://doi.org/10.1016/j.icarus.2004.07.028>
- Titus, T. N., Kieffer, H.H., and Christensen, P.R. (2003). Exposed water ice discovered near the south pole of Mars, 1048(2003). <http://doi.org/10.1126/science.1080497>
- Wolff, M. J. & Clancy, R. T. (2003). Constraints on the size of Martian aerosols from Thermal Emission Spectrometer observations. *Journal of Geophysical Research*, *108*(E9), 5097. <http://doi.org/10.1029/2003JE002057>
- Wolff, M.J., Smith, M.D., Clancy, R.T., Arvidson, R., Kahre, M., Seelos IV, F., Murchie, S., Savijärvi, H. (2009). Wavelength dependence of dust aerosol single scattering albedo as observed by the Compact Reconnaissance Imaging Spectrometer. *Journal of Geophysical Research*, *114*(6), 1-17. doi:10.1029/2009JE003350

*Chapter 5***MARS' SECULAR AMAZONIAN PRESSURE CYCLE, AS BUFFERED BY ITS
SOUTH POLAR CO₂ DEPOSIT****5.1. Introduction**

More than half a century ago, Leighton and Murray (1966) proposed that the martian polar caps were composed entirely of CO₂ in seasonal equilibrium with the atmosphere (which is 96% CO₂; Owen et al., 1977). Over the next few decades others provided evidence that the caps are, in fact, mostly H₂O ice (e.g. Ingersoll, 1974; Nye et al., 2000; Durham et al., 1999; Smith et al., 1999; Byrne and Ingersoll, 2003a ; Titus et al., 2003). While the south polar cap is frosted by a thin layer of perennial CO₂, referred to in this paper as the Residual South Polar Cap (RSPC; a.k.a unit Aa_{4b} (Tanaka et al., 2014)), the mass of RSPC (~1% of the modern martian atmosphere (Thomas et al., 2016)) is insufficient to buffer the atmosphere.

Recently, however, radar observations (Phillips et al., 2011; Bierson et al., 2016) revealed a CO₂ ice deposit with a mass equivalent to the current atmosphere buried under a capping layer of H₂O ice in the martian south polar cap. This discovery rekindles the notion that a large, solid CO₂ reservoir is in equilibrium with the atmosphere, albeit on longer than seasonal timescales. Intriguingly, the buried CO₂ deposit is nearly exactly coincident in planform with the RSPC (Phillips et al., 2011), with the two deposits separated by an intervening boundary layer of H₂O ice that is < 10 m thick (i.e., less than one wavelength of the Shallow Radar instrument used to detect the buried CO₂ (Bierson et al., 2016)). This suggests that the history of the two deposits may be intimately linked.

The possibility that the massive south polar CO₂ deposit is in secular equilibrium with the atmosphere provides the opportunity to characterize the martian pressure cycle throughout the Amazonian period (the past ~3 Ga). The secular pressure cycle is a basic feature of the martian climate and its fluctuations drive other fundamental aspects of the climate, such as the seasonal CO₂ cycle, the H₂O and dust cycles, the stability of liquid H₂O, atmospheric circulation patterns, and loss rates of the atmosphere to space. We therefore explore Mars' secular Amazonian pressure history as a function of its orbital history (Laskar et al., 2004) with an energy-balance model, using observational constraints from the modern CO₂ deposit.

We structure the paper as follows. In Section 5.2, we describe our numerical model. In Section 5.3, we present Mars' secular Amazonian pressure history. In Section 5.4, we discuss our results, their implications for the martian climate, and future avenues of investigation. Finally, we present our conclusions in Section 5.5.

5.2. Numerical Methods

We use a standard 1-dimensional energy-balance model (validated in Buhler et al., 2018) to explore the cycle of CO₂ deposition and sublimation on the surface of H₂O ice overlying a semi-infinite reservoir of buried CO₂ ice and to calculate the amount of energy transmitted to the buried CO₂ ice (Fig. 5.1). The energy-balance model is a surface radiative routine coupled to a subsurface heat conduction routine that solves for the incoming and outgoing power at the surface and the thermal structure of the H₂O ice layer at discrete time-steps. Surface energy balance is calculated at each time-step according to:

$$(5.1) \quad m_f c_p \frac{dT}{dt} = S_0(1 - A) - \epsilon_{CO_2} \sigma_B T^4 + L_{CO_2} \frac{dm_f}{dT} + k \frac{dT}{dz}$$

Here m_f is frost mass, c_p is CO_2 heat capacity, T is temperature, t is time, S_0 is solar normal flux, A is albedo, ϵ_{CO_2} is emissivity, σ_B is the Boltzmann constant, L_{CO_2} is latent heat of CO_2 sublimation, k is thermal conductivity, and z is depth. In this paper, S_0 is the incoming flux at the top of the atmosphere (i.e. atmospheric effects are neglected; discussed in Section 4.3).

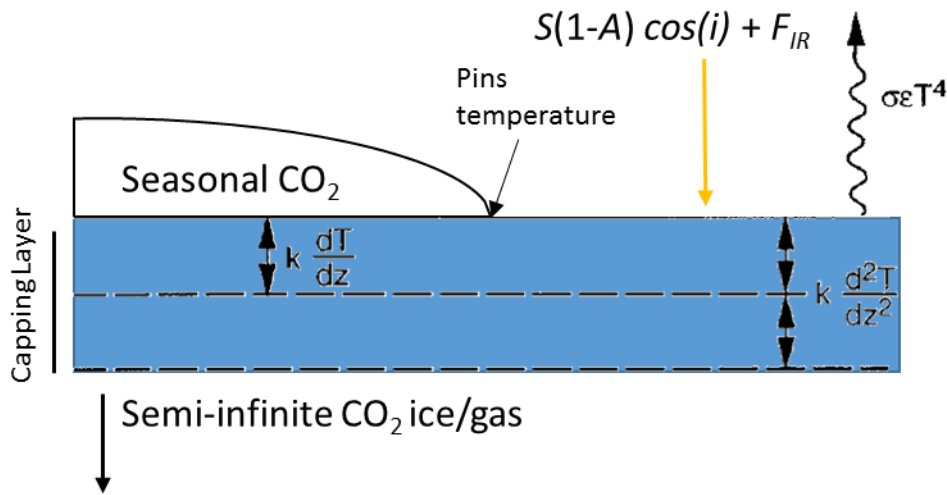


Figure 5.1. Schematic of the 1-d thermal model described in Section 5.2.

Subsurface heat conduction is modeled using an explicit numerical 1-dimensional scheme that solves the diffusion equation with temperature-independent thermal diffusivity at each timestep:

$$(5.2) \quad \frac{dT}{dt} = \frac{k}{\rho c_p} \frac{d^2T}{dz^2}$$

Here ρ is the density of the H_2O ice layer. Throughout the paper we use $c_p = 1400 \text{ J kg}^{-1} \text{ K}^{-1}$, $\rho = 925 \text{ kg m}^{-3}$, and $k = 3.5 \text{ J m}^{-1} \text{ K}^{-1} \text{ s}^{-1}$ (tabulated values; e.g. Giaque and Stout (1936) and Slack

(1980)). We find that, in the calculations of interest in this study, varying these parameters within reasonable bounds does not materially affect the results.

Runs were performed over annual insolation cycles. For all the model results shown here, the model was run to convergence (i.e. the subsurface temperature was identical two years in a row). This typically occurred after 3-4 years.

Condensation (sublimation) of surface CO₂ ice occurs when the surface temperature drops below (rises above) the frost condensation temperature T_{cond} . The model treats this by first calculating the surface energy balance at each time-step, ignoring CO₂ condensation (sublimation). If, after this calculation, the temperature would have dropped below (risen above) T_{cond} , then an amount of CO₂ that balances out that energy deficit (excess) is added to (subtracted from) the inventory of condensed CO₂. T_{cond} is calculated from the atmospheric pressure P (in Pa) using the laboratory-derived empirical relation from Hourdin et al. (1993) (see equation 27 of Pilorget et al. (2011)⁶):

$$(5.3) \quad T(P)_{cond} = \frac{1}{0.00734 - 0.000324 \log(0.01 \times P)}$$

The atmosphere is treated as an infinite reservoir of CO₂ (i.e. the inventory of condensed CO₂ on the ground does not affect the pressure). Conceptually, this approach represents modeling how a small patch of ground responds to a global steady-state climate without the patch itself influencing the climate.

The basal boundary condition (at the interface between the H₂O and the buried CO₂) was set to the CO₂ frost point determined by the atmospheric pressure plus overburden pressure from

⁶ We note that the 0.0734 term in Pilorget et al. (2011) Eq. 27 should read 0.00734.

the H₂O layer, which simulates a buried CO₂ deposit that is sealed off from the atmosphere on seasonal timescales. Using other boundary conditions did not materially change our results (see appendix).

The annual pressure curve is imposed to be a scaling of a polynomial fit to the Viking 1 lander pressure data (Hess et al., 1979). The Viking 1 pressure data was scaled linearly when adjusting the total mass of the atmosphere and exponentially when adjusting for elevation (using the well-known martian atmospheric scale height of 11.1 km). We also performed model runs using a constant value of the mean scaled Viking 1 pressure and find that this does not change the calculated net energy balance by more than ~0.1% as compared to including the Viking 1 pressure variations. This indicates that the seasonal pressure behavior does not have a large effect on the annual calculation and justifies our choice to not explicitly model the global seasonal cycle. Pressure throughout this paper is reported as a scaling fraction of the inventory of CO₂ available for driving the Viking 1 pressure cycle. For succinctness, we refer to this inventory as the modern atmospheric inventory.

Throughout this paper we use a CO₂ albedo A_{CO_2} that is dependent on insolation F_S , following the relationship (Guo et al., 2010):

$$(5.4) \quad A_{CO_2} = 0.532 + 8.72 \times 10^{-4} \times F_S$$

We discuss this choice in Section 5.4.3.

5.3. The Secular Amazonian Pressure Curve

5.3.1 Conceptual Framework and Approach

We model the net annual energy deposition onto a layer of H₂O ice capping a buried CO₂ deposit in the presence of a seasonal CO₂ condensation-sublimation cycle. Net energy deposition is determined by taking the difference between the total annual incoming solar energy and outgoing thermal emission energy (Equation 5.1, Figure 5.2). We find that the net annual energy deposition is ≤ 0 only when CO₂ survives the summer. This is true in all model runs we perform, regardless of the choice of model parameters, as long as $A_{H_2O} < A_{CO_2}$.⁷

This means that, in the presence of a seasonal CO₂ condensation-sublimation cycle, the minimum stability criteria (net energy deposition ≤ 0) for a buried CO₂ deposit beneath a H₂O layer occurs only when the seasonal CO₂ persists annually. This means that the stability of the buried CO₂ is dependent only on the insolation (a function of orbital parameters and latitude) and the properties of the CO₂. Strikingly, the equilibrium solution is thus independent of the presence of the H₂O layer. Therefore there exists a unique solution for equilibrium atmospheric pressure P_{eq} (the pressure for which net energy deposition is zero) for a given set of orbital parameters and CO₂ properties for any location on Mars. This can be written in closed form for the case of a circular orbit:

$$(5.5) \quad \frac{F_{\odot}}{\pi} \cos(\phi - \varepsilon) (1 - A_{CO_2}) = \epsilon_{CO_2} \sigma_B \times T(P)_{cond}^4$$

Here F_{\odot} is the solar constant at Mars, ϕ is latitude, ε is obliquity, A_{CO_2} is the CO₂ albedo, ϵ_{CO_2} is the CO₂ emissivity, and $T(P)_{cond}$ is the pressure-dependent frost condensation temperature (Eq. 5.3). For an eccentric orbit, there is no closed-form solution like Eq. 5.5 because there is no closed-

⁷ This is somewhat surprising given that, in the absence of a seasonal CO₂ frost cycle, the H₂O layer is fairly easily able to protect underlying CO₂. See appendix for details.

form solution relating the mean anomaly to the eccentric anomaly (i.e. Kepler's equation).

Nevertheless, there is still a unique P_{eq} for eccentric orbits because there is a deterministic insolation function for a given orbital configuration. Note that, due to our choice of an insolation-dependent A_{CO_2} (Section 5.2), there is also a deterministic A_{CO_2} for each orbital configuration, so P_{eq} is a unique function of the orbital parameters.

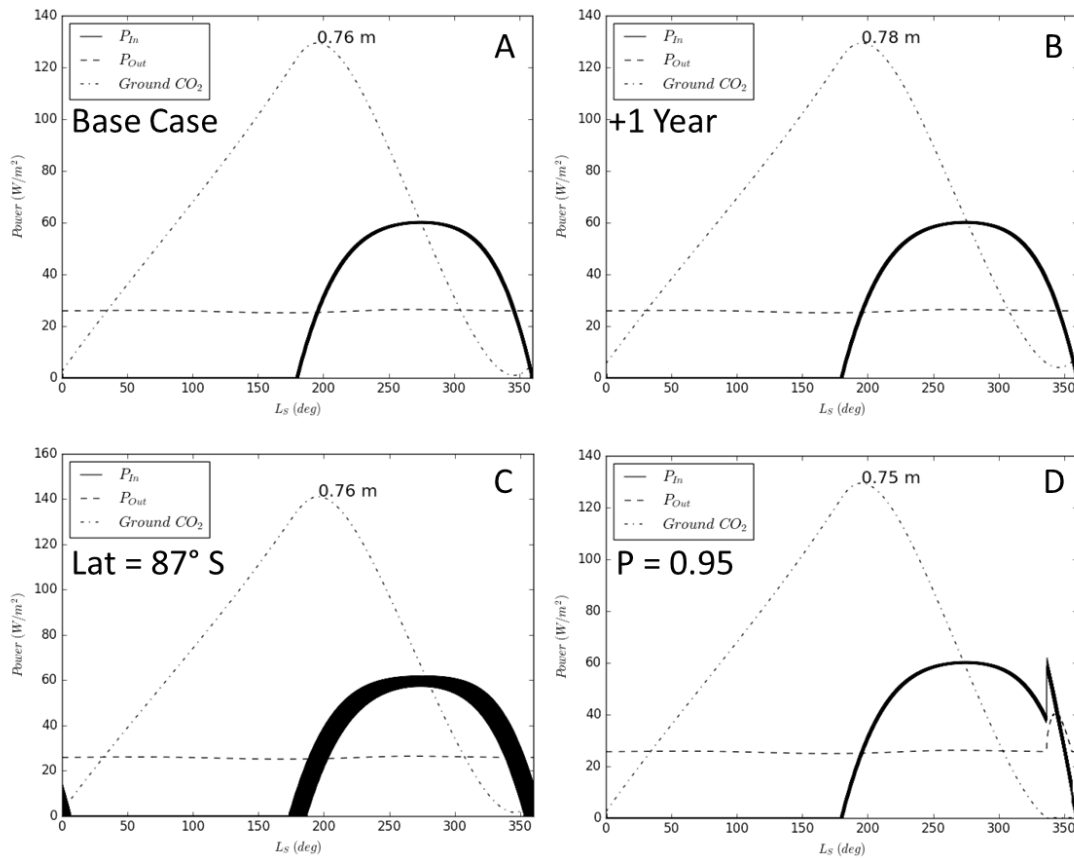


Figure 5.2. 1-d thermal model outputs showing the incoming power (solid), outgoing power (dashed). The thickness of CO_2 on the ground (dash-dot) is normalized to the thickness printed at its peak. L_S is solar longitude. **A.** The base model is the modern orbital configuration ($\epsilon = 25.19^\circ$, $e = 0.0934$, $\varpi = 251^\circ$), $\phi = 89.5$ S, $P = 1.0 \times MAI$, elevation is 4750 m, $\epsilon_{CO_2} = \epsilon_{H_2O} = 1.0$, $A_{H_2O} = 0.4$, A_{CO_2} is determined by Eq. 5. H_2O thickness = 1 m. **B.** The base case run for an additional year after convergence. Note that the CO_2 thickness has increased by 2 cm. **C.** Same as A, but at $\phi = 87.0$ S. Note that CO_2 still persists throughout the year. **D.** Same as A, but with $P = 0.95$, which is below P_{eq} . Note the spike in incoming power at $L_S \sim 330$ when the CO_2 disappears

and the H₂O is exposed and the corresponding rise in outgoing power as the H₂O temperature rises above the frost temperature. The net annual energy deposition is $+3 \times 10^7 \text{ J m}^{-2}$.

Our conceptual framework closely resembles the annually persistent RSPC blanketing the buried CO₂ ice. We therefore confidently proceed to calculate a lookup table of P_{eq} as a function of ε (gridded from 2.5°-80° in 2.5° steps), eccentricity e (0-0.21 in 0.01 steps), and longitude of perihelion ϖ (0°-360° in 15° steps, defined here with respect to the moving equinox). When constructing the lookup table, we fix $\phi = 89.5^\circ \text{ S}$, elevation = 4750 m (values typical of the RSPC), and $\epsilon_{CO_2} = 1$ (e.g. Paige and Ingersoll, 1985). We also perform a model runs at $\phi = 87.0^\circ \text{ S}$, with similar results (e.g Figure 5.2c). We discuss our choice of parameters and the ramifications of our conceptual framework in Section 5.4.

5.3.2 The Equilibrium Pressure as a Function of Orbital Elements

Figure 5.3 shows P_{eq} as a function of ϖ and e for a range of slices in ε . P_{eq} generally increases with increasing e . P_{eq} also generally increases with ε until ε surpasses $\sim 50^\circ$, at which point P_{eq} begins decreasing. The decrease of P_{eq} at high ε occurs because A_{CO_2} is insolation-dependent; we discuss this further in Section 5.4.3. Above $e \approx 0.05$ and $\varepsilon \approx 25^\circ$, P_{eq} increases rapidly when the southern summer solstice approaches perihelion ($\varpi = 270^\circ$), when Mars is closest to the sun and experiences a short, intense southern summer.

We test the success of our lookup table by using it to calculate the expected modern P_{eq} . Interpolating from the lookup table, we find that, under modern orbital conditions ($\varepsilon_{obl} = 25.19^\circ$, $e = 0.0933$, $\varpi = 251^\circ$), the polar CO₂ deposit is in energy balance equilibrium with a CO₂ inventory 0.97 times the mass of the modern atmospheric inventory, validating the model.

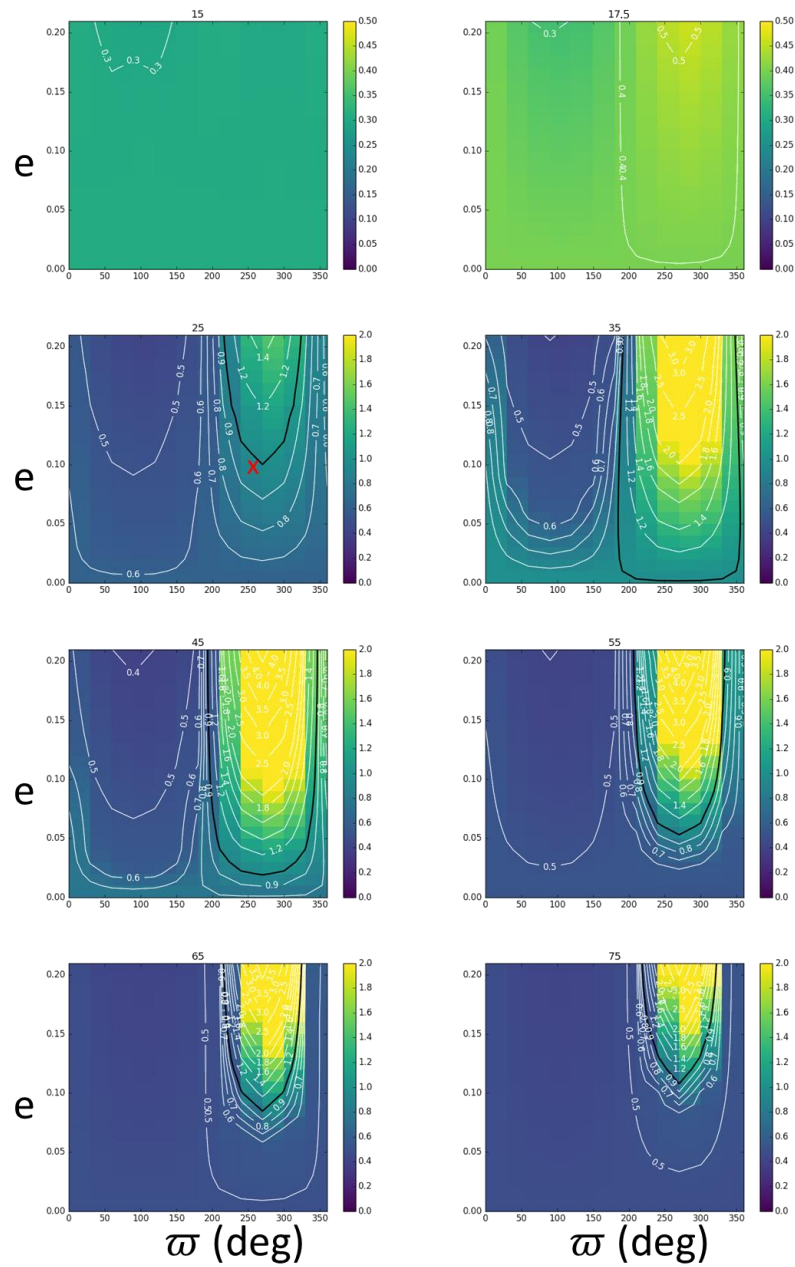


Figure 5.3. The equilibrium pressure P_{eq} solution as a function of e and ϖ for various values of ε (labelled at the top of each panel). Contours and color bars are for P_{eq} given in units of the modern atmospheric inventory. The red x in the $\varepsilon = 25^\circ$ marks the approximate value of the modern orbital configuration (note that $\varepsilon = 25.19^\circ$ in the modern orbit). Note the change in scale for $\varepsilon = 15^\circ$ and 17.5° .

5.3.3 The Pressure History from -21 Ma to +11 Ma

We now reconstruct the equilibrium pressure curve from -21 to +11 Ma by interpolating the equilibrium pressure from our lookup table to the orbital solutions from Laskar et al. (2004) (Figures 5.4, 5.5). The overall shape of the secular pressure curve is characterized by low amplitude, long-wavelength variations superposed by high amplitude, high frequency variations.

This shape occurs because there are two timescales of importance when considering the evolution of the martian orbital elements. The shorter timescale is the circulation time of ϖ , which is ~ 50 kyr. The longer timescale is the Lyapunov time for e and ε , which are both ~ 5 Myr (Laskar and Robutel, 1993; Laskar et al., 2004). Thus, the low amplitude, long-wavelength variations are due to the slow traverse through climate regimes set by the evolution of ε and e (Figure 5.4 a, b). The high frequency variations map to the ~ 50 kyr circulation of ϖ , with the high amplitude due to the rapid increase of P_{eq} when summer solstice occurs near perihelion (Figure 5.3).

It is also interesting to note that the model predicts that Mars is currently in a period where P_{eq} has been increasing at an average rate of approximately $\sim 0.0026\% \text{ yr}^{-1}$ or $\sim 0.02 \text{ Pa yr}^{-1}$ over the past 1 kyr. This implies that the atmosphere may have gained $\sim 0.8 \text{ Pa}$ in the past 42 years since the Viking 1 lander pressure measurements. This is far below the optimistic estimate of $\sim 10 \text{ Pa}$ error given by Haberle et al. (2014) for comparing the pressures measured by Viking 1 and the Mars Science Laboratory and is consistent with their determination of no net change in the atmospheric pressure between Viking 1 and the Mars Science Laboratory measurements.

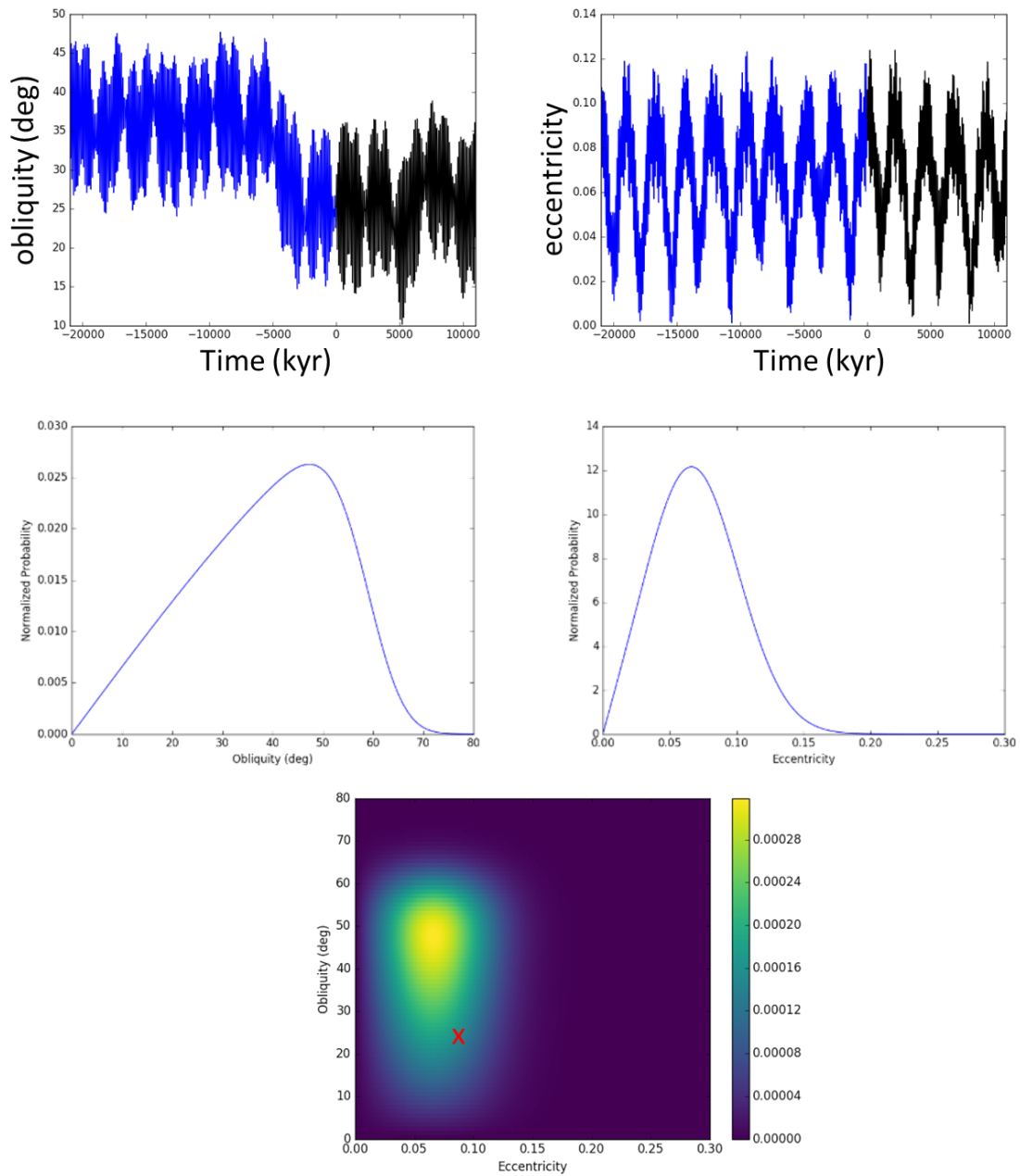


Figure 5.4. Orbital solutions from Laskar et al. (2004). The numerical solutions for the martian **A.** obliquity and **B.** eccentricity from -21 Ma to +11 Ma. Blue shows past values and black shows future values. **C.** The probability distribution of obliquity over 3 Ga. **D.** The same for eccentricity. **E.** The joint probability distribution for obliquity and eccentricity over 3 Ga. The red x marks the value of the modern orbital configuration.

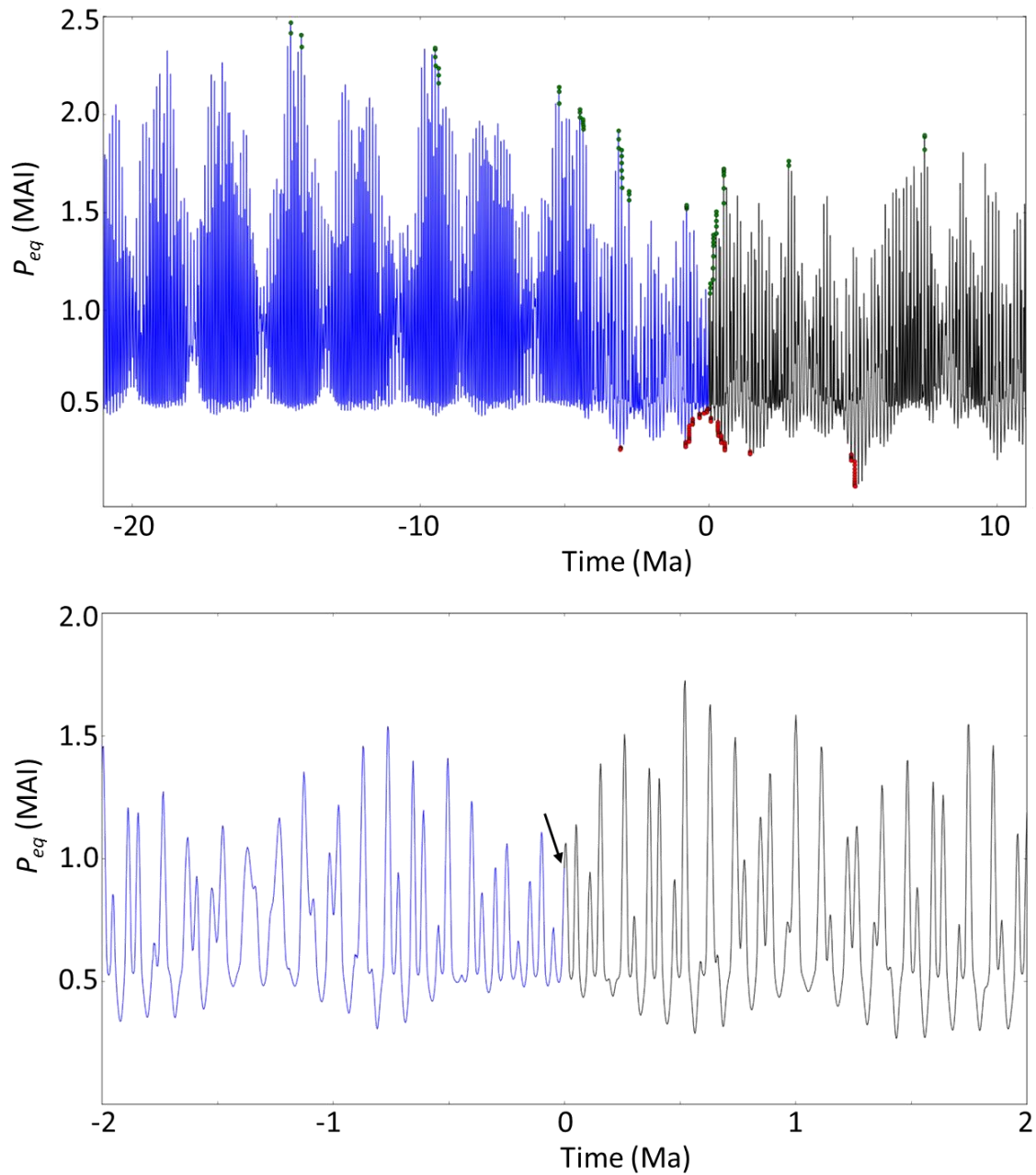


Figure 5.5. The equilibrium pressure solution from **A.** -21 Ma to +11 Ma and **B.** -2 to +2 Ma. Arrow indicates modern day. Blue shows past values and black shows future values. Green (red) points in A. show pressure maxima (minima) that have not been exceeded between their occurrence and the present. The values of the maxima are given in Table 5.1.

5.3.4 The Age of the South Polar CO₂ Deposit

Once P_{eq} exceeds the total martian inventory of CO₂, the south polar CO₂ ice deposit cannot maintain equilibrium with the atmosphere and totally ablate. The most recent time this occurred sets the age of the south polar CO₂ ice deposit

Haberle et al. (2008) and Guo et al. (2009, 2010) estimate that the modern atmospheric inventory is 2.66×10^{16} kg and 2.83×10^{16} kg, respectively. Here we adopt the mean value of 2.75×10^{16} kg for definitiveness. Bierson et al. (2016) calculate that the mass of the buried CO₂ is 2.4×10^{16} kg of CO₂. This implies a total martian inventory of 5.15×10^{16} kg of CO₂, or 1.87 times the modern atmospheric inventory.

Time before present	P_{eq}	P_*
0	0.97	0.89
100 kyr	1.10	1.01
400 kyr	1.23	1.12
500 kyr	1.40	1.28
760 kyr	1.54	1.41
2.8 Myr	1.60	1.46
3.0 Myr	1.82	1.66
3.1 Myr	1.92	1.75
4.4 Myr	1.97	1.80
4.5 Myr	2.03	1.86
5.2 Myr	2.14	1.96
9.4 Myr	2.23	2.04
9.5 Myr	2.34	2.14
14 Myr	2.41	2.20
15 Myr	2.47	2.26

Table 5.1. Timing of pressure maxima that have not been exceeded between their occurrence and the present. P_{eq} are the values from the nominal solution at 4750 m, as plotted in Figure 5.5. P_* are scaled to 3750 m. Pressure values are given in multiples of modern atmospheric inventory.

P_{eq} maxima are shown in Figure 5.5 and listed in Table 5.1. Before proceeding, we note that the base of the CO₂ deposit is ~1 km lower than the modern RSPC (Bierson et al., 2016). Therefore we scale the maxima of the P_{eq} obtained from our model run at 4750 m (the top of the deposit) to find the elevation-corrected equilibrium pressure P_* according to $P_* = P_{eq}/(\exp(-z/H))$, where z is -1 km, and H is the martian atmospheric scale height (11.1 km).

The last time the equilibrium pressure exceeded 1.87 times the modern atmospheric inventory was 5.2 yra ago. However, we note that the mass of the buried CO₂ deposit is not well constrained because radar coverage is not available over its full extent and thus the Bierson et al. (2016) estimate relies on extrapolation to areas not covered by radar. Additionally, our model fit to the modern atmospheric inventory, while excellent, also differs by ~3% from the pressure measured by the Viking 1 lander. Nevertheless, if the estimate of the buried CO₂ is overestimated by a factor of ~2 the polar CO₂ deposit would still survive the P_{eq} maximum at 2.8 Myr and thus have last been ablated at the 3.0 Myr P_{eq} maximum. On the other hand, if the buried CO₂ is underestimated by ~6%, the polar CO₂ deposit would have survived the P_{eq} maximum at 5.2 Myr and thus have persisted since the 9.4 Myr P_{eq} maximum. These estimates are also much longer than the few $\times 10^5$ yr age estimated by Bierson et al. (2016), probably because they focus on variations in ε and do not consider the variation of ϖ .

Notably, these timescales are comparable to the south polar layered deposit impact crater age date of 14.5 ± 7.2 Myr (for a nominal impactor flux or 7.25 ± 3.6 Myr for a high impactor flux (Herkenhoff and Plaut, 2000)). This may indicate that the persistence of the buried CO₂ deposit has helped to stabilize the south polar layered deposits through climate regimes in which the

north polar layered deposits were destroyed. This may be key to understanding the longstanding mystery of why the south polar layered deposits are much older than the ~100 kyr north polar layered deposits (Herkenhoff and Plaut, 2000).

5.3.5 Pressure Characterization over 3 Ga

On long timescales, the martian orbit is chaotic, so it is not possible to reconstruct a unique solution for P_{eq} . However, the chaotic evolution creates a smooth probability distribution for e and ε (equations 13 and 23 of Laskar et al., 2004; Figure 5.4c-e) that we use to statistically characterize P_{eq} over the past 3 Gyr (the Amazonian). Note that the evolution of e and ε is not coupled (e.g. Box 1 of Laskar and Robutel, 1993), so their probability distributions can be treated independently to create a joint probability distribution (Figure 5.4e). Additionally, on timescales much longer than the ~50 kyr circulation of ϖ , we may treat ϖ as uniformly randomized with respect to e and ε .

We first examine the behavior of P_{eq} as a function of e and ε normalized over ϖ (Figure 5.6) to understand martian P_{eq} regimes. Conceptually, these regimes are characteristic P_{eq} behavior during climate epochs in which ε and e remain generally near the same value. These epochs last approximately ~1-2 Myr (related to the ~5 Ma Lyapunov time); this timescale can be seen by inspecting Figures 5.4a-b and 5.5. During residence in a particular climate epoch, ϖ will cycle many (several tens of) times, sampling near the minimum and maximum P_{eq} values of the P_{eq} regime characteristic of that epoch.

Three fundamental P_{eq} regimes emerge. The first (low- P_{eq}) regime occurs for pressures below 0.4 times the modern atmospheric inventory (MAI, Figure 5.6a). P_{eq} exceeds $0.4 \times \text{MAI}$ for almost

all e - ε pairings when $\varepsilon > \sim 20^\circ$, so these do not have access to this regime. When $\varepsilon < 20^\circ$, P_{eq} is dependent almost exclusively on ε and decreases with decreasing ε (e.g. Figure 5.3a-b).

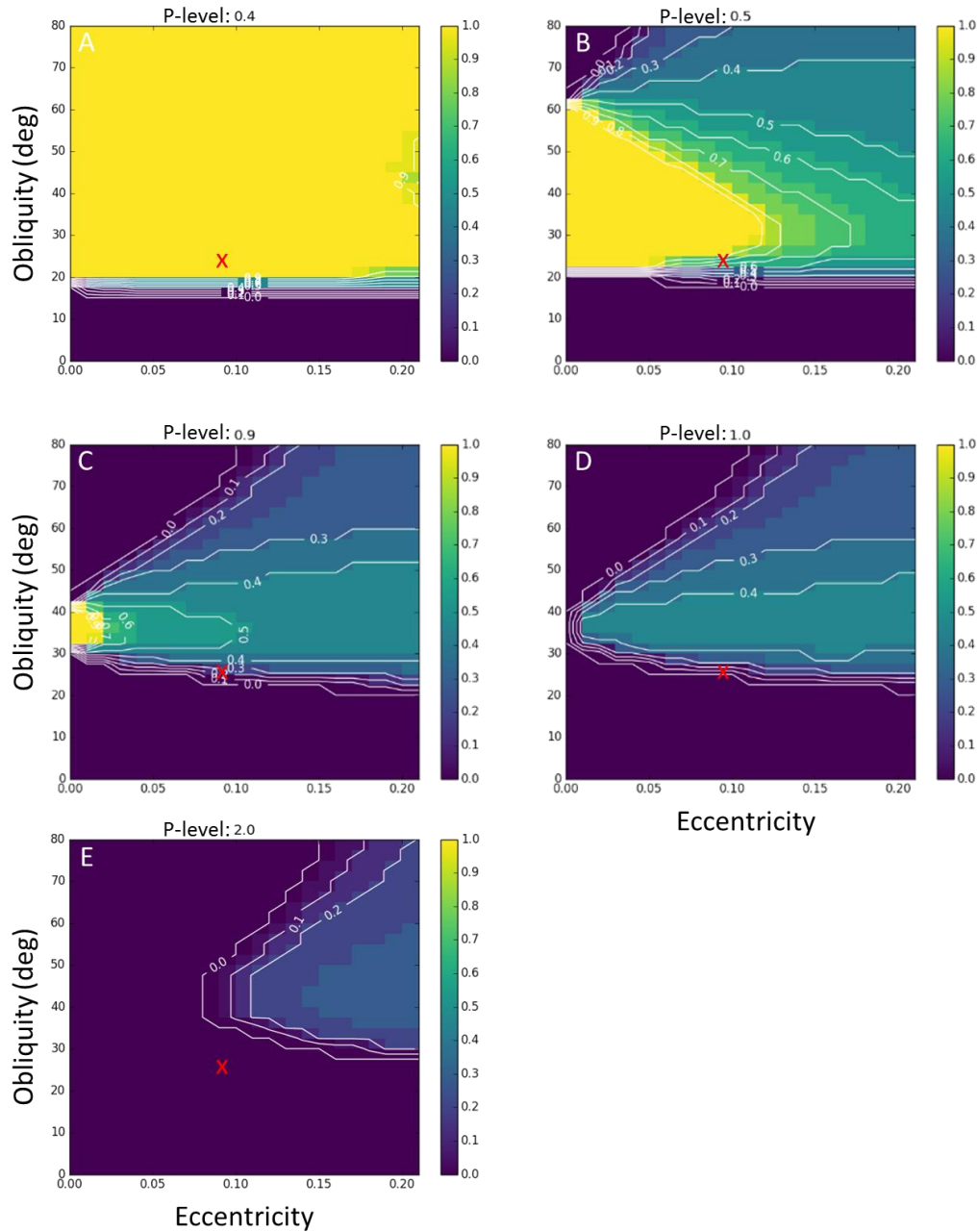


Figure 5.6. Panels show the fraction of ϖ values for which P_{eq} exceeds a particular pressure for the given e - ε pairing (labeled at the top of each panel). The red x's mark the value of the modern orbital configuration.

The second (mid- P_{eq}) regime occurs for $0.4 < P_{eq} < 1.0 \times \text{MAI}$ (Figure 5.6b-c). Moderate- ε , moderate-to-low- e orbits are in this P_{eq} range for most values of ϖ and all orbits with $\sim 20^\circ < \varepsilon < \sim 65^\circ$ have access to this range for at least some values of ϖ (compare Figure 5.6b and d).

The third (high- P_{eq}) regime occurs for $P_{eq} > 1.0 \times \text{MAI}$ (Figure 5.6d-e). All e - ε pairs with $\sim 30^\circ < \varepsilon < \sim 40^\circ$ have access to this range for at least some values of ϖ , and roughly half of all ϖ configurations for these pairs lie in this regime. Many configurations with $\varepsilon < \sim 40^\circ$ also have access to this regime for at least some values of ϖ , although this access drops off with decreasing e . Access to this high- P_{eq} regime occurs when southern summer solstice nears perihelion (see Figure 5.3).

We now examine three climatic characteristics of interest: the probability of Mars at particular instantaneous P_{eq} , and the probability of being in a climate epoch characterized by a particular minimum or maximum pressure (Figure 5.7). For the probability of observing a particular instantaneous P_{eq} , we multiply the ϖ -normalized P_{eq} distribution in e - ε phase space by joint e - ε probability distribution. For the probability of being in a climate epoch characterized by a particular minimum (maximum) P_{eq} , we multiply the distribution of the minimum (maximum) P_{eq} reached for each e - ε by the joint e - ε probability distribution.

The instantaneous P_{eq} distribution (Figure 5.7a) is strongly peaked around 0.4 - $1.0 \times \text{MAI}$ because this mid- P_{eq} regime is accessible to most moderate- ε , moderate-to-low- e orbits, at the peak of the joint e - ε probability distribution. There is a sharp drop off in the probability of instantaneous $P_{eq} < 0.4 \times \text{MAI}$ because these P_{eq} are only accessible to orbital configurations with $\varepsilon < \sim 20^\circ$, which lie off the peak of the joint e - ε probability distribution. The probability of instantaneous $P_{eq} > 1.0$

× MAI drops off slowly because these states become more probable at progressively higher e (Figure 5.6d) and the probability of reaching higher e drops off with an extended tail (Figure 5.4d).

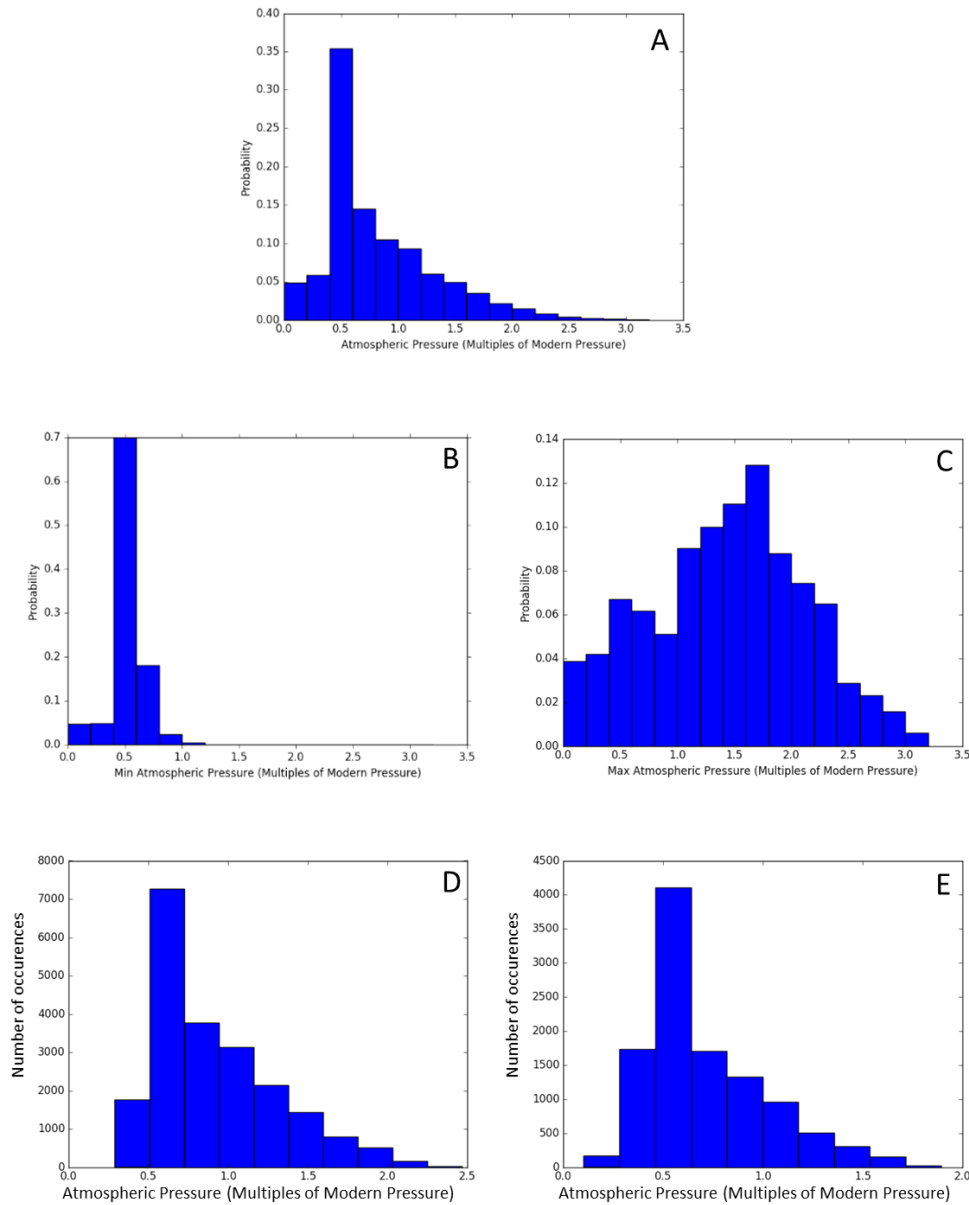


Figure 5.7. **A.** The probability distribution of instantaneous P_{eq} values over 3 Ga. **B.** The probability distribution of climate epochs with particular minimum values of P_{eq} . **C.** The probability distribution of climate epochs with particular maximum values of P_{eq} . **D.** The distribution of instantaneous P_{eq} values over the past 21 Ma. **E.** The distribution of instantaneous P_{eq} values over the coming 11 Ma.

The probability of being in a climate epoch characterized by a particular minimum P_{eq} is tight and sharply peaked. Most climate epochs do not frequently reach P_{eq} below $0.4 \times \text{MAI}$ because these low P_{eq} only occur when $\varepsilon < \sim 20^\circ$, as discussed. On the other hand, the probability of being in a climate epoch characterized by a particular maximum P_{eq} is much broader due to the sensitive behavior of P_{eq} when southern summer occurs near perihelion. Together, these two distributions create the flat-bottomed, stochastically peaked distribution of P_{eq} apparent in Figure 5.5, particularly beyond ~ 5 Myr ago, when ε was near 45° (Figure 5.4). Now that the average ε is near 20° , P_{eq} minima are beginning to sample below $0.4 \times \text{MAI}$. The P_{eq} distribution between -21 Myr and +11 Myr (Figure 5.7d-e) appear typical of the distribution 3 Ga P_{eq} distribution.

Finally, the probability of being in a climate epoch characterized by a maximum P_{eq} greater than the total inventory of martian CO_2 ($1.87 \times \text{MAI}$) is 24%. Thus we may estimate that approximately every four Lyapunov times, or ~ 20 Myr, P_{eq} will overcome the capacity of martian CO_2 inventory and the south polar CO_2 deposits will completely ablate.

5.4. Discussion

5.4.1 Self-Stabilization of the RSPC-Buried CO_2 System

In Section 5.3.1 we found that the south polar CO_2 deposit is in equilibrium with the atmosphere only when exposed surface CO_2 persists throughout the year. We now explore the consequence of this stability criterion as the martian orbit evolves.

The martian orbit can evolve either toward decreasing solar power or increasing solar power absorbed at the south pole. If absorbed solar power is decreasing, then the CO₂ frost temperature decreases to keep the thermally emitted power in parity, which lowers P_{eq} and thus CO₂ condenses onto the surface deposit to lower the atmospheric pressure. During deposition, impurities (e.g. H₂O and dust) will inevitably be incorporated into the growing deposit (cf. Haberle and Jakosky, 1990). The surface CO₂ deposit is now a thick, exposed dollop of CO₂ with some impurities.

Now consider the case when absorbed solar power is increasing. The CO₂ frost temperature decreases to keep the thermally emitted power in parity with the increasing absorbed power, which raises P_{eq} and thus CO₂ sublimates from the top of the surface deposit to raise the atmospheric pressure. As the CO₂ sublimates, the impurities are left behind to form a lag deposit on its upper surface. However, because P_{eq} is slowly changing, the system is only slightly out of equilibrium. Therefore, most of the CO₂ exchanging from the top of the CO₂ deposit is seasonal CO₂ deposited that year and only a small amount of old CO₂ is lost. Additionally, this old CO₂ is lost only at the very end of summer, so the lag left behind from this old CO₂ is almost immediately buried under new seasonal CO₂. The following year, P_{eq} has increased again, so the buried CO₂ again loses slightly more CO₂ than it gained during winter. A little more lag builds up, but again only at the very end of summer, so it is again almost immediately buried by new seasonal CO₂ deposition.

Even though the newly formed lag deposit we have just imagined is thin, it is conceptually equivalent to a thick lag deposit, so long as the buried CO₂ deposit can communicate with the atmosphere on short timescales ($< 10^4$ yr, the timescale of ϖ circulation). Thus, the presence of the RSPC with net-neutral mass balance (as observed by Thomas et al., 2016) separated from the

main deposit by a thin lag layer is the natural outcome of a CO₂ deposit (that contains some impurities) evolving in equilibrium with the atmosphere.

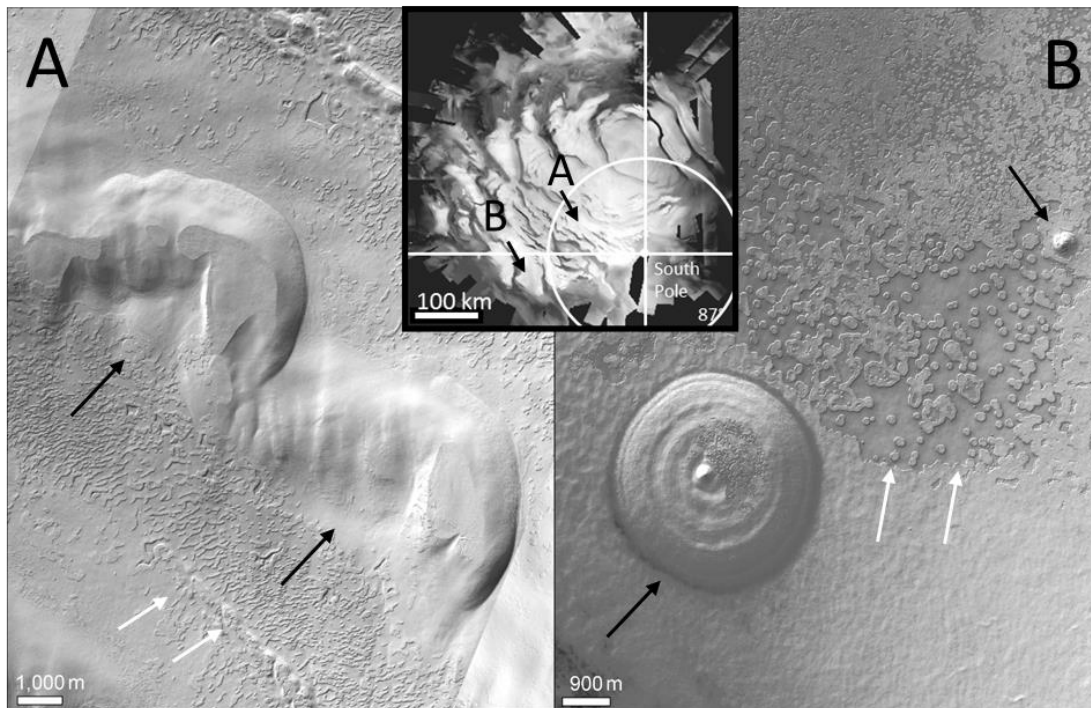


Figure 5.8. Black arrows show large amphitheater (left) and circular (right) depressions on the surface of the martian south polar H₂O ice cap. White arrows indicate mesas and smaller pits and troughs in the CO₂ south polar residual cap.

We note that the exchange of CO₂ from the buried CO₂ to the atmosphere could occur with spatial or temporal inhomogeneity, or both. Spatial inhomogeneity could mean, for example, lateral gas flow to cracks or other areas of weakness (slow, annual leaking). Temporal inhomogeneity could mean, for example, the buildup of pressurized gas beneath the H₂O layer leading to sporadic, explosive releases. Either way, kilometer-scale pits, troughs, and depressions in the H₂O ice layer between the RSPC and the buried CO₂ deposit are compelling evidence that

mass is being lost from the buried CO₂ deposit to the atmosphere (Figure 5.8; see also Phillips et al., 2011).

Nevertheless, we may consider the fate of a buried CO₂ deposit sealed off from the atmosphere. Now if the orbit is evolving such that absorbed solar power is increasing, the P_{eq} will continue to increase, as before, so at the end of summer the H₂O layer will be exposed and there will be net positive energy deposition. The only ways available to balance the energy budget are either to release latent heat by sublimating some of the H₂O ice or by conducting energy to the sealed CO₂ deposit. Either option is unsustainable. In the first case, the H₂O layer will be destroyed, potentially at a rate of centimeters or tens of centimeters per year depending on the annual insolation (e.g. Jakosky et al., 1995). In the second case, the entombed CO₂ will sublime, pressurizing until the H₂O layer eventually ruptures. Meanwhile, P_{eq} is continuing to rise, so less seasonal CO₂ is deposited, exposing the H₂O for longer and longer each year, progressively increasing the rate of energy deposition. Clearly, in this scenario, there will be no RSPC. Thus, the presence of the RSPC is a strong indicator that the buried CO₂ deposit is not sealed off from the atmosphere.

For completeness, we note that long-term changes in frost properties could provide an alternative explanation for the presence of an RSPC in the case of a sealed buried CO₂ deposit. For example, the albedo may have changed to match the P_{eq} instead of P_{eq} evolving to match a persistent albedo. This could occur, for example, if the mode of deposition (e.g. snowfall properties) have changed in time in response to a changing climate. However, this hypothesis is less satisfying because it involves a serendipitous response of CO₂ properties to P_{eq} .

5.4.2 Second Order Characteristics of the RSPC

The RSPC consists of 1-10 m-thick mesas of CO₂ ice with morphologies that quasi-stably persist from year to year, with inter-mesa regions in which CO₂ does not persist annually (e.g. Buhler et al., 2017). At first, this description of the RSPC seems different from a seasonal deposit that barely persists throughout the year, as we have been discussing. However, the spatial inhomogeneity of the RSPC and the existence of stable 1-10 m deposits can be understood if the atmospheric pressure is slightly higher than P_{eq} and there is a mechanism to make holes in RSPC.

If the pressure is slightly higher than P_{eq} , then the RSPC will thicken (Section 5.4.1). A model run using modern parameters, using $1.0 \times \text{MAI}$ atmospheric pressure shows that the RSPC should thicken by $\sim 2 \text{ cm yr}^{-1}$ (recall that our model finds equilibrium at $0.97 \times \text{MAI}$). A thickening rate on the order of a few cm yr^{-1} is consistent with the estimates of vertical change in the RSPC made by Thomas et al. (2016). Of course, the RSPC is riddled with pits that form when the surface of the RSPC collapses (Buhler et al., 2017). The spatial frequency of pits and their lateral erosion rate act together to erode the entire RSPC on the timescale of decades to centuries (Byrne and Ingersoll, 2003; Thomas et al., 2016). Thus, a deposit thickening at a rate of a few cm yr^{-1} will characteristically thicken to $\sim 1\text{-}10 \text{ m}$ before being destroyed laterally. Moreover, once pits erode down to the H₂O layer, there is some delay before these bare regions are again covered by CO₂ that survives the summer (e.g. Thomas et al. 2005; Buhler et al., 2017). During this delay time there will be net positive energy deposition onto these bare spots, destabilizing the underlying buried CO₂, which will act to maintain the pressure slightly above the nominal P_{eq} for a RSPC without holes. Although a RSPC with holes in it represents a different hysteresis state than a RSPC without holes and violates our assertion in Section 5.3.1 that there is a single P_{eq} for each orbital

state, the decadal timescales on which the RSPC morphology apparently cycles means that the effect this hysteresis has on P_{eq} is small.

5.4.3 Future Modeling and Assumptions

Our simple model predicts the modern P_{eq} surprisingly accurately. However, there are potential complexities to our simple framework that bear further discussion. For example, we ignore the effect of the atmosphere and snowfall, both of which will change the details of the energy balance model. However, given the success of our simple model, we defer an investigation of these processes to a later investigation.

Our two largest overarching assumptions are that the RSPC is a special region of deposition and that the albedo is insolation dependent and persistently follows the same insolation dependency throughout the Amazonian.

The RSPC is indeed a special location because of its high albedo, which surpasses that of the north polar seasonal CO₂ deposits by ~25% (e.g. Paige and Ingersoll, 1985). This high albedo is likely set by its high proportion of deposition by snowfall, which is ultimately set by topographic effects that drive weather systems in the modern climate (Colaprete et al., 2005). It is possible that, under different climate (orbital) regimes, these weather patterns could change and this should be investigated. However, the existence of the buried CO₂ deposit in this location indicates that is a special region of CO₂ deposition over secular timescales, suggesting that the polar weather pattern found by Colaprete et al. (2005) is persistent across a wide range of climate regimes.

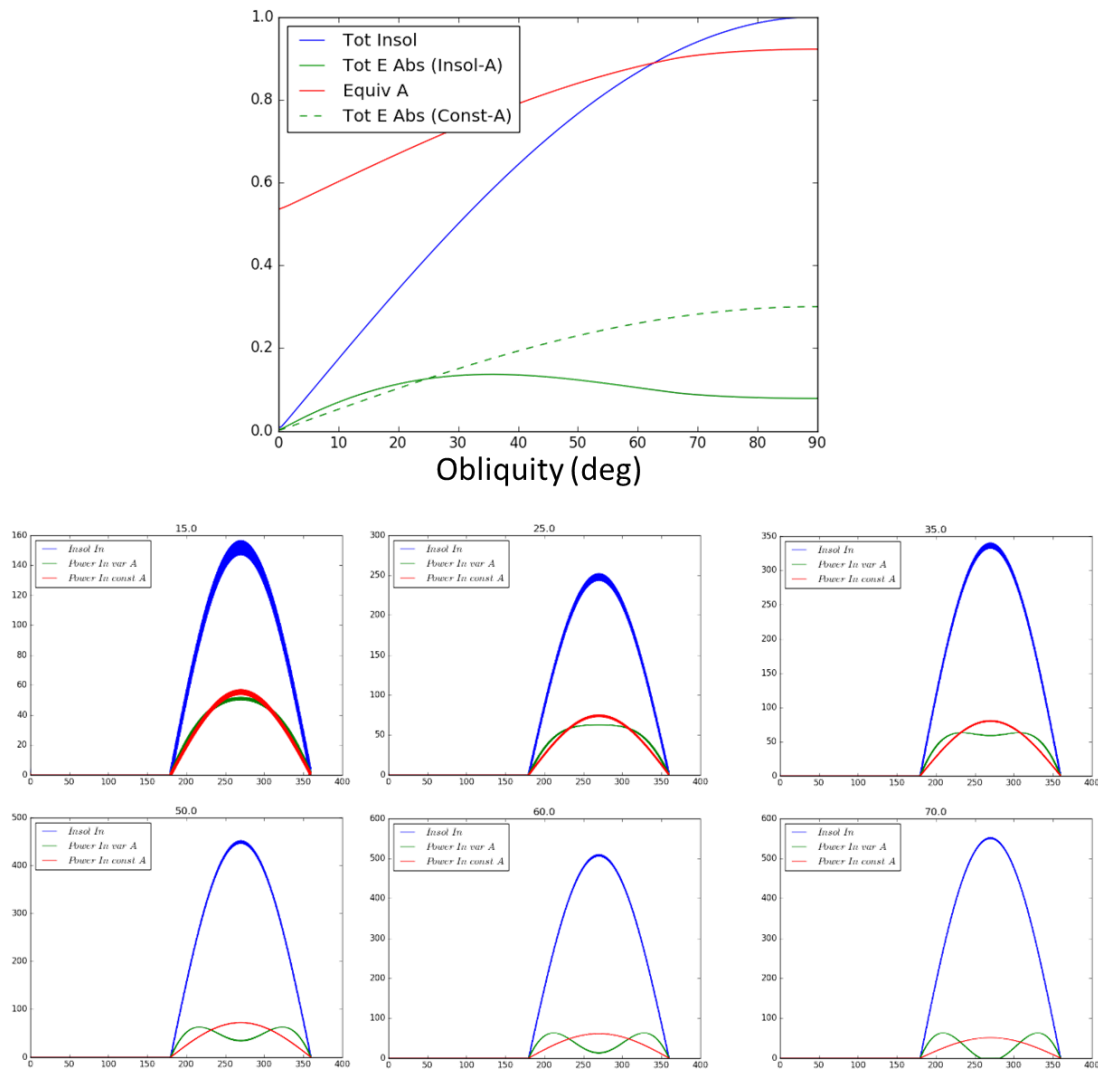


Figure 5.9. Top. Normalized total annual incident insolation (blue), normalized total absorbed insolation based on Eq. 5.5 (green) and the fraction of reflected insolation (red) as a function of obliquity. The dashed green line shows the total energy absorption for constant-albedo CO_2 matched to the equivalent constant albedo for the insolation-dependent albedo function. Solutions are for a circular orbit at various obliquities. Note the much smaller energy deposition for the insolation-dependent albedo case than for the constant albedo case. **Bottom panels.** Annual curve of the incident insolation (blue) and absorbed insolation based on Eq. 5.5 (green) and the equivalent annual average albedo (red) for various obliquities. A prior is imposed such that ACO_2 never surpasses a value of unity.

The assumption of an insolation-dependent albedo has a damping effect on the P_{eq} solutions as compared to the assumption of a constant, insolation-independent albedo (Figure 5.9). Although the mechanism for the insolation-dependence is unknown, our use of it is justified by the consistent observation that it occurs (e.g. Paige and Ingersoll, 1985; Guo et al., 2010). It is also unclear whether the albedo is actually insolation dependent or whether it is incidence-angle dependent because it has only been observed under modern orbital configurations. If the albedo is actually dependent on the incidence angle then it will not be as effective at reflecting sunlight at higher values of the solar constant at Mars (i.e. when Mars is closer to the sun, as occurs for perihelion at high e). Thus, the P_{eq} solutions will rise (fall) for higher (lower) values of the solar constant at Mars. Additionally, the exact relationship between insolation and albedo may not hold for very high values of insolation, for example at values of insolation above 537 W m^{-2} , where Eq. 5.5 predicts $A_{CO_2} > 1$. Nevertheless, Eq. 5.5 is the best description available for A_{CO_2} , although an improved theoretical and laboratory understanding of the insolation-dependent albedo phenomenon for CO_2 is clearly desirable.

5.5. Conclusions

We show that the south polar CO_2 deposits are in secular equilibrium with the atmosphere and extend a conceptual framework describing their evolution. This conceptual framework explains the presence of the residual south polar cap (RSPC) and shows that the RSPC is the natural consequence of a CO_2 deposit that contains impurities evolving through a climate characterized by rising pressure. We also demonstrate that the H_2O layer separating the RSPC and the buried

CO₂ is inconsequential for the energy balance of the CO₂ deposit, but rather only the annual insolation and CO₂ frost properties are important. Therefore, there is a unique equilibrium pressure for the martian atmosphere for every orbital configuration, except for a small hysteresis effect that occurs because the RSPC is spatially nonuniform.

We then calculate the equilibrium pressure as a function of obliquity, eccentricity, and longitude of perihelion with respect to the moving equinox using an energy balance model. Using these solutions, we reconstruct the equilibrium pressure solution from -21 Myr to +11 Myr and statistically characterize the equilibrium pressure states over the past 3 Gyr based on the Laskar et al. (2004) orbital solution. Our model predicts an equilibrium of 0.97 times the modern atmosphere for the modern orbital configuration, which is excellent agreement for such a simple model. The pressure solution shows that Mars is currently in a period of increasing pressure, at a rate of $\sim 0.02 \text{ Pa yr}^{-1}$.

Finally, the most recent time the equilibrium pressure exceeded the capacity of the entire martian CO₂ inventory was 5.2 Myr ago, which sets the age of the polar CO₂ deposit. Notably, this timescale is similar to the crater-age date of the south polar layer deposits (SPLD), suggesting that the polar CO₂ deposits play an important role in stabilizing the SPLD.

5.6 Appendix. The Effect of an H₂O Ice Cap on Buried CO₂ Ice

In order to isolate and understand the effect of a capping layer of H₂O ice on the energy balance of underlying CO₂ ice, we consider a simplified model setup. In this simplified setup, a circular orbit is imposed and seasonal frost buildup is ignored (equivalently, the no mass is added to the condensed inventory of CO₂ ice). This means that the wintertime temperature is set to the pressure-dependent frost point, but latent heat of the CO₂ phase change is ignored (the third term

on the right-hand side of Eq. 5.1). Essentially, this means that the temperature immediately begins to rise above the frost point as soon as the sun comes above the horizon at the beginning of spring (Figure 5.A1). We test the net annual energy balance of this setup under a range of pressures, latitudes, obliquities, H₂O ice thicknesses, and H₂O ice albedos (Figures 5.A2 and 5.A3). Note that the CO₂ ice albedo is not relevant in this simple case because CO₂ is not present when the sun is above the horizon.

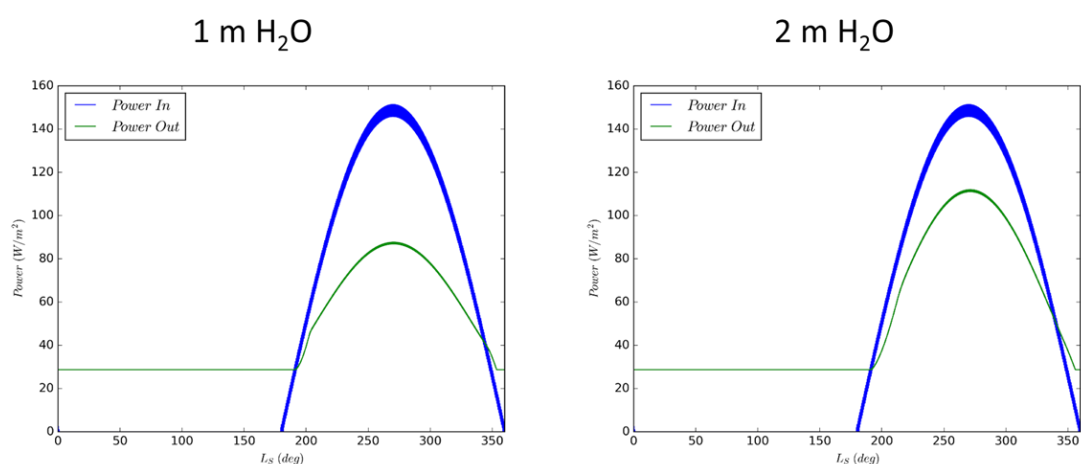


Figure 5.A1. Incoming solar power and outgoing emitted power for a semi-infinite reservoir of CO₂ ice sealed by a layer of H₂O ice under modern conditions at 89.5° S. Note the difference in outgoing power during the summer ($\sim L_s$ 180-360). Note also that the power out during the winter ($\sim L_s$ 0-180) is nonzero and determined by the pressure-dependent condensation temperature. H₂O albedo is set to 0.4. Left: H₂O thickness is 1 m. Right: H₂O thickness is 2 m.

We also test the model under two lower boundary conditions (at the interface between the H₂O and the buried CO₂). In the first case (Figure 5.A2a), the lower boundary temperature condition is set to the frost point determined by the atmospheric pressure alone, which simulates a buried CO₂ deposit that is in communication with the atmosphere (i.e. the H₂O ice layer is permeable to CO₂ gas on seasonal timescales, e.g. through cracks). In the second case (Figure 5.A2b), the lower

boundary temperature condition is set to the frost point determined by the atmospheric pressure plus overburden pressure from the H₂O layer, which simulates a buried CO₂ deposit that is sealed off from the atmosphere on seasonal timescales.

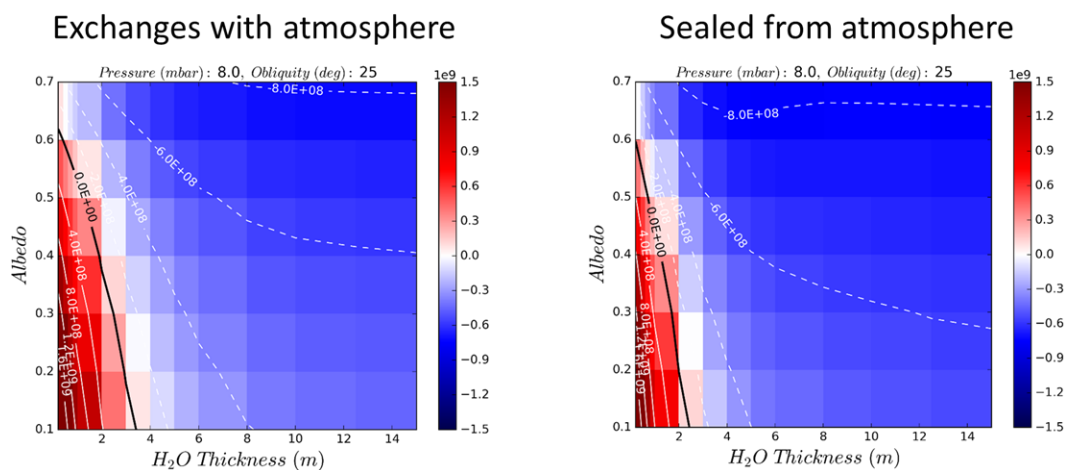


Figure 5.A2. Net annual energy balance for a semi-infinite reservoir of CO₂ ice under a layer of H₂O ice for modern conditions [circular orbit imposed] at 89.5° S. Left: CO₂ in exchange with atmosphere. Right: CO₂ is sealed off from atmosphere. Color bar is in 10⁹ J m⁻¹ per Mars year.

The net energy balance of each model run is determined by taking the difference between the total annual incoming solar energy and outgoing thermal emission energy. Figure 5.A1 shows the annual incoming solar power and outgoing thermal power for two thicknesses of capping H₂O ice under identical, approximately modern conditions (Pressure $P = 8.0$ mbar, obliquity $\varepsilon = 25^\circ$, latitude = 89.5° S, H₂O albedo $A_{H_2O} = 0.4$) and lower boundary condition set assuming that the buried CO₂ is sealed off from the atmosphere. The general shape of the curves is typical of all model runs. Figure 5.A2 shows the net annual energy for model runs a range of H₂O ice thicknesses and albedos under the same conditions as Figure 5.A1. The run with an H₂O thickness

of 1 m (Figure 5.A1a) has net positive annual energy balance, while the run with an H₂O thickness of 2 m (Figure 5.A1b) has net negative annual energy balance.

It may initially seem paradoxical that an overlying layer of H₂O, which has a lower albedo than CO₂ and can stably reach temperatures >100 K higher than the CO₂ frost point, could stabilize underlying CO₂. However, this can be understood by considering the following inequality describing the radiative surface energy balance:

$$(5.6) \quad S_0(1 - A_{H_2O}) - \epsilon\sigma_B T_{H_2O}^4 < S_0(1 - A_{CO_2}) - \epsilon\sigma_B T_{CO_2}^4$$

The left-hand side is the net power received by a surface of H₂O ice (incoming solar power minus outgoing thermal emission); the right-hand side is for a surface of CO₂ ice. There are two competing effects determining whether the net energy balance is lower for a surface of CO₂ ice or for H₂O ice. The lower albedo of H₂O ice compared to CO₂ (~0.4 vs ~0.7, e.g. Byrne et al., 2008) increases the energy absorbed and transferred to underlying CO₂. However, the fact that the H₂O temperature can rise above the CO₂ frost point increases the outgoing flux and thus decreases the amount of energy conducted to underlying CO₂. This effect is particularly powerful because outgoing flux is proportional to temperature to the fourth power.

Comparing the larger magnitude of the summertime outgoing thermal power in the 2-m-thick run versus the 1-m-thick run illustrates the importance of this effect. In the 2-m-thick case, the surface is further from the interface with buried CO₂, is thus not as strongly affected by the cold (CO₂ frost-point) basal boundary condition, and so can rise to higher temperatures (and emit more power) than in the 1-m-thick case. An equivalent way to conceptualize this is that the 1-m-thick case is less stable because heat is conducted more quickly down to the underlying CO₂ ice because the H₂O layer is thinner.

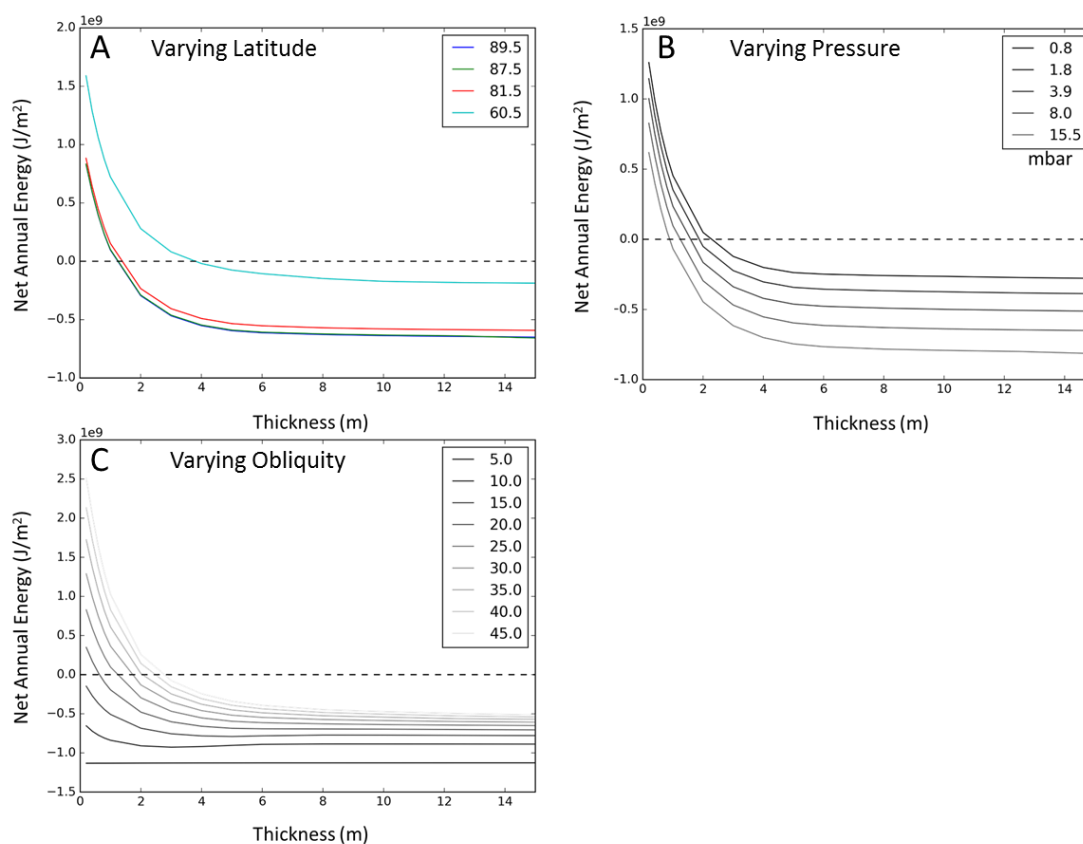


Figure 5.A3. Net annual deposited energy balance for a semi-infinite reservoir of CO₂ ice sealed under a layer of H₂O ice for modern conditions at various A. latitude (units in deg), B. pressures (units in mbar) at 89.5° S, and C. obliquities (units in deg) at 89.5° S.

The inequality in Eq. 5.6 elucidates the pattern of stability in albedo vs. H₂O-thickness phase space (Figure 5.A2). Increasing the albedo of the H₂O ice decreases the amount of absorbed incoming power and increasing the thickness of the H₂O ice allows summertime temperatures to rise higher, increasing the emitted thermal power. Both of these effects lead to lower net annual energy balance.

The differences between the net annual energy balance using different basal boundary conditions (Figure 5.A2) can also be understood in this framework. The basal temperature

boundary condition is higher in the case representing the buried CO₂ sealed off from the atmosphere than in the case representing the buried CO₂ in communication with the atmosphere. This is because of the increased pressure arising from including the overburden pressure of the H₂O ice in the sealed case, meaning that the equilibrium frost-point temperature is higher. The higher temperature of the basal boundary condition in the sealed case means that the summertime surface temperature can rise higher for an equivalently thick H₂O ice layer, increasing the emitted thermal power and leading to lower net annual energy balance. This can be equivalently conceptualized as the buried CO₂ frost being stabilized at higher temperatures by the overburden pressure.

The difference in choice of lower boundary condition leads to only small changes in the net annual energy. Increasing H₂O thickness by ~30% for equivalent A_{H_2O} in the unsealed case restores parity.

Figure 5.A3 shows how varying the latitude, obliquity, and pressure affects the net annual energy balance. The results shown are for a $A_{H_2O} = 0.4$ (a typical value, e.g. Byrne et al. (2008)) and the assumption of a circular orbit. At lower latitudes and higher obliquities more solar power is delivered to the surface because summer is longer. The net annual energy balance is not significantly affected by varying the latitude down to ~80° S, and even at 60° S, a covering of ~4 m of pure H₂O would lead to a net zero annual energy balance. Varying the obliquity likewise only modestly affects the energy balance. Between obliquities of 20-45°, the net energy balance is zero for H₂O ice thicknesses of ~1-3 m; ~45° is the maximum obliquity reached in the past 21 Myr (Laskar et al., 2004). For $\epsilon < 20^\circ$, the net energy balance is negative for all thicknesses of H₂O ice.

The primary effect of changing the pressure is on the temperature of frost point, which affects the emitted power during the winter. Higher pressure increases the frost temperature, leading to greater emitted power and a lower net annual energy balance. Ranging the pressure between ~0.1-2 times the modern average atmospheric pressure has a similarly modest effect (Figure 5.A3).

References

Bierson, C.J., Phillips, R.J., Smith, I.B., Wood, S.E., Putzig, N.E., and Byrne, S., 2016. Stratigraphy and evolution of the buried CO₂ deposit in the Martian south polar cap. *Geophysical Research Letters* 43, 4172-4179.

Buhler, P.B., Ingersoll, A.P., Ehlmann, B.L., Fassett, C.I., Head, J.W. (2017). How the Martian Residual South Polar Cap Develops Quasi-Circular and Heart-Shaped Pits, Troughs, and Moats. *Icarus* 286, 69-93.

Buhler, P. B., Piqueux, S., Ingersoll, A. P., Ehlmann, B. L., and Hayne, P. O., 2018. EnTOMBR: An Energy Balance Model for Exploring the Sequestration of the Massive Martian Buried CO₂ Ice Deposit. LPSC 49 #2878

Byrne, S. & Ingersoll, A.P., 2003a. A sublimation model for the martian south polar ice features. *Science* 299, 1051-1053.

Byrne, S. & Ingersoll, A.P., 2003b. Martian climatic events on timescales of centuries: Evidence from feature morphology in the residual south polar ice cap. *Geophysical Research Letters* 30, 2-

Colaprete, A., Barnes, J.R., Haberle, R.M., Hollingsworth, J.L, Kieffer, H.H., and Titus, T.N., 2005. Albedo of the south pole on Mars determined by topographic forcing of atmosphere dynamics. *Nature* 435, 184-187.

Durham, W.B. & Stern, L.A., 2001. Rheological properties of water ice—applications to satellites of the outer planets. *Annual Reviews of Earth Science* 29, 295-330.

Guo, X., Lawson, G.W., Richardson, M.I., Toigo, A., 2009. Fitting the Viking lander surface pressure cycle with a Mars general circulation model. *J. Geophys. Res.* 114 (E07006), 1–19.

Guo, X., Richardson, M. I., Soto, A., and Toigo, A., 2010. On the mystery of the perennial carbon dioxide cap at the south pole of Mars. *Journal of Geophysical Research E: Planets* 115, 1-13.

Haberle, R.M. & Jakosky, B.M., 1990. Sublimation and Transport of Water from the North Residual Polar Cap on Mars. *Journal of Geophysical Research* 95, 1423-1437.

Haberle, R. M., F. Forget, A. Colaprete, J. Schaeffer, W. V. Boynton, N. J. Kelly, and M. J. Chamberlain (2008), The effect of ground ice on the Martian seasonal CO₂ cycle, *Planet. Space Sci.*, 56(2), 251–255

Haberle, R.M. et al., 2014. Secular climate change on Mars: An update using one Mars year of MSL pressure data. *American Geophysical Union (Fall)*. Abstract 3947.

Herkenhoff, K., and J. Plaut 2000. Surface ages and resurfacing rates of the polar layered deposits on Mars. *Icarus* 144, 243–255.

Hiesinger, Hess, S.L., Henry, R.M., Tillman, J.E., 1979. The seasonal variation of atmospheric pressure on Mars as affected by the south polar cap. *J. Geophys. Res.* 84, 2923– 2927

- Hourdin, F., Le Van, P., Forget, F., Talagrand, O., 1993. Meteorological variability and the annual surface pressure cycle on Mars. *J. Atmos. Sci.* 50, 3625–3640.
- Ingersoll, A.P., 1974. Mars: The case against permanent CO₂ frost caps. *Icarus* 79, 3403-3410.
- Jakosky, B.M., Henderson, B.G., and Mellon, M.T., 1995. Chaotic obliquity and the nature of the Martian climate. *Journal of Geophysical Research* 100, 1579-1584.
- Laskar, J., and Robutel, P., 1993. The chaotic obliquity of the planets. *Nature* 361, 608-612.
- Laskar, J., Correia, A.C.M., Gastineau, M., Joutel, F., Levrard, B., Robutel, P., 2004. Long term evolution and chaotic diffusion of the insolation quantities of Mars. *Icarus* 170, 343-364.
- Nye, J.F., Durham, W.B., Schenk, P.M., and Moore, J.M., 2000. The instability of a south polar cap on Mars composed of carbon dioxide. *Icarus* 144, 449-455.
- Owen, T., Biemann, K., Rushneck, D.R., Biller, J.E., Howarth, D.W., and Lafleur, A.L., 1977. The composition of the atmosphere at the surface of Mars. *Journal of Geophysical Research* 82, 4635-4639.
- Paige, D. A., and A. P. Ingersoll (1985), Annual heat balance of the Martian polar caps: Viking observations, *Science*, 228, 1160–1168
- Phillips, R.J., Davis, B.J., Tanaka, K.L., and 14 others, 2011. Massive CO₂ ice deposits sequestered in the south polar layered deposits of Mars. *Science* 332, 838-841.
- Pilorget, C., Forget, F., Millour, E., Vincendon, M., Madeleine, J.B., 2011. Dark spots and cold jets in the polar regions of Mars: New clues from a thermal model of surface CO₂ ice. *Icarus* 213, 131-149.

Smith, D.E., Zuber, M.T., Solomon, S.C., Phillips, R.J., Head, J.W., Garvin, J.B., Duxbury, T.C., et al., 1999. The global topography of Mars and implications for surface evolution. *Science* 284 (5419), 1495–1503.

Tanaka, K.L., Skinner, J., Dohm, J.M., Irwin, R.P., Kolb, E.J., Fortezzo, C.M., Hare, T.M., et al., 2014. Geologic map of Mars. U.S. Geol. Surv. Geol. Invest. 3292

Thomas, P.C., Malin, M.C., James, P.B., Cantor, B.A., Williams, R.M.E., Gierasch, P., 2005. South polar residual cap of Mars: features, stratigraphy, and changes. *Icarus* 174 (2 SPEC. ISS.), 535–559.

Thomas, P.C., Calvin, W., Cantor, B., Haberle, R., James, P.B., Lee, S.W., 2016. Mass balance of Mars' residual south polar cap from CTX images and other data. *Icarus* 268, 118–130

Titus, T.N., Kieffer, H.H., & Christensen, P.R., 2003. Exposed water ice discovered near the south pole of Mars. *Science* 299, 1048-1051.

*Chapter 6***CONCLUDING THOUGHTS****6.1. Introduction**

Over the past three decades the census of known planets orbiting other stars has exploded from zero to well over 3700⁸ and Pluto has now joined the ranks of solar system bodies with high resolution observations. In this context, the results of this thesis highlight the growing importance and opportunities for comparative planetology.

6.2. Gas Giant Interior Properties

HAT-P-13b has increased the number of planets with measured core masses from two (Jupiter and Saturn) to three. So far, measurements of these three planets are all consistent with core masses near 10 earth masses and thus the formation by core accretion (e.g. Pollack et al., 1996), although there are still considerable uncertainties and it cannot be ruled out that both HAT-P-13b and Jupiter have no core (Fortney and Nettleman, 2010; Buhler et al., 2016). Aside from improving the interior models used to convert from the Love number to the interior properties (e.g. Nettelmann et al., 2012) and additional observations of these planets—such as the ongoing Juno mission at Jupiter (Bolton, 2010)—we may hope to gain a greater understanding of the interior properties and formation pathways of giant planets by growing the census of HAT-P-13b-like

⁸ Shneider, J. “Interactive Extra-solar Planets Catalog”. The Extrasolar Planets Encyclopedia. Retrieved May 1, 2018.

planets. These additional observations will be crucial to testing theories for giant planet and planetary system formation.

The Kepler 424 (Endl et al. 2014), WASP-41 (Neveu-VanMalle et al. 2015), HAT-P-44, HAT-P-45, and HAT-P-46 (Hartman et al. 2014) systems are potential known candidates (Figure 6.1). However, the characteristics of these systems are not as favorable as in the case of the HAT-P-13 system because the expected equilibrium eccentricity is either very low or the relationship between the eccentricity and the Love number is shallow, so the eccentricity does not differentiate strongly between Love numbers. This means that the eccentricity must be determined with precision that is currently difficult to achieve. Another complication is that these systems have not been as extensively studied as the HAT-P-13 system, so their properties are much less well known, further obscuring the relationship between their eccentricity and Love number. Currently, these systems are so poorly understood that the eccentricity of the hot Jupiters are in all cases indistinguishable from zero. In some cases the presence of a perturbing outer companion is not even confirmed (but is strongly suspected). Further observation would be able to resolve these degeneracies.

The most potentially favorable system is currently HAT-P-44b, although degeneracy in the radial observations (measurements of the Doppler shift of the host star as it is tugged toward and away from the observer by an orbiting planet), means that there are several potential orbital configurations for the externally perturbing putative third body in the system (i.e. a HAT-P-13c analogue). Two potential orbital configurations place the external perturber at either an orbit of 220 days or 870 days. If the perturber is on the closer-in orbit, the precision of the eccentricity measurement required to meaningfully distinguish the Love number of HAT-P-44b is similar to the case of HAT-P-13b (Figure 6.1b). However, if the external perturber is on the more distant

orbit, the necessary measurement precision is much higher because the perturber would have a diminished effect on the orbital evolution of HAT-P-44b (Figure 6.1c). Unfortunately, for the prospects of determining the core mass of HAT-P-44b, the 870-day orbit of the external perturber is more likely (Hartman et al. 2014).

It is therefore prudent to continue to improve the characterization of these potential HAT-P-13 analogue systems, particularly the HAT-P-44 system, given their potential to increase the currently very limited sample of gas giants with core mass determinations. On the bright side, with the search for exoplanets continuing unabated, we may hope to find more HAT-P-13b analogues and increase our capability for comparative planetology and understanding of the interior properties and formation pathways of gas giant planets.

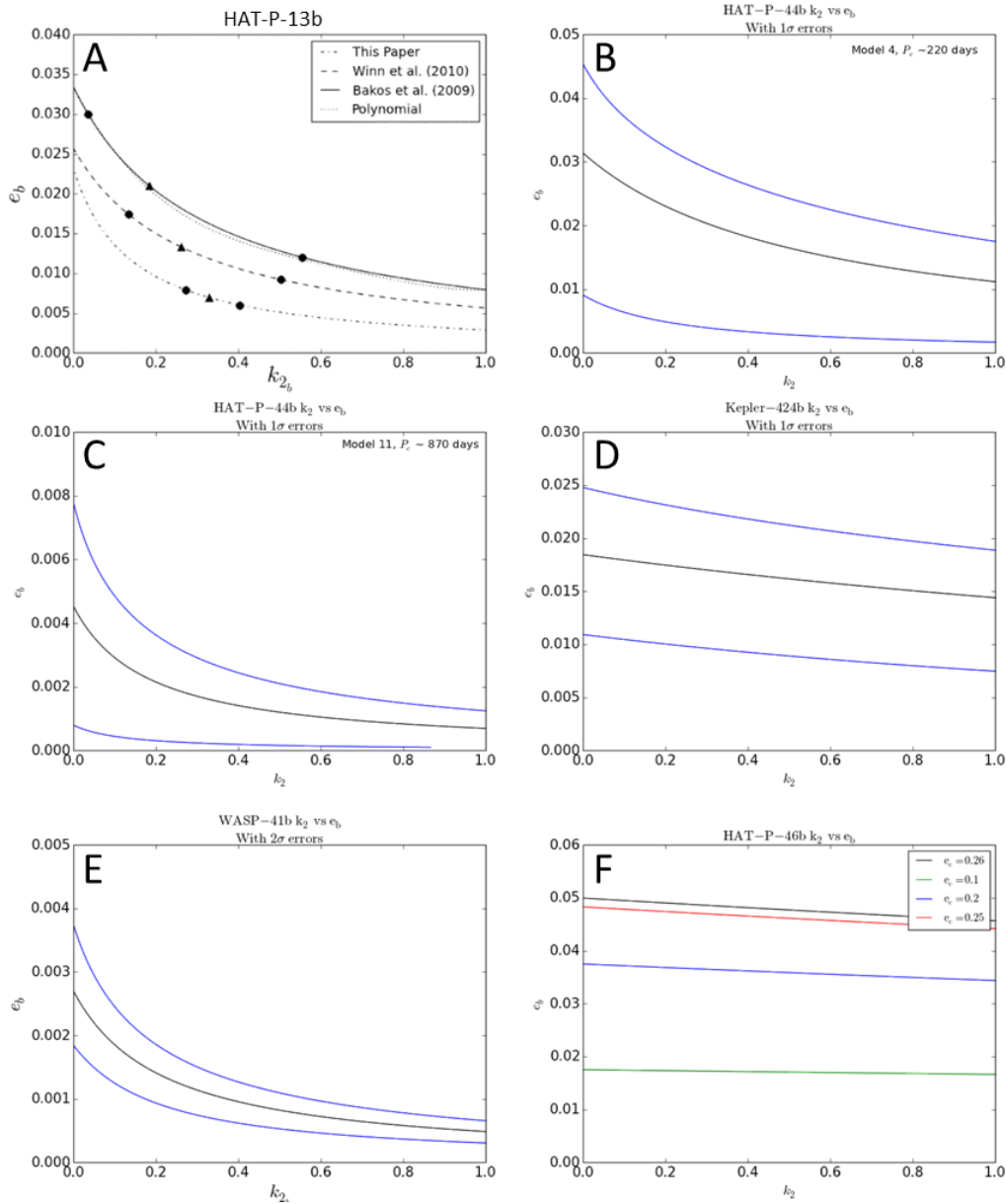


Figure 6.1. **A.** Relationship between eccentricity e_b and Love number k_{2b} for the HAT-P-13 system parameters measured by different studies, including the fourth-order polynomial approximation given in Batygin et al. (2009). The best-fit (triangles) and 1σ (circles) uncertainties in e_b reported by each study are plotted on their respective e_b - k_{2b} curves. The curves do not include uncertainties in the e_b - k_{2b} relationship due to measurement errors. **B.** The e_b - k_{2b} relationship for HAT-P-44b if the external perturber has a 220-day orbit. Blue lines indicate 1σ uncertainty in the relationship due to uncertainties in other system properties. **C.** Same, but if the external perturber has an 870-day orbit. **D.** Same for Kepler-424b. **E.** Same for WASP-41b. **F.** Same for HAT-P-46b, but different lines now represent the relationship for different values of external perturber eccentricity e_c .

6.2. Climates and Surfaces of Bodies with Atmospheres Controlled by Vapor Pressure

Equilibrium

The *New Horizons* mission revealed that the plutonian surface hosts unexpected diversity and complexity of landforms akin to those found on Mars (Stern et al., 2015). The distinct, yet similar secular climate cycles on both bodies will allow us to make comparative inquiries into climates driven by the condensation, sublimation, and redistribution of volatile surface ices under the influence of variable insolation forcing. These inquiries will become even more valuable as we explore terrestrial exoplanets in increasing detail because, while methods exist for characterizing exoplanetary atmospheres (e.g. Seager and Deming, 2010), we are far from being able to measure the properties of exoplanetary surfaces. Thus, the insights gained from studying Mars and Pluto will be instrumental in interpreting the general climate and surface properties of these distant planets. Study of the climates of icy worlds in preparation for comparative planetology is particularly timely following the recent (April, 2018) launch of the Transiting Exoplanet Survey Satellite (TESS), which will search for terrestrial planets around nearby stars, including potential Mars analogues (Ricker et al., 2010).

One such avenue for comparison is the secular condensation and deposition cycle on Sputnik Planitia and the secular evolution of the martian south polar CO₂ deposit. Bertrand et al. (2018) model the sublimation and deposition patterns in Sputnik Planitia and find that over the past two million years, the central region of Sputnik Planitia experiences net deposition, while the northern region experiences net accumulation. Thus, Sputnik Planitia experiences net deposition and net accumulation states that are contemporaneous but spatially distinct, while these two states are likely co-spatial but temporally distinct for the martian polar CO₂ deposits. Furthermore, the central and southern regions of Sputnik Planitia also have the potential to provide insight into the

surface processes and morphological development of the south polar CO₂ deposits during periods of falling atmospheric pressure (net surface deposition). This is invaluable because my model results indicate that the martian pressure will not begin falling again for another 7000 years, which is a long time to wait.

References

Batygin, K., Bodenheimer, P., and Laughlin, G., 2009. Determination of the Interior Structure of Transiting Planets in Multiple-Planet Systems. *The Astrophysical Journal*, 704, pp. L49-L53.

Bertrand, T., Forget, T, Umurhan, O.M, Grundy, W.M., Schmitt, B., Protopapa, S., Zanarif, A.M., White, O.L., Schenk, P.M., Singer, K.N, and 5 others, 2018. The nitrogen cycles on Pluto over seasonal and astronomical timescales. *Icarus* 309, 277-296

Bolton, S. J. and the Juno Science Team, 2010. The Juno Mission. *Proceedings of the International Astronomical Union S269*, 92-100

Buhler, P.B., Knutson, H.A., Batygin, K., Fulton, B.J., Fortney, J.J., Burrows, A., Wong, I. (2016). Dynamical Constraints on the Core Mass of Hot Jupiter HAT-P-13b, *The Astrophysical Journal* 821, pp. 26-37

Endl, M., Caldwell, D. A., Barclay, T., Huber, D., Isaacson, H., Buchhave, L. A., Brugamyer, E., Robertson, P., Cochran, W. D., MacQueen, P. J., and 6 others, 2014. Kepler-424 b: A "Lonely" Hot Jupiter That Found A Companion. *The Astrophysical Journal*, 795, pp. 151-164.

Fortney, J. J. & Nettelmann, N., 2010. The interior structure, composition, and evolution of giant planets. *Space Science Reviews*, 152, pp. 423-447.

Hartman, J. D., Bakos, G. Á., Torres, G., Kovács, G., Johnson, J. A., Howard, A. W., Marcy, G. W., Latham, D. W., Bieryla, A., Buchhave, L. A., and 19 others, 2013. HAT-P-44b, HAT-P-45b, and HAT-P-46b: Three Transiting Hot Jupiters in Possible Multi-Planet Systems. *The Astronomical Journal*, 147, pp. 128-146.

Nettelmann, N., Becker, A. Holst, B. and Redmer, R., 2012. Jupiter models with improved ab initio hydrogen equation of state (H-REOS.2). *The Astrophysical Journal* 750, 52

Neveu-VanMalle, M., Queloz, D., Anderson, D. R., Brown, D. J. A., Collier Cameron, A., Delrez, L., Díaz, R. F., Gillon, M., Hellier, C., Jehin, E., and 7 others, 2016. Hot Jupiters with relatives: discovery of additional planets in orbit around WASP-41 and WASP-47. *Astronomy & Astrophysics*, 586, pp. A93(1-12).

Pollack, J. B., Hubickyj, O., Bodenheimer, P., Lissauer, J. J., Podolak, M., and Greenzweig, Y., 1996. Formation of the giant planets by concurrent accretion of solids and gas. *Icarus*, 124, pp. 62-85.

Ricker, G.R, Latham, D.W., Vanderspek, R. K., Ennico, K. A., Bakos, G., Brown, T. M., Burgasser, A. J., Charbonneau, D., Clampin, M., Deming, L. D., and 1 others, 2010. Transiting Exoplanet Survey Satellite (TESS). AAS Meeting #215, id.450.06

Seager, S. & Deming, D., 2010. Exoplanet Atmospheres. *Annual Review of Astronomy and Astrophysics* 48, 631-672